**DOT/FAA/TC-26/15**

Federal Aviation Administration
William J. Hughes Technical Center
for Advanced Aerospace
Aviation Research Division
Atlantic City International Airport
New Jersey 08405

# National Airport Pavement Test Facility Construction Cycle 9

# Volume 3—Geosynthetic Test

March 2026

Final Report

U.S. Department of Transportation
**Federal Aviation Administration**

# NOTICE

**Technical Report Documentation Page**

| | | |
|---|---|---|
| 1. Report No.<br>DOT/FAA/TC-26/15 | 2. Government Accession No. | 3. Recipient's Catalog No. |

| | |
|---|---|
| 4. Title and Subtitle<br>NATIONAL AIRPORT PAVEMENT TEST FACILITY CONSTRUCTION CYCLE 9<br>VOLUME 3—GEOSYNTHETIC TEST | 5. Report Date<br>March 2026 |
| | 6. Performing Organization Code<br>ANG-E262 |
| 7. Author(s)<br>Hasan Kazmee*, Scott Murrell*, Lia Ricalde*, Timothy Parsons*, Ebenezer Duah*, David R. Brill, and Daniel I. Offenbacker | 8. Performing Organization Report No. |
| 9. Performing Organization Name and Address<br>U.S. Department of Transportation<br>Federal Aviation Administration<br>Airport Pavement R&D Section<br>William J. Hughes Technical Center for Advanced Aerospace<br>Atlantic City International Airport, NJ 08405<br>*ARA, Inc<br>2628 Fire Road<br>Suite 300<br>Egg Harbor Twp, NJ 08234 | 10. Work Unit No. (TRAIS) |
| | 11. Contract or Grant No.<br>692M15-20-D-00004 |
| 12. Sponsoring Agency Name and Address<br>U.S. Department of Transportation<br>Federal Aviation Administration<br>Airport Engineering Division<br>800 Independence Ave., SW<br>Washington, D.C. 20591 | 13. Type of Report and Period Covered<br>Final Report |
| | 14. Sponsoring Agency Code<br>AAS-100 |

15. Supplementary Notes

The FAA Airport Technology Research and Development Contracting Officer's Representative (COR) is Murphy Flynn.

16. Abstract

Construction Cycle 9 (CC9) was the ninth in a series of full-scale airport pavement tests performed at the Federal Aviation Administration (FAA) National Airport Pavement Test Facility, the fifth involving flexible pavements. It contained four test areas: fatigue, geosynthetics, cement-treated permeable base, and overload. This report addresses the geosynthetics test area, which consisted of two test items: LFC-3N with a geotextile separation fabric between the subgrade and subbase plus a Class B geogrid at the subbase/base interface, and LFC-3S with just the geotextile. These test items were subjected to simulated full-scale aircraft trafficking along with a control test item (LFC-4S) with similar materials and thickness but not containing geosynthetics. The goal of this test was to quantify any improvement in performance of the geosynthetic test items when compared to the control test item. Data were collected through laboratory and in situ testing, visual evaluation, and embedded pavement sensors. Researchers analyzed the effect of construction practices on pavement performance and compared pavement responses in all structural layers, in particular examining how the accumulation of permanent deformation is affected by the presence or absence of geogrid reinforcement and geotextile separation fabric. All three test items experienced structural failure before the end of traffic. Test items with geosynthetic elements had greater surface upheaval, rutting, and crack density than the control section; however, this was attributed to improper compaction of the sublayers during construction. The embedded sensors indicated that the geogrid increased the resistance to permanent deformation in the granular subbase layer. Despite accumulating higher surface rutting (attributed to the underlying compaction issues), the geogrid-reinforced test item LFC-3N exhibited lower upheaval than the other test items when trafficked beyond the pass where the failure criterion was met (1-in. dilative heave). The inclusion of geogrid aided in lateral confinement and resulted in lower permanent deformation in the subbase layer of LFC-3N than in the subbase layers of the LFC-3S and LFC-4S.

| | |
|---|---|
| 17. Key Words<br>National Airport Pavement Test Facility, NAPTF, Construction Cycle 9, CC9, Geosynthetics, Geogrid | 18. Distribution Statement<br>This document is available to the U.S. public through the National Technical Information Service (NTIS), Springfield, Virginia 22161. This document is also available from the Federal Aviation Administration William J. Hughes Technical Center for Advanced Aerospace at actlibrary.tc.faa.gov. |

| | | | |
|---|---|---|---|
| 19. Security Classif. (of this report)<br>Unclassified | 20. Security Classif. (of this page)<br>Unclassified | 21. No. of Pages<br>142 | 22. Price |

**Form DOT F 1700.7** (8-72) Reproduction of completed page authorized

# TABLE OF CONTENTS

APPENDICES

# LIST OF FIGURES

LIST OF TABLES

# LIST OF ACRONYMS

| | |
|---|---|
| 2D | Two Duals in Tandem (four-wheel) |
| 3D | Three Duals in Tandem (six-wheel) |
| 3-D | Three-dimensional |
| AASHTO | American Association of State Highway and Transportation Officials |
| AC | Asphalt concrete |
| ASTM | American Society for Testing and Materials |
| ASG | Asphalt strain gauge |
| AUPP | Area under pavement profile |
| BDI | Base damage index |
| BE | Bender element |
| CBR | California bearing ratio |
| CC | Construction cycle |
| CC9 | Construction cycle 9 |
| CD | Crack density |
| CH | High-plasticity clay |
| CS | Coil sensor |
| DBP | Deflection basin parameter |
| D-PSPA | Portable Seismic Properties Analyzer for Unbound Layers |
| ERDC | U.S. Army Engineer Research and Development Center |
| F2 | Shape factor |
| FAA | Federal Aviation Administration |
| FAA AC | FAA Advisory Circular |
| HMA | Hot mix asphalt |
| HTITS | High-temperature indirect tensile strength |
| HWD | Heavy weight deflectometer |
| IDT | Indirect tensile |
| ISM | Impulse stiffness modulus |
| LiDAR | Light Detection and Ranging |
| LSG | Longitudinal strain gauge |
| LWD | Light weight deflectometer |
| MC | Moisture content |
| MEPDG | Mechanistic-Empirical Pavement Design Guide |
| NAPTF | National Airport Pavement Test Facility |
| NAPTV | National Airport Pavement Test Vehicle |
| NDT | Nondestructive test |
| OMC | Optimum moisture content |
| PC | Pressure cell |
| PG | Performance grade |
| PSPA | Portable seismic properties analyzer |
| QA/QC | Quality Assurance/Quality Control |
| QS | Quick shear |
| SSR | Subgrade stress ratio |
| SU | Sampling unit |
| TSG | Transverse strain gauge |
| UCS | Unconfined compressive strength |

# EXECUTIVE SUMMARY

From 2020 to 2024, the Federal Aviation Administration (FAA) executed a series of full-scale traffic tests on flexible airport pavements at the National Airport Pavement Test Facility (NAPTF), designated Construction Cycle 9 (CC9). Within CC9, the geosynthetic test was designed to test the performance of flexible airport pavements with geosynthetic structural elements. This report addresses three test items within CC9: LFC-3N, LFC-3S, and LFC-4S. LFC-3N incorporated a geotextile separation fabric between the subgrade and subbase and a Class B geogrid at the subbase/base interface, while LFC-3S had just the geotextile. LFC-4S was the control test item, which had similar materials and thickness but did not incorporate geosynthetics. All three test items were subjected to simulated full-scale aircraft traffic. The goal was to quantify any improvement in performance of the geosynthetic-reinforced test items relative to the control test item.

This report covers data collection and analysis from the construction, pre-traffic, and traffic testing phases. During the construction phase, materials were carefully characterized through laboratory and in situ testing. During traffic, data were acquired from regular visual surveys, nondestructive testing (NDT), and embedded pavement sensors. Embedded sensors were in all layers to enable researchers to analyze the effect of geogrid reinforcement on pavement responses to load. Accumulation of permanent deformation in the individual pavement layers was also examined using strategically placed inductive coil sensors.

All three test items experienced a classic flexible pavement structural failure, including deep ruts accompanied by substantial upheaval of the pavement surface outside the limits of applied traffic. However, throughout the test, the geosynthetic-reinforced test items exhibited greater surface upheaval, rutting, and crack density than the control section. This unexpected result was attributed to improper compaction of the sublayers during construction. A more detailed analysis based on embedded sensor data indicated that the geogrid increased the resistance to permanent deformation in the granular subbase layer. Despite accumulating higher surface rutting (attributed to the underlying compaction issues), the geogrid-reinforced test item LFC-3N exhibited less upheaval than its counterparts when trafficked beyond the nominal failure condition (approximately 1 in. of upheaval). The inclusion of a geogrid aided in lateral confinement and resulted in lower permanent deformation in the subbase layer of LFC-3N than in LFC-3S or LFC-4S.

Due to the construction issues that were identified and the small number of test items analyzed, this report recommends further full-scale testing of geosynthetics as possible structural elements in airport flexible pavements.

# 1. INTRODUCTION

Geosynthetics have been used in highway applications for layer separation, filtration for drainage, mitigation of reflective cracking, and reinforcement of unbound pavement layers. Several studies on highway applications of geogrid reinforcement have shown an overall improvement in the service life of the pavement system. Jersey et al. (2012) constructed and tested a full-scale geogrid-reinforced pavement system under accelerated loading. They used a geogrid for base reinforcement under thin asphalt overlays and compared its rutting performance to two different unreinforced pavement systems with a thicker asphalt overlay. Jersey et al. (2012) found that the geogrid-reinforced pavement system had considerably less rutting after 100,000 equivalent single axle loads compared to the thicker asphalt overlay. Similar findings regarding the benefits of geogrid reinforcement have been documented in literature using both laboratory and field assessments (Al-Qadi et al., 2012; Jayalath et al., 2021; Robinson et al., 2017, 2018, 2020).

There has been considerably less research on the benefits of using geosynthetic materials as structural elements in airport pavements. Previous research at the U.S. Army Engineer Research and Development Center (ERDC) investigated geogrid-reinforced sections using reduced-scale box tests (Jersey et al., 2012). ERDC also performed full-scale testing of geogrid-stabilized roadway pavements on weak subgrades (Norwood & Tingle, 2014; Robinson, 2022). However, there is a lack of full-scale test data on flexible pavements built to Federal Aviation Administration (FAA) standards and including geosynthetic materials. The Construction Cycle 9 (CC9) geosynthetics test at the National Airport Pavement Test Facility (NAPTF) was intended to address this research gap.

FAA Advisory Circular (FAA AC) 150/5370-10H, *Standard Specifications for Construction of Airports*, allows but does not require the use of geogrids and/or layer separation geotextiles under Item P-154, Subbase Course (FAA, 2018). The FAA standards currently do not provide for any reduction in layer thicknesses based on the use of geosynthetic materials.

## 1.1 PROBLEM STATEMENT/ RESEARCH NEED

The FAA Reauthorization Act of 2018, Section 558 states:

> The Administrator of the Federal Aviation Administration, to the extent practicable, shall encourage the use of durable, resilient, and sustainable materials and practices, including the use of geosynthetic materials and other innovative technologies, in carrying out the activities of the Federal Aviation Administration. (FAA Reauthorization Act of 2018, 2018).

The CC9 geosynthetics test in NAPTF was conducted in part in response to this statutory requirement. To determine the merit of using geosynthetics as a structural element in rigid and flexible airfield pavement design and the benefits gained from this application, the FAA performed full-scale accelerated pavement testing using simulated full-scale aircraft loads on geosynthetic-augmented airport pavement structures.

## 1.2 OBJECTIVE AND SCOPE

The objective of the CC9 geosynthetic test area was to assess the effect of geosynthetic inclusions on flexible airport pavement performance. The test considered two types of geosynthetic materials added to a standard flexible airport pavement structure:

- Geogrid reinforcement placed in the unbound base layer
- Geotextile separation fabric placed between the clay subgrade and the granular subbase

## 1.3 NATIONAL AIRPORT PAVEMENT TEST FACILITY TERMINOLOGY

### 1.3.1 Test Terminology

The following sections define terms and phrases commonly used at the NAPTF.

Construction Cycle (CC). CC refers to the overall test project including design, construction, traffic testing, post-traffic testing, data collection, data analysis, and final demolition. Each CC is developed with specific test objectives. Typically, a CC is dedicated to either rigid or flexible pavement testing.

Test Area. Each CC is divided into multiple test areas as required by the test objectives. Dividing the test pavement into test areas allows the FAA to conduct multiple experiments simultaneously. A test area can be made up of one or more test items.

Transition Area. Transition areas separate the test items in the longitudinal direction, avoiding abrupt changes in layer thickness at test item boundaries. Transition areas are of sufficient length to allow vehicle start-up and shutdown while maintaining a constant speed and load over the test items themselves.

Test Item. A test item is a unit of pavement within the test area characterized by a unique combination of pavement structure and test traffic. For CC9, each test area was divided into two test items, designated north and south, on the corresponding sides of the facility centerline. Each test item is designated by an identifier consisting of three letters, followed by a dash and two additional characters.

- The first letter corresponds to the strength of the subgrade (L = low strength, M = medium strength, or H = high strength).
- The second letter corresponds to the type of pavement structure (F = flexible or R = rigid).
- The third letter corresponds to the type of base (S = stabilized, C = conventional/unstabilized, or G = slab-on-grade/no base).
- The last two characters give the sequential numbering of the test item, and whether it is on the north (N) or south (S) side of the centerline.

As an example, in this report the designation LFC-5N refers to the north test item of Test Area 5 that is built on a low-strength subgrade (L), using a flexible (F) pavement, with an aggregate (i.e., conventional, C) base course. Test items are numbered from west to east.

Wander Pattern. The National Airport Pavement Test Vehicle (NAPTV), shown in Figure 1, executes a wander pattern consisting of a repeated sequence of 66 passes arranged in 9 longitudinal tracks. The lateral spacing between adjacent tracks is 10.25 in. The NAPTF wander pattern is designed to approximate a normal lateral distribution of aircraft traffic with a standard deviation from centerline equal to 30.54 in.

Figure 1. National Airport Pavement Test Vehicle

### 1.3.2 Work Item Modifiers

In general, NAPTF test items follow the material and construction standards in FAA Advisory Circular 150/5370-10H, *Standard Specifications for Construction of Airports* (FAA, 2018). However, research objectives may require deviation from some aspects of the standard. To indicate that the construction specification is altered, work items are modified with the following designations: M = Modified, R = Research, MR = Modified Research. Material items listed below are modified from the standard FAA specifications.

- P-152MR Subgrade: Work Item P-152MR is a prepared subgrade composed of soil that provides the specified design California bearing ratio (CBR) values for test items constructed on low strength subgrades. The subgrade material is prepared in the excavated bed of the NAPTF or the FAA Subgrade Processing building in accordance with the project specifications.

- P-209MR Crushed Aggregate Base Course: Work Item P-209MR is a base course composed of crushed aggregate.

- P-401MR Asphalt Mix Pavement Surface Course: Work Item P-401MR is a hot mix asphalt (HMA) pavement course composed of mineral aggregate and asphalt binder mixed in a central mixing plant, placed on a prepared base or stabilized course, and compacted. It can be used for multiple pavement courses but is typically used as a surface course.

## 2. DESIGN AND CONSTRUCTION OF TEST AREAS

CC9 was built on the west end of the NAPTF building. All test areas were built on clay subgrade with a nominal CBR of 5 (hence "low strength," L). The CC9 geosynthetics test area consisted of three test items, designated LFC-3N, LFC-3S, and LFC-4S, as shown in Figure 2. LFC-4S had no geogrid reinforcement or geotextile separation layer and served as the control. LFC-3N included both a geogrid and geotextile fabric, and LFC-3S contained a geotextile fabric only. Locations within the test area are identified by stations and offset left (north) or right (south) of the centerline, in feet. The geosynthetic test items were constructed between station 1+20 and 2+25. Allowing for the 3-ft shoulders, the center of traffic for test item LFC-3N was at lateral offset -15 ft, and the center of traffic for the two south test items LFC-3S and LFC-4S were at +15 ft. As shown in Figure 2, each test item was 33 ft wide by 45 ft long, with 15-ft transition areas separating the test items.

Figure 3 shows cross-sections of the pavement structures. All three test items had identical pavement layers except for the presence or absence of geotextiles and geogrid. A biaxial geogrid was installed at the bottom of the crushed aggregate base course layer with a nonwoven geosynthetic fabric separating the granular subbase and compacted subgrade in test item LFC-3N. Only the nonwoven separation fabric was placed at the bottom of the granular subbase in test item LFC-3S. The control test item had neither geogrid nor geosynthetic separation fabric. All three test items had approximately 5-in.-thick plant mix bituminous pavement on top of an approximately 8-in.-thick crushed aggregate base course layer over 29-in.-thick granular subbase.

The instrumentation layout was designed considering traffic wander. As discussed in Section 1.3.1, the traffic followed a defined wander pattern giving an approximately normal lateral distribution. The center positions of the north and south carriages (see Figure 1) were set at transverse offsets -15 and +15 ft, respectively. Those center offsets were assigned to wander track 0. At the outermost wander positions (tracks -4 and 4), the outer wheels of the load modules could traverse 5,662 ft north and south of center offsets. For example, the outer wheels of LFC-3N operated between -9.338 and -20.662 ft. Areas outside these limits were considered untrafficked. Further details on the wander pattern are presented in Section 4.

## 2.1 REVIEW OF CONSTRUCTION, QUALITY CONTROL, AND ASSURANCE

### 2.1.1 Placement and Compaction of Subgrade (P-152MR)

The CC9 subgrade (P-152MR) consists of two clay materials. The upper subgrade is Dupont clay, classified by the Unified Soil Classification system as a high-plasticity clay (CH) with a plastic limit of 19 and liquid limit of 56. Approximately 5 feet below the surface of Dupont clay is County

Sand and Stone clay (classified as MH-CH), which was originally placed during CC1 construction. Both materials were sourced from the Delaware Bay area, approximately 40 miles west of the NAPTF. Subgrade material was either reprocessed (tilled, spread/shifted, recompacted) in situ to meet the required grade at the target CBR, or new material was added and processed in situ to the target CBR. When new material was required, it was brought to the NAPTF from a stockpile located in a subgrade processing facility yard adjacent to the NAPTF.

As shown in Figure 3, LFC-3N is the only section of the three that incorporated P-152 fill from the stockpile. This fill added complexity to achieving a uniform strength subgrade. The existing subgrade prior to construction already included two types of Dupont clay. With the addition of the fill there were three variations of subgrade with distinct strength-moisture relationships. As a result, achieving a consistent subgrade for LFC-3N, LFC-3S, and LFC-4S was problematic. Additional details pertaining to the prepared subgrade placement can be found in Tomlinson et al. (2022).

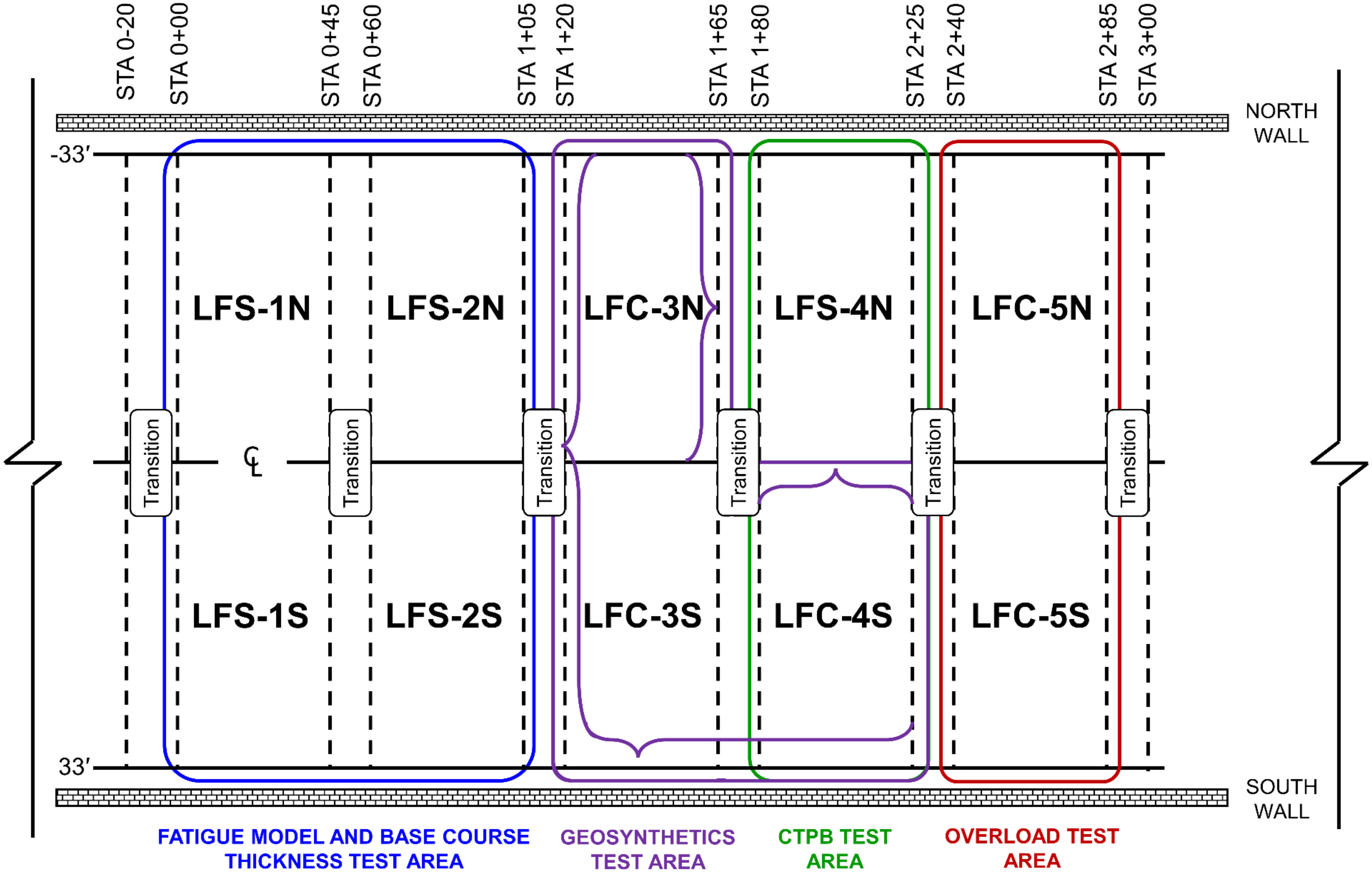

Figure 2. Plan View of the CC9 Test Areas and Items

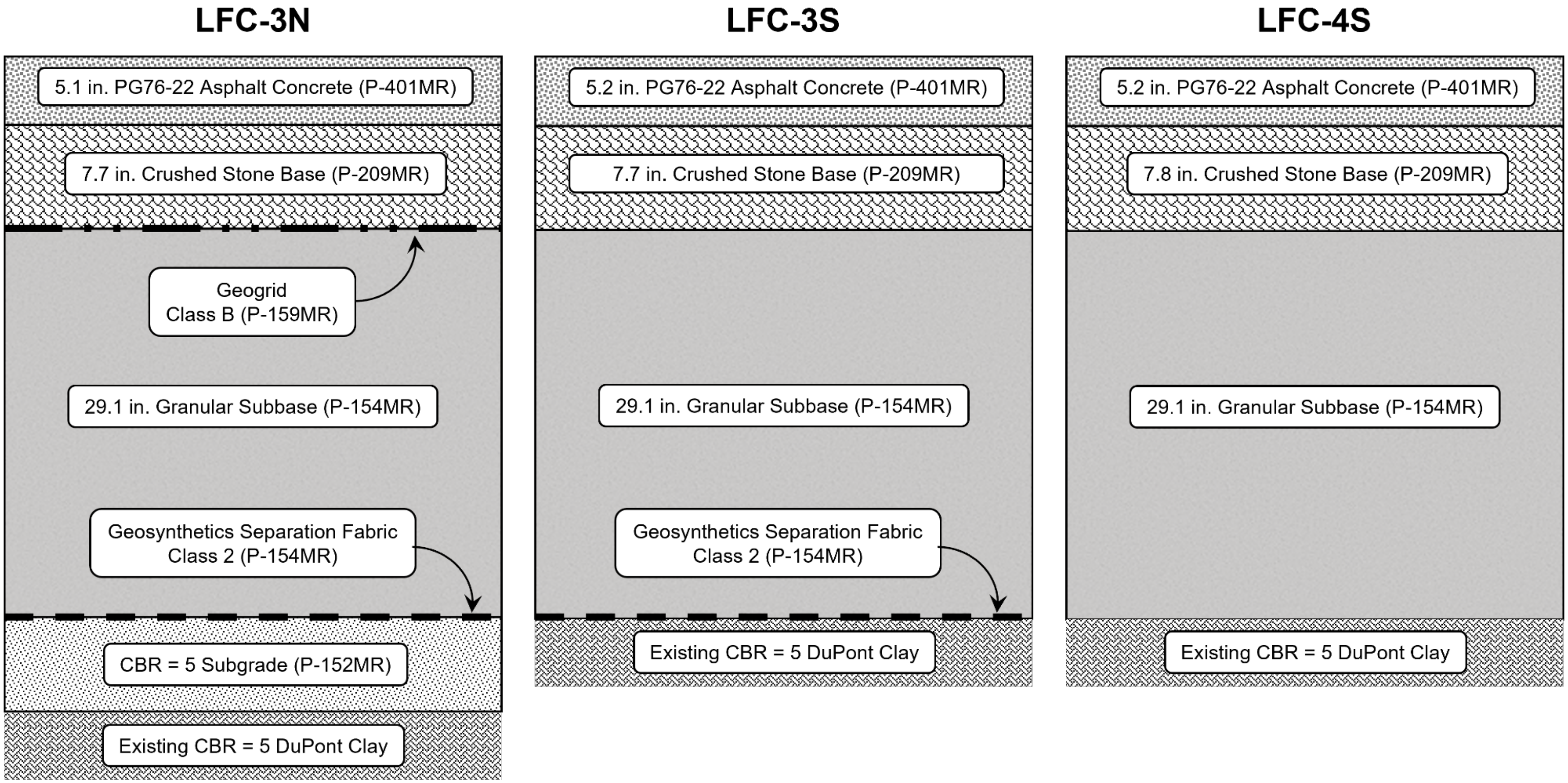

Figure 3. As-Built Cross-Sections of Geosynthetic Test Items

### 2.1.2 Placement and Compaction of Subbase Course (P-154 MR)

The subbase was a carbonate-based, manufactured sand placed in lifts ranging from 5 to 10 in. for all layers. Steel drum rollers were used to compact each lift. Compaction was performed in both longitudinal and transverse directions throughout the test items. A nuclear density gauge was used to determine density and moisture content (MC) at depths that did not exceed the lift thickness. Measurements were made at two random locations in each test item, and the average of those values had to meet or exceed the target dry density of 138.3 pcf, with a MC between 2% and 6%. In establishing these criteria, the target density corresponded to the maximum density on the modified Proctor curve at 6% MC. A maximum of 6% MC was chosen since that was the highest value for which no drain-down was observed during laboratory testing.

### 2.1.3 Placement and Compaction of Base Course (P-209MR)

The base layer material was a blend of three diabase granular materials sourced from Birdsboro Quarry in Skippack, PA. The base was placed in lifts of 4 to 8 in. Steel drum rollers were used to compact each lift. A nuclear density gauge was used to determine density and MC. Two random locations were selected in each test item for acceptance testing, and the average of those values was required to meet or exceed the target dry density of 151.3 pcf, with a MC between 1.5% to 5.5%. The target density corresponded to the maximum density on the modified proctor curve. A maximum of 5.5% MC was chosen since that was the highest value where no drain-down was observed during laboratory testing.

### 2.1.4 Paving and Compaction of Asphalt Concrete

The asphalt mixture conformed to the FAA P-401MR specification as presented in Tomlinson et al. (2022). The nominal maximum aggregate size was 0.75 in. Table 1 lists the complete gradation. A performance grade (PG) 76-22 asphalt binder was used with a binder content of 5% (by total mixture weight). The asphalt layer was placed in two lifts. A nuclear density gauge was used to monitor compaction of the test area during compaction. For the first lift, the asphalt was paved and compacted using a static roller. Rollers were used in static mode to protect the instrumentation embedded in the asphalt layer. For the second lift, two rollers were operated in vibratory mode until density was achieved as indicated by the nuclear gauge. A final roller pass in static mode removed any roller marks.

Table 1. Aggregate Gradation for P-401MR

| Sieve Designation | Contractor-Provided Percent Passing, % | Percent Passing Band, % |
|---|---|---|
| 1 in. (25 mm) | 100.0 | 100 |
| 3/4 in. (19 mm) | 97.1 | 90–100 |
| 1/2 in. (12.5 mm) | 84.0 | 68–88 |
| 3/8 in. (9.5 mm) | 74.4 | 60–82 |
| No. 4 (4.75 mm) | 52.0 | 45–67 |
| No. 8 (2.38 mm) | 36.0 | 32–54 |
| No. 16 (1.19 mm) | 25.2 | 22–44 |
| No. 30 (600 µm) | 17.8 | 15–35 |
| No. 50 (300 µm) | 11.4 | 9–25 |
| No. 100 (150 µm) | 7.2 | 6–18 |
| No. 200 (75 µm) | 4.0 | 3–6 |

### 2.1.5 Mechanical Properties of Geosynthetics and Geogrid

A Class 2 separation fabric was installed between the subgrade and subbase in test items LFC-3N and LFC-3S. The nonwoven geotextile had a CBR puncture strength of 434 lb. The reported grab tensile strengths in the machine and cross directions were 201 and 172 lb, respectively. The reported trapezoid tear strength for both machine and cross directions was 77 lb. (see Appendix F of Tomlinson et al., 2022). The 12.5-ft-wide fabric was placed transversely across the width of the test item with an overlap of 18 in. for each transverse placement.

A Class B geogrid was installed between the P-154MR subbase and P-209MR base in test item LFC-3N. The biaxial geogrid had a 1.5-in.-square aperture with minimum rib thicknesses of 0.04 and 0.03 in. in the machine and cross-machine directions. The reported tensile strengths at 2% strain, 5% strain, and ultimate strength were 450, 890, and 1370 lb/ft, consecutively. The biaxial geogrid was cut into three widths (13.1 ft, 8.3 ft, and 13.1 ft) and placed longitudinally from station 1+13 to station 1+73, with a 1.5-ft overlap between cuts.

## 2.2 IN-PLACE TESTING FOR CONSTRUCTION UNIFORMITY

Tables 2 and 3 list the acceptance and characterization tests run on each pavement layer in the CC9 geosynthetics test area. Detailed test results for acceptance and characterization are available in Tomlinson et al. (2022), Appendices D and E. A total of 45 material characterization tests were run: 12 on the clay subgrade (P-152MR), 11 on the granular subbase (P-154MR), 10 on the crushed granular base (P-209MR), and 12 on the asphalt (P-401MR). During the period of testing, the NAPTF NextGen Pavement Materials Laboratory was closed for several months due to the COVID-19 health emergency, and various laboratory tests were delayed.

Table 2. Listing of Characterization Tests for CC9 Granular Materials

| Test | P-152MR | P-154MR | P-209MR |
|---|---|---|---|
| Vane shear | X | | |
| LWD | X | X | X |
| D-PSPA | X | X | X |
| GeoGauge | X | X | X |
| DCP | X | X | |
| Atterberg limits | X | X | X |
| Specific gravity | X | X | X |
| Modified proctor | X | X | X |
| CBR (Laboratory) | X | | |
| Repeated load permanent deformation | X | X | X |
| Resilient modulus | X | X | X |
| Unconfined compressive strength (Quick shear) | X | X | X |
| Sieve analysis | | X | X |

DCP = Dynamic cone penetrometer
D-PSPA = Portable seismic properties analyzer for unbound layers
LWD = Light weight deflectometer

Table 3. Listing of Characterization Tests for Asphalt Material

| **Test** | **P-401MR** |
|---|---|
| Sieve analysis | X |
| PSPA | X |
| Gmb/Gmm | X |
| Ignition oven | X |
| Dynamic modulus/Flow number | X |
| HTITS | X |
| TSR | X |
| DCT | X |
| APA | X |
| Beam fatigue | X |
| Density (Nuclear gauge) | X |
| HWD | X |

APA = Asphalt pavement analyzer
DCT = Disc-shaped compact tension
Gmb/Gmm = Bulk specific gravity/theoretical maximum specific gravity
HWD = Heavy weight deflectometer
HTITS = High-temperature indirect tensile strength
PSPA = Portable seismic properties analyzer
TSR = Tensile strength ratio

Light weight deflectometer (LWD) modulus values were determined from Boussinesq’s half-space equation (Mooney & Miller, 2009). The stress distribution factors listed in Table 4 are those recommended by Bilodeau and Doré (2014), assuming Poisson's ratios and LWD plate radii are as listed in Table 4.

$$E = \frac{f \times (1 - \nu^2) \times \sigma_0 \times a}{d_0} \tag{1}$$

where:

$E$ = LWD modulus,
$f$ = stress distribution factor,
$\nu$ = Poisson's ratio,
$\sigma_0$ = contact stress,
$a$ = plate radius, and
$d_0$ = center deflection.

Table 4. Properties and Assumptions for the Determination of LWD Modulus

| Layer | Poisson's Ratio | Stress Distribution Factor | Plate Radius (in.) |
|---|---|---|---|
| Subgrade | 0.4 | 4/3 | 5.9 |
| Granular Subbase | 0.35 | 8/3 | 5.9 |
| Crushed Aggregate Base | 0.35 | 8/3 | 3.0 |

### 2.2.1 Subgrade

Table 5 lists material properties tested on the subgrade. Figure 4 plots in situ CBR for the geosynthetics test area. The subgrade CBR values ranged from 4.2% to 5.9%, which was within acceptable tolerance (±1% of the target CBR 5%).

Table 5. Summary of In-Place Characterization of Clay Subgrade

| | LFC-3N | | | LFC-3S | | | LFC-4S | | |
|---|---|---|---|---|---|---|---|---|---|
| **Properties** | **Avg.** | **Std. Dev.** | **COV %** | **Avg.** | **Std. Dev.** | **COV %** | **Avg.** | **Std. Dev.** | **COV %** |
| CBR, % | 4.8 | 0.6 | 12.6 | 4.8 | 0.5 | 9.5 | 5.3 | 0.5 | 10.0 |
| MC, % | 27.0 | N/A | N/A | 27.1 | N/A | N/A | 27.1 | N/A | N/A |
| In situ dry density, pcf | 97.3 | N/A | N/A | 96.9 | N/A | N/A | 95.5 | N/A | N/A |
| Shear strength, psi | 14.7 | 1.8 | 12.2 | 18.4 | 3.9 | 21.2 | 14.6 | 3.4 | 23.1 |
| LWD modulus, ksi | 5.5 | 2.7 | 49.3 | 6.7 | 3.4 | 50.8 | 4.7 | 3.4 | 72.1 |
| Seismic modulus, ksi | 14.8 | 2.2 | 14.8 | 15.7 | 2.7 | 17.4 | 15.9 | 2.3 | 14.4 |
| GeoGauge modulus, ksi | 11.3 | 2.2 | 19.2 | 13.1 | 1.8 | 13.9 | 11.6 | 2.4 | 20.5 |

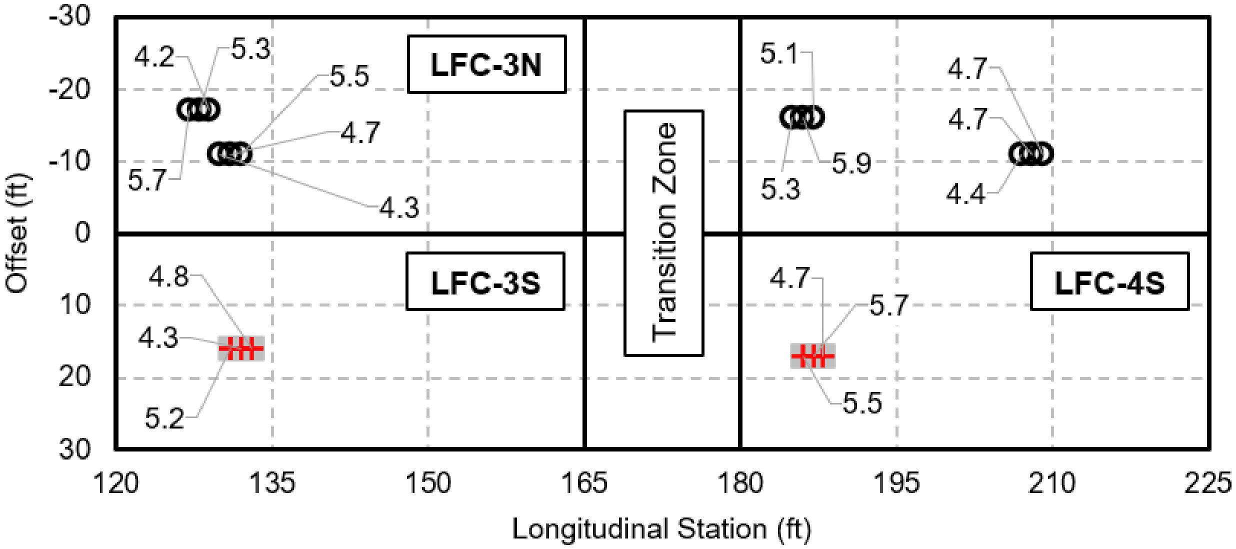

Figure 4. Subgrade CBR Values in Geosynthetics Test Items

Figure 5 plots the results of vane shear tests against the transverse offset. Test item LFC-3N exhibited the least variability in strength. The lowest strength was observed around the center area of test item LFC-4S.

Modulus values varied considerably depending on the device used to measure them. As a general point of reference, consider the widely used conversion formula E = 1500 × CBR. That is, based on the nominal CBR 5, expect approximately *E* = 7.5 ksi. Among the test devices considered, LWD exhibited the highest variability and lowest modulus values. LWD modulus values were closest to those predicted by the above empirical formula.

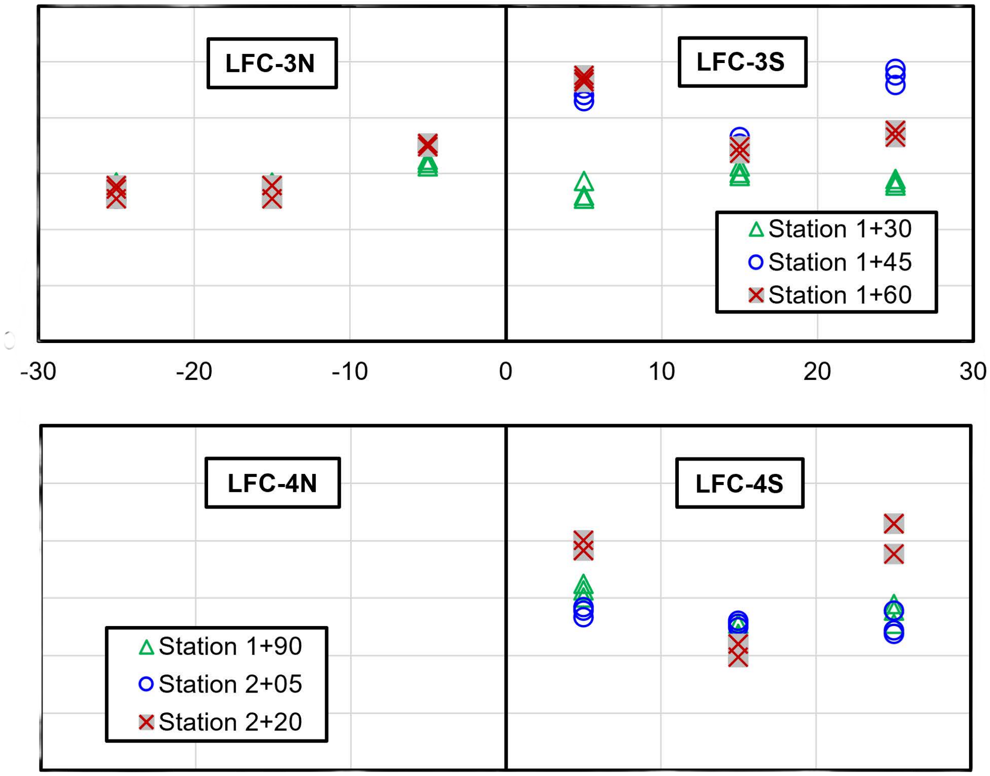

Figure 5. As-Built Subgrade Shear Strength in Geosynthetics Test Items Measured with Vane Shear Tests

### 2.2.1.1 Light Weight Deflectometer Modulus

Subgrade stiffness was measured with LWD equipment. Figure 6 plots modulus values determined from LWD for three test items. The LWD modulus values were plotted against the contact stresses to evaluate the stress-dependency of fine-grained soils. As expected for low-strength clay soil, the modulus values decreased with increasing contact stress. All test items exhibited lower strength near the transition zone regardless of the transverse offsets. At the highest stress level, test item LFC-3S exhibited relatively high stiffness variability.

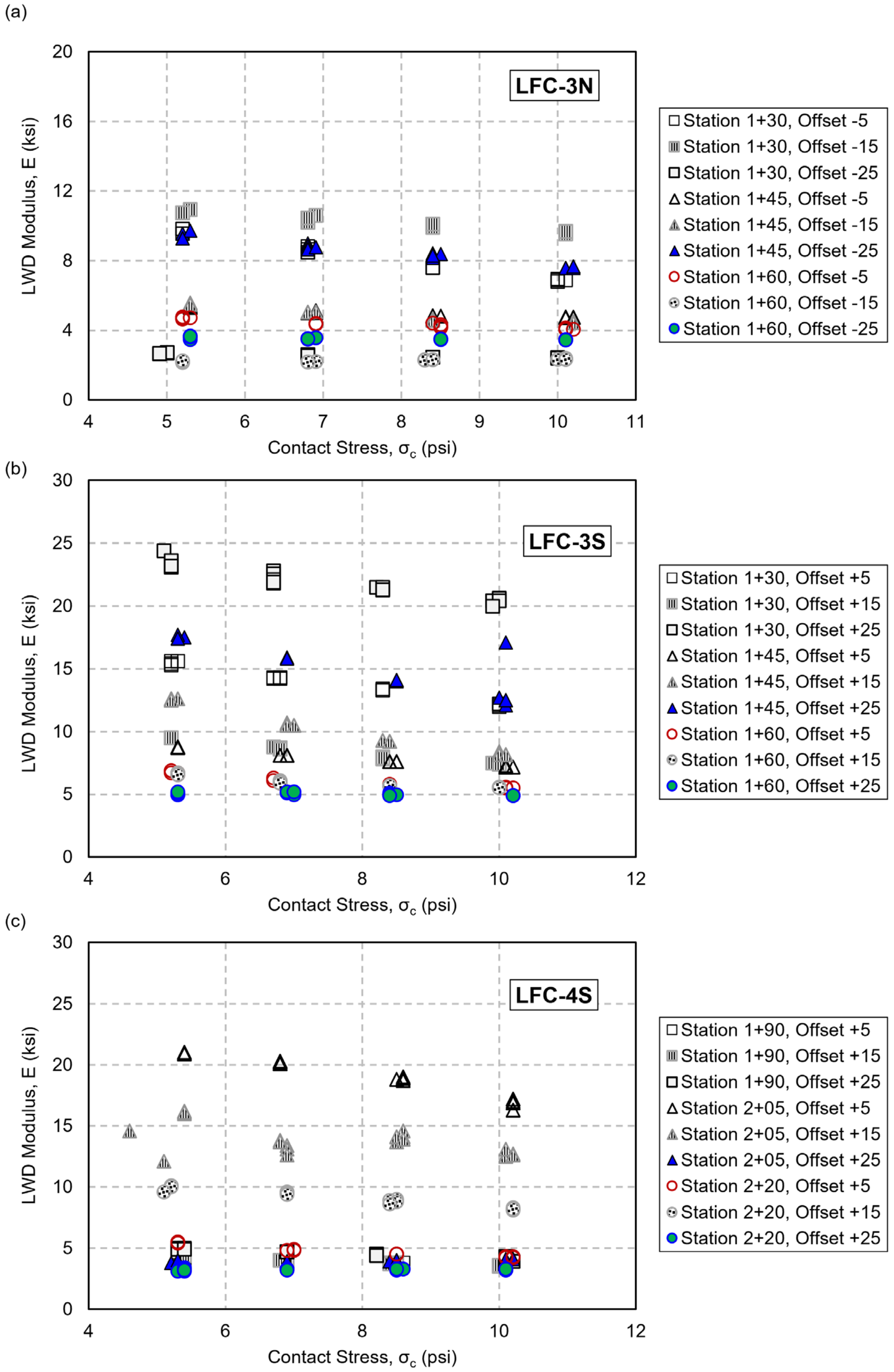

Figure 6. As-Built Subgrade Modulus in Geosynthetics Test Items Measured with LWD

### 2.2.1.2 Seismic Modulus

Seismic moduli of the subgrade layers were measured using the portable seismic properties analyzer for unbound layers (Portable Seismic Properties Analyzer for Unbound Layers [D-PSPA]) device (Nazarian et al., 1993). According to Figure 7, the lowest seismic modulus was recorded at the +5 ft offset at stations 1+30 and 1+45. The highest variability in seismic modulus values was found in test item LFC-4S at transverse offset +25 ft. The highest seismic modulus was also recorded along that same offset.

### 2.2.1.3 GeoGauge Modulus

Figure 8 plots GeoGauge modulus values against transverse offset distance. Contrary to the D-PSPA measurements, the highest variability in GeoGauge modulus values at the center offset was for test items LFC-3N and LFC-4S.

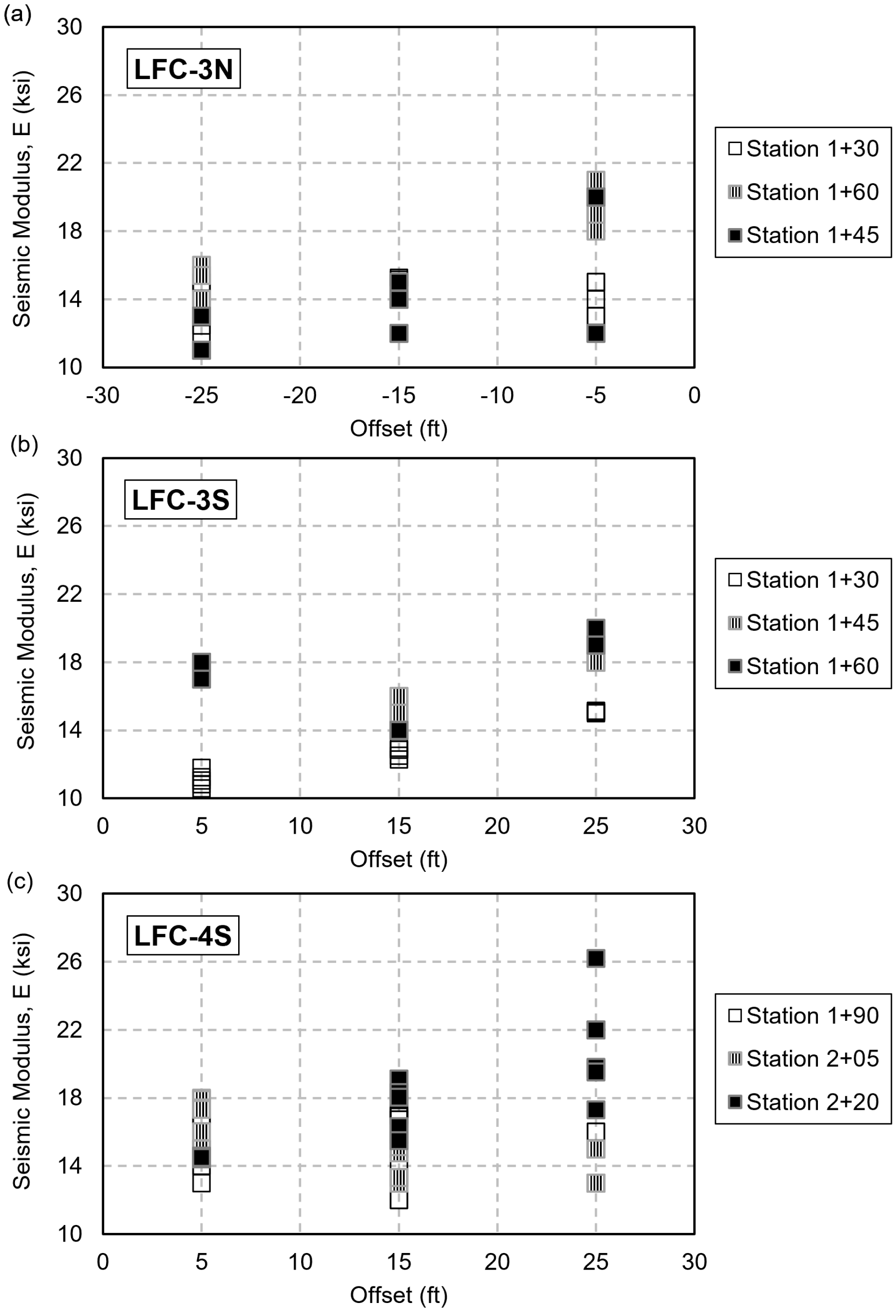

Figure 7. As-Built Subgrade Seismic Modulus in Geosynthetics Test Items Measured with D-PSPA

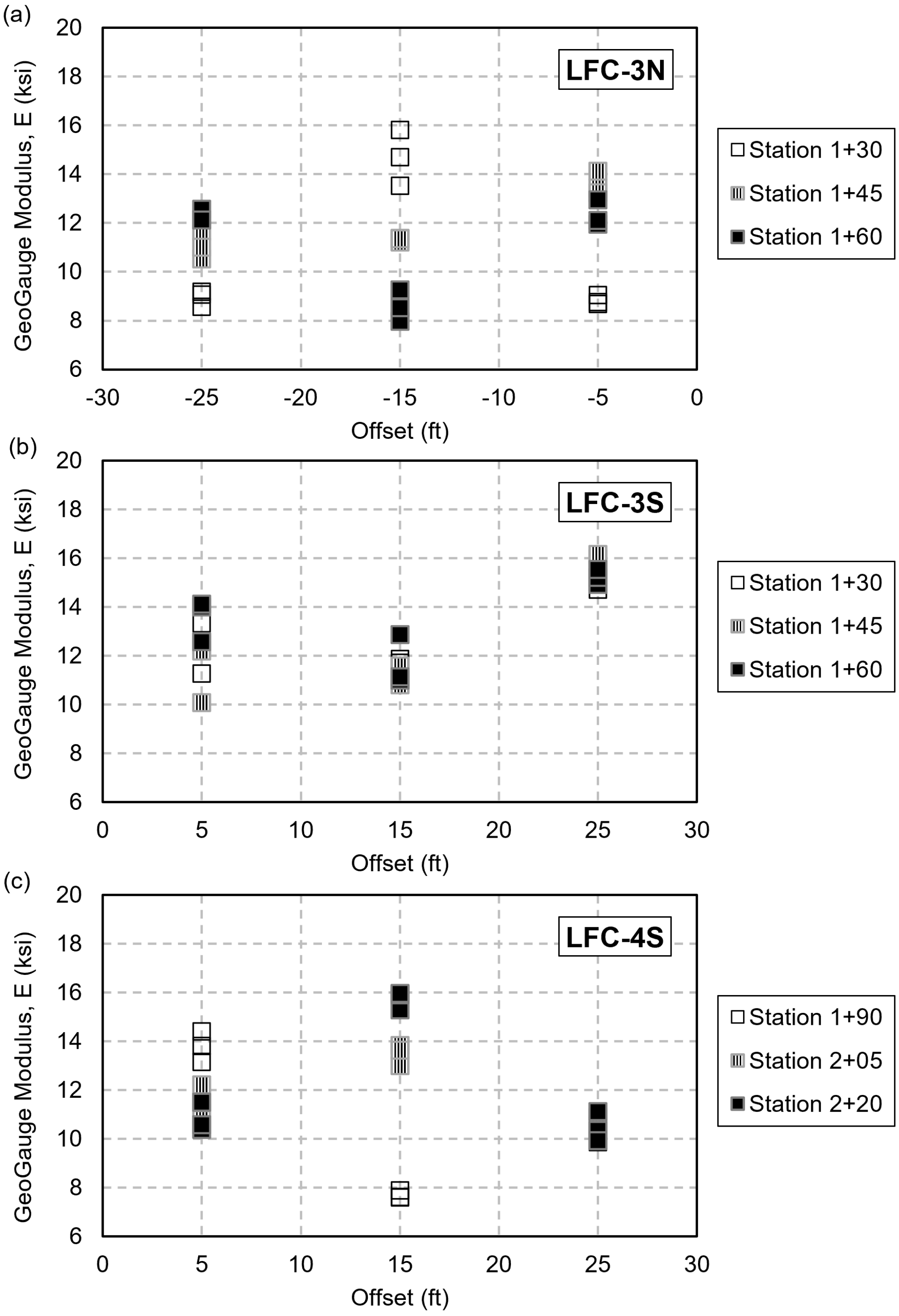

Figure 8. As-Built Subgrade Modulus in Geosynthetics Test Items Measured with GeoGauge

### 2.2.2 Granular Subbase

Table 6 lists summary statistics for five material properties measured on the granular subbase. Seismic modulus values measured with the D-PSPA device were on average about four times higher than moduli from LWD and GeoGauge. Chang et al. (2011) documented that the zone of influence can extend up to 12 in. under LWD impulse loading. GeoGauge and D-PSPA have shallower depths of influence. Therefore, the LWD modulus values may have been impacted by the subgrade layer underneath, leading to consistently lower magnitudes.

Table 6. Summary of In-Place Characterization of Granular Subbase Layer

| | **LFC-3N** | | | **LFC-3S** | | | **LFC-4S** | | |
|---|---|---|---|---|---|---|---|---|---|
| **Properties** | **Avg.** | **Std. Dev.** | **COV, %** | **Avg.** | **Std. Dev.** | **COV %** | **Avg.** | **Std. Dev.** | **COV %** |
| Density (nuclear), pcf | 138.9 | N/A | N/A | 141.1 | N/A | N/A | 138.9 | N/A | N/A |
| MC (nuclear), % | 3.6 | N/A | N/A | 3.1 | N/A | N/A | 4.2 | N/A | N/A |
| LWD modulus, ksi | 17.6 | 1.8 | 10.5 | 19.2 | 3.0 | 15.9 | 17.3 | 1.8 | 10.3 |
| Seismic modulus, ksi | 68.8 | 10.1 | 14.7 | 70.8 | 14.5 | 20.4 | 74.8 | 8.3 | 11.1 |
| GeoGauge modulus, ksi | 18.0 | 2.8 | 15.5 | 18.6 | 3.3 | 17.7 | 17.3 | 1.3 | 7.7 |

Figure 9 plots the LWD modulus at top of subbase against the corresponding LWD plate contact stresses. Figure 10 plots top-of-subbase seismic moduli (D-PSPA) against the transverse offset for all three test items. Figure 11 plots top-of-subbase GeoGauge moduli against the transverse offset.

Test items LFC-3N and LFC-4S exhibited small variation in modulus irrespective of measurement location. Modulus values plotted against the contact stresses substantiate the expected stress-hardening behavior of the granular subbase. In contrast, the observed decrease in subbase modulus values with increasing contact stresses in test item LFC-3S at station 1+30 indicates a stress-softening tendency. Improper compaction control or underlying moisture issues might have contributed to stress-softening behavior of a granular subbase with a nonwoven geotextile separation layer. The lowest subbase modulus was measured at the zero-offset position at station 1+30. The LWD modulus values also exhibited stress-softening behavior in the same area. From the GeoGauge data in Figure 11, the lowest modulus value was at station 1+45 and transverse offset +25 ft. For zero offset, the lowest GeoGauge modulus was at station 1+30 of test item LFC-3S, confirming similar data from the other two test methods.

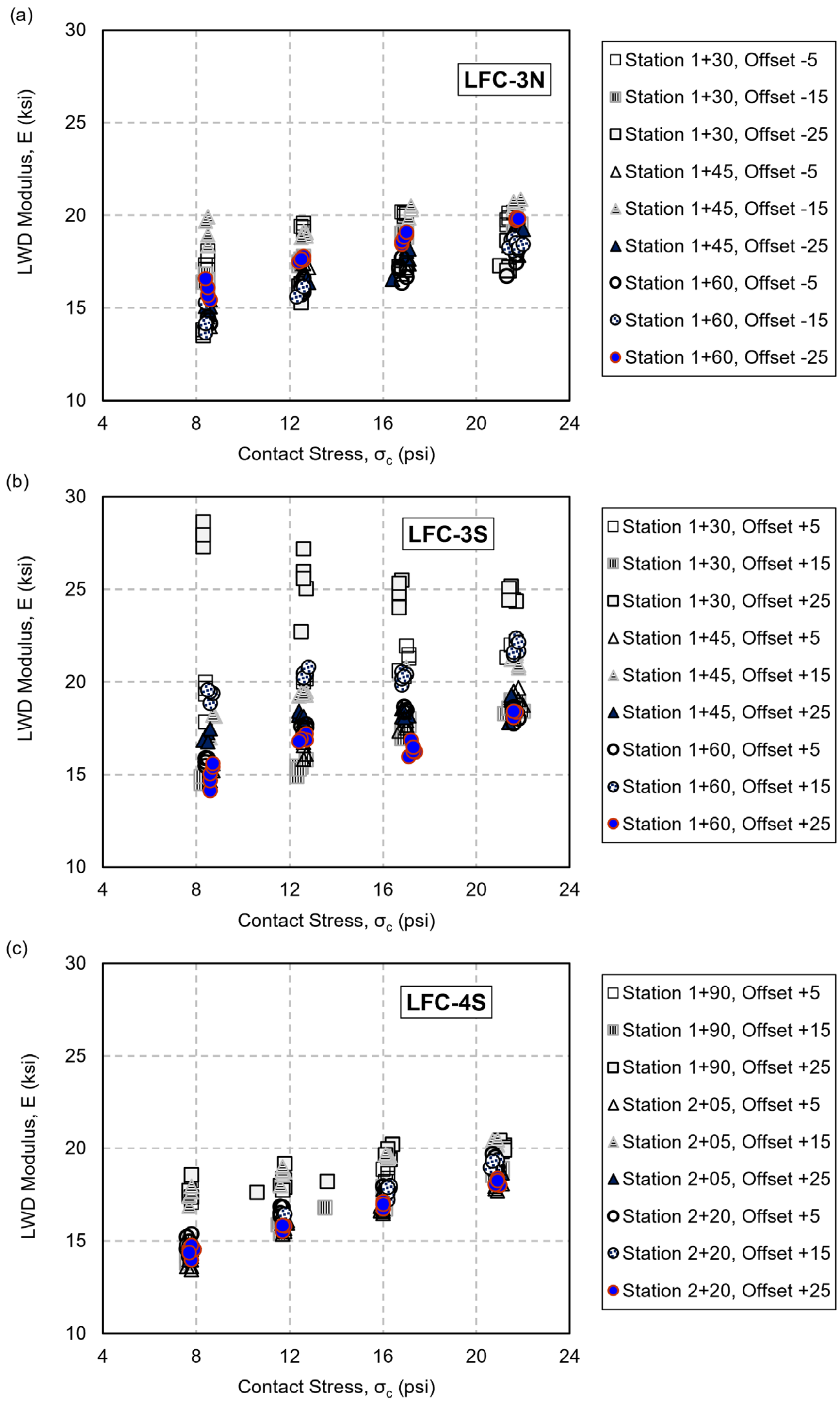

Figure 9. As-Built Subbase Modulus in Geosynthetic Test Items from LWD

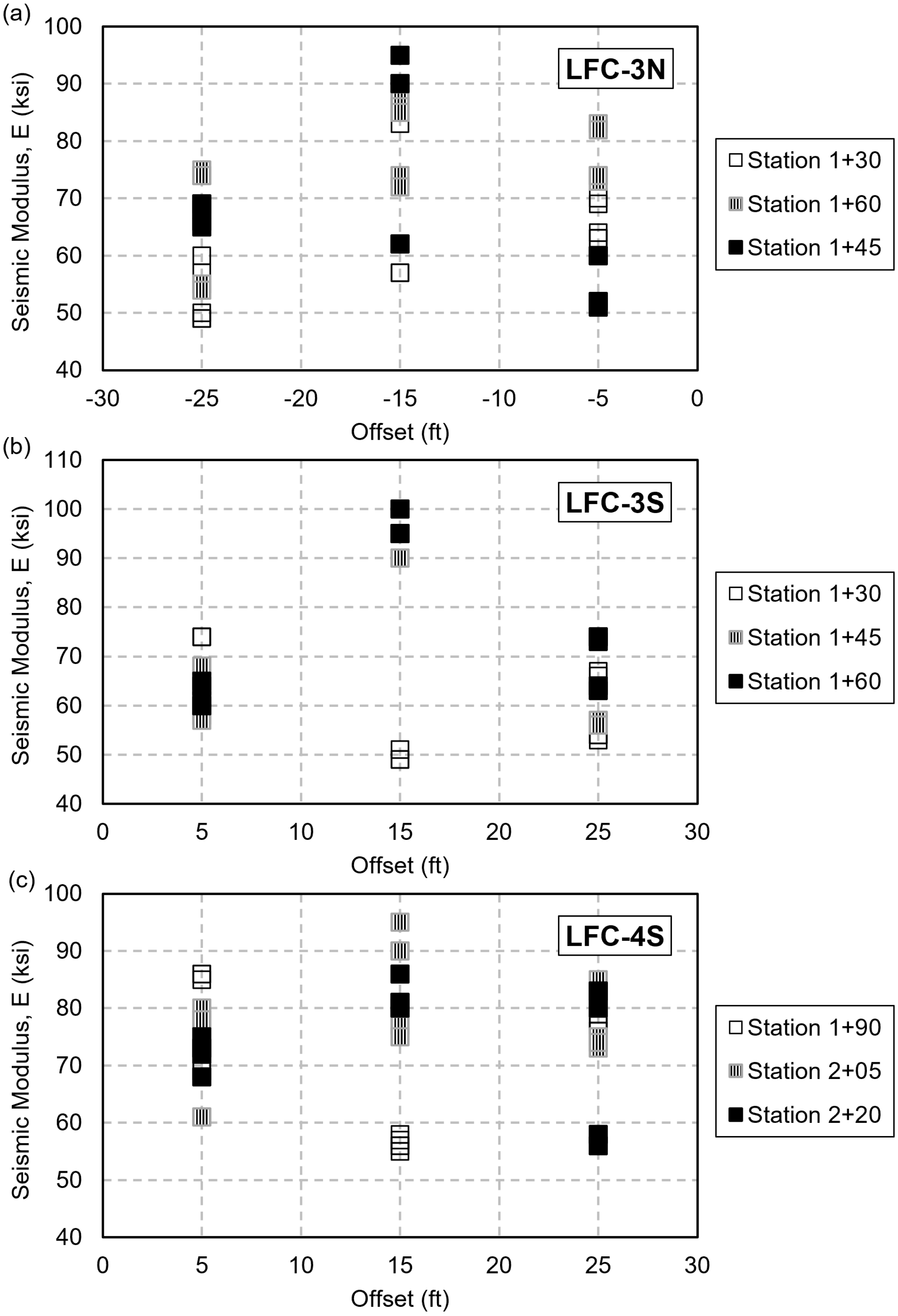

Figure 10. As-Built Subbase Modulus in Geosynthetic Test Items from D-PSPA

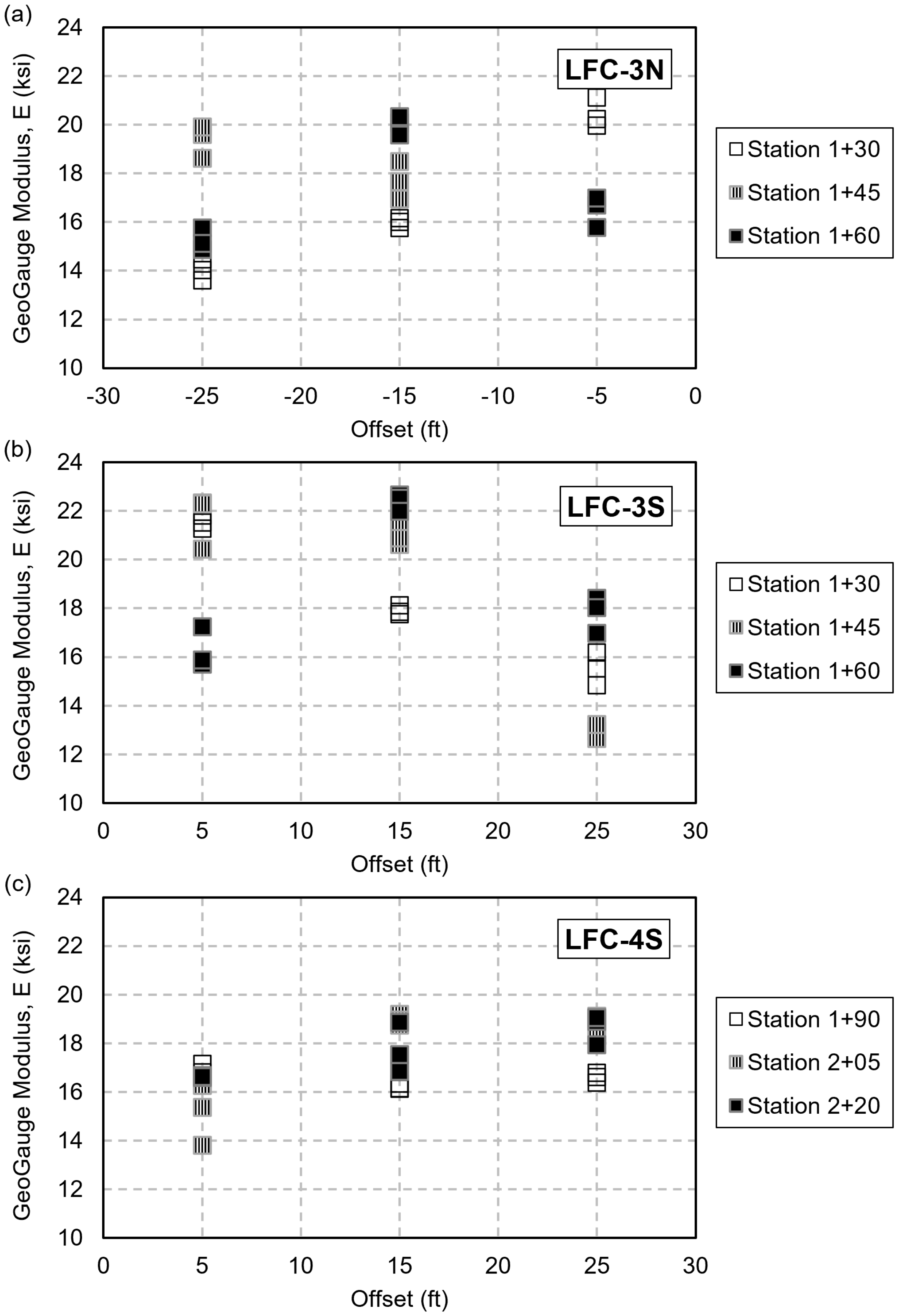

Figure 11. As-Built Subbase Modulus in Geosynthetic Test Items from GeoGauge

### 2.2.3 Base Course

Table 7 lists summary statistics for five material properties measured on the base course. Like the subbase layer (Section 2.2.2), D-PSPA gave higher modulus values than LWD and GeoGauge. One notable anomaly was the decrease in seismic modulus compared to the subbase (Table 6) despite the addition of crushed aggregate base, especially in the case of the geogrid reinforced test item LFC-3N. Average LWD and GeoGauge modulus values for test item LFC-3N were also low compared to corresponding modulus values for test items LFC-3S and LFC-4S. This is evidence of poor compaction control despite the installation of geogrid reinforcement.

Table 7. Summary of In-Place Characterization of Crushed Aggregate Base Layer

| | **LFC-3N** | | | **LFC-3S** | | | **LFC-4S** | | |
|---|---|---|---|---|---|---|---|---|---|
| **Properties** | **Avg.** | **Std. Dev.** | **COV %** | **Avg.** | **Std. Dev.** | **COV %** | **Avg.** | **Std. Dev.** | **COV %** |
| Density (Nuclear), pcf | 151.4 | N/A | N/A | 151.3 | N/A | N/A | 152.4 | N/A | N/A |
| MC (nuclear), % | 2.6 | N/A | N/A | 2.3 | N/A | N/A | 2.0 | N/A | N/A |
| LWD modulus, ksi | 25.7 | 2.2 | 8.6 | 31.9 | 3.5 | 11.1 | 29.2 | 3.0 | 10.3 |
| Seismic modulus, ksi | 44.8 | 7.5 | 16.8 | 66.2 | 11.1 | 16.8 | 67.6 | 11.0 | 16.3 |
| GeoGauge modulus, ksi | 11.4 | 1.1 | 9.6 | 13.9 | 1.6 | 11.3 | 14.1 | 1.6 | 11.4 |

Figure 12 plots the LWD modulus at top of base against the corresponding LWD plate contact stresses. Figure 13 plots top-of-base seismic moduli for the three test items against the transverse offset. Figure 14 plots top-of-base GeoGauge moduli against the transverse offset. Except for one location (offset -15 ft at station 1+60), the LWD moduli were much lower for test item LFC-3N (geogrid-reinforced) than for the other two test items. Seismic and GeoGauge modulus values (Figure 13 and Figure 14) confirmed the LWD results. At station 1+60 and -5 ft transverse offset, the GeoGauge modulus value was as low as 9 ksi. The intended benefits of lateral constraint from the geogrid reinforcement cannot be achieved without appropriate compaction control. Observations from the in-place testing underscore the compaction issues with the crushed aggregate base layer in test item LFC-3N.

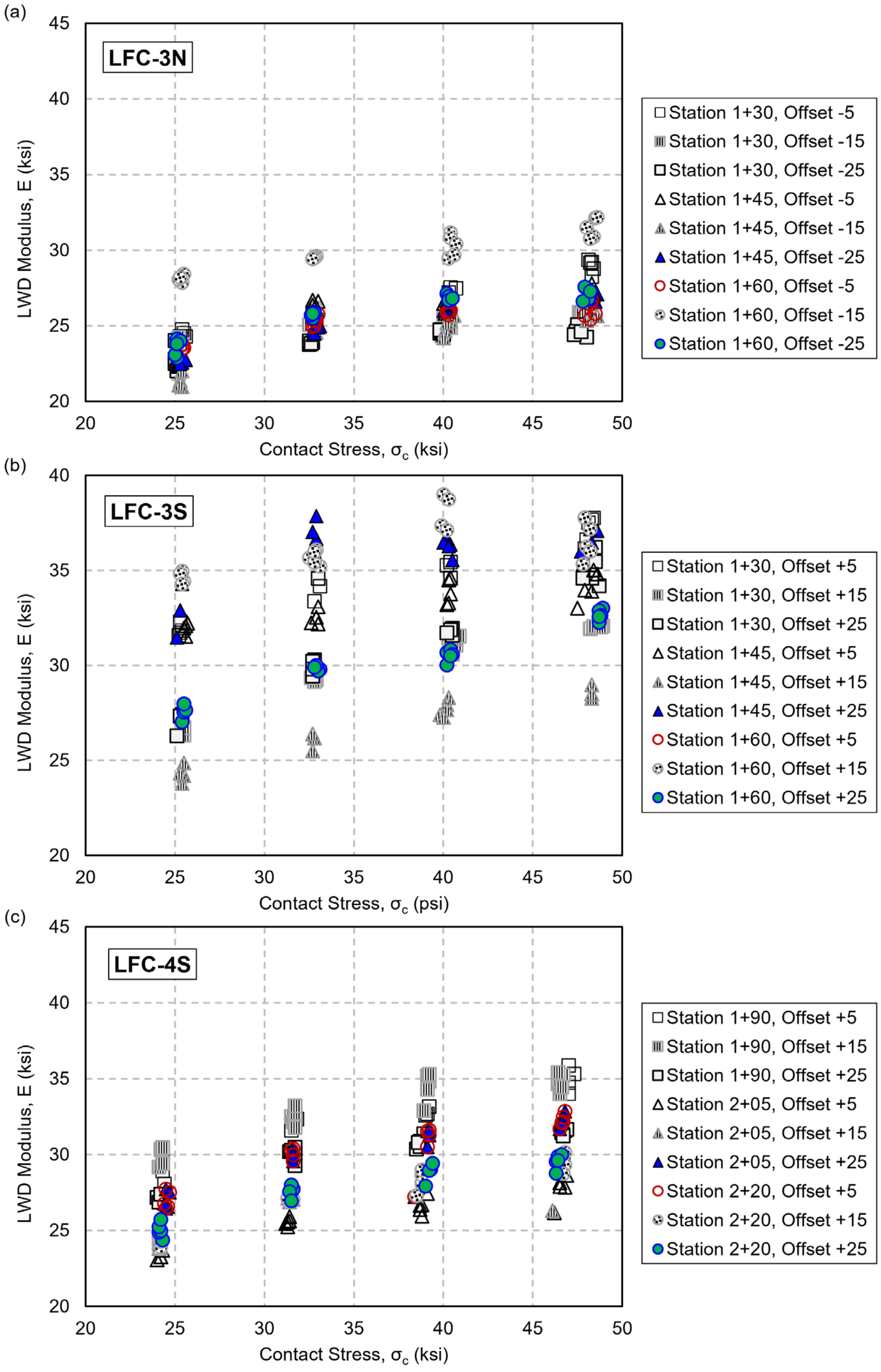

Figure 12. As-Built Base Modulus in Geosynthetic Test Items Measured with LWD

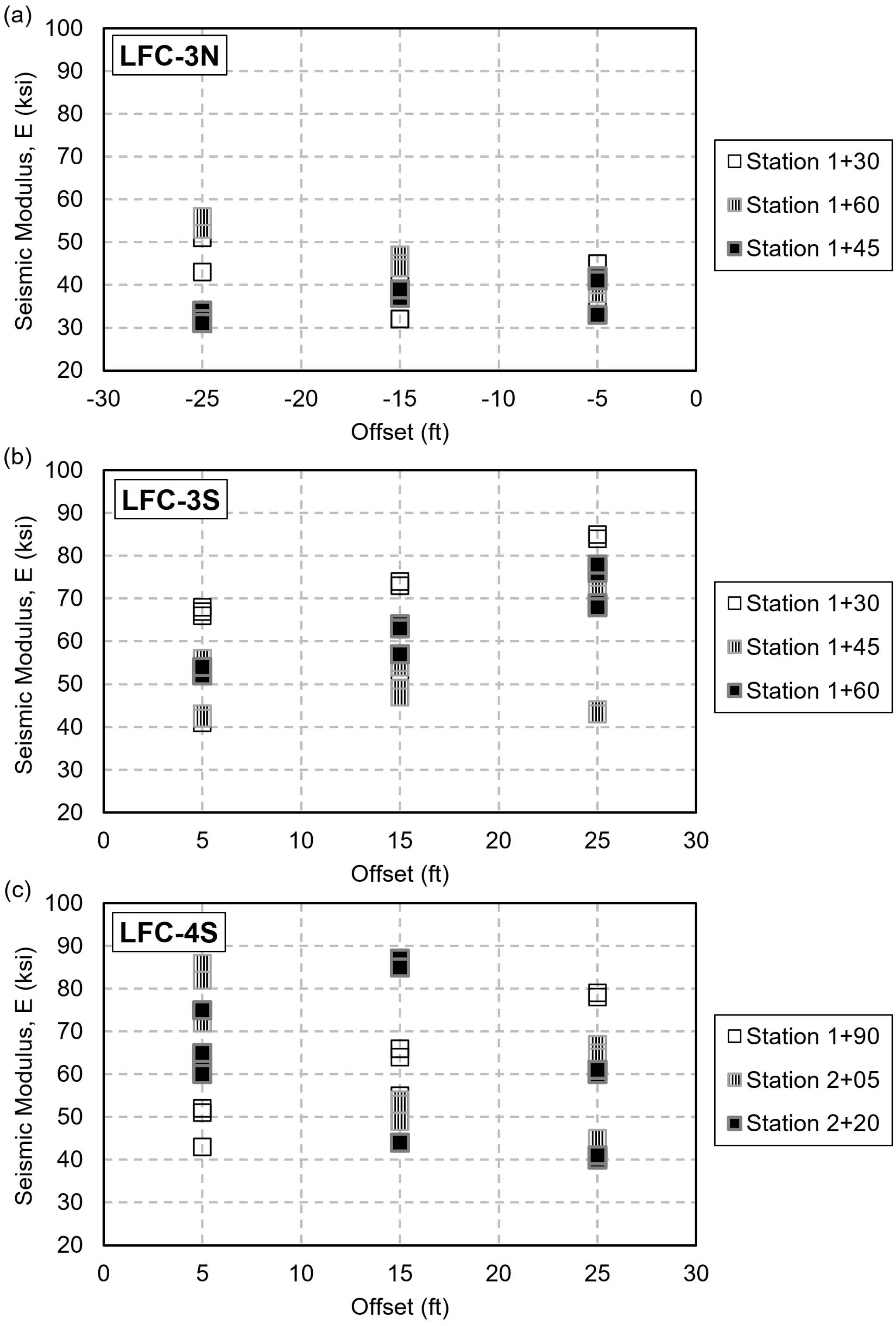

Figure 13. As-Built Base Modulus in Geosynthetic Test Items Measured with D-PSPA

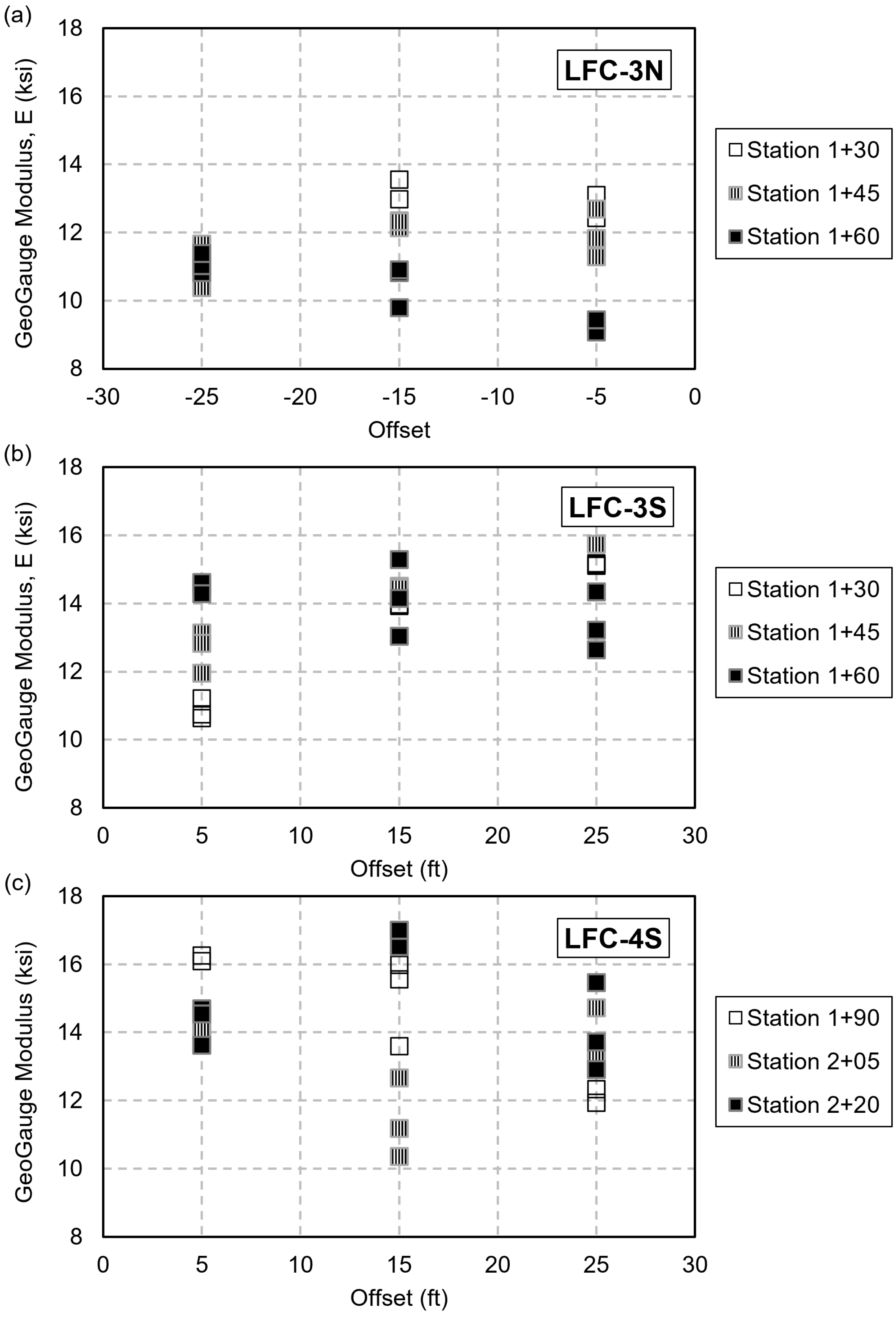

Figure 14. As-Built Base Modulus in Geosynthetic Test Items Measured with GeoGauge

### 2.2.4 Asphalt Concrete

Table 8 summarizes the Quality Assurance/Quality Control (QA/QC) results for the asphalt concrete (AC) surface layer. Mat and joint densities were measured in situ with the nuclear gauge. Air voids were determined in the laboratory from extracted AC cores. Seismic modulus values were measured directly on the surface using portable seismic properties analyzer (PSPA), and (as expected) were higher than the average elastic moduli backcalculated from heavy weight deflectometer (HWD) tests. Table 8 shows that the average mat density in LFC-3N was higher than LFC-3S and LFC-4S (by 3.5% and 2.3%, respectively). This could be attributed to the 0.1-in. variation in AC thickness.

Table 8. Summary of In-Place Characterization of Crushed Aggregate Base Layer

| **Properties** | **LFC-3N** | | | **LFC-3S** | | | **LFC-4S** | | |
|---|---|---|---|---|---|---|---|---|---|
| | **Avg.** | **Std. Dev.** | **COV %** | **Avg.** | **Std. Dev.** | **COV %** | **Avg.** | **Std. Dev.** | **COV %** |
| Mat density, % | 97.9 | N/A | N/A | 94.4 | N/A | N/A | 95.6 | N/A | N/A |
| Joint density, % | 91.3 | N/A | N/A | 91.3 | N/A | N/A | 91.2 | N/A | N/A |
| Laboratory air voids, % | 4.1 | N/A | N/A | 4.1 | N/A | N/A | 4.1 | N/A | N/A |
| Seismic modulus, ksi | 3,405.2 | 144.9 | 4.3 | 3,213.1 | 125.7 | 3.9 | 3,063.0 | 221.2 | 7.2 |
| Elastic modulus, ksi | 1,112.7 | 48.8 | 4.4 | 903.0 | 180.0 | 19.9 | 1,494.0 | 230.8 | 15.5 |

### 2.2.5 Heavy Weight Deflectometer Deflection Basin Parameters

Generally, modulus values are backcalculated from HWD tests, assuming a linear elastic system. This simplified analysis may significantly underestimate critical pavement responses and give an erroneous interpretation of pavement structural capacity. To better assess the structural capacity of the geosynthetics test items, researchers examined key deflection basin parameters (DBPs). The four DBPs considered were: impulse stiffness modulus (ISM), base damage index (BDI), shape factor (F2), and area under pavement profile (AUPP). Researchers focused on these DBPs because they may explain certain observed discrepancies in the base and subbase characterization (Sections 2.2.2 and 2.2.3). While the viscoelastic behavior of AC may also be a factor affecting the response to load, any variation among the three test items due to viscoelastic effects was assumed to be small (due to equal thickness and asphalt material properties).

Figure 15 shows a typical HWD deflection basin with seven geophone sensors, from which the following indexes can be computed:

- ISM: ISM is defined as the ratio of impulse load (P) to center deflection ($D_0$). ISM provides a basic comparative measure of structural capacity.

- BDI: Since a compaction issue was identified in the base course of geogrid reinforced test item LFC-3N, it was appropriate to examine the BDI. BDI values are calculated as the difference between deflections at the 12-in. and 24-in. offsets:

$$(BDI = D_{12} - D_{24}) \tag{2}$$

- F2: The shape factor F2 is defined as the normalized relative difference in deflections measured at 12-, 24- and 36-in. offsets, i.e., $F2 = (D_{12} - D_{36})/D_{24}$. This factor is sensitive to changes in AC thickness.
- AUPP: AUPP is the area under the deflection basin curve computed over a radial distance of 72 in. from the center of the load plate. This index is known to be an excellent indicator of tensile strain at the bottom of AC. For the sensor arrangement in Figure 15, the AUPP equation is:

$$AUPP = {}^{1}/_{2} \times \{11D_0 - 2(D_{12} + D_{24} + D_{36} + D_{48} + D_{60}) - D_{72}\} \tag{3}$$

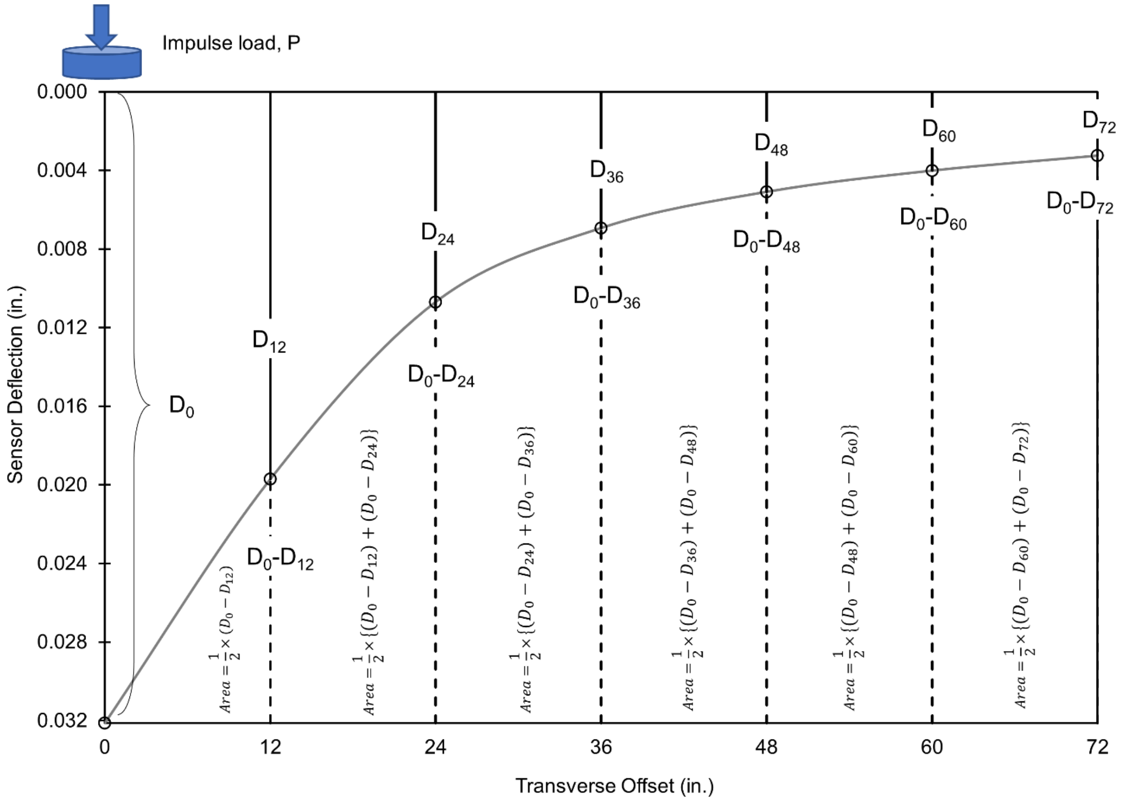

Figure 15. Sample HWD Deflection Basin

Figure 16 shows the above indexes for the three geosynthetics test items. ISM shows that the pavement structure was weaker in the center area of each test item relative to the outer areas. Confirming the observations from the base layer in situ characterization tests, the lowest ISM values (weakest structure) in the center area were for the geogrid-reinforced test item LFC-3N. That the highest BDI, F2 factor, and AUPP index values were found at the same offset is further evidence of poor compaction control in the base course of test item LFC-3N.

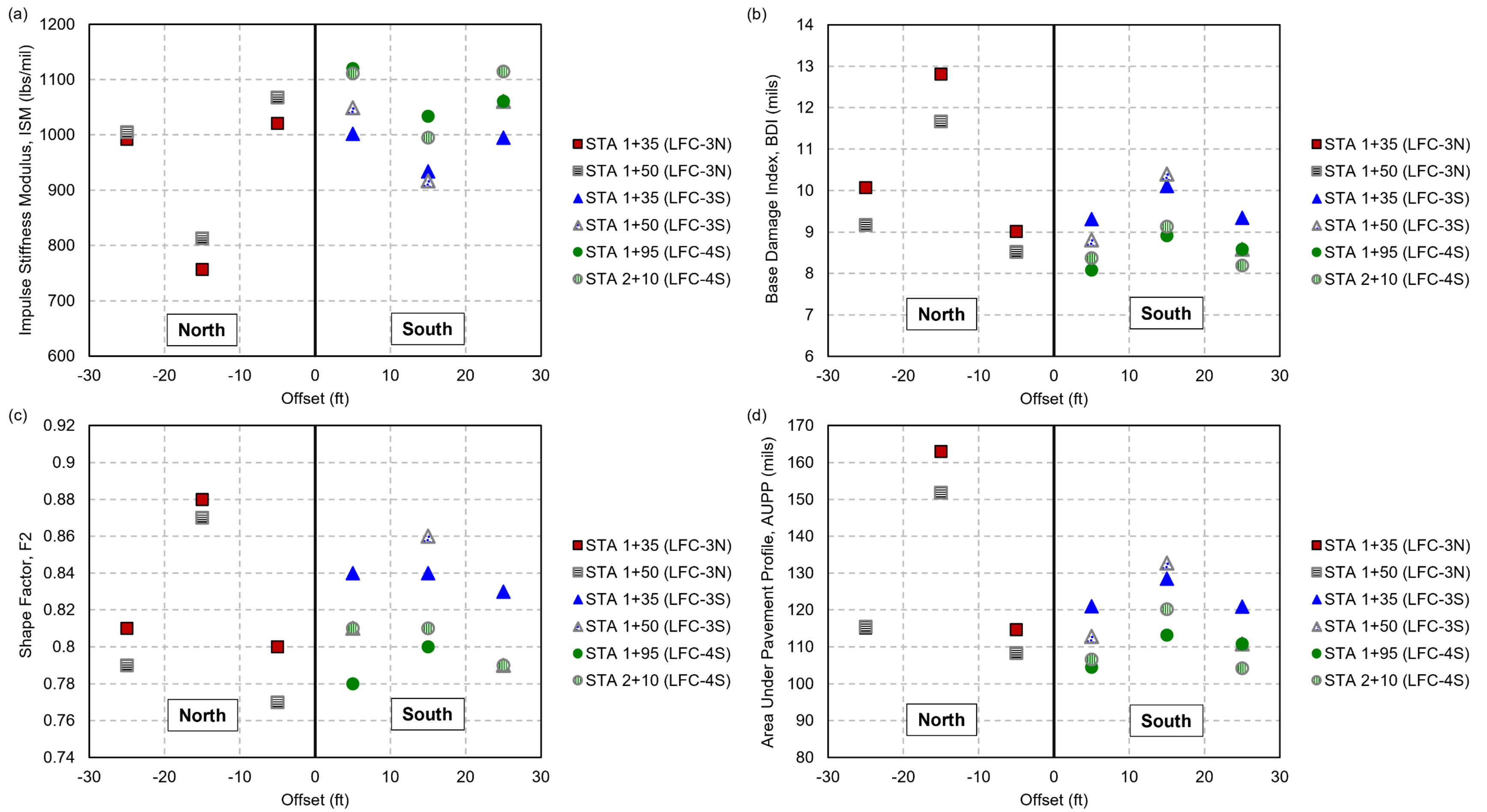

Figure 16. Plots for (a) ISM, (b) BDI, (c) Shape Factor, and (d) AUPP for Geosynthetics Test Items

## 2.3 REVIEW OF INSTRUMENTATION

Embedded sensors included asphalt strain gauges (ASGs), coil sensors (CSs), pressure cells (PCs), moisture sensors and thermocouples, in addition to bender elements (BEs) and SmartRock sensors as discussed below. Details of the installation are found in Tomlinson et al. (2022). Figure 17, Figure 18, and Figure 19 show the sensor layouts for the three test items making up the CC9 Geosynthetics test area. Appendix A lists sensor locations for each test item.

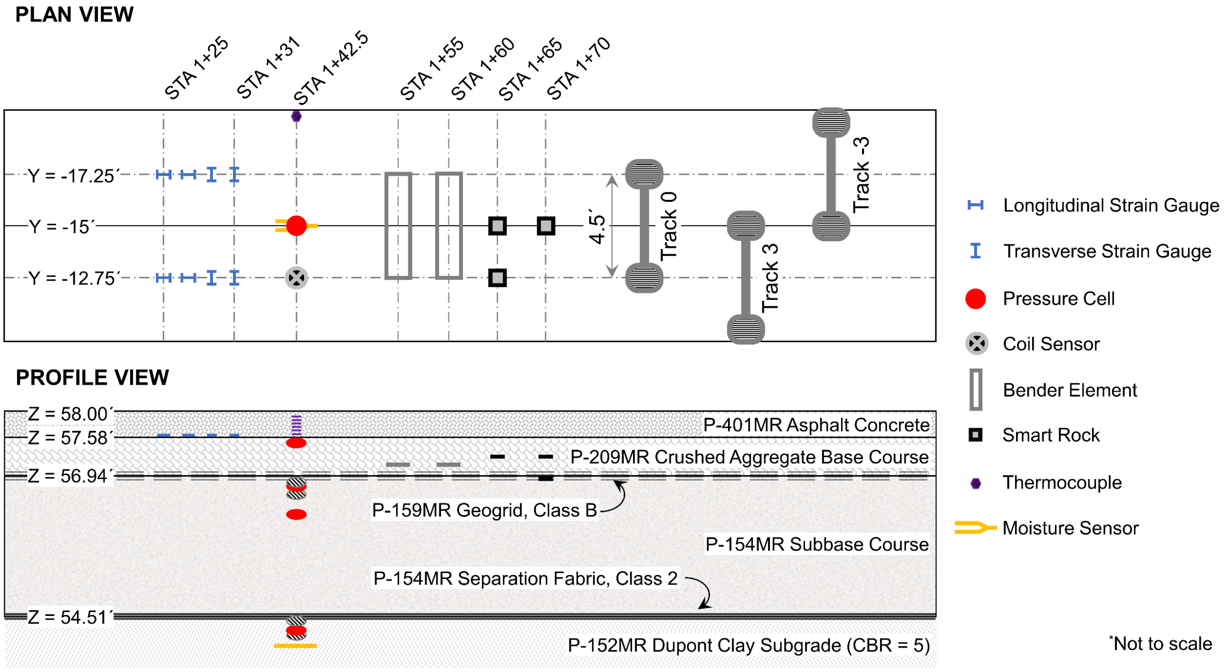

Figure 17. Layout of Instrumentation in LFC-3N (Geogrid-reinforced)

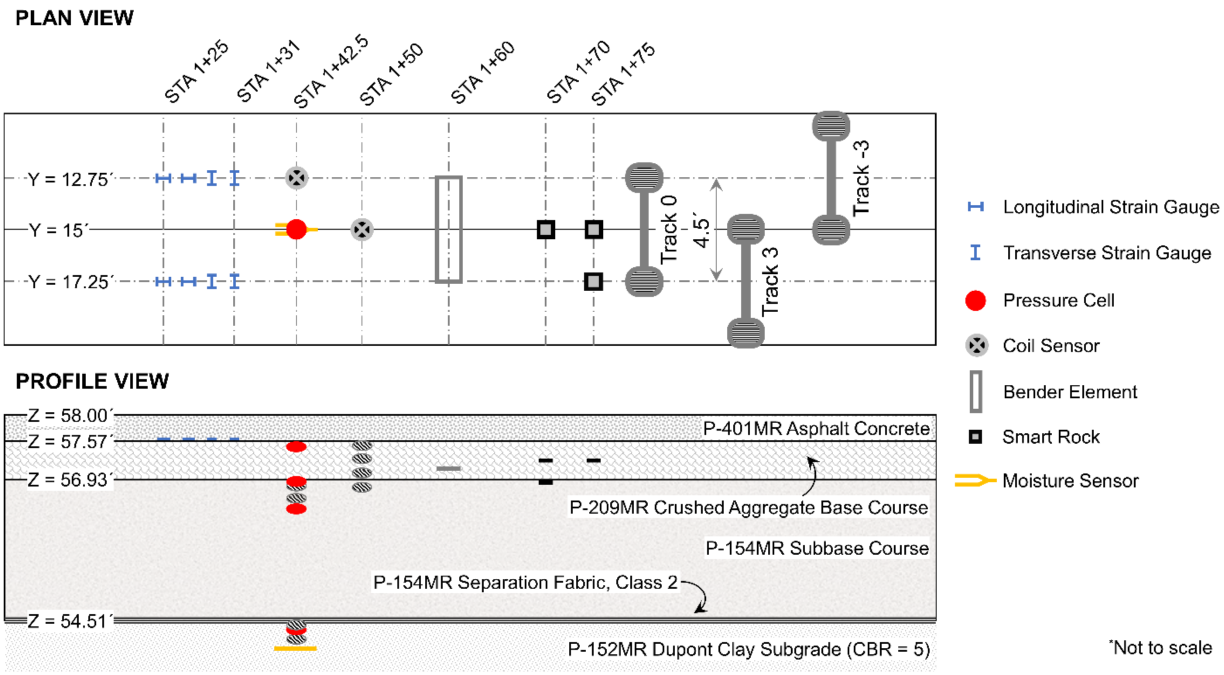

Figure 18. Layout of Instrumentation in LFC-3S (With geotextile separation layer)

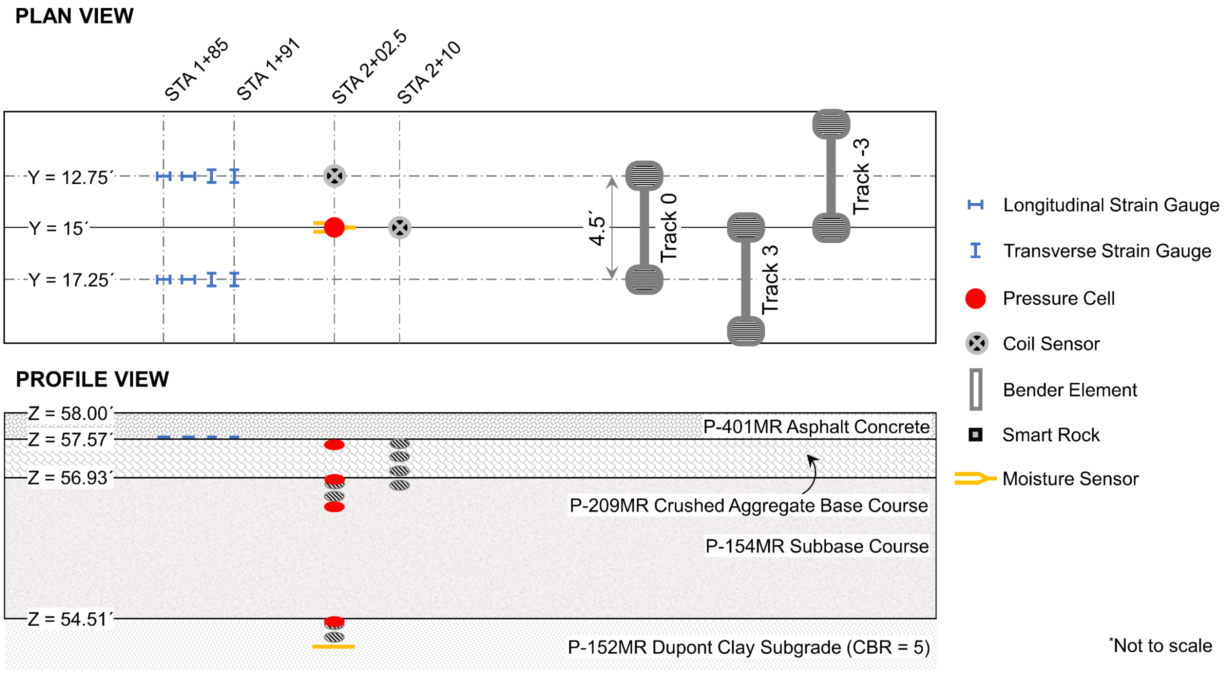

Figure 19. Layout of Instrumentation in LFC-4S (Control/no geosynthetics)

### 2.3.1 Asphalt Strain Gauges

Four longitudinal and four transverse strain gauges were installed in each test item to monitor the tensile strain at the bottom of the AC layer.

### 2.3.2 Pressure Cells

Each test item had four PCs. One PC was at the top of the base course in each test item. Two more PCs monitored compressive stresses at the top of the subbase and subgrade layers, respectively. A fourth PC was located 6 in. below the top of the subbase to monitor the effect of geogrid reinforcement and geotextile separation in the test items.

### 2.3.3 Coil Sensors

Paired induction CSs spaced at approximately 3 in. were installed near the top of the granular subbase and subgrade to measure the accumulation of permanent deformation in those layers. The CS system is used to determine the contributions of individual layers to total rutting at the asphalt surface. A “short stack” of three pairs was placed in the base layer at zero offset (15 ft) to determine the permanent deformation in the base course of test items LFC-3S and LFC-4S.

The induction-coil-based strain measurement system (known as ε-mu, an acronym for strain (ε) measuring unit) has been used extensively to monitor permanent deformation and strain in pavement subsurface layers. The system was originally developed by Selig and Grangaard (1970). The data acquisition process was later automated by Dawson (1994).

### 2.3.4 Static Sensors

A thermocouple tree consisting of six temperature probes was installed in the AC layer of test item LFC-3N. Moisture sensors were installed in the subgrade in each test item to monitor the influence of moisture on subgrade stress and strength under traffic.

### 2.3.5 Bender Elements

Bender element (BE) sensors employ shear wave transducers to measure the in situ shear modulus of unbound pavement materials. The shear modulus is estimated as the product of bulk density and the square of shear wave velocity. BE sensors have been used previously to quantify the localized stiffening of unbound granular materials around geogrid reinforcement (Byun & Tutumluer, 2017). As part of CC9, two BE sensors were installed in the geogrid reinforced base course of LFC-3N, and one BE sensor was placed in the base course of LFC-3S. The data from these sensors were used to quantify the benefit due to lateral restraint from the geogrid reinforcement. The analysis of the CC9 BE sensor data is covered in a separate report (Tutumluer & Qamhia, 2024).

### 2.3.6 SmartRock Sensors

Particle-shaped wireless devices, known as SmartRocks, have been used to monitor inter-particle contact forces and motion in real time (Liu et al., 2017). These devices, each equipped with force cells on the surface along a triaxial gyroscope, a triaxial accelerometer, and a triaxial magnetometer, can be useful for investigating principal stress rotation under simulated aircraft wander. As shown in Figure 17 through Figure 19, SmartRocks were installed in the geosynthetics test area to collect data on the discrete mobilization of coarse granular materials under the influence of simulated aircraft wander.

## 2.4 SUBGRADE MOISTURE CONDITION

Construction of CC9 was completed in December 2019 but traffic testing did not start until April 2021. In the interim, the volumetric moisture content $\theta_v$ was closely monitored from the embedded moisture sensors. Despite the test items being in an enclosed facility, moisture seepage and seasonal variation are known to affect $\theta_v$, hence in situ subgrade strength. Figure 20 shows the change in $\theta_v$ in the clay subgrade over time. Seasonal variation in MC was evident from the observed cyclic trend. The MC in test item LFC-3S (with the geotextile separation fabric) was consistently higher than in the other test items.

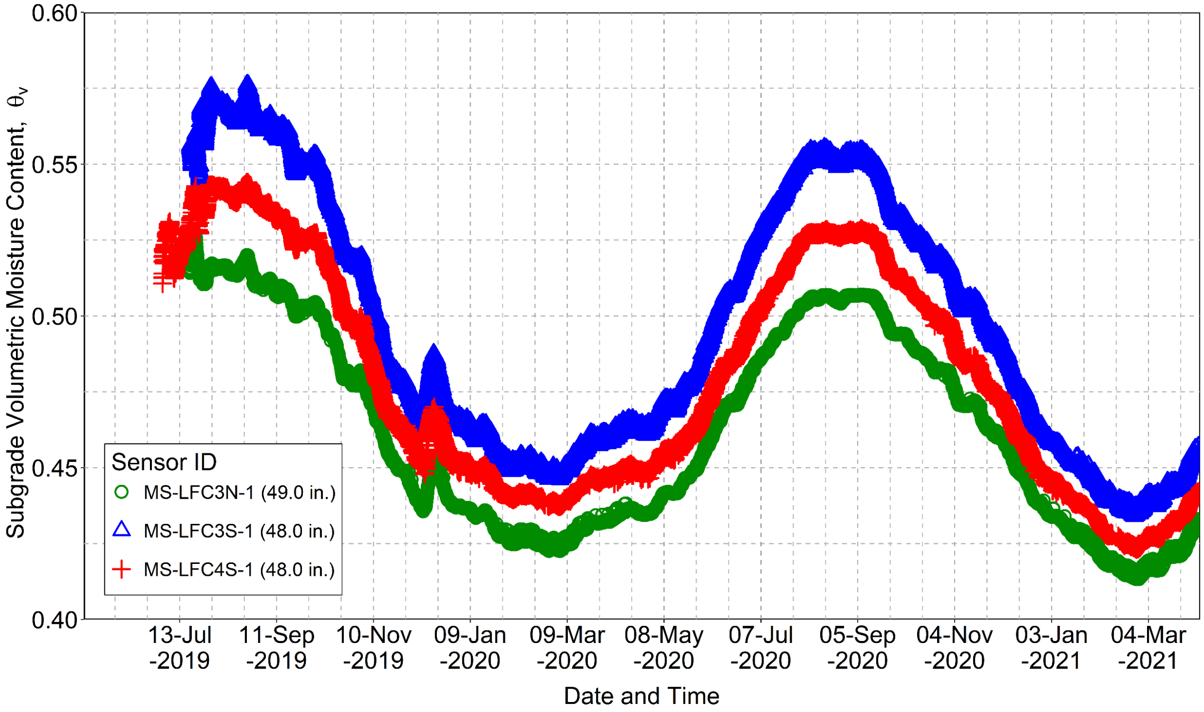

Figure 20. Change in Volumetric MC from Construction to Start of Traffic

## 3. LABORATORY MATERIAL CHARACTERIZATION

This section briefly reviews specific aspects of the CC9 material characterization testing program that help to explain observations from the geosynthetics test. Topics covered include

- moisture-density relations for granular materials;
- resilient modulus of subgrade and granular materials;
- shear strength of granular materials;

- dynamic modulus of AC; and
- rutting susceptibility test results for AC mixes.

The subgrade material specimens were collected in Shelby tubes (12 in. long and 3 in. diameter) at random locations at the top of the finished subgrade along the pavement center line. Four such specimens were taken within or near the geosynthetics test area (Table 9).

## 3.1 MOISTURE-DENSITY RELATIONS FOR GRANULAR LAYERS

Compaction requirements for the granular subbase (P-154MR) and base (P-209MR) materials were determined using modified compactive effort following ASTM D1557 (Method A) (ASTM, 2021). Moisture-density relationships are presented in Figure 21 and Figure 22. As reported in Tomlinson et al. (2022), the optimum moisture content (OMC) for P-154 was higher than that of P-209 due to the relatively higher percentage of fine content (10.2% and 3.4%, respectively passing the No. 200 sieve).

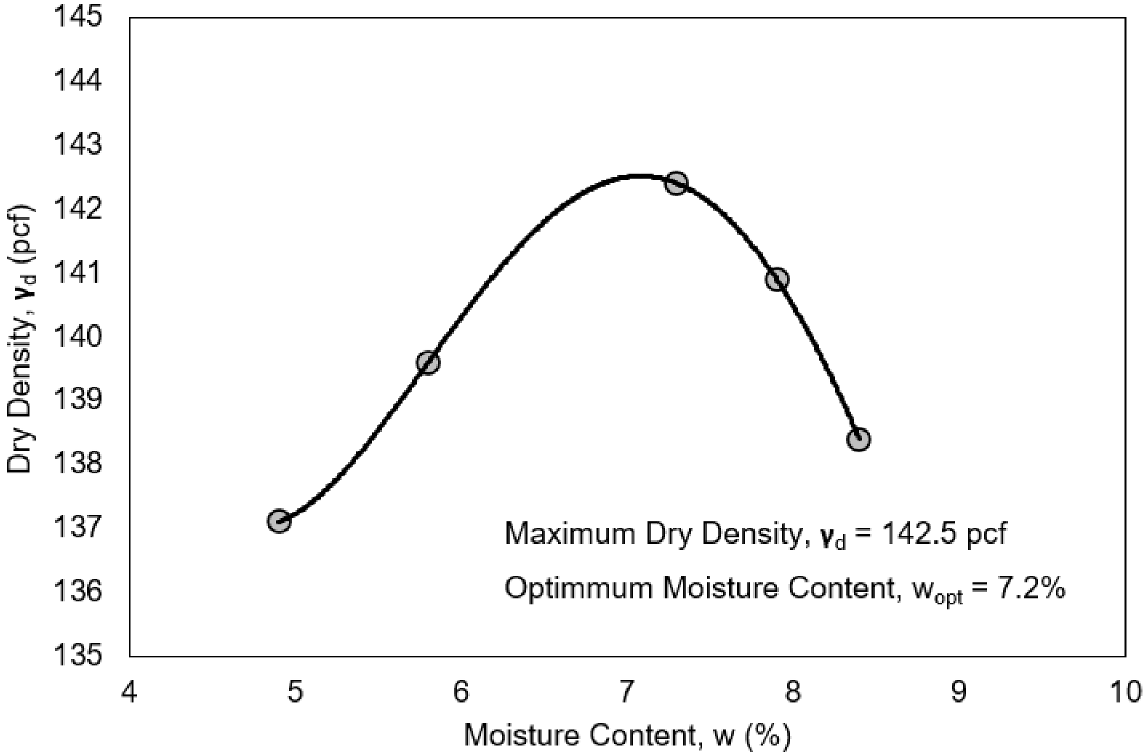

Figure 21. Moisture-Density Relationship of Granular Subbase (P-154MR)

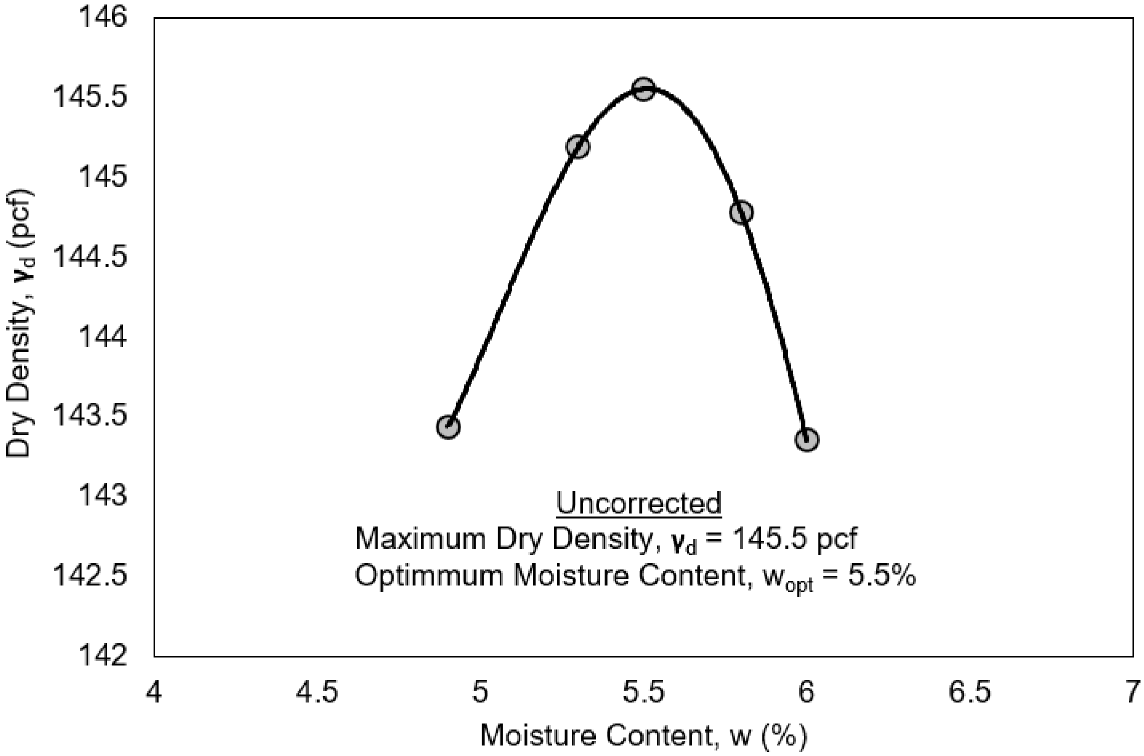

Figure 22. Moisture-Density Relationship of Crushed Aggregate Base (P-209MR)

## 3.2 STIFFNESS CHARACTERIZATION OF STRUCTURAL LAYER MATERIALS

Resilient modulus tests were performed on fine-grained subgrade (P-152MR), and granular subbase (P-154MR) and base (P-209MR) materials following American Association of State Highway and Transportation Officials (AASHTO) T307 (AASHTO, 2021). Compacted specimens were tested with three confining pressures and five cyclic deviator stresses, replicating 15 different stress sequences. Per AASHTO T307, confining pressures and deviator stresses were higher for granular materials. Estimated resilient moduli, bulk stresses, and octahedral shear stresses were fitted to the mechanistic-empirical pavement design guide (MEPDG) model (AASHTO, 2008) to characterize the nonlinear stress-dependent behavior of unbound aggregates. The MEPDG model is known popularly as the enhanced universal model because it can accommodate both stress-hardening and stress-softening behavior of geomaterials (AASHTO, 2008). The following equation describes the form of the enhanced universal model.

$$M_R = k_1 p_a \left(\frac{\theta}{p_a}\right)^{k_2} \left(\frac{\tau_{oct}}{p_a} + 1\right)^{k_3} \tag{4}$$

where:

$M_R$ = Resilient modulus,
$\theta = \sigma_d + 3\sigma_3$= Bulk stress,
$\sigma_d$ = Deviator stress,
$\sigma_3$ = Confining stress,

$\tau_{oct} = \frac{1}{3}\sqrt{(\sigma_1 - \sigma_2)^2 + (\sigma_{2-}\sigma_3)^2 + (\sigma_3 - \sigma_1)^2}$ = Octahedral shear stress,
$\sigma_1$ = Major principal stress,
$\sigma_2, \sigma_3$= Intermediate and minor principal stresses,
$p_a$= Atmospheric pressure,
$K, n$ = Model parameters obtained from multiple regression,
$k_1, k_2, k_3$ = Model parameters obtained from multiple regression.

Regression coefficient $k_1$ should take a positive value and is proportional to the elastic modulus of the material. Coefficient $k_2$ corresponds to the bulk stress term and should have a positive value. A positive bulk stress term indicates hardening behavior (where the resilient modulus of the unbound material increases with increasing confinement and deviatoric stresses). The value of $k_3$ relates to the shearing behavior and is expected to be negative. An increase in the octahedral shear stress and associated high shear stress coefficient leads to lower modulus values and indicates stress-softening behavior.

### 3.2.1 Subgrade Resilient Modulus

Resilient modulus tests were performed on the two samples of subgrade material collected from the CC9 overload test area. The resilient modulus test protocol (AASHTO T307) includes the quick shear (QS) test at zero confining pressure to obtain the unconfined compressive strength (UCS) of the material. Table 9 summarizes the test results. Of the four tests in this area, the lowest moisture content and highest unconfined strength were in test item LFC-3N. Resilient modulus values in Table 9 used confining pressure 2 psi and deviator stress 8 psi. The universal model fitted the data well for both samples as indicated by the high coefficient of determination.

### 3.2.2 Subbase Resilient Modulus

Resilient modulus tests were conducted following AASHTO T307 on samples collected from the CC9 granular subbase in three sampling units (SUs), of which two (SU1 and SU2) were located within the geosynthetic test area. SU1 covered test items LFS-3N and LFS-3S, and SU2 covered LFS-4N and LFS-4S. Figure 23 and Figure 24 show resilient modulus test data for P-154MR material in SU1 and SU2, respectively. Each set of tests consisted of three replicates. Corresponding universal model parameters are shown in the figures for each replicate. All tests were conducted under dry-of-optimum conditions. The final moisture content was approximately 2.5% below the OMC, which was chosen to be consistent with the field-measured nuclear density gauge testing in Table 6. Stress hardening behavior of the granular materials was evident, because the resilient modulus increased with increasing deviator stress and bulk stress.

Table 9. Summary of Subgrade (P-152MR) Resilient Modulus

| **Specimen ID** | **Test Item** | **Station** | **Offset (ft)** | **Moisture Content (%)** | | | **Dry Density (pcf)** | **Predictive Model Coefficients** | | | **Statistical Parameters** | | **Resilient Modulus, $M_R$ (psi)** | **Unconfined Compressive Strength (psi)** |
|---|---|---|---|---|---|---|---|---|---|---|---|---|---|---|
| | | | | **Average** | **Max** | **Min** | | $k_1$ | $k_2$ | $k_3$ | $S_e/S_y$ | $R^2$ *adj* | | |
| Station 1+11 | Transition 2S-3S | 1+11 | +1 | 27.4 | 30.3 | 25.8 | 95.6 | NA | NA | NA | NA | NA | NA | 14.6 |
| Station 1+65 | LFC-3N | 1+65 | -1 | 21.4 | 23.3 | 20.0 | 103.6 | 1266.8 | 0.272 | -3.387 | 0.125 | 0.98 | 8,464 | 28.3 |
| Station 1+81 | LFS-4N | 1+81 | -1 | 29.5 | 32.4 | 26.7 | 94.0 | 1326.8 | 0.210 | -3.305 | 0.166 | 0.97 | 9,060 | 18.7 |
| Station 1+94 | LFC-4S | 1+94 | +1 | 29.5 | 35.4 | 25.8 | 92.7 | 1535.8 | 0.503 | -5.223 | 0.173 | 0.97 | 6,668 | 17.5 |

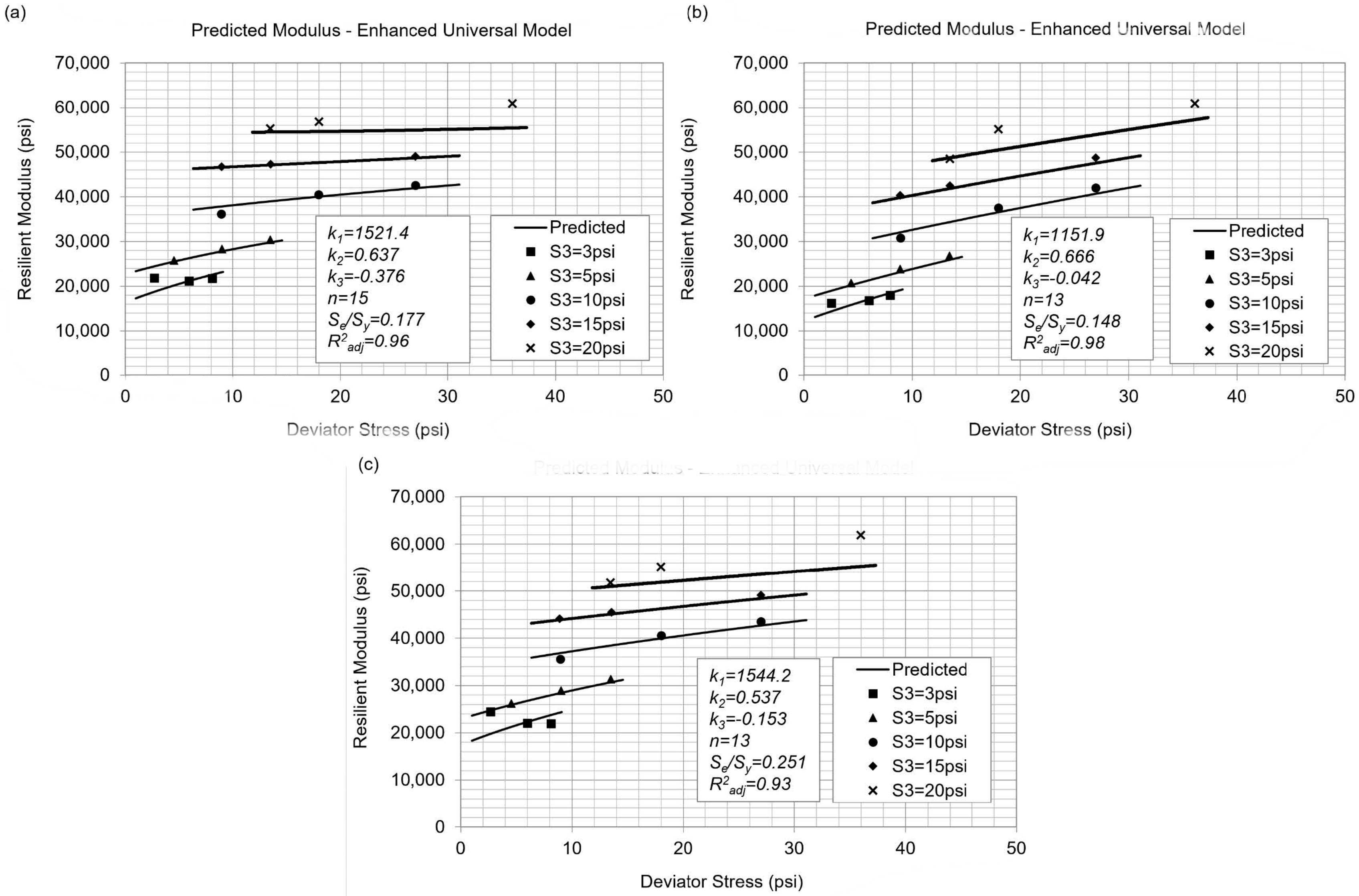

Figure 23. Resilient Modulus of Granular Subbase (P-154MR SU1—LFS-3N and LFS-3S)

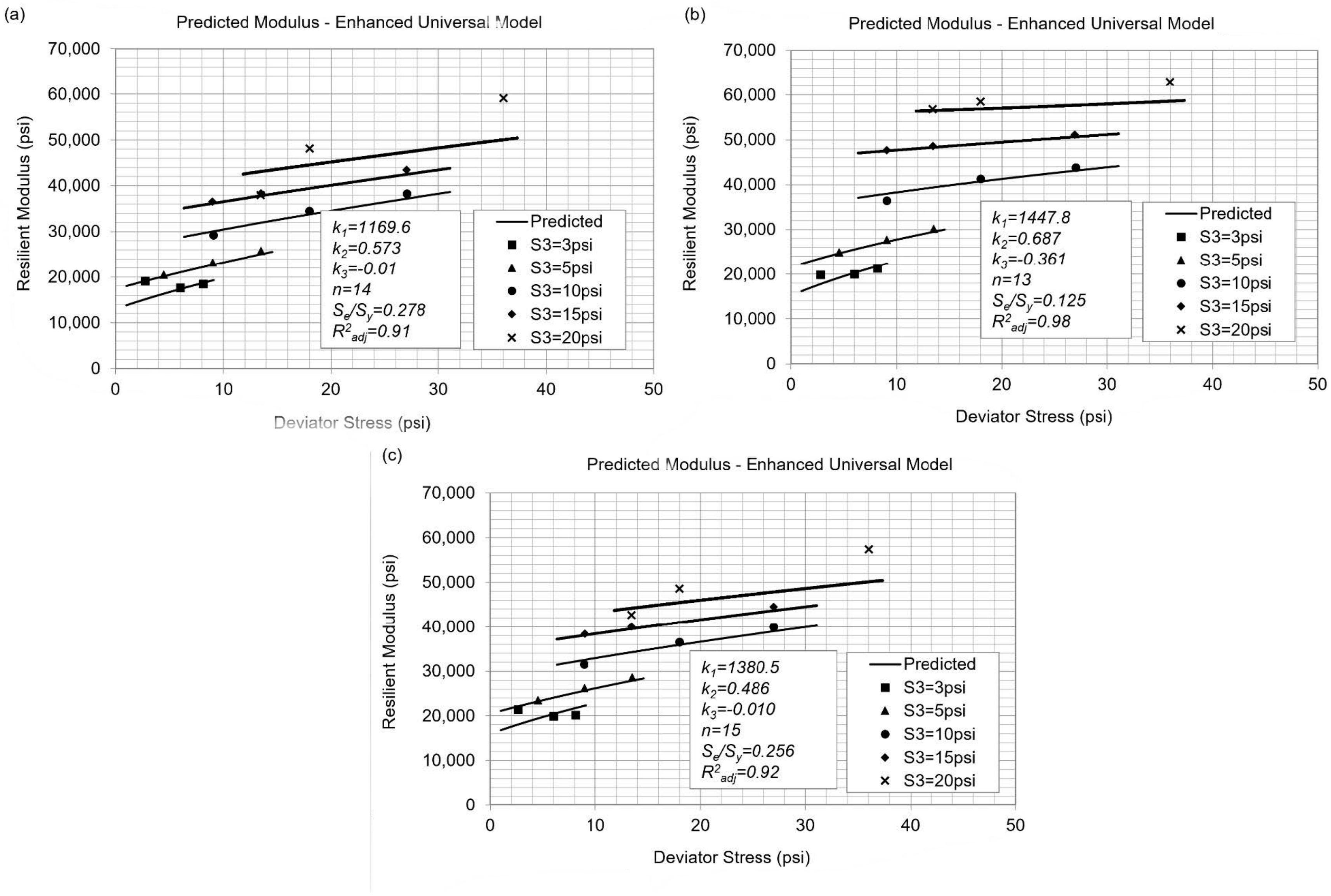

Figure 24. Resilient Modulus of Granular Subbase (P-154MR SU2—LFS-4S)

### 3.2.3 Base Course Resilient Modulus

Resilient modulus tests were conducted following AASHTO T307 on samples collected from the CC9 granular base course (P-209MR) in four SUs, of which two (SU2 and SU3) were located within the geosynthetic test area. SU2 covered test items LFS-3N and LFS-3S, and SU3 covered LFS-4S. Figure 25 and Figure 26 show resilient modulus test data for P-209MR material in SU2 and SU3, respectively. Each set of tests consisted of three replicates. As expected, the P-209MR material exhibited stress hardening behavior. The resilient modulus ranged from 20 to just over 100 ksi.

### 3.2.4 Asphalt Concrete Dynamic Modulus

Dynamic modulus tests were conducted on AC specimens following AASHTO T342-11 (AASHTO, 2019). Three specimens with a 4-in.-diameter and a 6-in.-trimmed height were tested at 4 °C (39 °F), 20 °C (68 °F), and 3 5°C (95 °F) using loading frequencies of 25, 10, 5.0, 1.0, 0.5, and 0.1 Hz. Figure 27 shows a summary of the dynamic modulus data, including the master curve, for the CC9 PG76-22 mixture.

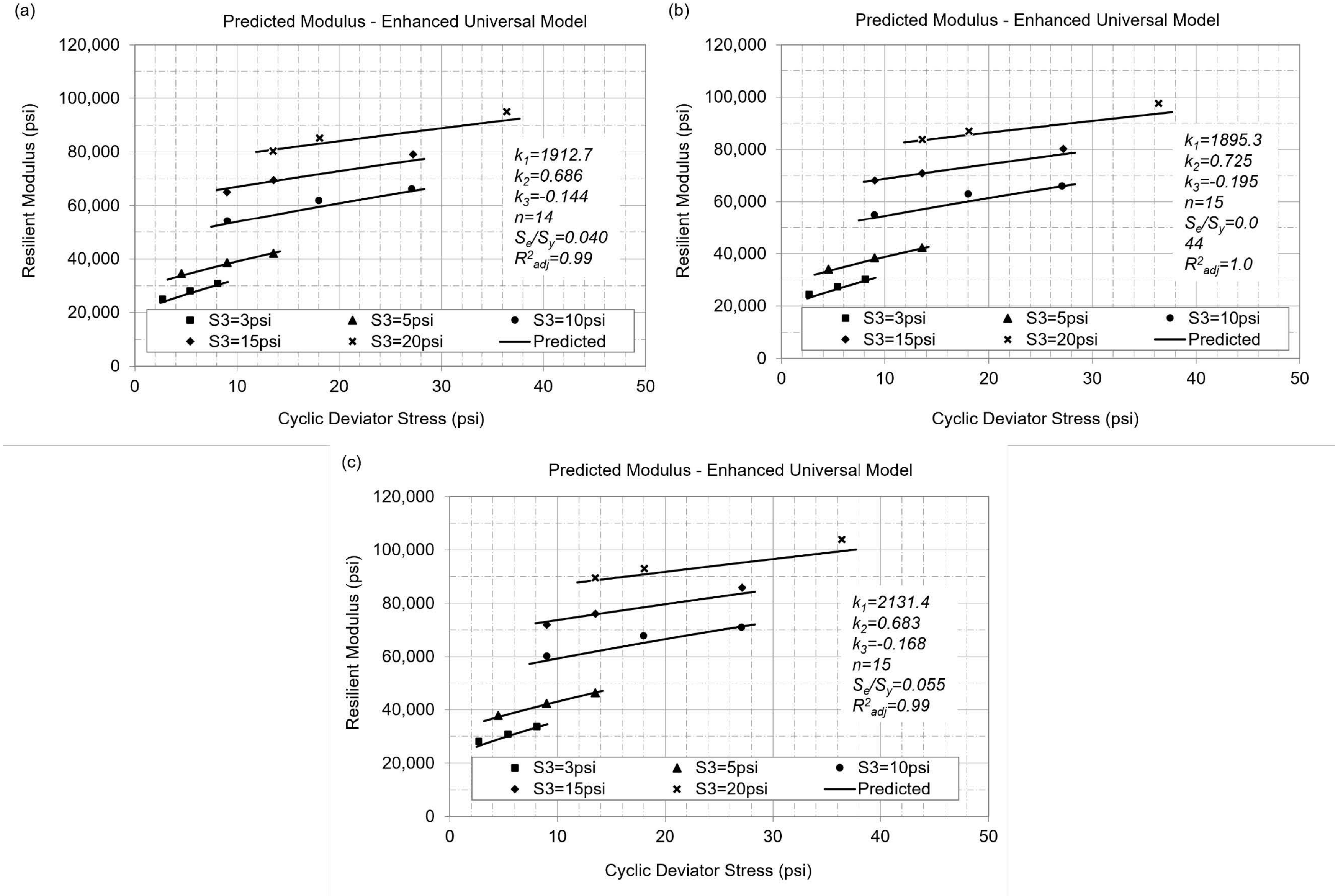

Figure 25. Resilient Modulus of Crushed Aggregate Base (P-209MR SU2—LFS-4N and LFS-4S)

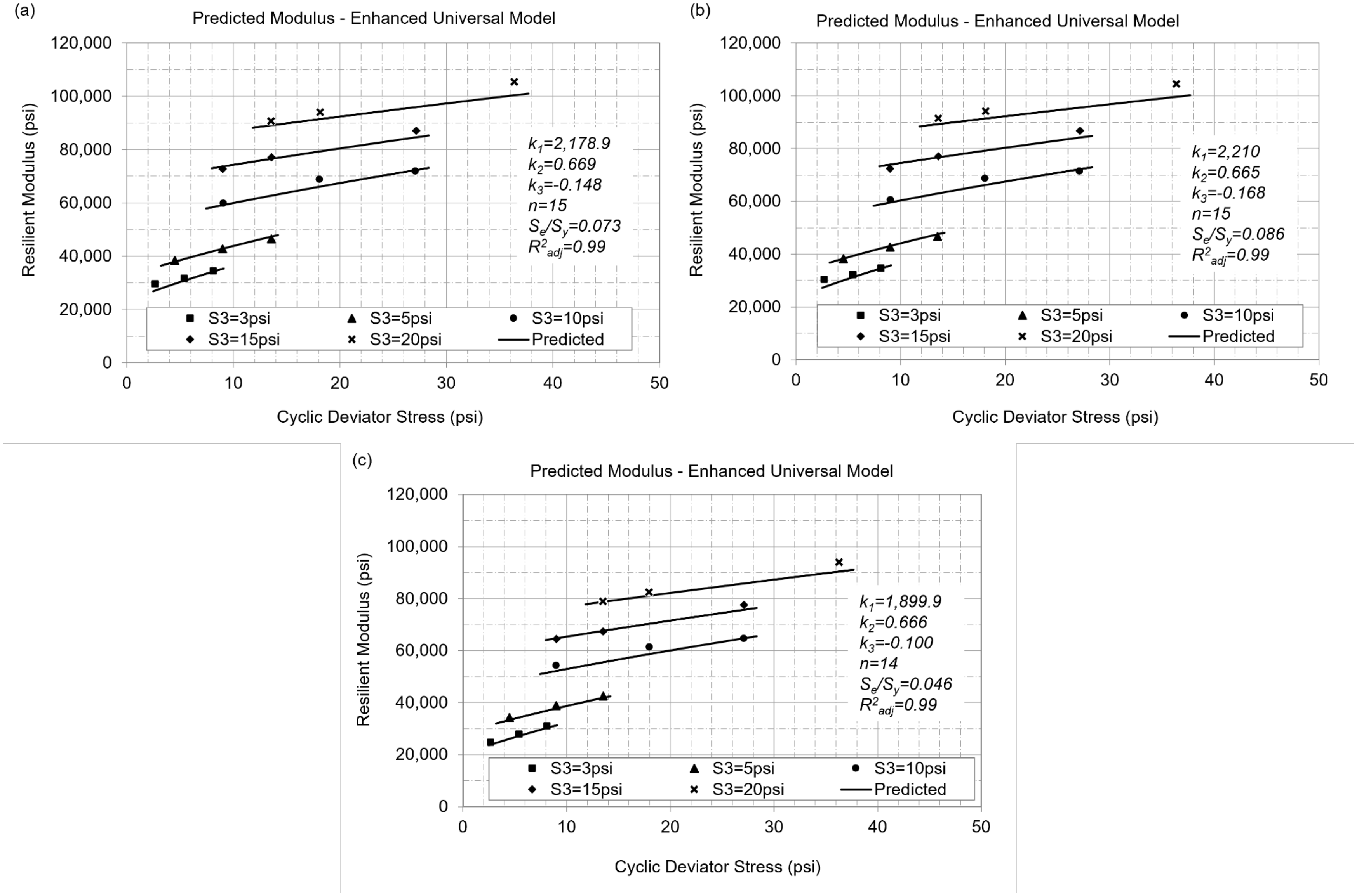

Figure 26. Resilient Modulus of Crushed Aggregate Base (P-209MR SU3—LFS-4S)

**Summary of Dynamic Modulus Test Results**

| Conditions | | Specimen 1 | | Specimen 2 | | Specimen 3 | | Average | Modulus | Average | Std Dev |
|---|---|---|---|---|---|---|---|---|---|---|---|
| Temperature (°C) | Frequency (Hz) | Modulus (ksi) | Phase Angle (Deg) | Modulus (ksi) | Phase Angle (Degree) | Modulus (ksi) | Phase Angle (Degree) | Modulus (ksi) | CV (%) | Phase (Deg) | Phase (Deg) |
| 4 | 0.1 | 966.5 | 22.9 | 1081.7 | 22.4 | 935.8 | 22.8 | **994.7** | 7.7 | **22.7** | 0.3 |
| | 0.5 | 1365.8 | 18.5 | 1530.9 | 18.1 | 1323.0 | 18.6 | **1406.6** | 7.8 | **18.4** | 0.3 |
| | 1.0 | 1551.8 | 16.9 | 1741.2 | 16.5 | 1498.2 | 17.0 | **1597.1** | 8.0 | **16.8** | 0.3 |
| | 5.0 | 1995.0 | 13.5 | 2240.3 | 13.1 | 1940.0 | 13.6 | **2058.4** | 7.8 | **13.4** | 0.3 |
| | 10.0 | 2190.5 | 12.2 | 2463.5 | 11.8 | 2135.0 | 12.3 | **2263.0** | 7.8 | **12.1** | 0.3 |
| | 25.0 | 2447.5 | 10.7 | 2758.2 | 10.3 | 2392.0 | 10.8 | **2532.6** | 7.8 | **10.6** | 0.3 |
| 20 | 0.1 | 161.7 | 33.9 | 211.8 | 32.5 | 205.8 | 33.3 | **193.1** | 14.2 | **33.2** | 0.7 |
| | 0.5 | 310.8 | 32.9 | 405.2 | 31.4 | 391.6 | 31.4 | **369.2** | 13.8 | **31.9** | 0.9 |
| | 1.0 | 400.2 | 32.0 | 519.8 | 30.4 | 496.6 | 30.1 | **472.2** | 13.4 | **30.8** | 1.0 |
| | 5.0 | 691.0 | 27.3 | 872.7 | 25.8 | 821.9 | 25.2 | **795.2** | 11.8 | **26.1** | 1.0 |
| | 10.0 | 836.9 | 25.3 | 1048.9 | 23.9 | 979.3 | 23.4 | **955.0** | 11.3 | **24.2** | 1.0 |
| | 25.0 | 1055.6 | 22.5 | 1312.9 | 21.0 | 1211.1 | 20.5 | **1193.2** | 10.9 | **21.3** | 1.0 |
| 35 | 0.1 | 46.1 | 32.7 | 57.4 | 29.9 | 48.0 | 30.7 | **50.5** | 12.0 | **31.1** | 1.5 |
| | 0.5 | 91.5 | 36.0 | 110.2 | 33.9 | 92.3 | 34.5 | **98.0** | 10.8 | **34.8** | 1.1 |
| | 1.0 | 123.7 | 37.6 | 147.8 | 35.6 | 124.4 | 36.2 | **132.0** | 10.4 | **36.5** | 1.0 |
| | 5.0 | 281.1 | 33.9 | 323.4 | 32.6 | 282.5 | 32.9 | **295.7** | 8.1 | **33.1** | 0.7 |
| | 10.0 | 380.0 | 32.5 | 433.1 | 31.3 | 380.9 | 31.6 | **398.0** | 7.6 | **31.8** | 0.6 |
| | 25.0 | 537.7 | 30.1 | 607.1 | 29.2 | 538.2 | 29.6 | **561.0** | 7.1 | **29.6** | 0.5 |

**Dynamic Modulus Master Curve Parameters**

| Fitting Parameters | |
|---|---|
| **Max** | 3245 |
| **Min** | 7.766 |
| **Beta** | -0.829 |
| **Gamma** | -0.679 |
| **EA** | 160674 |
| **Goodness of Fit:** | |
| **R$^2$** | 0.97 |
| Se/Sy | 0.12 |

**Notes:**

Dynamic modulus data have been converted to US units. Reference Temperature is 20°C

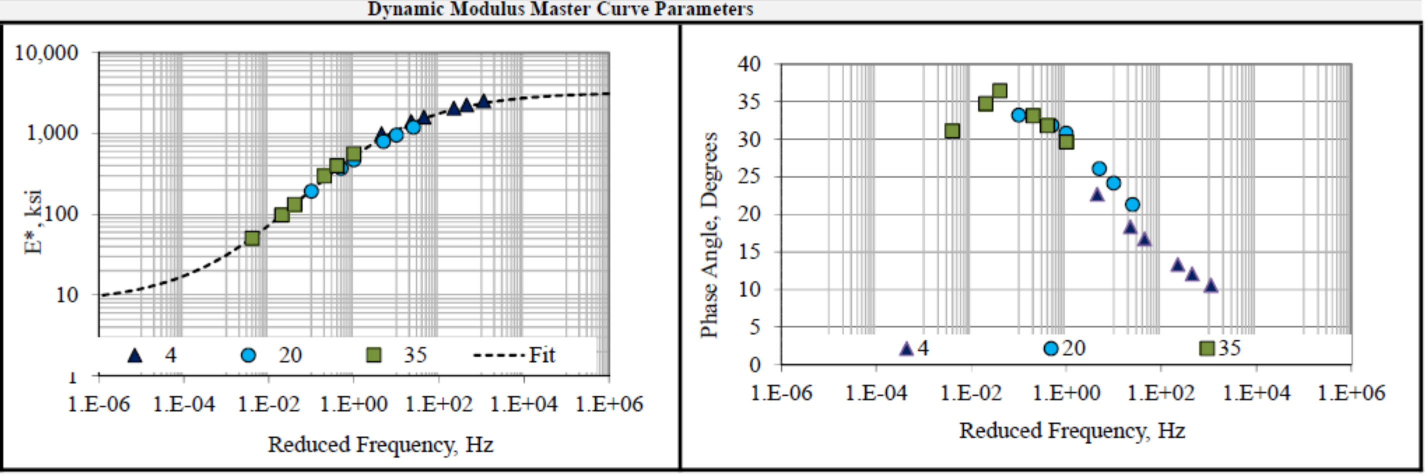

Figure 27. (a) Dynamic Modulus Test Summary, (b) Master Curve, and (c) Phase Angle Master Curve for CC9 PG76-22 Asphalt Mixture

## 3.3 STRENGTH CHARACTERIZATION OF STRUCTURAL LAYER MATERIALS

### 3.3.1 Subbase Shear Strength

Following the resilient modulus test procedure (Section 3.2.2), QS tests were conducted on the granular subbase (P-154MR) replicated at three confining pressures (5, 10, and 15 psi). QS tests followed the University of Illinois method (Chow, 2014). As noted in Section 3.2.2, the MC was intentionally dry of optimum. The fitted Mohr-Coulomb failure envelopes in Figure 28 show the cohesion coefficients $c$ and angles of internal friction $\phi$ for LFC-3N and LFC-3S (SU1), and for LFC-4S (SU2).

### 3.3.2 Base Course Shear Strength

Figure 29 shows Mohr-Coulomb failure envelopes for three confining pressures for the crushed aggregate base materials (P-209MR) in the geosynthetics test area. Failure envelopes show $c$ and $\phi$ for LFC-3N and LFC-3S (P-209MR SU2) and for LFC-4S (P-209MR SU3). Average $c$ values were slightly lower than for the subbase material, and average $\phi$ were slightly higher (Section 3.3.1).

### 3.3.3 High-Temperature Indirect Tensile Strength Test

Three asphalt samples of the polymer-modified PG 76-22 material used in the geosynthetics test area were tested using an indirect tensile (IDT) testing apparatus following a temperature-modified protocol. IDT tests followed the standard ASTM D6931-17 procedure (ASTM, 2017) except the temperature was increased from 25 °C (77 °F) to 40 °C (104 °F), hence these tests are referred to as high-temperature indirect tensile strength (HTITS) tests. Research indicates that the HTITS test correlates well with AC rutting (Kazmee et al., 2019; Li et al., 2015) and may serve as a rutting performance indicator (Batioja-Alvarez et al., 2024). Table 10 summarizes the HTITS test results.

Table 10. High-Temperature Indirect Tensile Strength Test Results for PG 76-22 Mixture used in CC9 Geosynthetic Test Items (All samples tested at 40 °C.)

| Sample No. | Air Void, % | Indirect Tensile Strength, psi |
|---|---|---|
| 76-13 | 4.9 | 53.7 |
| 76-14 | 4.6 | 47.9 |
| 76-15 | 4.6 | 56.6 |

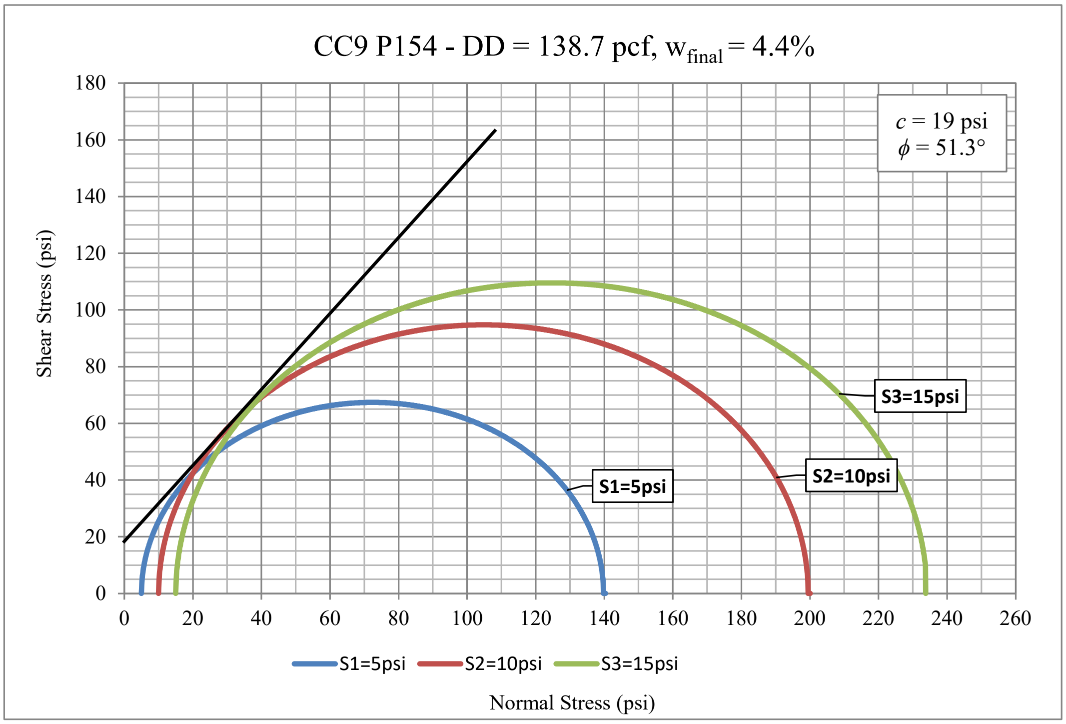

(a) P-154MR SU1

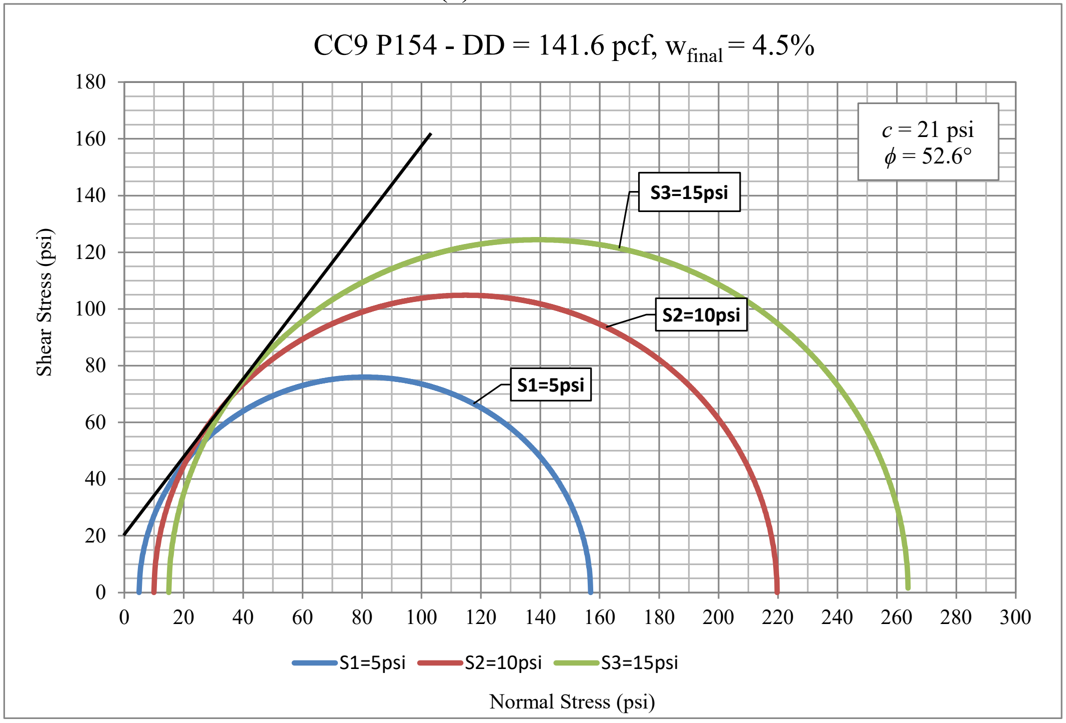

(b) P-154MR SU2

Figure 28. Shear Strength of Granular Subbase

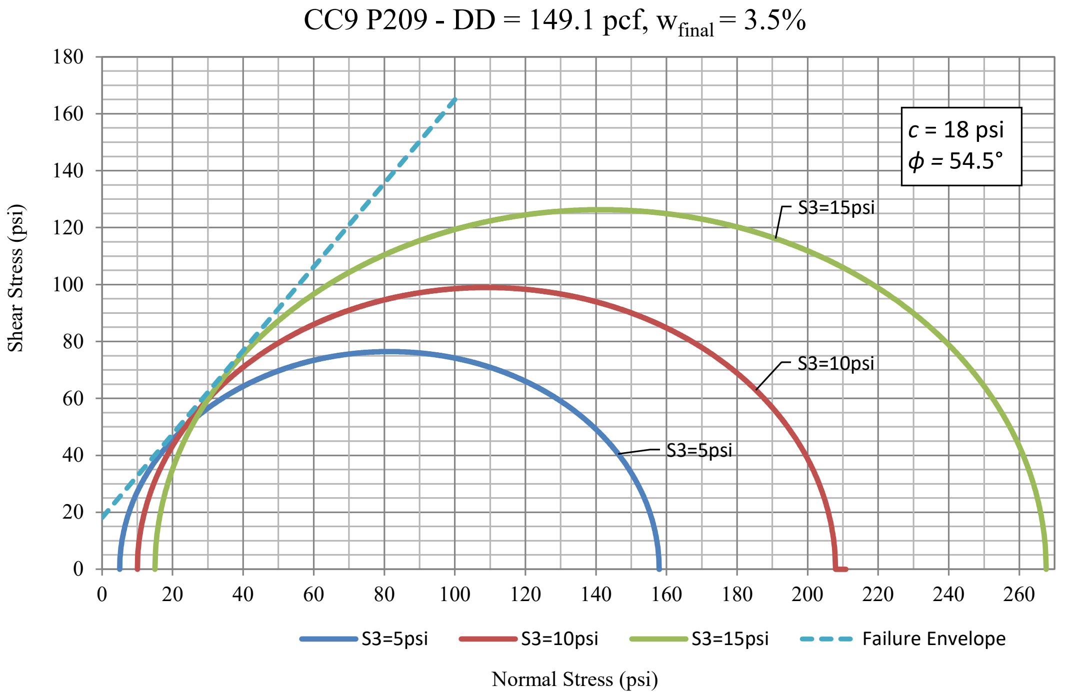

(a) P-209MR SU2

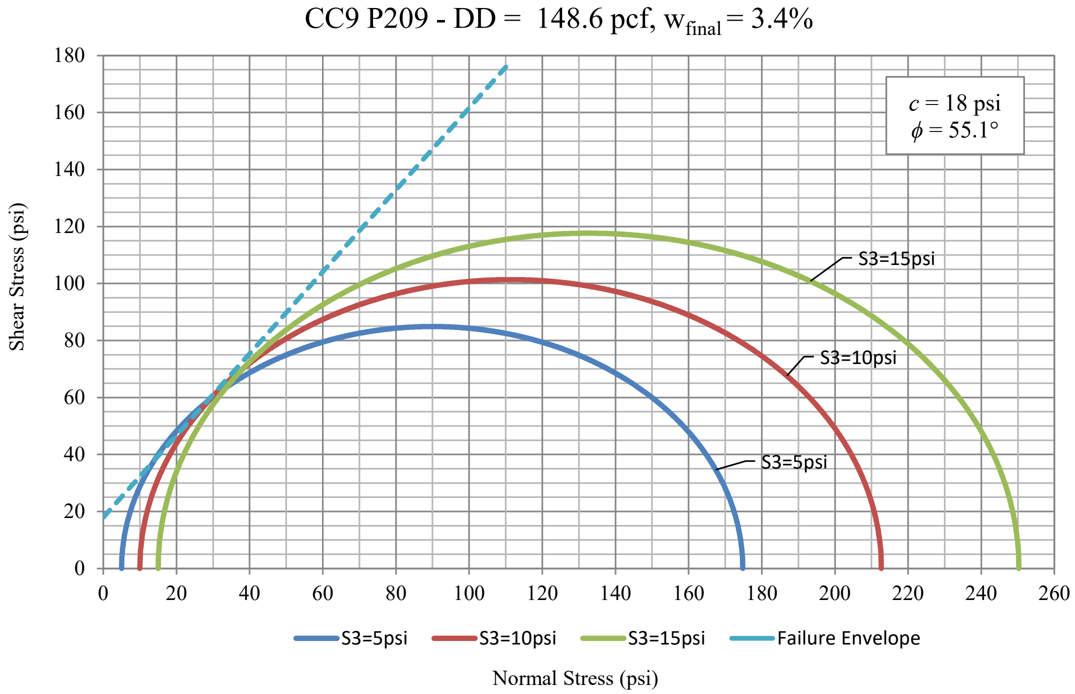

(b) P-209MR SU3

Figure 29. Shear Strength of Crushed Aggregate Base

## 3.4 DISPARITY BETWEEN LABORATORY AND IN-PLACE CHARACTERIZATION

Based on laboratory compaction tests (Section 3.1), OMCs of the granular subbase and crushed aggregate base were 7.2% and 5.5%, respectively. Granular layers were placed and compacted dry of optimum, as confirmed by nuclear density gauge data. To represent in situ conditions, the resilient modulus and shear strength tests were conducted on unbound specimens compacted to approximately 2.5% below OMC. For LWD tests on the finished granular subbase, the contact stresses were maintained between 8 and 22 psi, and the highest backcalculated LWD modulus was 20 ksi. By contrast, in laboratory resilient modulus tests run at similar deviatoric stresses, the subbase resilient modulus was significantly higher, in the range of 20 to 55 ksi. Similarly, for the base course material, the laboratory resilient modulus values varied from 60 to 100 ksi over a deviatoric stress range of 25 to 50 psi, while the highest LWD modulus (with similar contact stresses) was only about 39 ksi. Some disparity in field-versus-laboratory modulus is expected, considering the differences in testing methodology and equipment, and the fact that the LWD captures contributions from all layers, including lower-modulus layers under the layer being tested. However, the large disparity suggests that either (a) the nuclear gauge estimated moisture contents were erroneous, or (b) field compaction control was inadequate.

# 4. TRAFFIC TESTS ON GEOSYNTHETIC TEST ITEMS

## 4.1 PRE-TRAFFIC TESTS

### 4.1.1 Slow-Roll Response Tests

The slow-roll response test was executed November 6–20, 2020, on geosynthetic test items LFC-3 and LFC-4. Pavement responses (stresses, strains, and deflections) were recorded for the following gear configurations: single (S), dual (D), two duals in tandem (2D), and three duals in tandem (3D). The response test variable matrix was as follows:

- Vehicle speed (mph): 0.5, 1.6, 2.5
- Gear offset from centerline (ft): ±8.25, ±10.50, ±12.75, ±15.00, ±17.25, ±19.50
- Wheel loads (lb): 12,000, 24,000, 36,000
- Tire pressure: 255 psi
- Passes: two passes for each wheel load at each offset (one forward, one return)

Sensor functionality was assessed under various loads and speeds. Observations from the slow-roll response tests are discussed in the traffic testing summary report (CC9 Technical Report Vol. 1) (Kazmee et al., 2026).

Figure 30 and Figure 31 show examples of ASG slow-roll test data. In Figure 30 (LFC-3S), the four longitudinal strain gauges (LSGs) all responded as expected to increasing wheel load and decreasing vehicle speed. In Figure 31 (LFC-4S), there were some anomalous transverse strain gauge (TSG) responses. TSG-LFC-4S-3 appears to be an unreliable gauge, responding inconsistently to increases in load in Figure 31(a), and responding disproportionately to changes in vehicle speed in Figure 31(b).

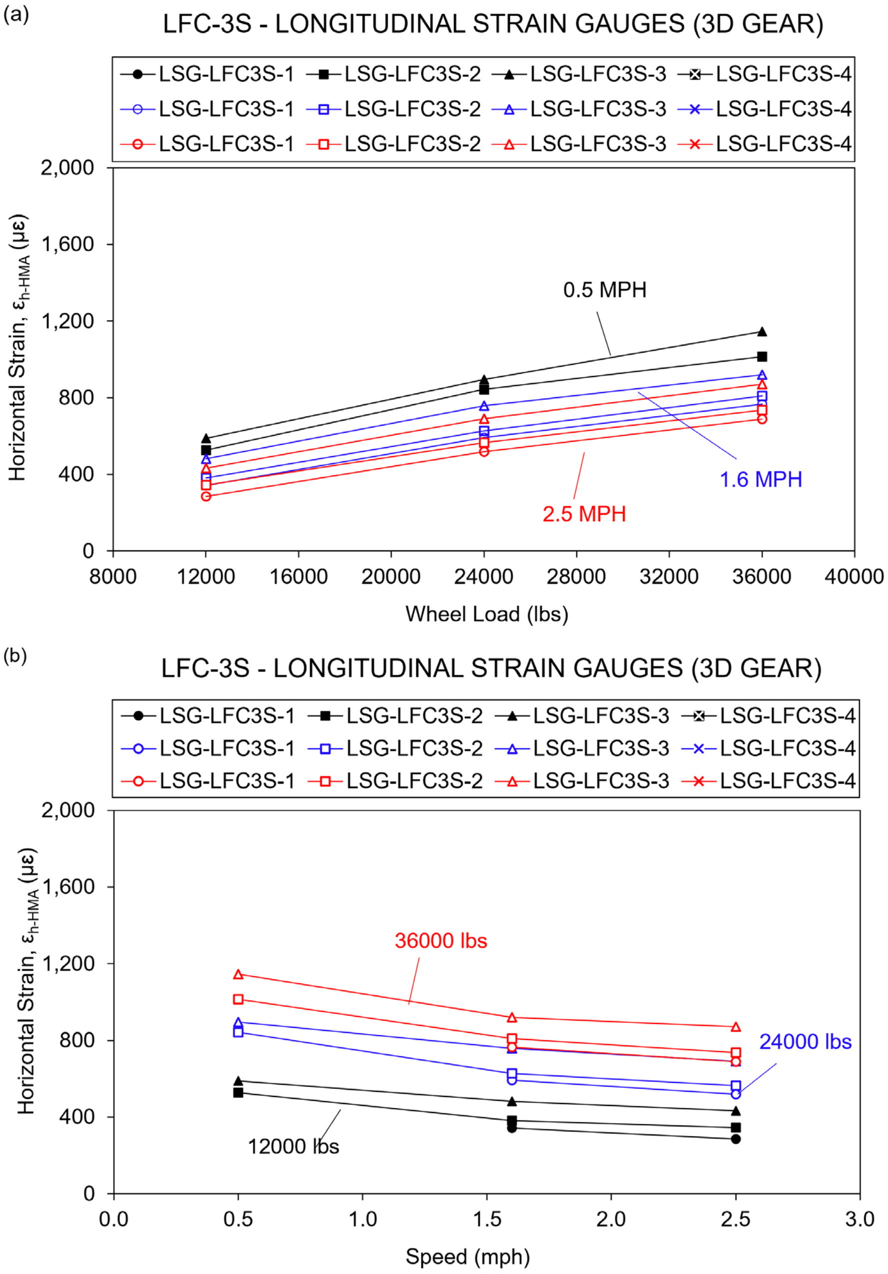

Figure 30. Slow-Roll Response of LSGs in LFC-3S: (a) Effect of Wheel Load and (b) Effect of Vehicle Speed

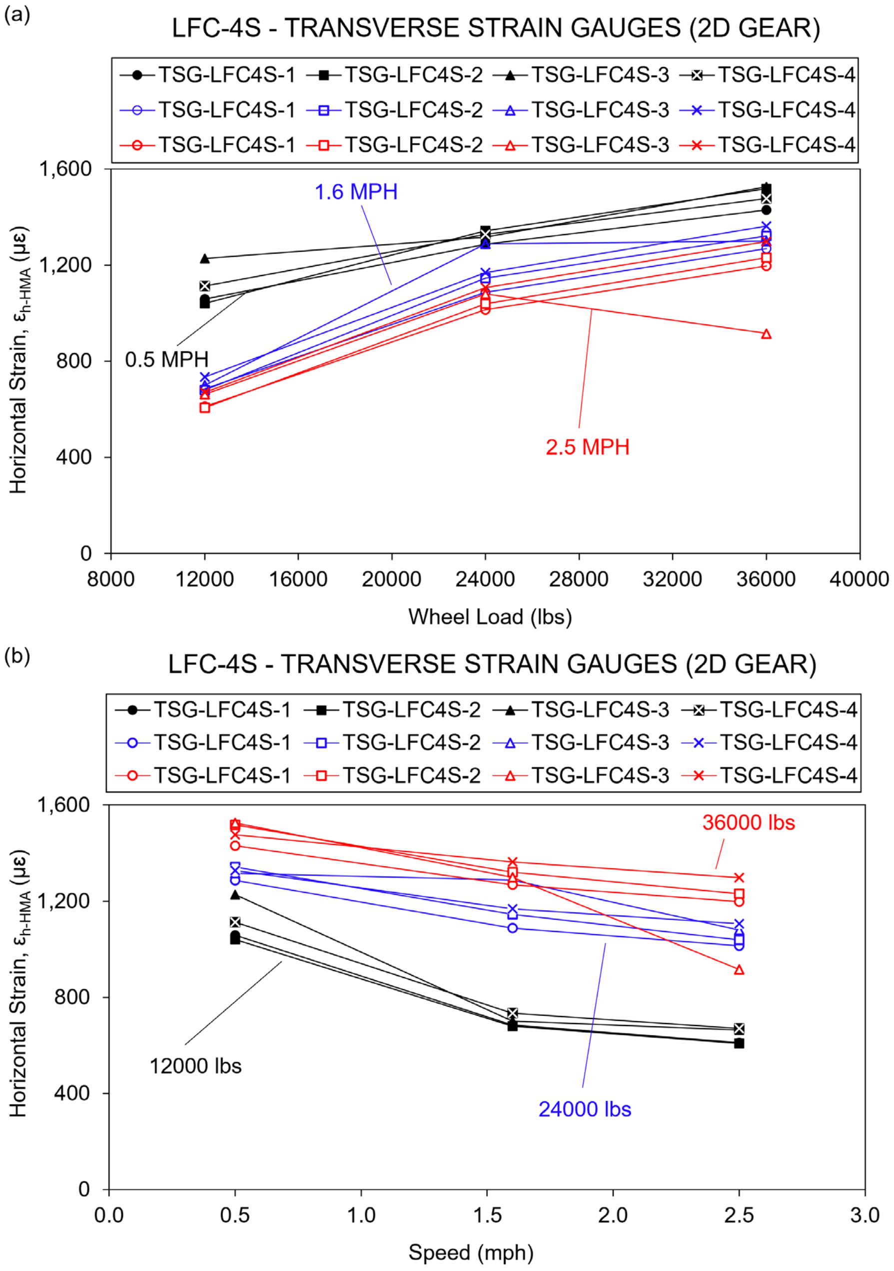

Figure 31. Slow-Roll Response of TSGs in LFC-4S: (a) Effect of Wheel Load and (b) Effect of Vehicle Speed

Figure 32 shows PC slow-roll test data for LFC-3N, under the D-gear load. As expected, the stress generally increased with wheel load and decreased with vehicle speed. However, PC-LFC-3N-1 (top of base) shows a maximum stress of about 90 psi. In the slow (0.5-mph) test, the stress response did not increase when the wheel load increased from 24,000 to 36,000 lb. This indicates that the PCs exceeded their capacity (were saturated) under the 36,000-lb D-gear load. PCs had a standard rating of 58.0 psi but could read up to 1.5 times their rated pressure (87 psi) per the manufacturer's specification. The slow-roll tests appear to bear this out, and a close examination of the response curve at 36,000 lb (Figure 33) reveals a saturation zone near the peak stress. The response to the 24,000-lb/wheel D gear is still within range, but the response to the 36,000 lb/wheel D gear is cut off, so the peak values appear to be equal. As discussed in Section 5, the fact that the PCs at the top of the base were undersized limited their value for analysis and probably led to their early failure.

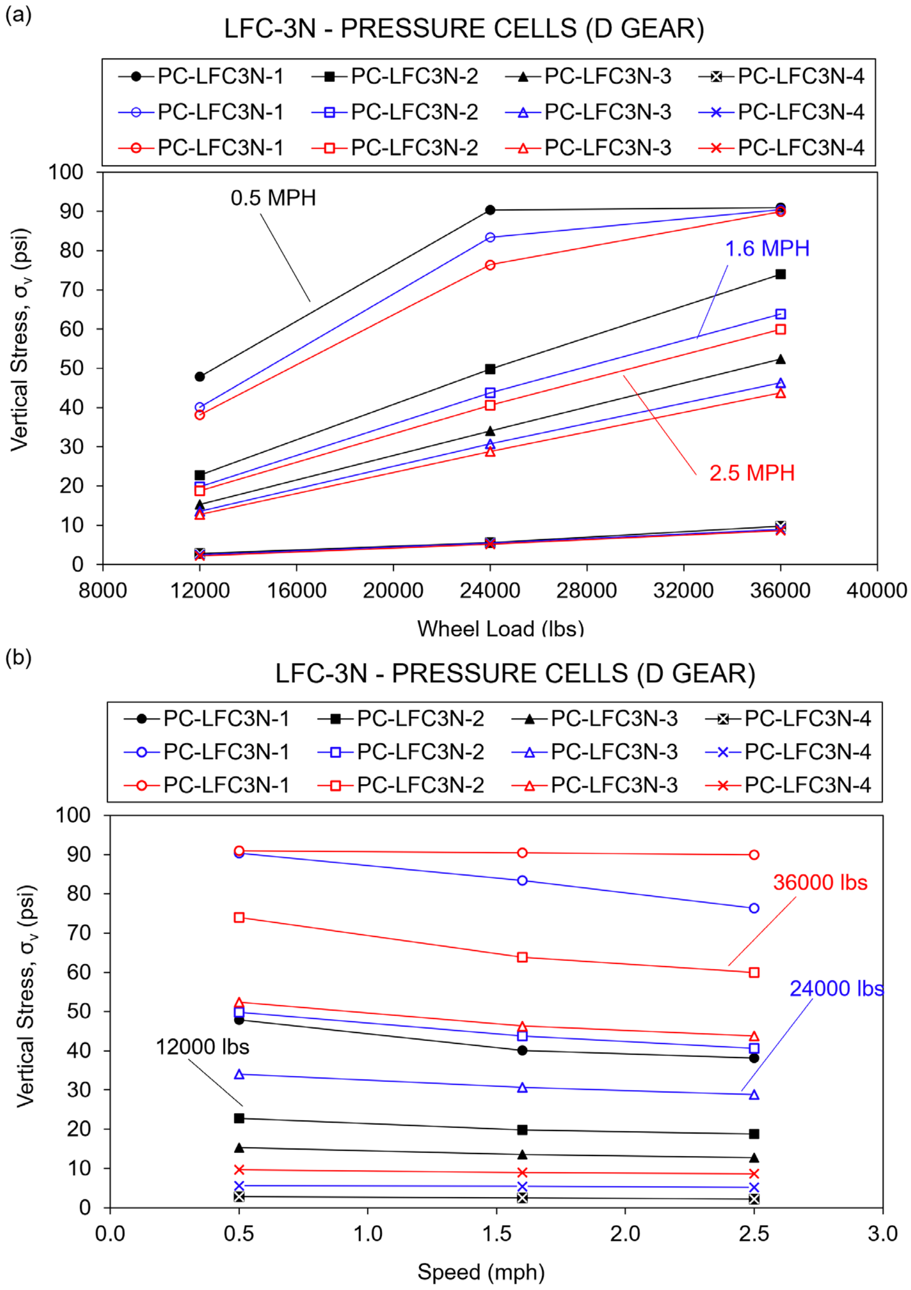

Figure 32. Slow-Roll Response of PCs in LFC-3N: (a) Effect of Wheel Load and (b) Effect of Vehicle Speed

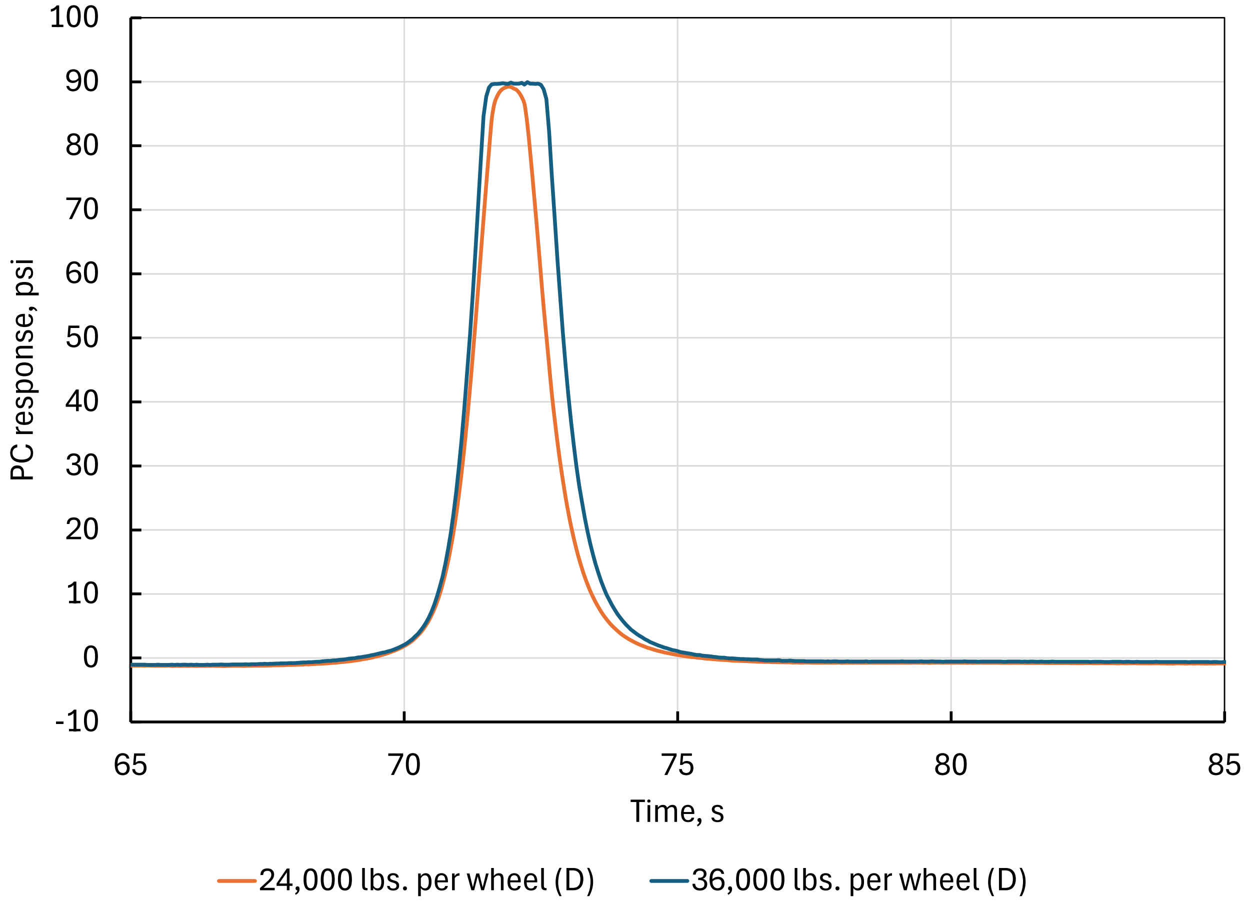

Figure 33. Slow-Roll (0.5 mph) Response of PC-LFC3N-1 Showing Signal Saturation at High Loads (Test Date November 13, 2020)

### 4.1.2 Proof-Roll Wander

A proof-roll sequence was applied using the carriage positions, as shown in Table 11 and Figure 34. As expected, the magnitudes of peak stresses and strains decreased with increasing lateral distance between the embedded sensor and loading wheel. Proof-rolling used a D gear at 20,000 lb per wheel.

Table 11. Carriage Positions for Each Pass of Proof-Roll Wander

| Pass Sequence | Direction | Carriage Centerline Location (ft) | |
|---|---|---|---|
| | | North | South |
| 1 | W–E | -19.34 | 2.68 |
| 2 | E–W | -19.34 | 2.68 |
| 3 | W–E | -18.507 | 3.513 |
| 4 | E–W | -18.507 | 3.513 |
| 5 | W–E | -17.674 | 4.346 |
| 6 | E–W | -17.674 | 4.346 |
| 7 | W–E | -16.841 | 5.179 |
| 8 | E–W | -16.841 | 5.179 |
| 9 | W–E | -16.008 | 6.012 |
| 10 | E–W | -16.008 | 6.012 |
| 11 | W–E | -15.175 | 6.845 |
| 12 | E–W | -15.175 | 6.845 |
| 13 | W–E | -14.342 | 7.678 |
| 14 | E–W | -14.342 | 7.678 |
| 15 | W–E | -13.509 | 8.511 |
| 16 | E–W | -13.509 | 8.511 |
| 17 | W–E | -12.676 | 9.344 |
| 18 | E–W | -12.676 | 9.344 |
| 19 | W–E | -11.843 | 10.177 |
| 20 | E–W | -11.843 | 10.177 |
| 21 | W–E | -11.01 | 11.01 |
| 22 | E–W | -11.01 | 11.01 |
| 23 | W–E | -10.177 | 11.843 |
| 24 | E–W | -10.177 | 11.843 |
| 25 | W–E | -9.344 | 12.676 |
| 26 | E–W | -9.344 | 12.676 |
| 27 | W–E | -8.511 | 13.509 |
| 28 | E–W | -8.511 | 13.509 |
| 29 | W–E | -7.678 | 14.342 |
| 30 | E–W | -7.678 | 14.342 |
| 31 | W–E | -6.845 | 15.175 |
| 32 | E–W | -6.845 | 15.175 |
| 33 | W–E | -6.012 | 16.008 |
| 34 | E–W | -6.012 | 16.008 |
| 35 | W–E | -5.179 | 16.841 |
| 36 | E–W | -5.179 | 16.841 |
| 37 | W–E | -4.346 | 17.674 |
| 38 | E–W | -4.346 | 17.674 |
| 39 | W–E | -3.513 | 18.507 |
| 40 | E–W | -3.513 | 18.507 |
| 41 | W–E | -2.68 | 19.34 |
| 42 | E–W | -2.68 | 19.34 |

W = West, E = East

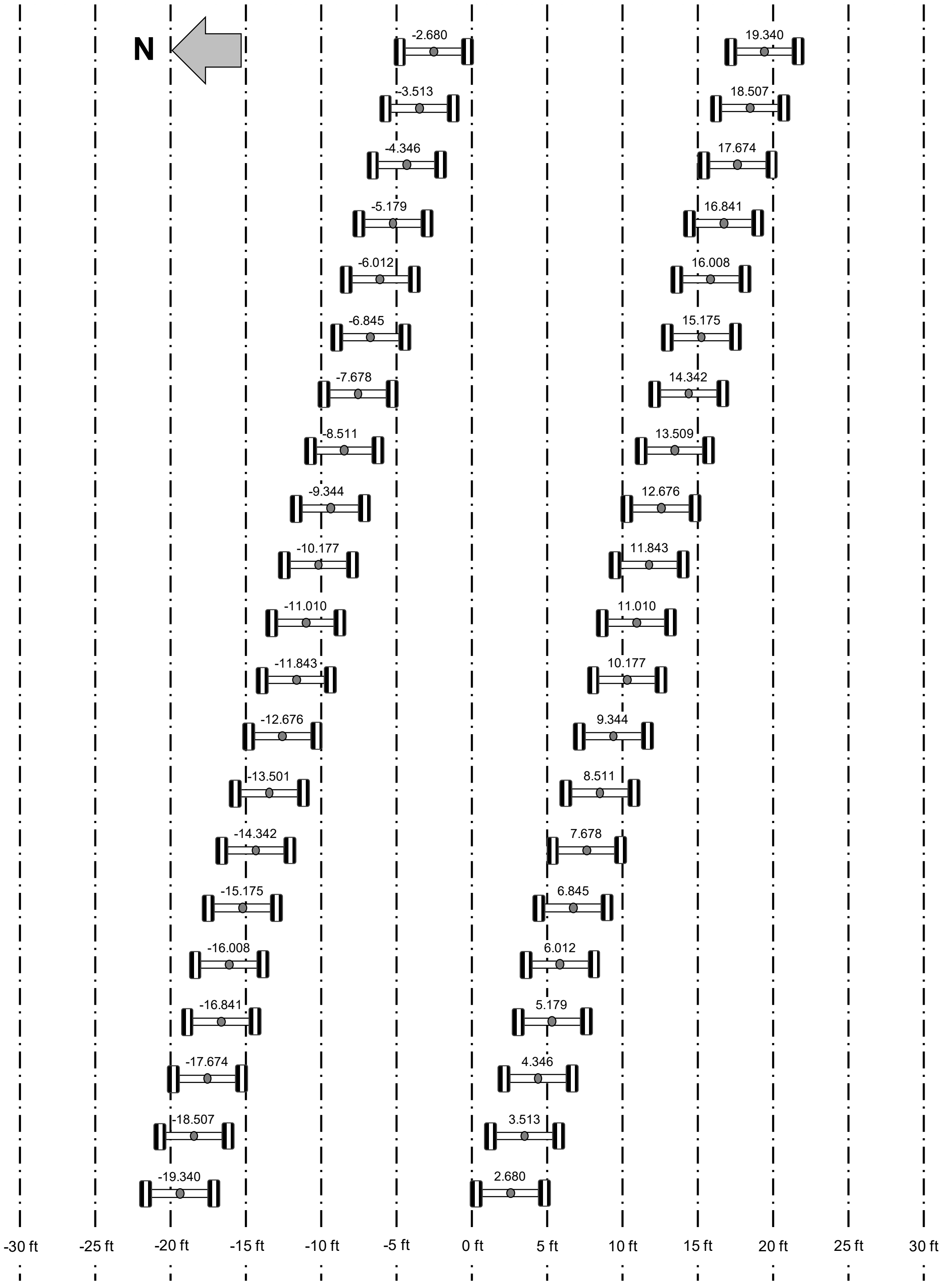

Figure 34. Carriage Positions for Each Pass of Proof-Roll Wander

## 4.2 TRAFFIC TESTING AND MONITORING

### 4.2.1 Wander Pattern

The wander pattern consists of 66 passes arranged in 9 wheel tracks, as shown in Table 12 and Figure 35. Passes are in both directions, west-to-east (odd) and east-to west (even). The even-numbered (return) pass is always along the same track as the preceding odd-numbered pass, but in the opposite direction. The complete wander pattern is listed in Table 13.

Table 12. Construction Cycle 9 Traffic Wander Wheel Track Locations

| **Track No.** | **Carriage Centerline Location, ft** | |
|---|---|---|
| | **North** | **South** |
| -4 | -18.412 | 11.588 |
| -3 | -17.559 | 12.441 |
| -2 | -16.706 | 13.294 |
| -1 | -15.853 | 14.147 |
| 0 | -15.000 | 15.000 |
| 1 | -14.147 | 15.853 |
| 2 | -13.294 | 16.706 |
| 3 | -12.441 | 17.559 |
| 4 | -11.588 | 18.412 |

Table 13. Construction Cycle 9 Complete Wander Sequence

| Pass Sequence | Direction | Track No. | Carriage Centerline Location (ft) | |
|---|---|---|---|---|
| | | | North | South |
| 1 | W–E | -4 | -18.412 | 11.588 |
| 2 | E–W | -4 | -18.412 | 11.588 |
| 3 | W–E | -2 | -16.706 | 13.294 |
| 4 | E–W | -2 | -16.706 | 13.294 |
| 5 | W–E | 0 | -15.000 | 15.000 |
| 6 | E–W | 0 | -15.000 | 15.000 |
| 7 | W–E | 2 | -13.294 | 16.706 |
| 8 | E–W | 2 | -13.294 | 16.706 |
| 9 | W–E | 4 | -11.588 | 18.412 |
| 10 | E–W | 4 | -11.588 | 18.412 |
| 11 | W–E | 3 | -12.441 | 17.559 |
| 12 | E–W | 3 | -12.441 | 17.559 |
| 13 | W–E | 1 | -14.147 | 15.853 |
| 14 | E–W | 1 | -14.147 | 15.853 |
| 15 | W–E | -1 | -15.853 | 14.147 |
| 16 | E–W | -1 | -15.853 | 14.147 |
| 17 | W–E | -3 | -17.559 | 12.441 |
| 18 | E–W | -3 | -17.559 | 12.441 |
| 19 | W–E | -4 | -18.412 | 11.588 |
| 20 | E–W | -4 | -18.412 | 11.588 |
| 21 | W–E | -2 | -16.706 | 13.294 |
| 22 | E–W | -2 | -16.706 | 13.294 |
| 23 | W–E | 0 | -15.000 | 15.000 |
| 24 | E–W | 0 | -15.000 | 15.000 |
| 34 | E–W | -1 | -15.853 | 14.147 |
| 35 | W–E | -3 | -17.559 | 12.441 |
| 36 | E–W | -3 | -17.559 | 12.441 |
| 37 | W–E | 3 | -12.441 | 17.559 |
| 38 | E–W | 3 | -12.441 | 17.559 |
| 39 | W–E | 1 | -14.147 | 15.853 |
| 40 | E–W | 1 | -14.147 | 15.853 |
| 41 | W–E | -1 | -15.853 | 14.147 |
| 42 | E–W | -1 | -15.853 | 14.147 |
| 43 | W–E | -3 | -17.559 | 12.441 |
| 44 | E–W | -3 | -17.559 | 12.441 |
| 45 | W–E | -2 | -16.706 | 13.294 |
| 46 | E–W | -2 | -16.706 | 13.294 |
| 47 | W–E | 0 | -15.000 | 15.000 |
| 48 | E–W | 0 | -15.000 | 15.000 |
| 49 | W–E | 2 | -13.294 | 16.706 |
| 50 | E–W | 2 | -13.294 | 16.706 |
| 51 | W–E | -2 | -16.706 | 13.294 |
| 52 | E–W | -2 | -16.706 | 13.294 |
| 53 | W–E | 0 | -15.000 | 15.000 |
| 54 | E–W | 0 | -15.000 | 15.000 |
| 55 | W–E | 2 | -13.294 | 16.706 |
| 56 | E–W | 2 | -13.294 | 16.706 |
| 57 | W–E | 1 | -14.147 | 15.853 |

| Pass Sequence | Direction | Track No. | Carriage Centerline Location (ft) | |
|---|---|---|---|---|
| | | | North | South |
| 25 | W–E | 2 | -13.294 | 16.706 |
| 26 | E–W | 2 | -13.294 | 16.706 |
| 27 | W–E | 4 | -11.588 | 18.412 |
| 28 | E–W | 4 | -11.588 | 18.412 |
| 29 | W–E | 3 | -12.441 | 17.559 |
| 30 | E–W | 3 | -12.441 | 17.559 |
| 31 | W–E | 1 | -14.147 | 15.853 |
| 32 | E–W | 1 | -14.147 | 15.853 |
| 33 | W–E | -1 | -15.853 | 14.147 |

| Pass Sequence | Direction | Track No. | Carriage Centerline Location (ft) | |
|---|---|---|---|---|
| | | | North | South |
| 58 | E–W | 1 | -14.147 | 15.853 |
| 59 | W–E | -1 | -15.853 | 14.147 |
| 60 | E–W | -1 | -15.853 | 14.147 |
| 61 | W–E | 1 | -14.147 | 15.853 |
| 62 | E–W | 1 | -14.147 | 15.853 |
| 63 | W–E | -1 | -15.853 | 14.147 |
| 64 | E–W | -1 | -15.853 | 14.147 |
| 65 | W–E | 0 | -15.000 | 15.000 |
| 66 | E–W | 0 | -15.000 | 15.000 |

W = West, E = East

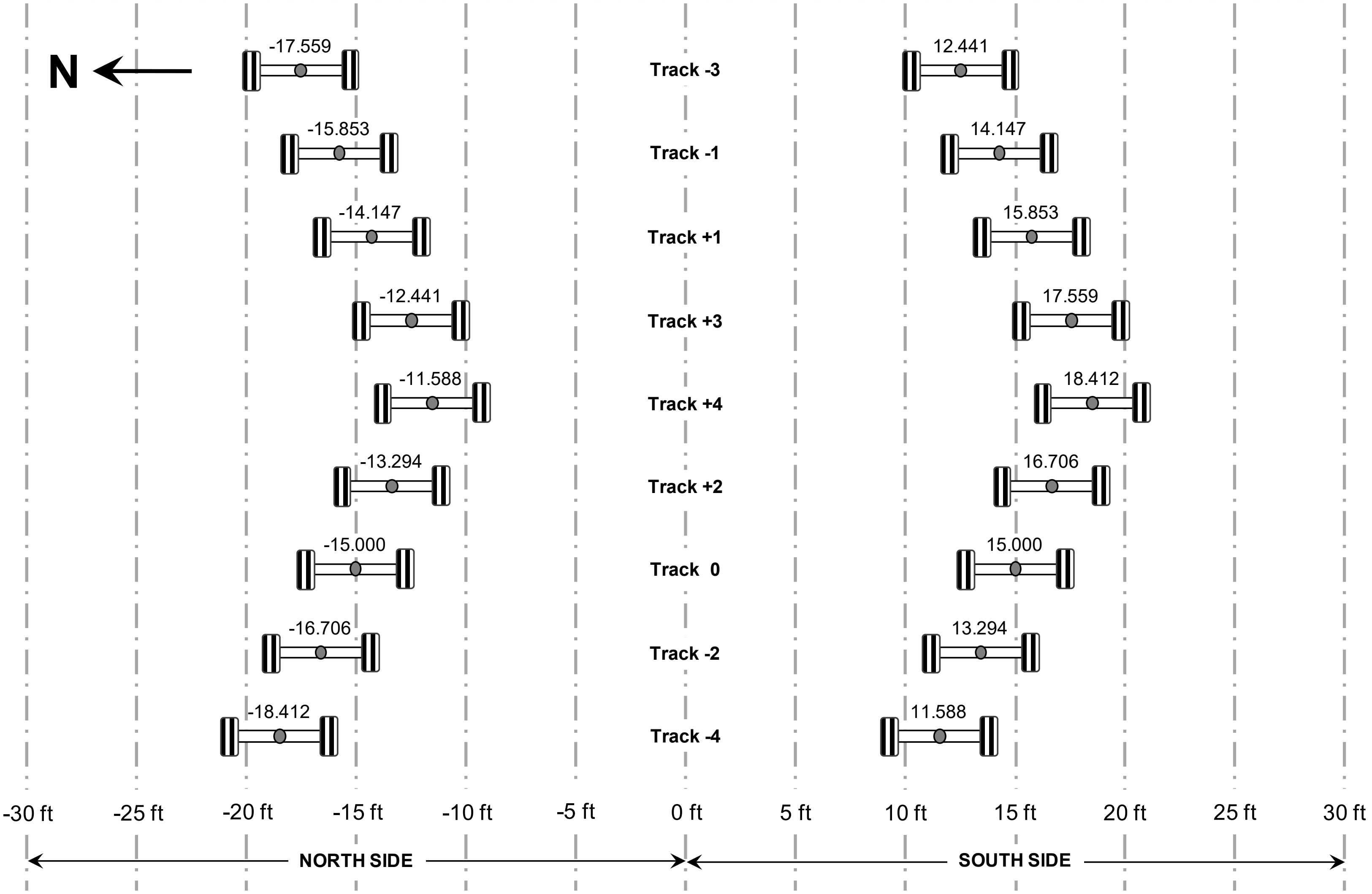

Figure 35. Construction Cycle 9 Traffic Wander Wheel Tracks

### 4.2.2 Failure Criteria

Ahlvin et al. (1971) defined two failure criteria:

(i) Surface upheaval of the pavement adjacent to the traffic wander exceeded 1 in. or
(ii) Surface cracking so severe that the pavement no longer remained waterproof.

The same failure criteria were adopted in all preceding flexible pavement CCs.

### 4.2.3 Traffic History

Table 14 lists the key events during CC9 trafficking with dates. Traffic on the geosynthetics test items LFC-3N/S and LFC-4S is highlighted in yellow. For all passes, the NAPTV was configured as a 3D gear with a wheel load of 58,000 lb and nominal tire pressure of 255 psi.

Table 14. Construction Cycle 9 Traffic Summary

| **Dates** | **Passes on Test Items** | | | **Load Description** |
|---|---|---|---|---|
| | **LFS-1/2** | **LFC-3/4** | **LFC-5** | |
| 04/05/2021–06/03/2021 | 5,544 | 5,544 | 0 | Traffic test items 1-4 |
| 07/01/2021 | 0 | 0 | 66 | 1st Overload LFC-5N |
| 07/01/2021–07/28/2021 | 0 | 0 | 5478 | Traffic LFC-5 only |
| 08/02/2021–10/14/2021 | 7,066 | 7,066 | 7,066 | Traffic all test items |
| 10/15/2021–02/21/2022 | 0 | 0 | 0 | Vehicle down for maintenance |
| 02/22/2022–03/28/2022 | 3,956 | 3,956 | 3,956 | Resume traffic all test items |
| 03/29/2022 | 0 | 0 | 66 | 2nd overload LFC-5N |
| 03/29/2022–10/05/2022 | 24,354 | 24,354 | 24,288 | Traffic all test items |
| 10/12/2022 | 0 | 0 | 396 | 3rd overload LFC-5N |
| 10/13/2022–12/21/2022 | 0 | 0 | 15,312 | Traffic LFC-5 only |
| 01/03/2023–03/29/2023 | 13,728 | 0 | 0 | Traffic test items LFS-1/2 |
| 01/25/2024–04/02/2024 | 20,460 | 0 | 0 | Traffic test items LFS-1/2 |
| Total | 75,108 | 40,920 | 56,628 | |

### 4.2.4 Routine Monitoring and Testing

#### 4.2.4.1 Dynamic Responses

Dynamic responses are sensor responses triggered by an NAPTV pass. Dynamic responses included:

- Horizontal strains (bottom of HMA layer)
- Permanent deformation using coil sensors
- Vertical stresses from pressure cells

#### 4.2.4.2 Static Responses

Static sensor responses were collected hourly. Static sensor responses included temperature and moisture data. Subgrade moisture sensors record volumetric moisture content. Volumetric moisture content $\theta_v$ measured with the embedded gauges may be converted to gravimetric MC using the formula:

$$w = \theta_v \times \frac{\rho_{water}}{\rho_{soil}} \tag{5}$$

where:

$w$ = gravimetric moisture content,
$\rho_{water}$ = density of water, and
$\rho_{soil}$ = laboratory-determined dry density of subgrade soil (as listed in Table 9).

#### 4.2.4.3 Manual Distress Survey

Visual distress surveys were performed daily in accordance with ASTM D5340-20 (ASTM, 2020), after each day's traffic. In addition to the standard survey data, researchers marked and measured very fine cracks (i.e., those that would be disregarded in a standard condition survey). All cracks were marked on the surface, and the beginning and end coordinates of the cracks were recorded to track their progression. Appendix C presents logs of observed cracks for the three test items that constitute the geosynthetics test. Detailed reference maps were prepared for each inspection, in which the cracks were color-coded, identifying the date first observed and the associated number of passes. Thus, new crack initiation and the propagation of existing cracks were tracked using color-coded maps. Appendix D contains distress maps for the three test items.

#### 4.2.4.4 Straightedge Rut Measurements

To monitor the accumulation of surface ruts, transverse surface profiles were measured with a 16-ft straightedge in accordance with ASTM E1703 (ASTM, 2015). The maximum rut depth value along the full length of the beam was measured with a dial gauge and recorded. This measurement was performed at two stations within each test item. Ruts were measured at the end of each trafficking day.

#### 4.2.4.5 Heavy Weight Deflectometer and Portable Seismic Properties Analyzer Test

HWD and PSPA tests were conducted at 2-week intervals during testing to monitor structural changes. HWD testing was conducted with a four-drop loading sequence beginning with a nominal 36,000-lb seating load, followed by 12,000-lb, 24,000-lb, and 36,000-lb (nominal) loads. Deflection basin parameters were normalized to the 36,000-lb load level. HWD tests were conducted at two stations and three lateral offsets (±5, ±15, and ±25 ft) in each test item. Tests at the ±15-ft offset location represented the center of traffic, while the other offsets were in the non-trafficked areas.

### 4.2.4.6 Three-Dimensional Laser Scanning

Three-dimensional (3-D) laser scanning using a Leica ScanStation P20 was used to track the relative change in surface elevations over time. Light Detection and Ranging (LiDAR) scans were conducted prior to trafficking and during trafficking at regular intervals to track changes in surface elevation with traffic. For each measurement set, a proprietary design and documentation software (AutoCAD® 3D) was used to generate the Cartesian coordinates from the random 3-D-point cloud elevations. The resulting 1-in., regularly spaced coordinates were then input into a C# programming language-based software (named SurfaceD) to compute a 3-D surface map, transverse profiles, and surface upheaval magnitudes.

### 4.2.5 Routine Performance Measurements

### 4.2.5.1 Crack Growth

Crack maps developed during the manual distress survey were reviewed to track the first appearance and progress of cracks. Surface distresses included longitudinal cracks in the trafficked area that later developed into interconnected, or alligator, cracks. For each test item, lengths of individual cracks and areas of alligator cracks were carefully measured and recorded in a schematic as they appeared. Figure 36(a) shows a typical longitudinal crack at the wander limit, and Figure 36(b) shows the evolution from linear cracks to alligator cracks. (Cracks have been highlighted on the pavement surface using markers).

(a) Linear crack at edge of traffic area

(b) Area of alligator cracking

Figure 36. Surface Distress Types, Test Item LFC-3N

### 4.2.5.2 Crack Density

Crack density (CD) is a metric for damage quantification and is defined as the portion of pavement surface that is occupied by distresses. A grid of uniform elements or units was established for each test item. If any portion of a unit is distressed, the entire unit area is considered distressed. The CD area is determined by counting the number of units exhibiting distresses. Therefore, the accuracy of CD increases with the number of discrete units within the area of interest. Crack measurements with an adequately small unit size can ensure a true representation of the distressed surface. Following CC7 practices (Garg et al., 2020), the CDs of CC9 test items were computed using 1-ft by 1-ft unit size in the traffic area only.

## 5. TEST RESULTS AND DISCUSSION

This section is organized by the following topics:

- Section 5.1 discusses surface distresses: surface upheaval, surface rutting, and cracking.
- Section 5.2 discusses the key pavement sensor responses: ASG, PC, and CS.
- Section 5.3 discusses results from nondestructive tests (NDTs).

### 5.1 SURFACE DISTRESS MONITORING

#### 5.1.1 Upheaval and Rutting

All three test items experienced deep ruts accompanied by large upheavals outside the traffic lane. As discussed in Section 4.2.2, upheavals exceeding 1 in. in flexible pavements are characteristic of a classic bearing capacity failure. By this standard, all three test pavements failed structurally before the end of traffic (Figure 37).

Figure 38 shows the evolution of surface upheaval with traffic in test items LFC-3N (geogrid plus geotextile), LFC-3S (geotextile only), and LFC-4S (control). Upheaval is measured relative to the original surface grade outside of the trafficked area. Figure 37 is annotated to show significant events that affected the observed upheaval trend. Appendix B gives the stations and offsets at which the maximum upheavals were recorded for each date. Positive upheaval values greater than approximately 1 in. are associated with subgrade shear failure. As shown in Figure 38, the upheaval increased sharply after the start of summer 2022 (approximately pass 27,000). Test item LFC-3S (geosynthetic separation layer only) consistently had the highest upheaval.

Upheaval and rut were monitored by means of 3-D laser scanning (Section 4.2.4.6). Rut and upheaval for a given number of passes were determined by subtracting a baseline surface elevation (measured before the start of traffic) from the elevation at that pass number.

Section 2 discusses the in situ characterization of the granular layers, and notes evidence of poor compaction control in the granular subbase layer (P-154MR) of LFC-3S and the crushed aggregate base layer (P-209MR) of LFC-3N. Those construction issues are believed to have contributed to the high levels of rutting observed in the geosynthetic-reinforced test items and obscured the presumed benefits of incorporating geosynthetics. Figure 37 shows that LFC-3S was the first test item to reach the set failure condition of 1-in. surface upheaval, followed by LFC-3N and LFC-4S, in that order. Lateral restraint and increased bearing capacity could not be ensured with the geogrid due to improper compaction control of the base layer in LFC-3N. Nevertheless, the tension membrane effect was manifested as a lower rate of upheaval at a later stage of trafficking compared to the control (LFC-4S). The maximum upheaval in the control test item LFC-4S was higher than that of LFC-3N by the end of traffic.

(a) (b)

Figure 37. Final Surface Condition of Geosynthetic Test Items: (a) View Facing Northeast Toward the Geosynthetics Test Area Showing Heavily Deformed Surface (November 8, 2022) and (b) Upheaval, Test Item LFC-3S (November 3, 2022)
(The trafficked area is on the left. The shoulder was initially level with the curb [right].)

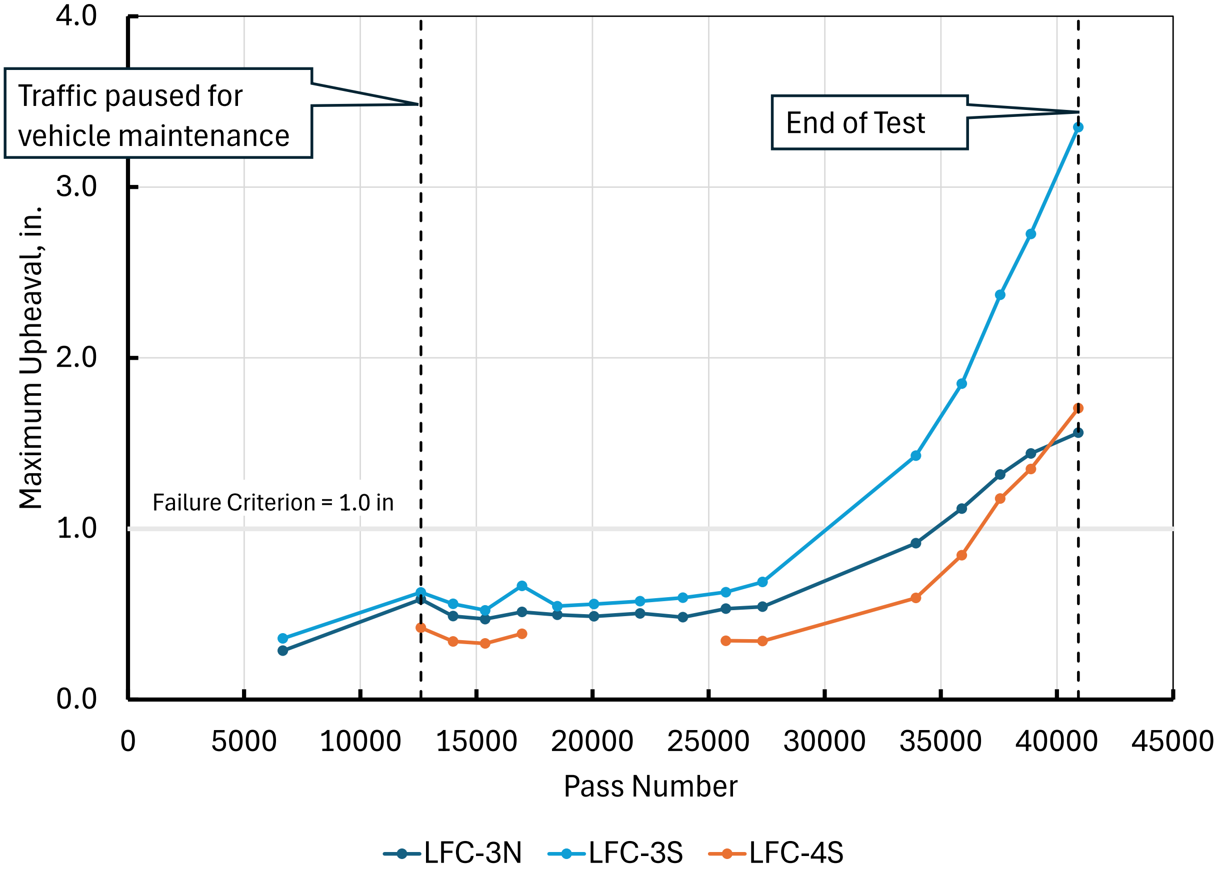

Figure 38. Evolution of Surface Upheaval in Geosynthetics Test Items

Figure 39 shows rut measurements taken using a 16-ft physical straightedge. The straightedge rut was measured from peak (or more precisely, from a point on a straight line connecting two peaks) to trough in the deformed section. As shown in Figure 39, straightedge ruts were measured at two stations within each test item. Rutting initially accumulated rapidly, with all test items reaching a rut depth of 1.5 in. by 10,000 passes. In this initial consolidation phase, the ruts in both geosynthetic-reinforced test items (LFC-3N and LFC-3S) were higher than the control (LFC-4S). After 12,600 passes, the test was paused for extended vehicle maintenance (Section 4.2.3). When traffic resumed following the winter cold weather, the asphalt had stiffened and the rate of rut accumulation decreased. The lateral confinement benefit of the geogrid in LFC-3N only became evident at about 38,000 passes when the total rut in the non-geogrid test item LFC-3S surpassed it and continued to increase. However, at this point all three test items were structurally failed. Regardless, the accumulated surface rut in control test item LFC-4S was consistently less than in either of the two reinforced test items.

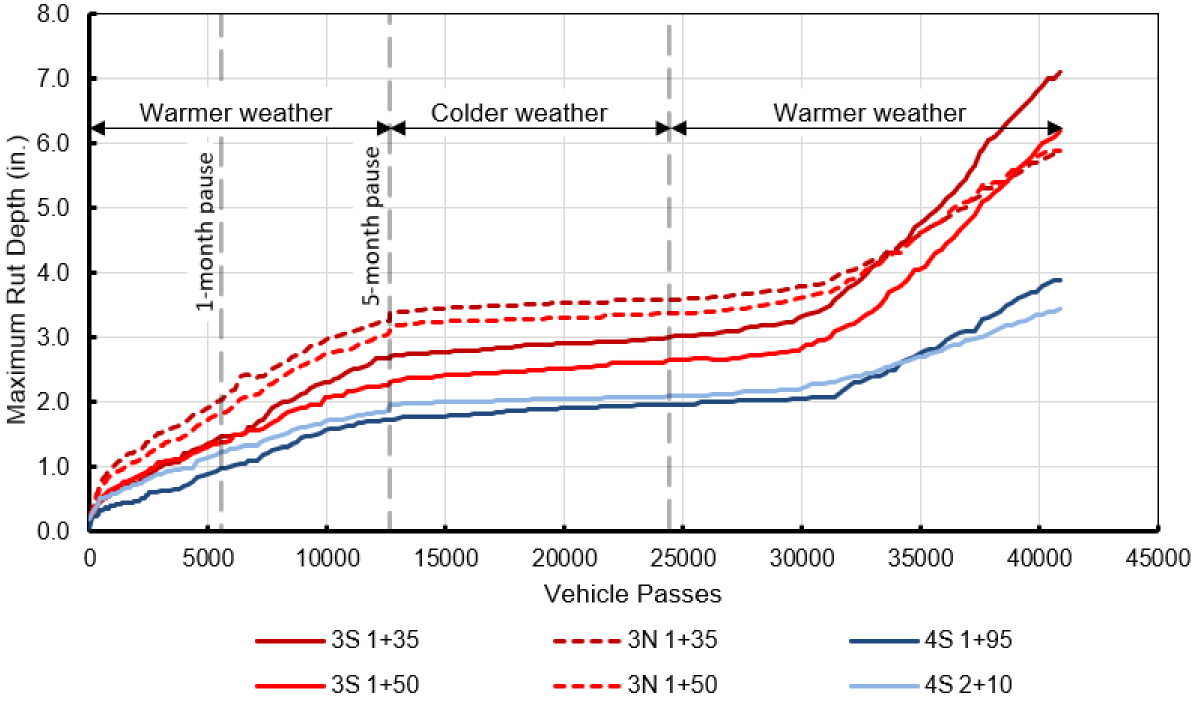

Figure 39. Rut Accumulation from Physical Straightedge in Geosynthetics Test Items

### 5.1.2 Cracking

Engineers performed regular visual surveys on the test items to track surface distresses. Data acquired from visual surveys were added to crack maps. Figure 40 and Figure 41 show the condition of the three test items after the end of traffic. In Figure 40 and Figure 41, cracks are color-coded by the date on which they were first observed (Table 15), so it is possible to track the evolution of distresses. Referring to the traffic history in Table 14, traffic was applied to the test area over four periods of varying duration, but surface cracks only appeared during the last period of traffic (March 29–October 5, 2022). Therefore, crack maps are shown only for this last period. Crack maps for specific days can be found in Appendix D. The series of crack maps in

Appendix D shows the gradual transition from individual longitudinal cracks to defined areas of intersecting (alligator) cracks after about 20,000 passes in the geosynthetic test items LFC-3A and LFC-3B.

Using the distress mapping data, engineers calculated cracking areas and CD for the three test items. Following the procedure in Section 4.2.5.2, the test item surface was divided into 1-ft squares. Since each test item is 30 ft by 45 ft, the number of squares is 1,350. For calculating CD, a square was considered damaged if at least one marked crack impinged on it. Table 16 summarizes the CD data by test item. Figure 42 shows the relationship between traffic and CD. The data are well-fitted by a four-parameter generalized logistic trend line, also known as a Richards model, of the following form:

$$\mathrm{CD} = \frac{a}{\left(1+exp(b-c\times N)\right)^{(1/d)}} \tag{6}$$

where:

$N$ is the pass number and
$a$, $b$, $c$, $d$ are parameters.

Support from the geogrid reinforcement may have improved load distribution in the underlying layers at a later stage of trafficking, thereby slowing the rate of crack accumulation in LFC-3N compared to LFC-3S. Table 17 gives the best-fit parameters for the CC9 data.

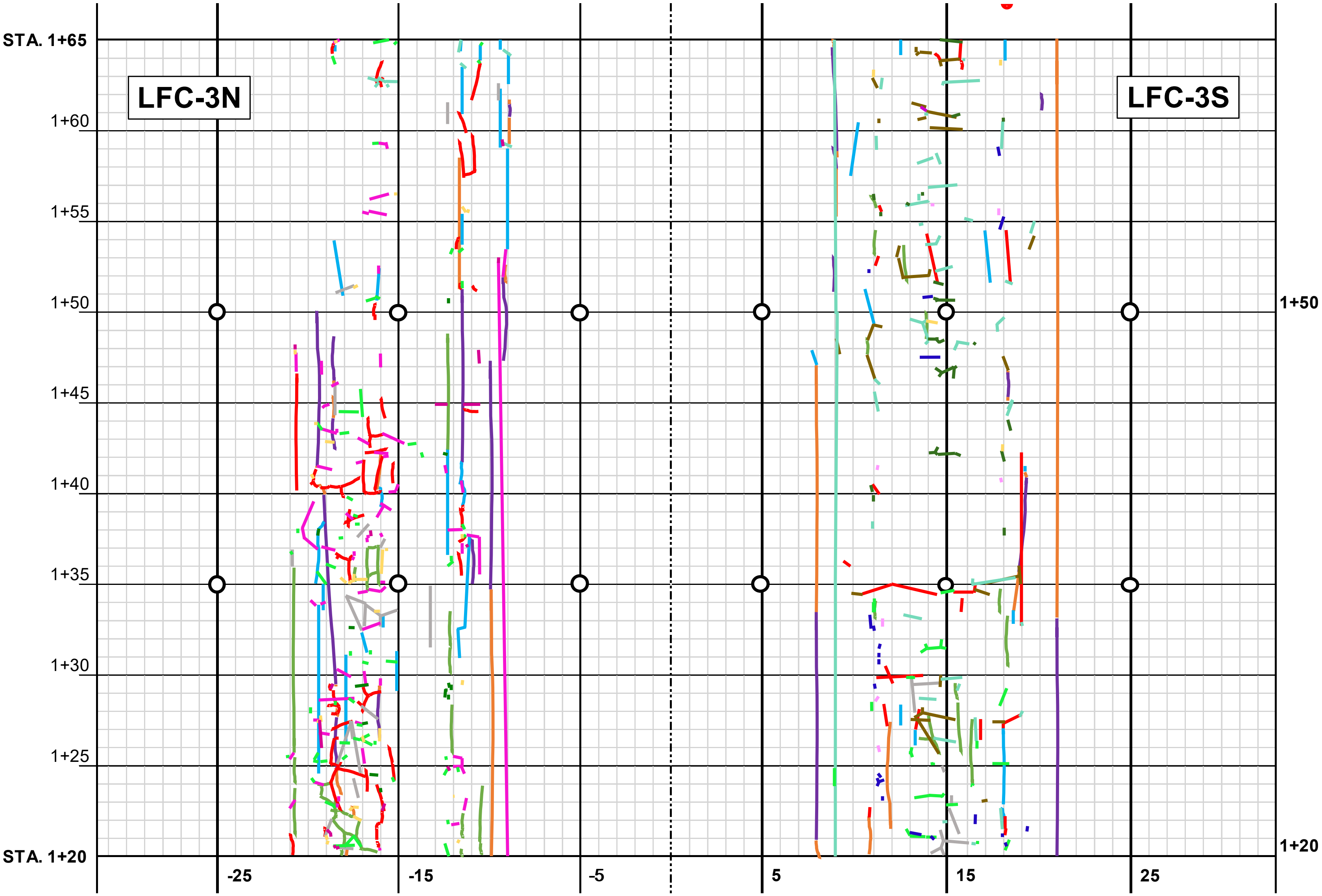

Figure 40. Crack Map for LFC-3S and LFC-3N (final condition as of October 7, 2022)

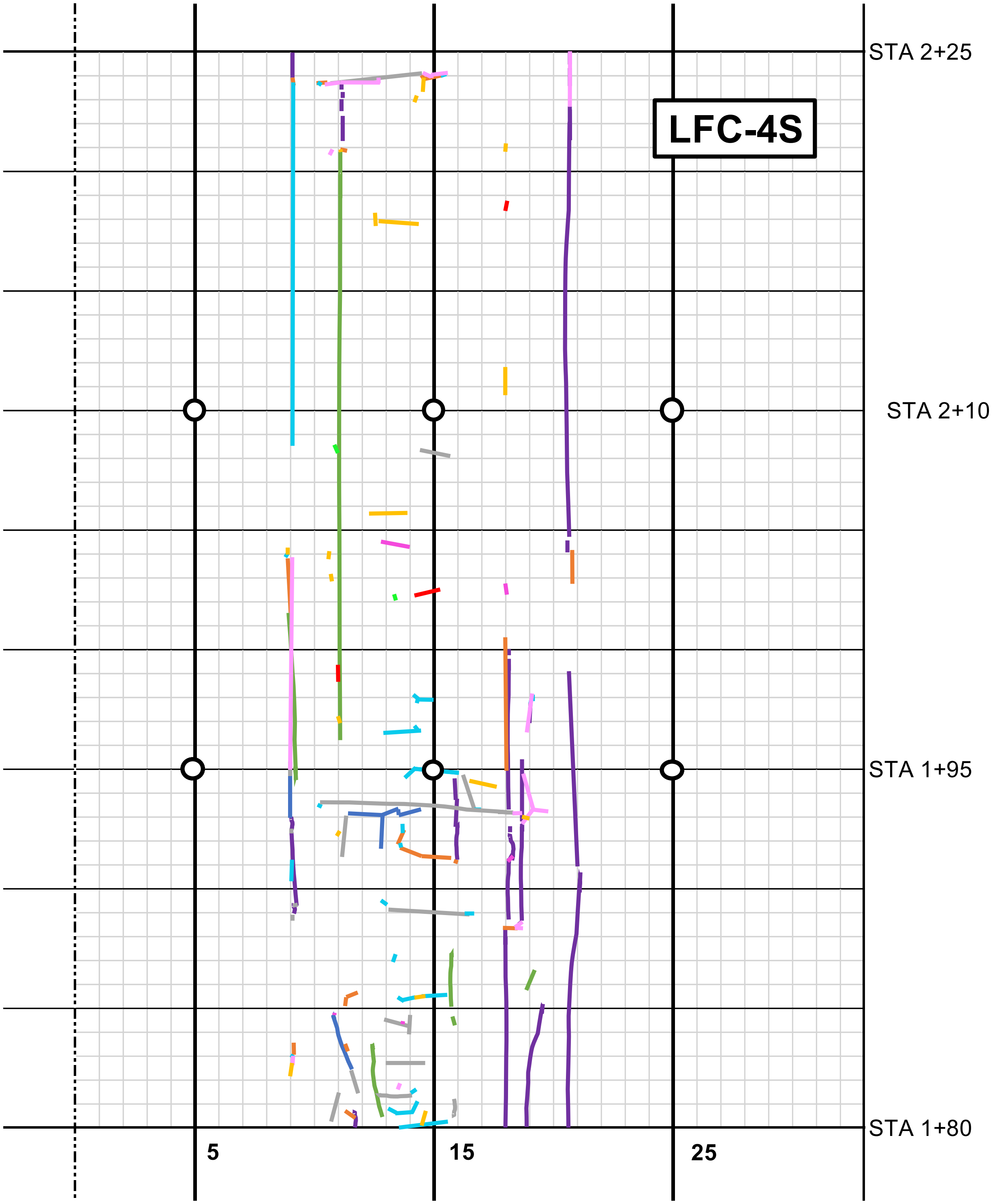

Figure 41. Crack Map for LFC-4S (final condition as of October 7, 2022)

Table 15. Crack Map Color Key

| Date | | Color | Date | | Color |
|---|---|---|---|---|---|
| LFC-3N/3S | LFC-4S | | LFC-3N/3S | LFC-4S | |
| 31-Mar-2022 | 22-Apr-2022 | 🟦 | 01-Jul-2022 | 22-Sep-2022 | 🟩 |
| 08-Apr-2022 | 27-Apr-2022 | 🟪 | 06-Jul-2022 | 07-Oct-2022 | 🟨 |
| 19-Apr-2022 | 05-May-2022 | 🟪 | 22-Jul-2022 | – | 🟧 |
| 28/29-Apr-22 | 27-May-2022 | 🟦 | 11-Aug-2022 | – | 🟧 |
| 05-May-2022 | 15-Jun-2022 | 🟦 | 25-Aug-2022 | – | 🟧 |
| 27-May-2022 | 01-Jul-2022 | 🟦 | 26-Aug-2022 | – | 🟫 |
| 01-Jun-2022 | 22-Jul-2022 | 🟦 | 14-Sep-2022 | – | 🟥 |
| 10-Jun-2022 | 11-Aug-2022 | 🟩 | 22-Sep-2022 | – | 🟥 |
| 15-Jun-2022 | 26-Aug-2022 | 🟩 | 07-Oct-2022 | – | 🟪 |

Table 16. Surface Cracking Data from Crack Maps

| Date | Pass No. | Cracked Area, SF | | | CD, % | | |
|---|---|---|---|---|---|---|---|
| | | 16962 | LFC-3S | LFC-4S | LFC-3N | LFC-3S | LFC-4S |
| 31-Mar-2022 | 16,962 | 68 | 46 | – | 5.04 | 3.41 | – |
| 08-Apr-2022 | 17,952 | 95 | 103 | – | 7.04 | 7.63 | – |
| 19-Apr-2022 | 18,876 | 169 | 129 | – | 12.52 | 9.56 | – |
| 22-Apr-2022 | 19,470 | – | – | 76 | – | – | 5.63 |
| 29-Apr-2022 | 20,064 | 217 | 159 | 90 | 16.07 | 11.78 | 6.67 |
| 05-May-2022 | 21,120 | 263 | 190 | 132 | 19.48 | 14.07 | 9.78 |
| 27-May-2022 | 23,826 | 280 | 202 | 160 | 20.74 | 14.96 | 11.85 |
| 01-Jun-2022 | 24,288 | 280 | 226 | – | 20.74 | 16.74 | – |
| 10-Jun-2022 | 25,740 | 305 | 226 | – | 22.59 | 16.74 | – |
| 15-Jun-2022 | 26,532 | 305 | 287 | 171 | 22.59 | 21.26 | 12.67 |
| 01-Jul-2022 | 28,314 | 316 | 302 | 202 | 23.41 | 22.37 | 14.96 |
| 06-Jul-2022 | 28,842 | 316 | 312 | – | 23.41 | 23.11 | – |
| 22-Jul-2022 | 31,218 | 317 | 320 | 205 | 23.48 | 23.70 | 15.19 |
| 11-Aug-2022 | 33,924 | 317 | 332 | 209 | 23.48 | 24.59 | 15.48 |
| 25-Aug-2022 | 35,904 | 318 | 333 | – | 23.56 | 24.67 | – |
| 26-Aug-2022 | 35,904 | 318 | 337 | 212 | 23.56 | 24.96 | 15.70 |
| 14-Sep-2022 | 37,614 | 319 | 337 | – | 23.63 | 24.96 | – |
| 22-Sep-2022 | 38,874 | 320 | 337 | 245 | 23.70 | 24.96 | 18.15 |
| 07-Oct-2022 | 40,722 | 329 | 345 | 255 | 24.37 | 25.56 | 18.89 |

Table 17. Parameters for Generalized Logistic Growth Model (Equation 6)

| Parameter | LFC-3N | LFC-3S | LFC-4S |
|---|---|---|---|
| $a$ | 2.36E+01 | 2.49E+01 | 1.85E+01 |
| $b$ | 3.94E+00 | 1.22E+01 | 3.96E+00 |
| $c$ | 4.06E-04 | 4.61E-04 | 1.81E-04 |
| $d$ | 3.42E-02 | 3.39E+00 | 9.65E-01 |

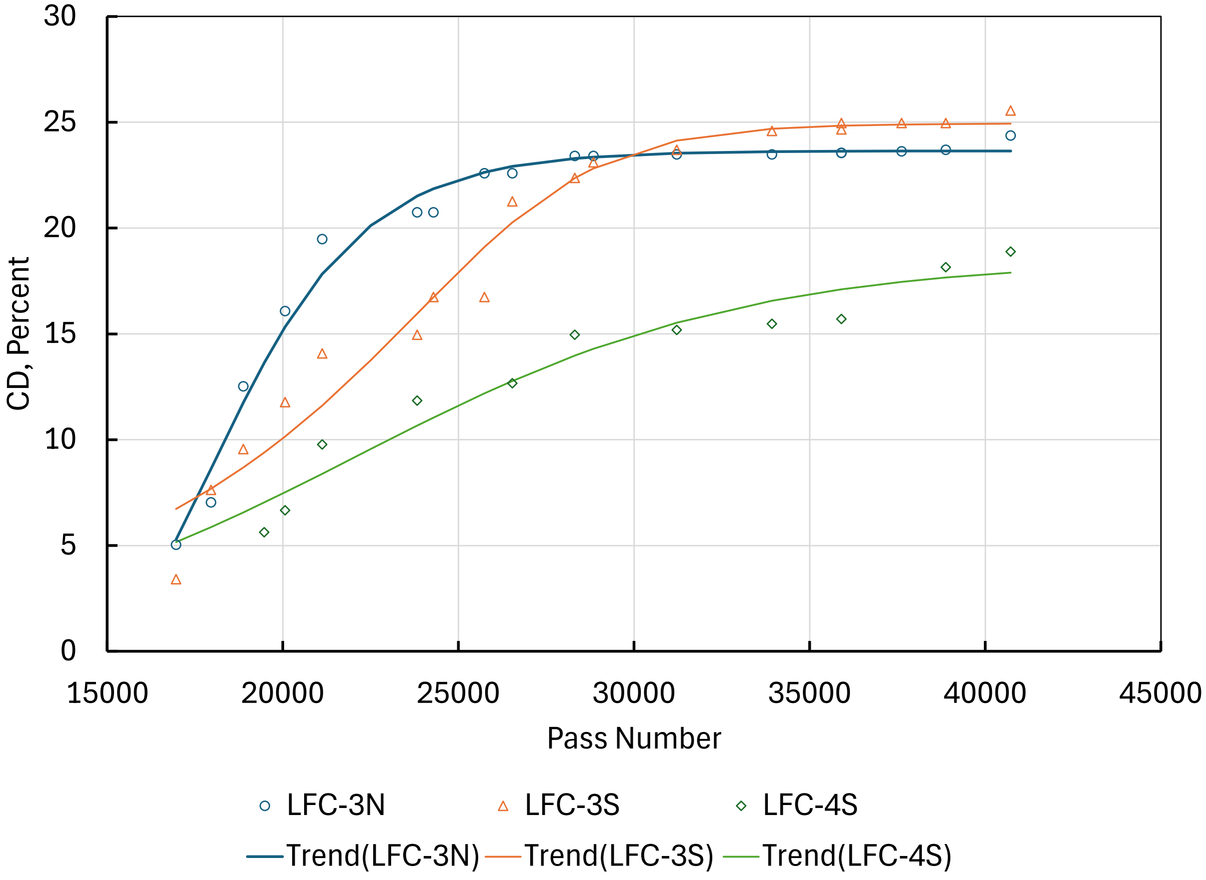

Figure 42. Growth of CD with Traffic

## 5.2 SENSOR RESPONSES

### 5.2.1 Asphalt Strain

Figure 43 through Figure 45 plot peak load-induced tensile strains from the start of the test up to 8,000 passes, at which point most of the sensors had failed due to large surface deformations. Graphs (a) and (c) of each figure show peak strain versus passes for LSGs and TSGs respectively, while graphs (b) and (d) in each figure plot peak strain against asphalt temperature. All temperature readings were taken at T-LFS-4N-6 and represent the hourly reading closest to the timestamp on the strain gauge reading. Peak transverse strains were generally higher than corresponding longitudinal tensile strains. As expected, peak strain magnitudes increased almost linearly with temperature.

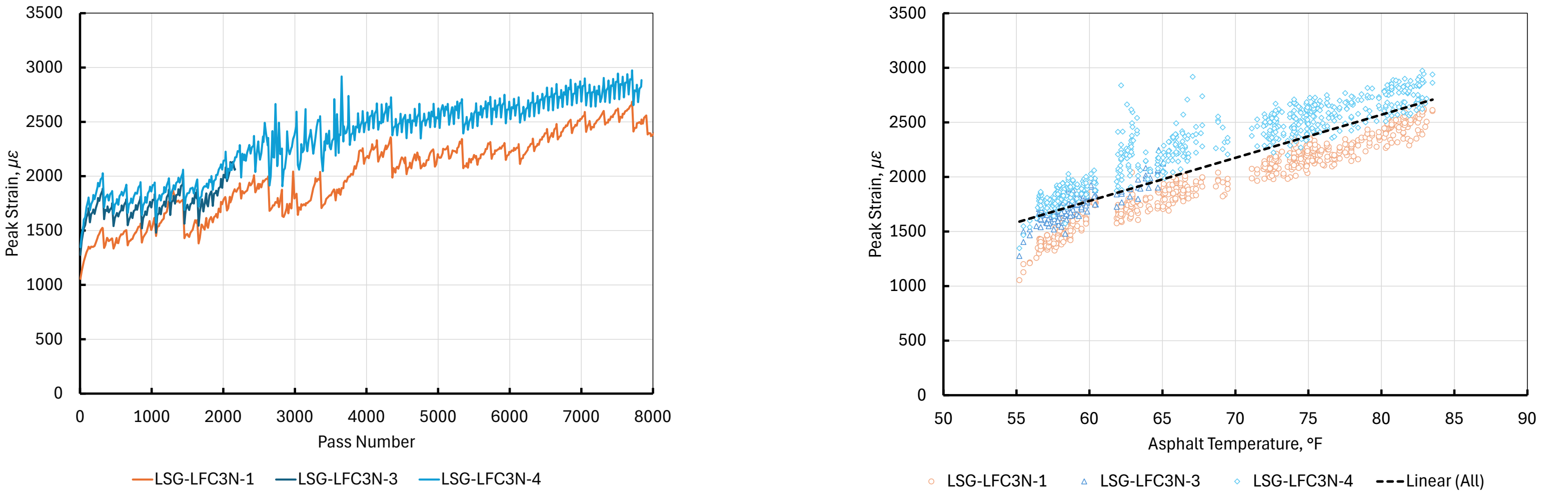

(a) Peak longitudinal strain vs. passes

(b) Peak longitudinal strain vs. asphalt temperature

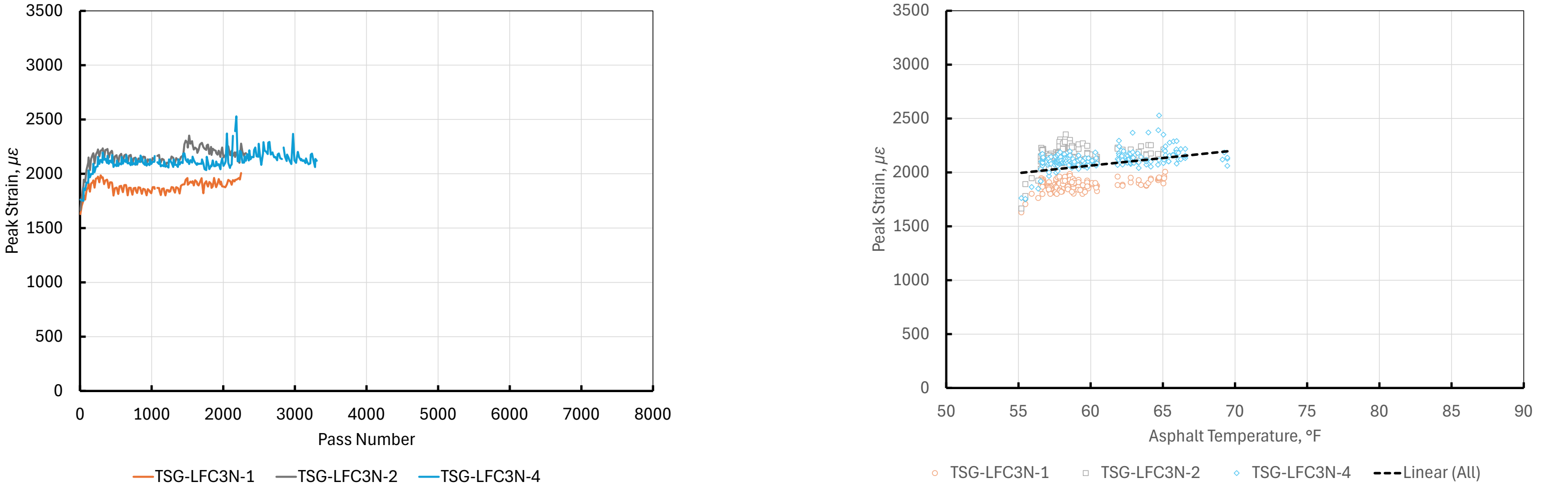

(c) Peak transverse strain vs. passes

(d) Peak transverse strain vs. asphalt temperature

Figure 43. Peak Tensile Strains at the Bottom of the Asphalt Layer, Test Item LFC-3N

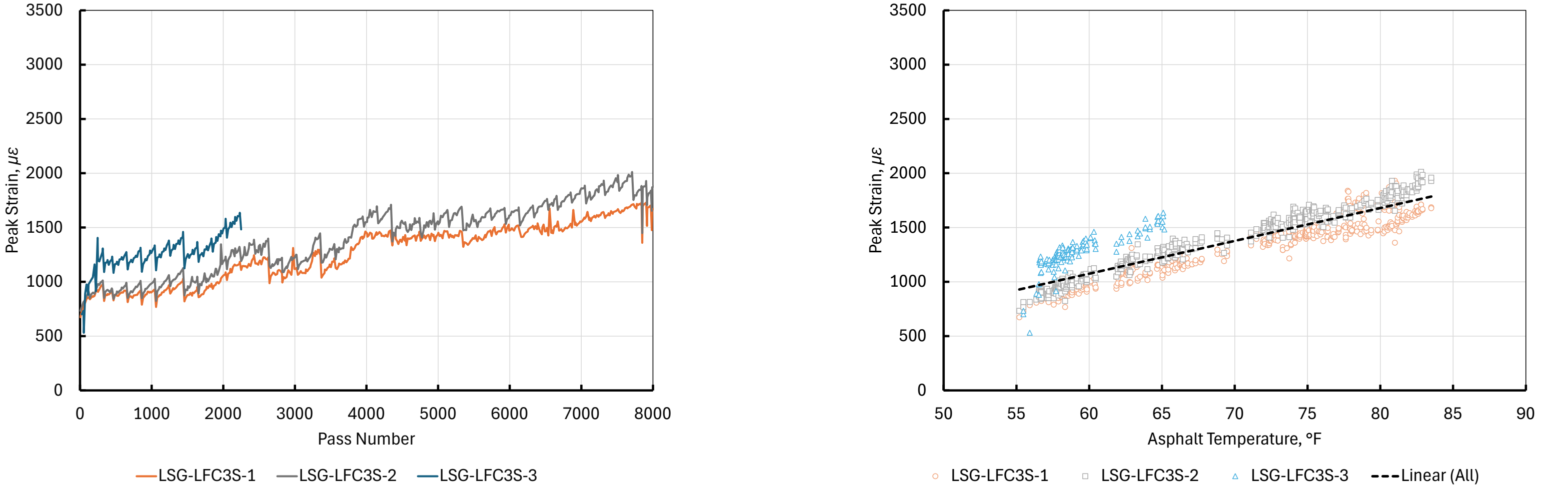

(a) Peak longitudinal strain vs. passes

(b) Peak longitudinal strain vs. asphalt temperature

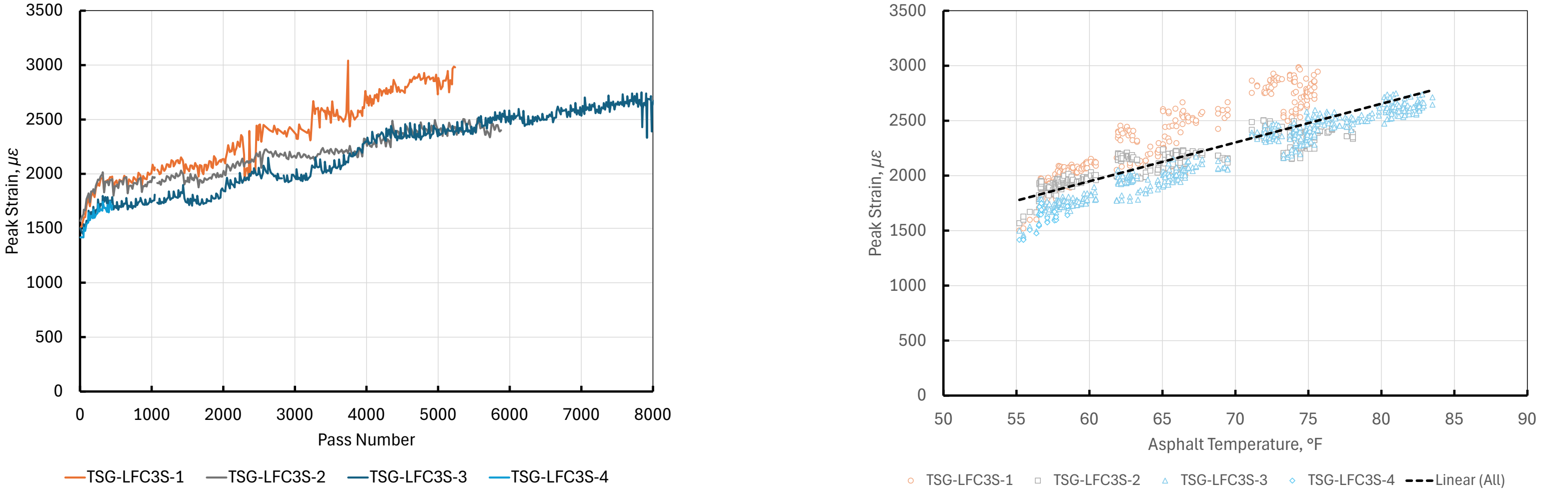

(c) Peak transverse strain vs. passes

(d) Peak transverse strain vs. asphalt temperature

Figure 44. Peak Tensile Strains at the Bottom of the Asphalt Layer, Test Item LFC-3S

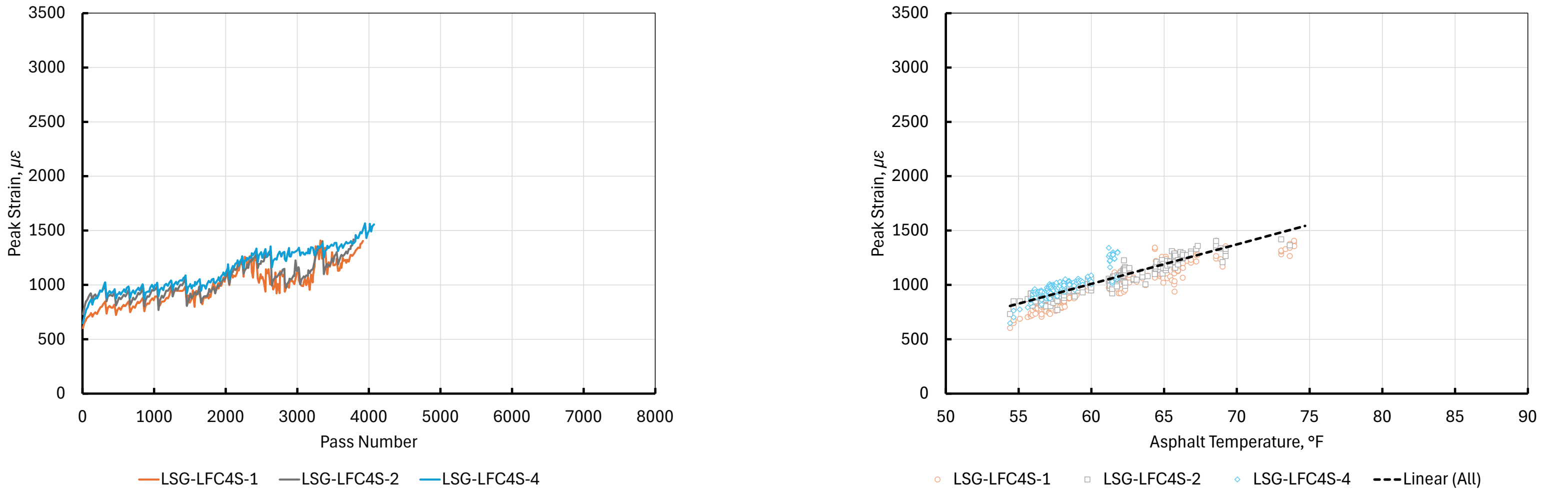

(a) Peak longitudinal strain vs. passes (b) Peak longitudinal strain vs. asphalt temperature

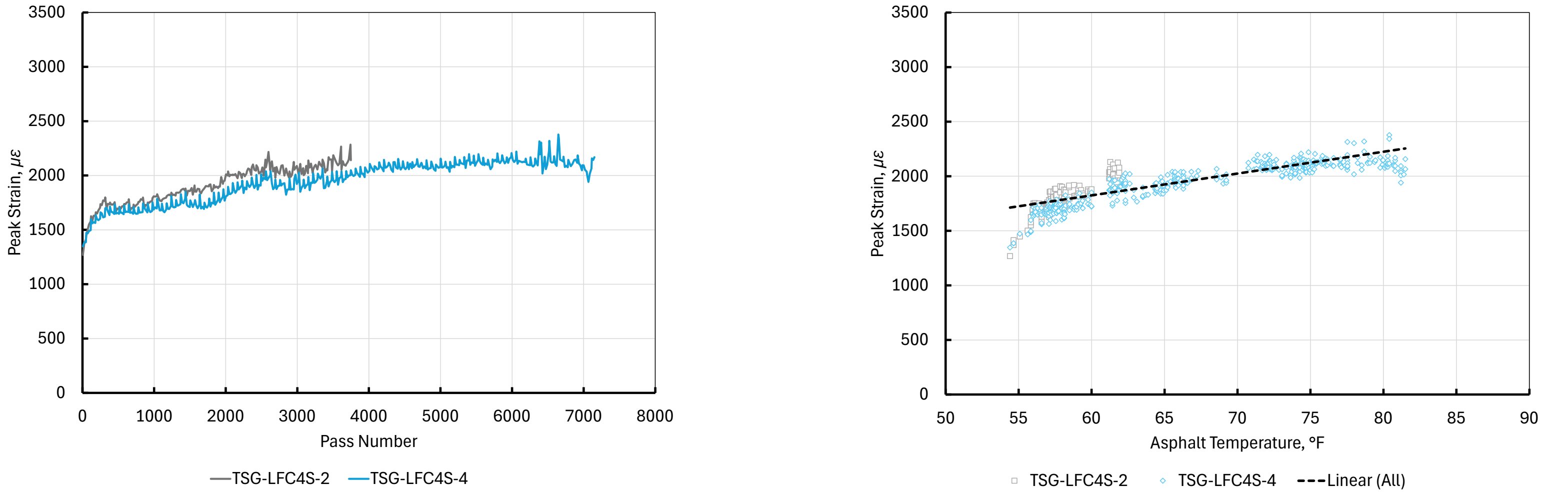

(c) Peak transverse strain vs. passes (d) Peak transverse strain vs. asphalt temperature

Figure 45. Peak Tensile Strains at the Bottom of the Asphalt Layer, Test Item LFC-4S

### 5.2.2 Crushed Aggregate Base Course

#### 5.2.2.1 Pressure Cells

As discussed in Section 4.1.1, PCs at the top of the P-209MR base layer were subjected to maximum stresses beyond their range, leading to signal saturation and early failure. The top-of-base PC in LFC-3N failed at about 6,500 passes. Top-of base PCs in LFC-3S and LFC-4S collected data through the vehicle pause at 12,610 passes but failed after the resumption of traffic.

Figure 46 shows peak responses for PC-LFC-3S-1 for the first six repetitions of the wander pattern. As discussed in the following section, responses on the critical tracks (tracks +3 and -3) tended to fall into three groups, determined by the track number of the preceding pass in the wander pattern. Peak stress increased significantly during the first wander pattern execution (passes 1–66) then stabilized above 90 psi. A rapid early stress increase may show densification of the granular material under the heavy gear loads. Above 90 psi, some of the peak signals are cut off, so PC responses above this limit could not be used for analysis.

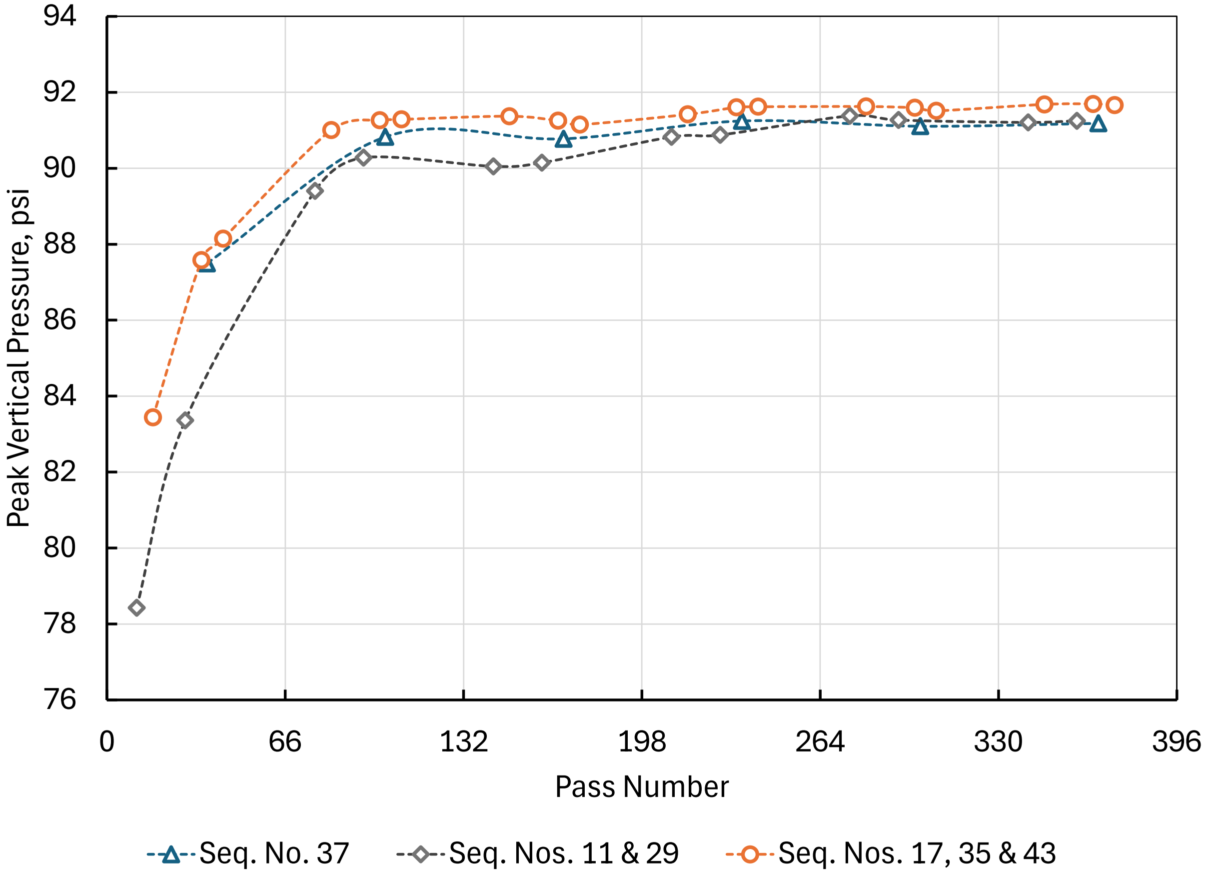

Figure 46. Peak Response for PC-LFC-3S-1 (top of P-209MR base) for Critical Tracks +3 and -3

### 5.2.2.2 Coil Sensors

CS pairs operated in both dynamic mode (to record vertical compressive strain under wheel loads) and static mode (to record permanent deformation). Permanent deformation was measured after each completed wander sequence consisting of 66 passes. In dynamic mode (during traffic), the measured vertical deformation under the moving 3D gear was converted to compressive strain by dividing it by the distance between the coils (adjusted for permanent deformation). Researchers developed a post-processing technique to extract the axial deformation information from the response, which was necessary because the passage of the vehicle caused the CS pairs to produce noisy, "hump"-shaped output in which the amplitude of the low-frequency "hump" exceeded the response of interest (Figure 47). The postprocessing algorithm applied two locally estimated scatterplot smoothing filters (coarse and fine) to the original data, and the axial deformation was determined from the difference between the two filtered data sets for each pass. A z-score-based peak detection algorithm was applied to the processed response to return the axial deformation for a given pass number.

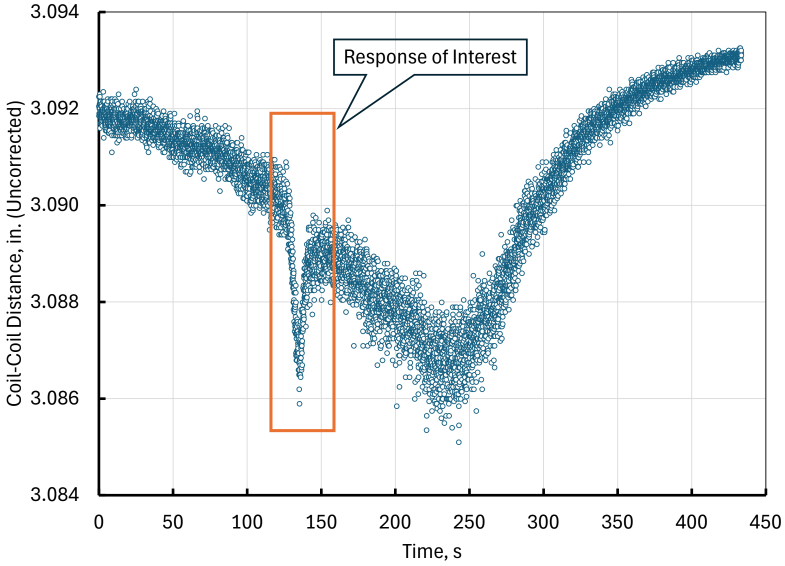

Figure 47. Example of an Uncorrected CS Response Illustrating the "Hump" Effect

As indicated in Section 2.3.3 and Figure 18 and Figure 19, LFC-3S and LFC-4S contained "short stacks" of three CS pairs, of which the upper two pairs (CS-LFC-3S-5/6 and CS-LFC-3S-6/7, and CS-LFC-4S-5/6 and CS-LFC-4S-6/7) were fully located within the base course. The lower pairs (CS-LFC-3S-7/8 and CS-LFC-4S-7/8) straddled the interface between base and subbase. Figure 48 plots cumulative permanent deformation versus pass number. All CS pairs had a nominal spacing of 75 mm (3 in.). CS pairs were individually calibrated in the laboratory prior to installation, so the maximum deformation that could be measured varied somewhat from pair to pair. However, it is clear from the deformation responses in Figure 48 that CS pairs in the base course were operating at or near their limit, and, as with the PC (Section 5.2.2.1), this probably contributed to early failure. In LFC-3S, the upper pair CS-LFC-3S-5/6 failed shortly after the start of traffic. For the other three pairs, permanent deformation followed a similar path up to about 5,000 passes, after which LFC-4S-6.7 diverged slightly. Eventually, all CS in the base course either failed or reached a plateau limit.

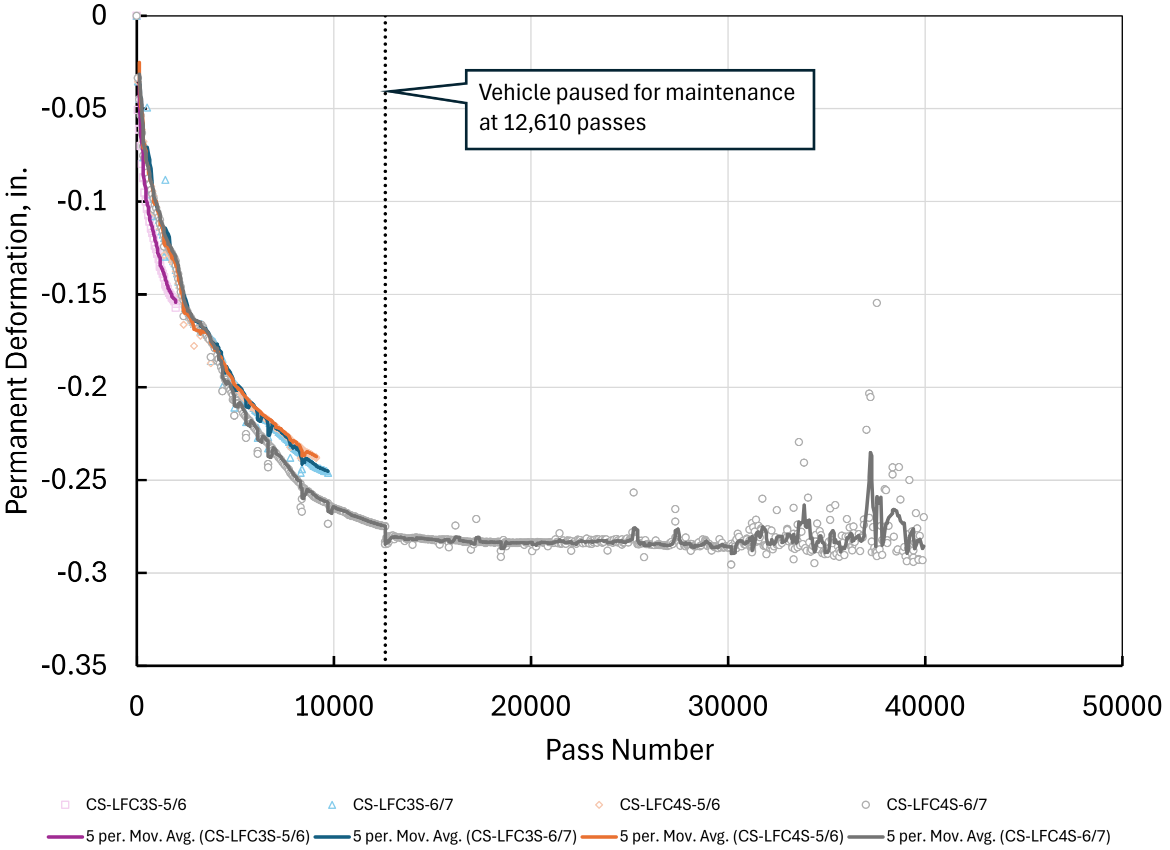

Figure 48. Permanent Deformation in CS Pairs in Crushed Aggregate Base Course

Figure 49 and Figure 50 show compressive strains computed from dynamic CS responses. As shown in Figure 46(a), CS-LFC5S-5/6 failed after less than 1,500 passes. Of the four sensor pairs fully within the base layer, only CS-LFC4S-7/8 continued to provide useable strain data after about 8,000 passes, but it also became progressively more unstable with additional traffic. The data in Figure 49 and Figure 50 represent peak strain values for all west-to-east vehicle passes on either track -3 or track +3, which placed one tire directly above the CS, causing maximum strain. According to layered elastic theory, all passes on the same track at the same load should induce approximately the same strain. In fact, the strain responses fell into three distinct clusters based on the track occupied by the previous pass. In the 66-pass repeated wander pattern (Section 4.2.1), the six passes 7, 11, 17, 29, 37, and 43 were all on tracks +3/-3 and proceeded from west to east. However, wander sequence numbers 17, 35, and 43 formed a cluster because they were all preceded in the wander pattern by a pass on track -1. Likewise, sequence numbers 11 and 29 were both preceded by passes on track 4, while sequence number 37 was preceded by track -3. The vehicle movement along a track causes rearrangement of particles within the granular layers and strongly affects the strain response for the following pass, in a highly repeatable pattern. Figure 49 and Figure 50 illustrate the importance of the load history in determining the load-induced strain for a given pass.

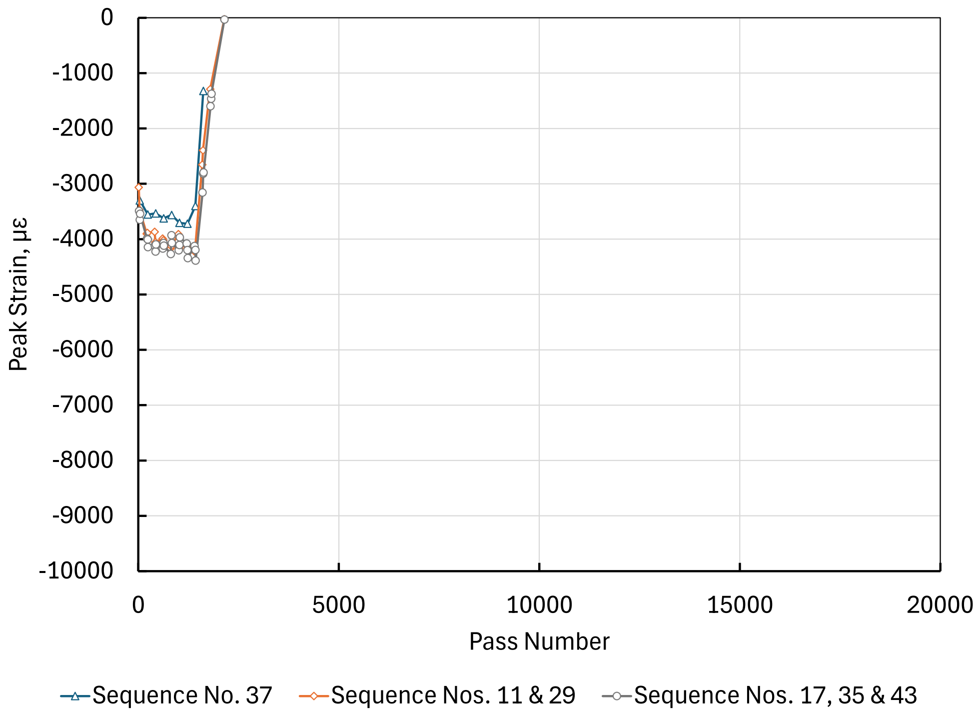

(a) CS-LFC-3S-5/6

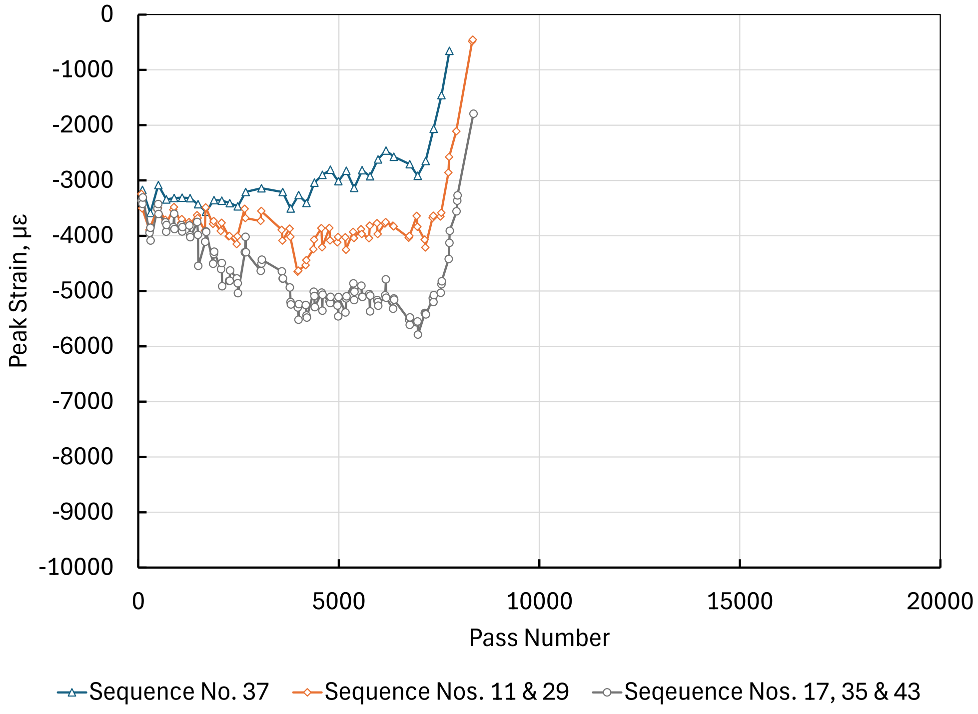

(b) CS-LFC-3S-5/6

Figure 49. Peak Vertical Strain in Crushed Aggregate Base Course, Test Item LFC-3S

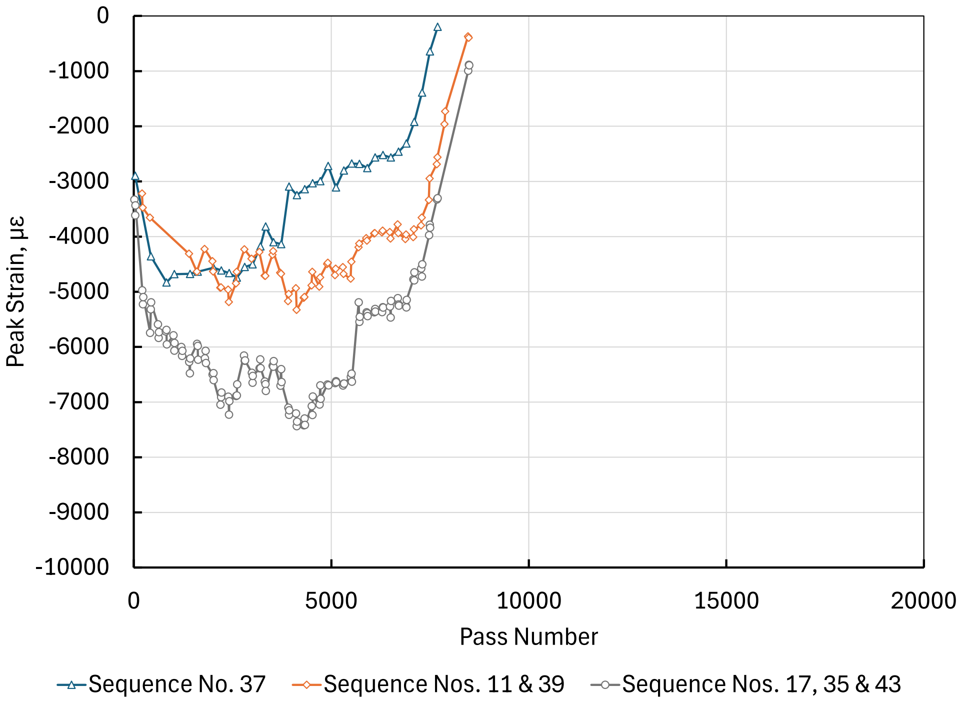

(a) CS-LFC-4S-5/6

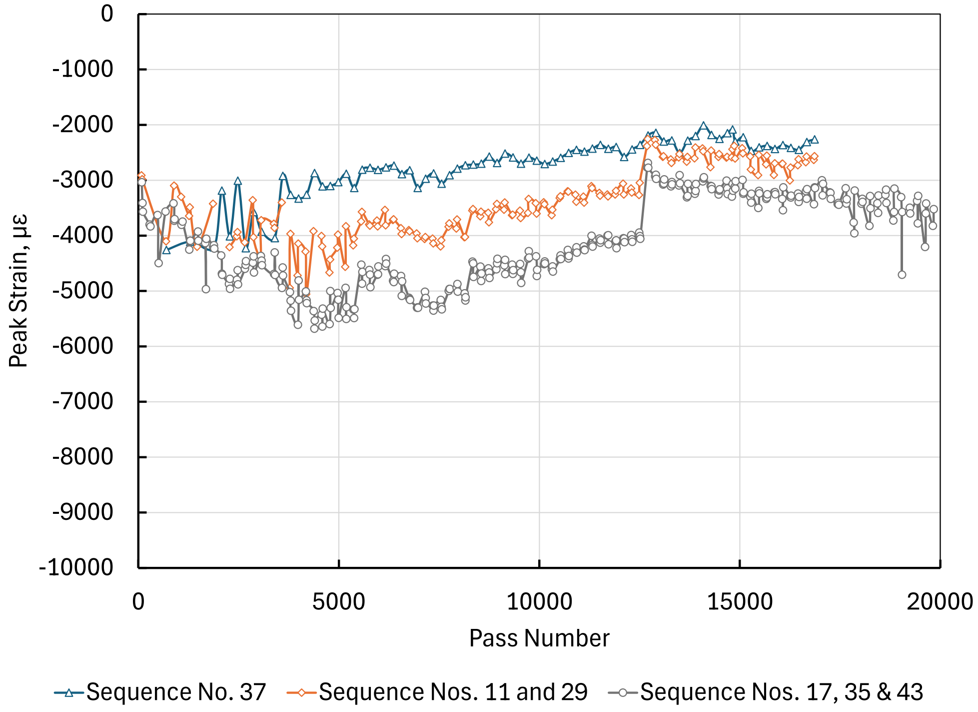

(b) CS-LFC-4S-7/8

Figure 50. Peak Vertical Strain in Crushed Aggregate Base Course, Test Item LFC-4S

Figure 51 plots permanent deformation of the CS pairs at the interface of the P-209MR crushed aggregate base and the P-154MR granular subbase for test items LFC-3S and LFC-4S. (There was no corresponding CS pair in LFS-3N because the geogrid would have interfered with installation.) At this depth, LFC-3S had much higher permanent deformation than the control LFC-4S, which may be attributed to lower stiffness of the LFC-3S subbase layer. LWD tests on the LFC-3S subbase (Section 2.2.2, Figure 9) showed localized stress-softening behavior. Furthermore, D-PSPA tests on the LFC-3S subgrade (see Figure 10) identified specific areas of low modulus along the center offset (+15 ft) close to where the CS pairs were placed, indicative of insufficient compaction. Figure 10 shows high variability of the seismic modulus especially in LFC-3S; both the low and high values were found at the center offset.

Figure 52 plots the compressive strain versus pass number at the base-subbase interface for test items LFC-3S and LFC-4S. As with the four upper CS pairs located fully within the base layer (Figure 49 and Figure 50), strain responses for the two pairs at the interface resolved into three distinct clusters determined by the track number of the preceding pass. Strain responses show evidence of seasonal variation. As expected, higher load-induced strains are associated with warmer temperatures and lower asphalt stiffness.

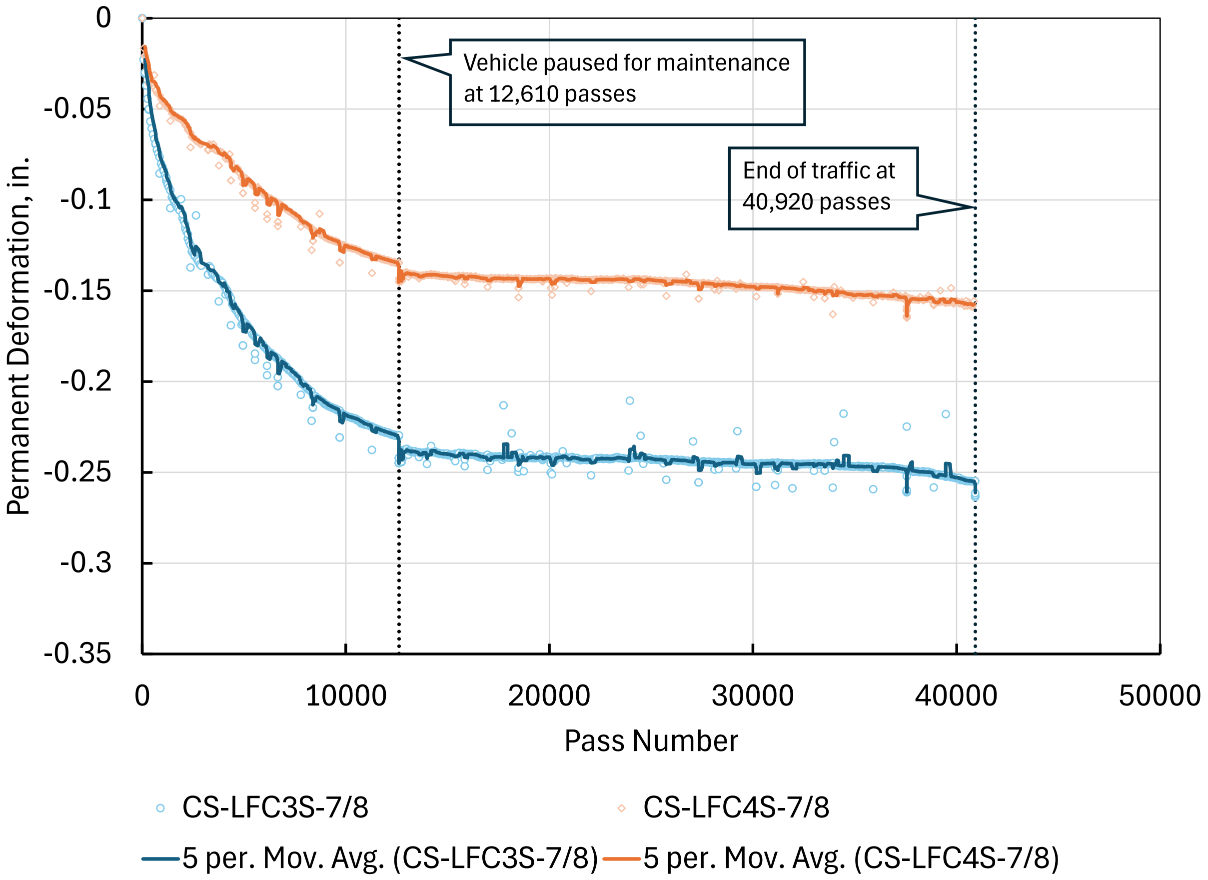

Figure 51. Permanent Deformation in CS Pairs at the Interface of the Base Course and the Granular Subbase

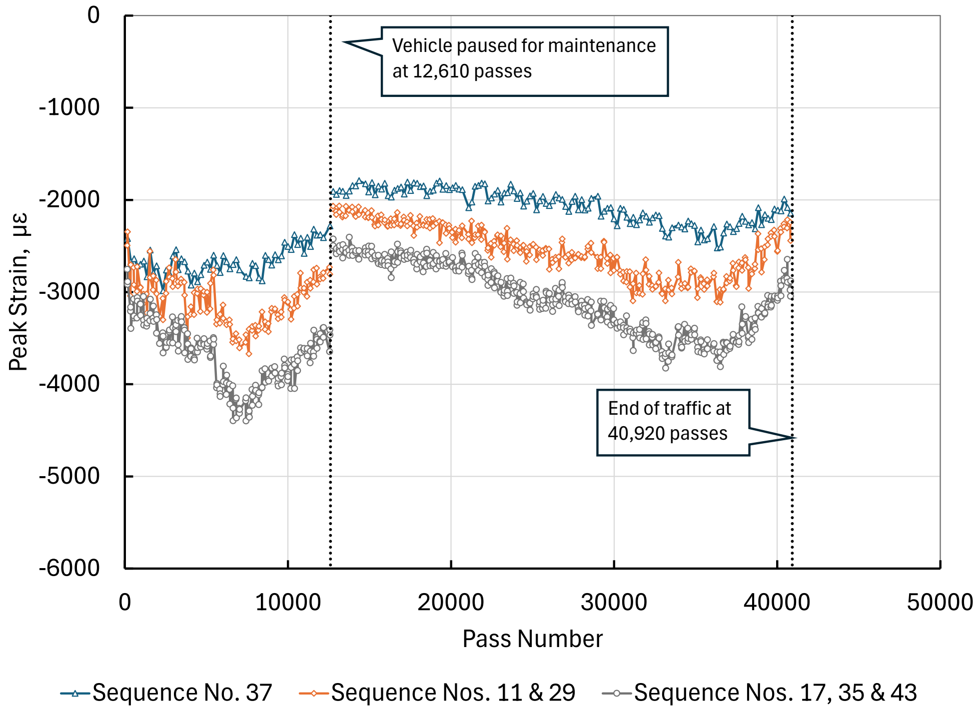

a) CS -LFC-3S-7/8

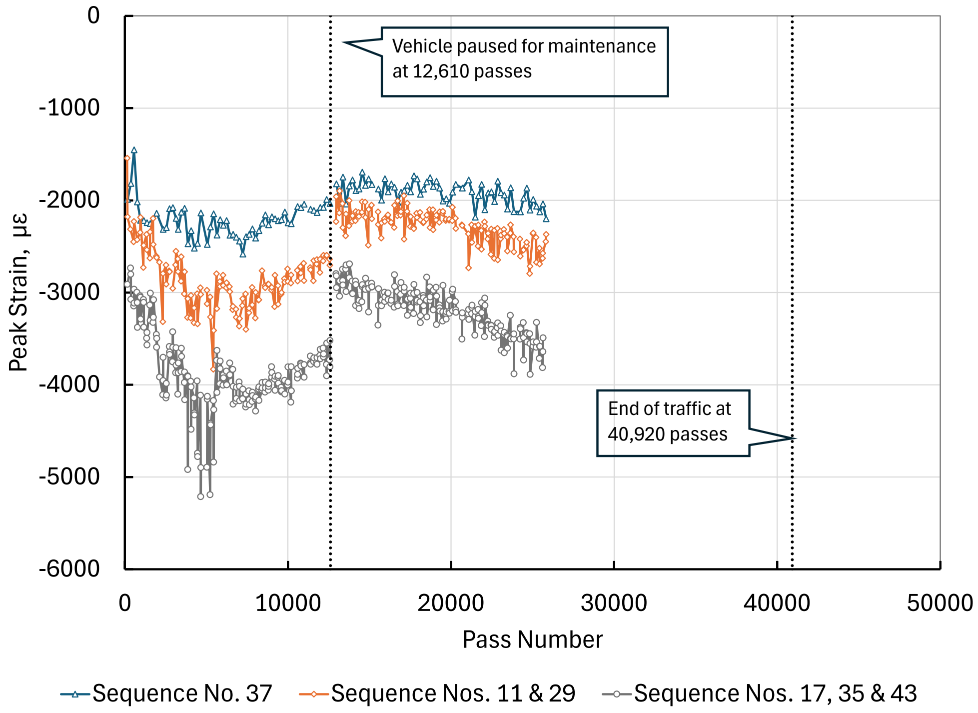

b) CS -LFC-4S-7/8

Figure 52. Peak Vertical Strain at Interface of Base and Subbase

#### 5.2.2.3 Bender Elements (Small-Strain Stiffness)

Researchers at the University of Illinois evaluated the adequacy of geogrid reinforcement by monitoring shear wave velocities and small-strain stiffness using the BE sensors described in Section 2.3. Kang et al. (2022) analyzed the BE responses during static dual-gear, dynamic slow-roll, and dynamic proof-roll tests. Incrementally increasing static loads led to increased shear wave velocities, which demonstrated the stress-hardening behavior of crushed aggregate base materials. Relative changes in shear wave velocities before and after the slow-roll and proof-roll tests corroborated the anti-shakedown effect described by Donovan (2009), Donovan et al. (2010), and Donovan and Tutumluer (2008). The geogrid-stabilized base course in LFC-3N registered up to 20% higher shear wave velocities compared to the unstabilized base courses in LFC-3S and LFC-4S, suggesting that geogrid reinforcement improves resistance to stiffness loss (Tutumluer et al., 2024).

In a follow-up study, Kang et al. (2023) investigated the variation in small-strain moduli during the CC9 traffic tests. Kang et al. (2023) developed a linear correlation between the laboratory-measured resilient moduli and small-strain moduli determined with shear wave transducers. That correlation was used to assess the in situ moduli from the embedded BE sensors. The researchers documented a steep drop in modulus values following the first completed wander pattern. The reduction in stiffness was attributed to particle reorientation associated with wheel wander. The in situ resilient modulus of the base course was estimated by dividing the vertical compressive stress from PCs by the compressive strain from CSs. Similar to the 2022 study, reduction in resilient moduli with successive passes demonstrated the anti-shakedown effect.

### 5.2.3 Granular Subbase

#### 5.2.3.1 Compressive Stresses from Pressure Cells

PCs were at the top of the P-154MR granular subbase and 6 in. below the top (except in LFC-3N, where they were placed 2 in. lower to avoid interfering with the geogrid). Figure 53 and Figure 54 plot compressive stress against passes for upper and lower PCs in the subbase. In general, the peak responses under traffic loads exceeded the pressure rating of the PC (Section 4.1.1), resulting in damage and early failure. Responses higher than about 90 psi generally had peaks cut off and are, therefore, unusable for analysis. Still, the responses from early in the test provide usable data.

From the start of the test, PC-LFC-3S-2 and PC-LFC-3S-3 reported significantly lower peak stresses than the corresponding sensors in the other two test items. The reason for this behavior is not clear. It is possible that PC-LFC-3S-2 and PC-LFC-3S-3 may have been displaced from their intended position during placement and compaction of the subbase and base layers, and this accounts for the lower pressure readings under critical tracks +3 and -3. However, this possibility must be confirmed by post-traffic investigations.

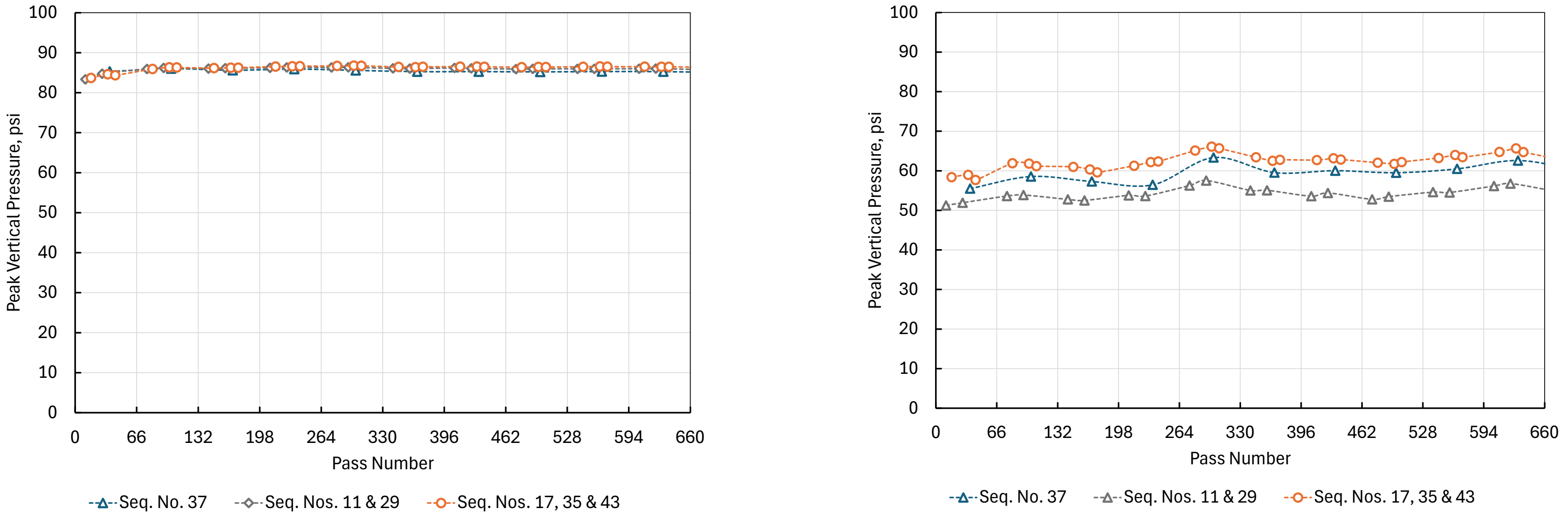

(a) PC-LFC-3N-2

(b) PC-LFC-3S-2

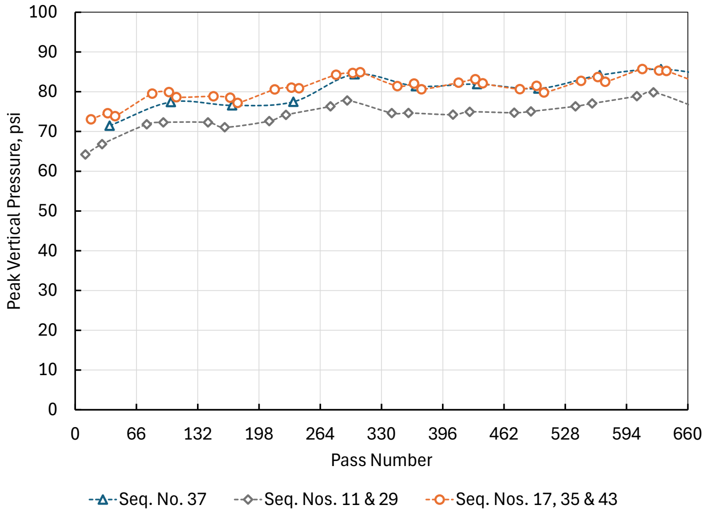

(c) PC-LFC-4S-2

Figure 53. Peak Stress Response (P-154 granular subbase) for Critical Tracks +3 and -3, PCs at Top of Subbase

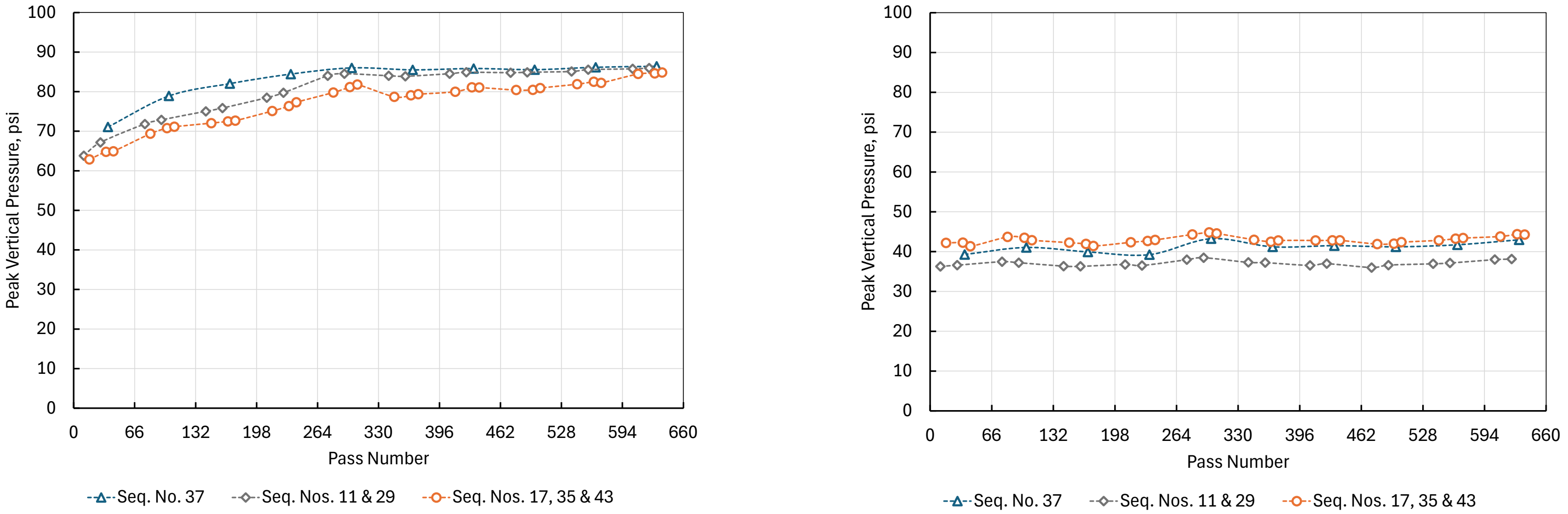

(a) PC-LFC-3N-3

(b) PC-LFC-3S-3

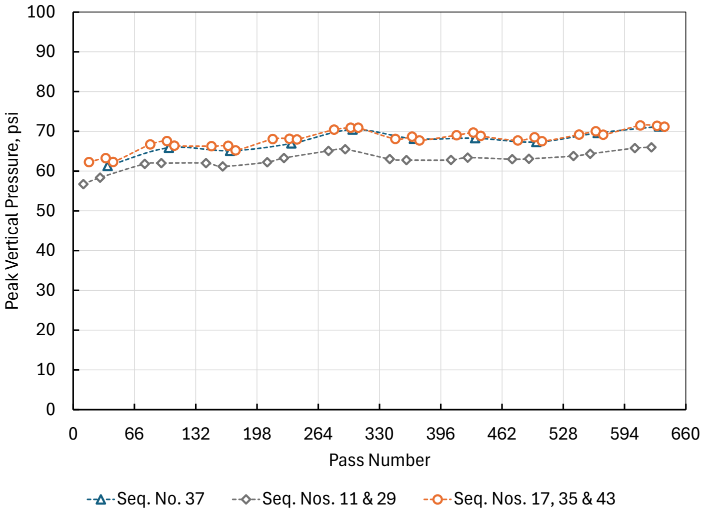

(c) PC-LFC-4S-3

Figure 54. Peak Stress Response (P-154 granular subbase) for Critical Tracks +3 and -3, PCs 6 in. Below Top of Subbase

#### 5.2.3.2 Permanent Deformation and Compressive Strains from Coil Sensors

Figure 55 plots permanent deformation against passes, as measured by CS pairs near the top of the granular subbase. Up to about 5,000 passes, the deformation trends for the three test items were roughly similar. Beyond 5,000 passes, there was a much lower rate of permanent deformation in LFC-3N (geogrid-reinforced) than in test items without a geogrid. This suggests some benefit from geogrid reinforcement in protecting the unbound granular layer, once the geogrid has deformed sufficiently to mobilize its strength.

Figure 56 plots peak vertical compressive strain at the top of the granular subbase against traffic. For CS pairs at the top of the subgrade, the critical track for peak strain was track 0. However, as described in Section 5.2.2, the peak response is also affected by the lateral position of the previous pass, due to particle rearrangement in the unbound layers. Referring to the wander pattern (Section 4.2.1), all west-to-east passes on track 0 were preceded by a pass on track -2, except for those in sequence number 65, which were preceded by track -1. This explains why the peak strain responses fell into two groups, as shown in Figure 54.

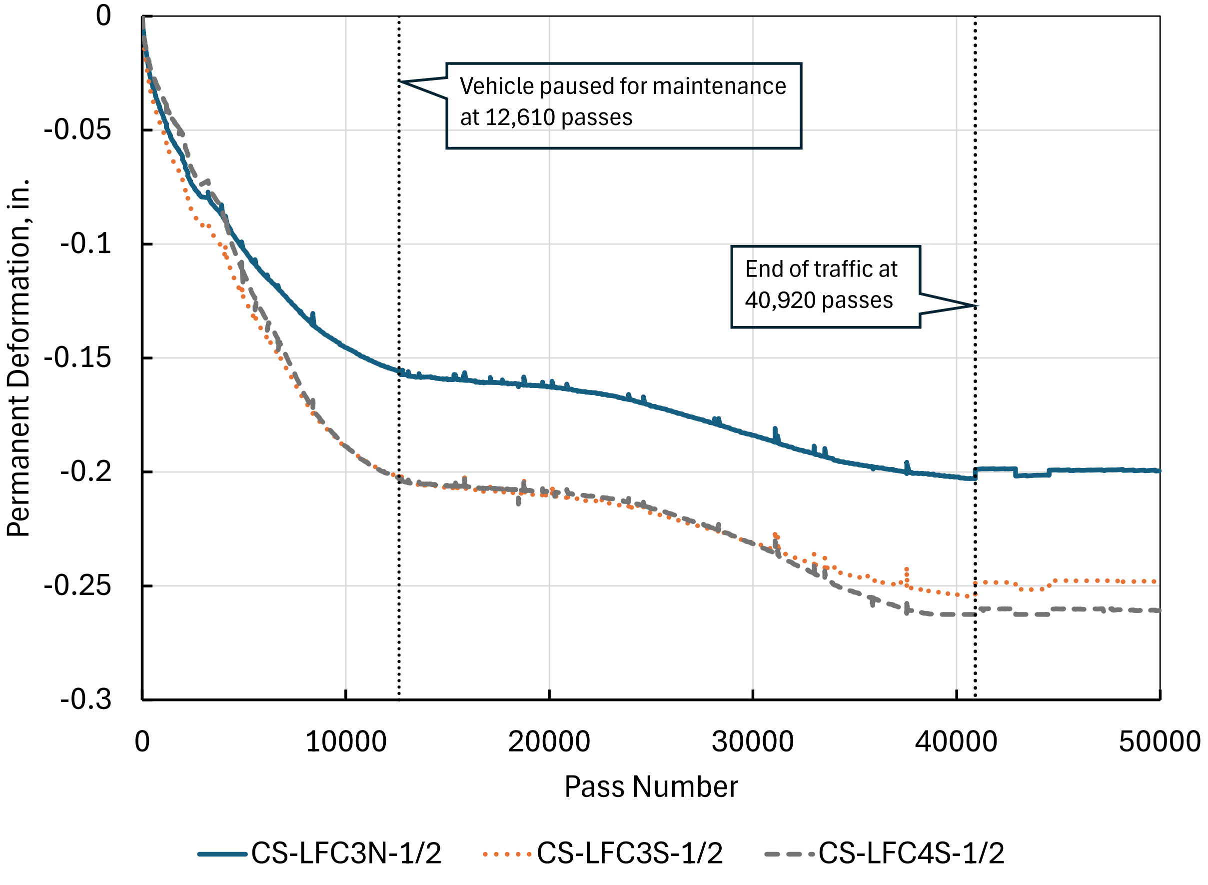

Figure 55. Permanent Deformation at Top of P-154MR Subbase

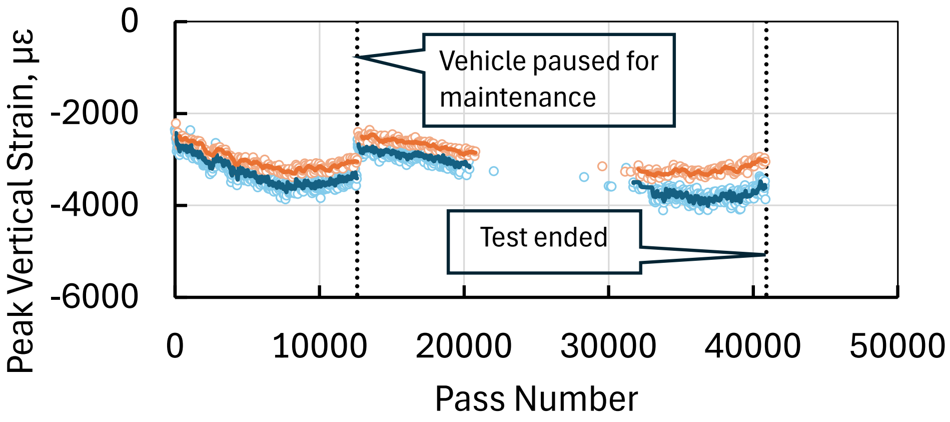

(a) CS-LFC-3N-1/2

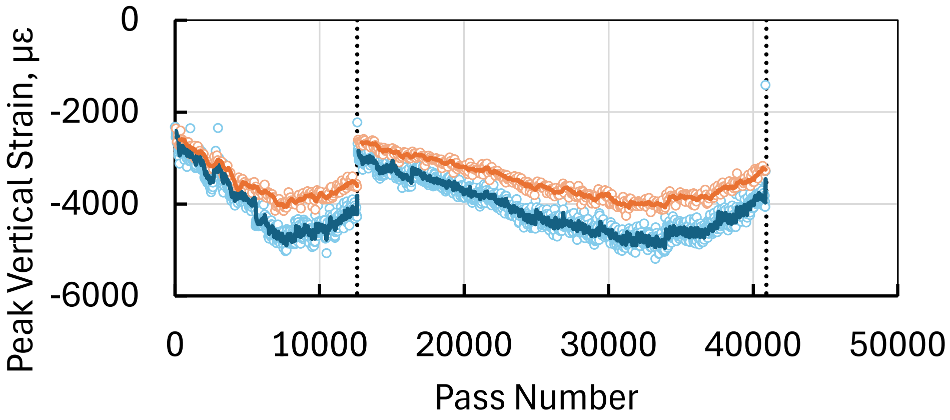

(b) CS-LFC-3S-1/2

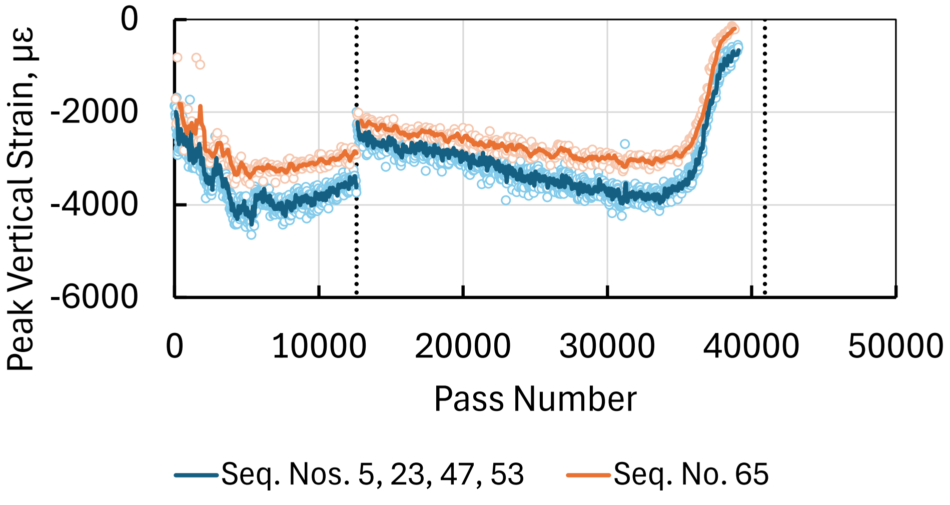

(c) CS-LFC-4S-1/2

Figure 56. Compressive Strain at Top of P-154MR Subbase
(Solid lines show 5-point moving average.)

No effect of the nonwoven geotextile separation fabric could be determined from the trends shown in Figure 53 and Figure 54. Up to the point where CS-LFC-4S-1/2 began to fail (at about 35,000 passes), the strain in LFC-3S with separation fabric was consistently higher than in the LFC-4S (control). However, this may be due to relatively lower stiffness of the LFC-3S subbase material as placed (Section 2.2.2) rather than to any specific geotextile effect.

### 5.2.4 Subgrade

#### 5.2.4.1 Compressive Stresses from Pressure Cells

Figure 57 shows peak top-of-subgrade, load-induced vertical stress versus number of passes. In contrast to vertical strains from CS pairs (Section 5.2.4.2), vertical stresses in the subgrade remained relatively stable throughout the test. Abrupt changes in the PC reading from LFC-4S in Figure 55(c) (at passes 1,452, 5,544, and following the pause at pass 12,610) are probably due to sensor malfunction. Higher peak stress in LFC-4S versus LFC-3N and LFC-3S is consistent with the shallower sensor depth (42 versus 44 in.) but may also indicate a beneficial effect from the geosynthetic separation fabric.

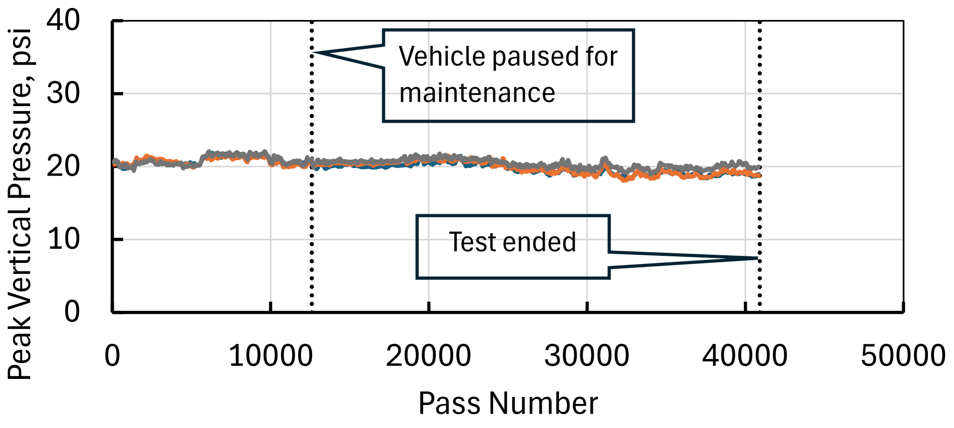

(a) PC-LFC-3N-4 (44 in. below grade)

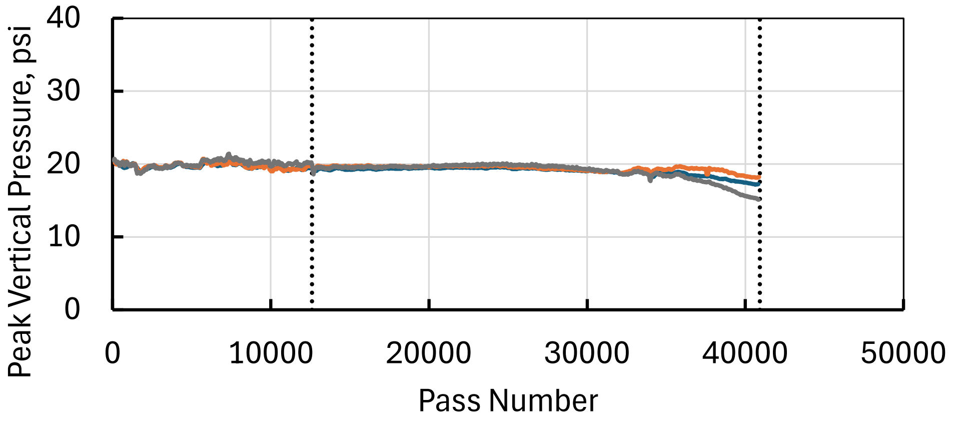

(b) PC-LFC-3S-4 (44 in. below grade)

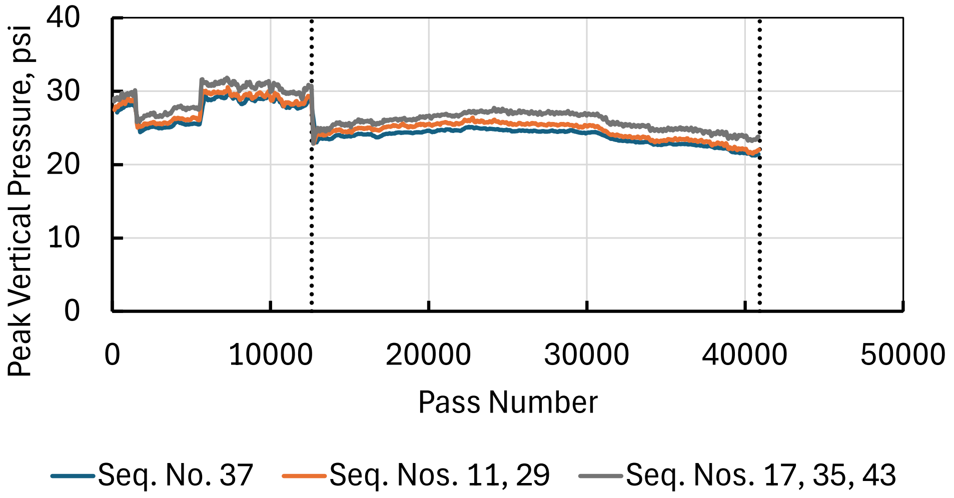

(c) PC-LFC-4S-4 (42 in. below grade)

Figure 57. Compressive Stress at Top of Subgrade (five-point moving average)

### 5.2.4.2 Permanent Deformation and Compressive Strains from Coil Sensors

Figure 58 plots permanent deformation at the top of the subgrade against the number of passes. After 7,500 passes, the rate of permanent deformation increased sharply in LFC-3S but remained stable in the other two test items. After the trafficking hiatus (October 2021 to February 2022), permanent deformation continued to increase in LFC-3S—first gradually, then rapidly, eventually reaching the sensor's limit at approximately 33,000 passes. After 40,000 passes, the readings recovered somewhat but should be considered unreliable due to the large distortions. Figure 58 is evidence of a bearing capacity failure in LFC-3S that did not affect LFC-3N or LFC-4S.

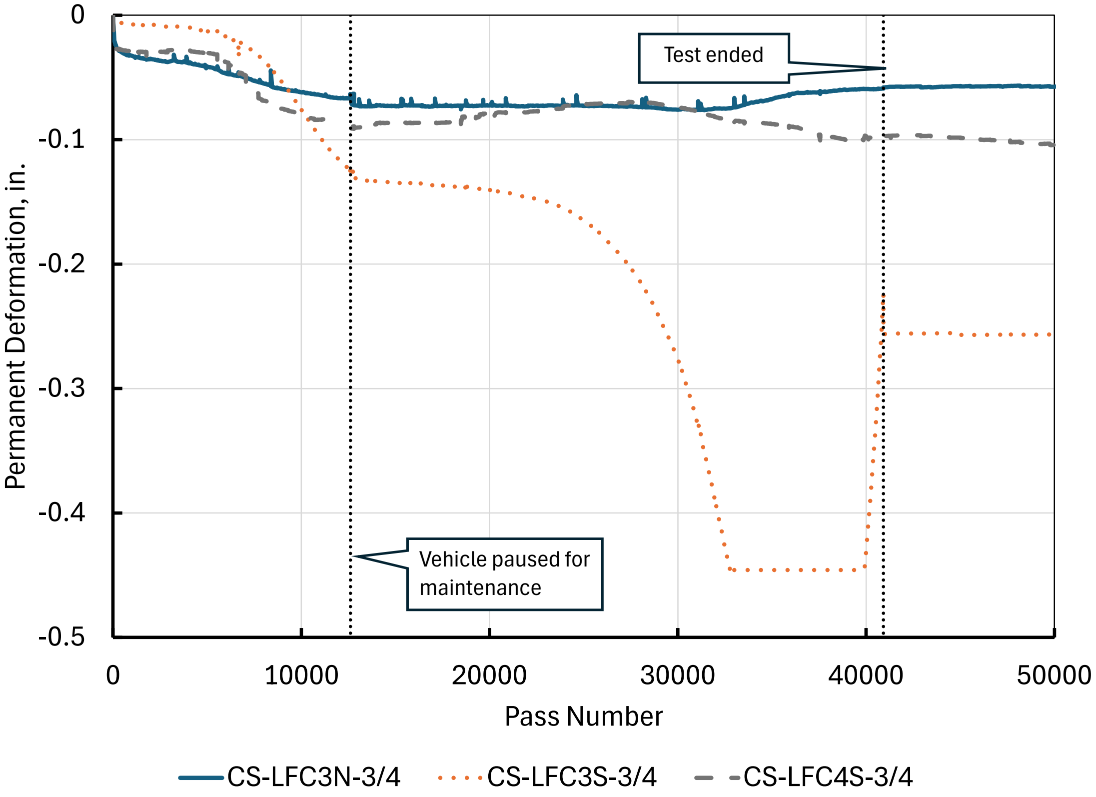

Figure 58. Permanent Deformation at Top of Subgrade

Permanent deformation in soils is linked to shear strength and to the quantity called subgrade stress ratio (SSR), defined as the ratio of deviator stress to unconfined compressive strength (Chow, 2014; Thompson & Bejarano, 1997). Volumetric MC in test item LFC-3S was consistently higher than in the other two test items during the time between construction and the initiation of traffic. Higher moisture levels lowered the effective stress and shear strength of the clay subgrade in LFC-3S relative to the companion test items. Although the compressive stresses were lower in LFC-3S, the lower strength associated with higher moisture content led to higher SSR. This higher SSR contributed to higher permanent deformation.

Test item LFC-3N (geogrid-reinforced) showed an initial high rate of subgrade deformation that slowed considerably with increasing traffic, then stabilized, never increasing beyond approximately 0.075 in. The final permanent deformation in the LFC-4S (control) subgrade was higher than that of LFC-3N (geogrid). Some of this difference may be attributed to the lower subgrade moisture content in LFC-3N, resulting in higher in situ shear subgrade strength compared to LFC-3S and LFC-4S. However, the tension membrane effect provided by the geogrid may also have played a role in reducing the long-term subgrade deformation. The tension membrane effect results from large permanent deformations, sufficient to mobilize resistance in the tensioned geogrid layer (Alimohammadi et al., 2021). Rapid rutting in LFC-3N at the beginning of the test followed by a period of stabilization may indicate that the tension membrane effect "kicked in" only after traffic caused significant permanent deformation.

Figure 59 shows subgrade compressive strain during traffic. Compressive strains from CS pairs in the subgrade exhibited seasonal variation linked to temperature-related changes in AC stiffness, similar to CS pairs in the base and subbase layers. However, the subgrade strain magnitudes were substantially higher than those in the base and subbase. This could be attributed to the large disparity in stiffness between fine-grained clay and coarse-grained unbound base and subbase materials. The compressive strains in test item LFC-4S (control) were consistently higher than strains in the other two test items. The subgrade coil sensor stacks were installed at an offset of 12.75 ft, which coincides with the tire path under wander track 0. In-place characterization of the as-built subgrade with LWD, D-PSPA, and GeoGauge indicated consistently lower stiffness in the center area (15-ft transverse offset) of LFC-3N than that in the other two test items (see Figures 6, 7, and 8).

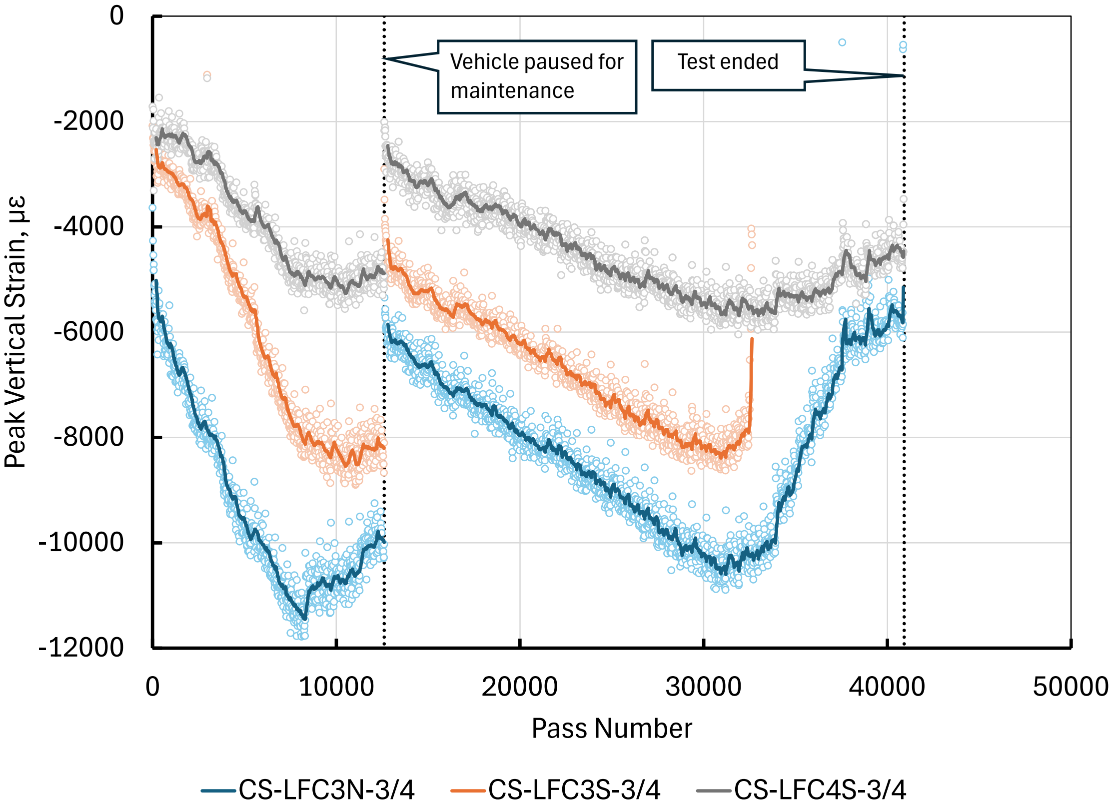

Figure 59. Compressive Strain at Top of Subgrade
(Solid lines show a 15-point moving average.)

### 5.2.4.3 Volumetric Moisture Content

Subgrade moisture content $\theta_v$ was monitored closely during the test. Figure 60 plots subgrade $\theta_v$ against traffic for all three test items. In Figure 60, the value of $\theta_v$ associated with a pass number is the hourly value closest in time to the pass (nearest 30 minutes). Figure 58 may be considered a continuation of Figure 20 (pre-traffic), which showed $\theta_v$ was consistently higher for LFC-3S than for LFC-3N and LFC-4S. Generally, this situation continued during traffic (except at the very end of the test). Initially, $\theta_v$ increased with traffic for all three test items. The LFC-3S subgrade exhibited a steep drop in $\theta_v$ during the 5-month pause when traffic was removed, behavior that was not reflected as strongly in the other two test items. As discussed in Offenbacker et al. (2026) with reference to the CC9 overload test, the change in volumetric moisture content relative to its value at the start of regular traffic (not the absolute value of $\theta_v$) was strongly correlated to vertical deflection under load at the top of the subgrade. Thus, the changes in soil moisture content following the start of traffic (and following the resumption of traffic after the 5-month pause) may help to explain the increasing magnitude of vertical compressive strain seen in Figure 59.

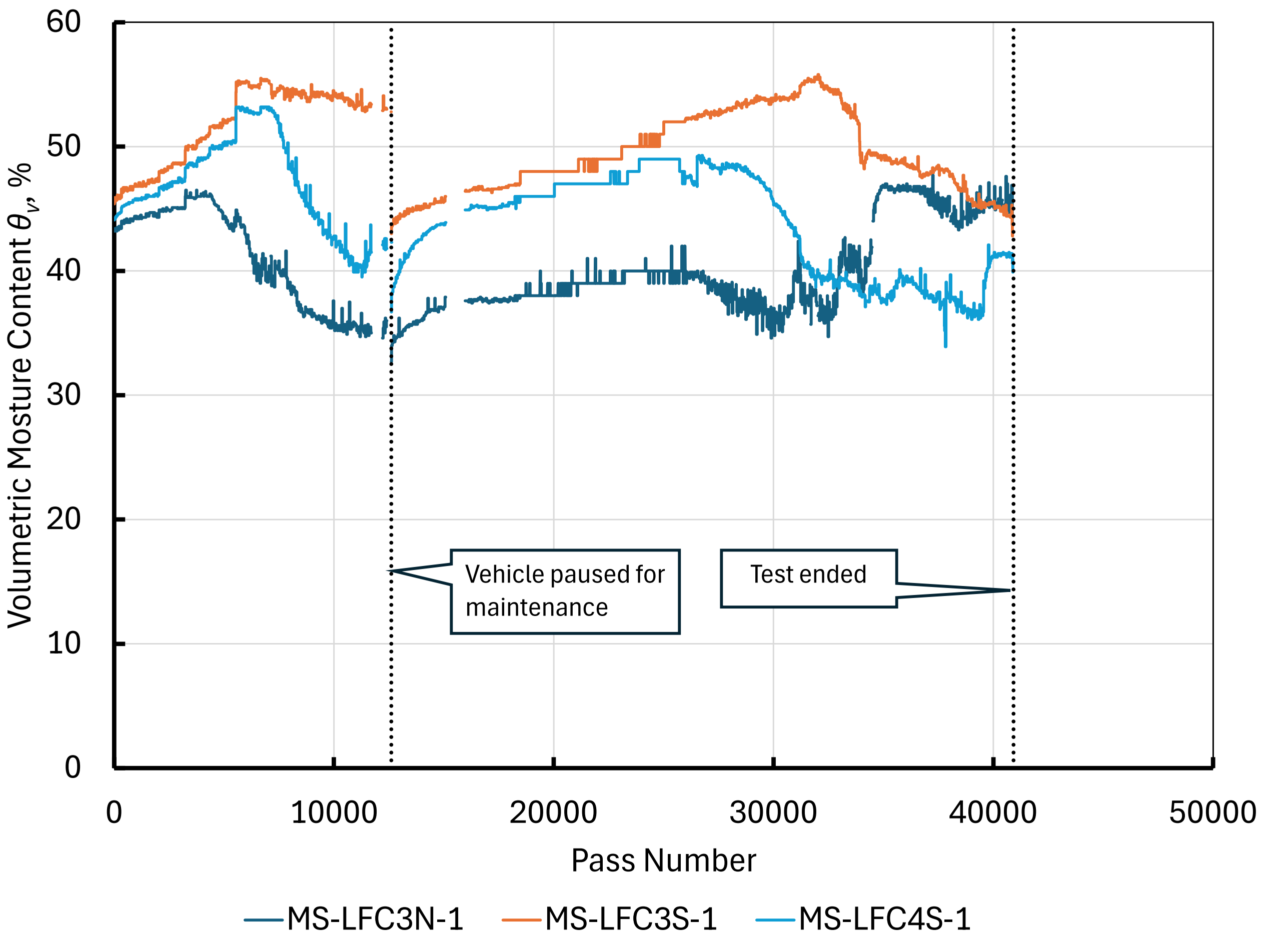

Figure 60. Change in Subgrade $\theta_v$ with Traffic

## 5.3 STRUCTURAL EVALUATION WITH NONDESTRUCTIVE TESTING

AUPP (defined in Section 2.2.5) is an excellent indicator of changes in structural layers because it includes the whole area under the deflection basin. In particular, the ratio of AUPP for HWD drop locations within traffic lanes to those outside of traffic lanes reveals the extent of load-induced damage. Referring to Section 2.2.5, HWD locations at ±15-ft offsets were within traffic lanes ($\text{AUPP}_{\text{Trafficked}}$), while those at ±5 ft and ±15 ft were outside of traffic lanes ($\text{AUPP}_{\text{Untrafficked}}$).

Figure 61 plots the ratio $\text{AUPP}_{\text{Trafficked}}/\text{AUPP}_{\text{Untrafficked}}$ versus pass number for the three test items. As expected, the AUPP ratios were consistently above one, but they did not consistently increase with traffic (as would be expected). Rather, all three test items saw a sharp increase in AUPP ratio after the start of traffic but only up to about 3,000 passes, after which there was little correlation between AUPP ratio and additional traffic. AUPP ratios in test item LFC-3N (geogrid-reinforced) were consistently higher than those in LFC-3S and LFC-4S. Also somewhat surprisingly, while the initial AUPP ratios in LFC-3S and LFC-4S (before any traffic damage) were approximately one, the initial ratio for LFC-3N was closer to 1.4, indicating insufficient compaction in the central area. Compaction control issues as discussed in Section 2 may have resulted in higher AUPP in the trafficked area of LFC-3N than in the corresponding trafficked areas of LFC-3S and LFC-4S.

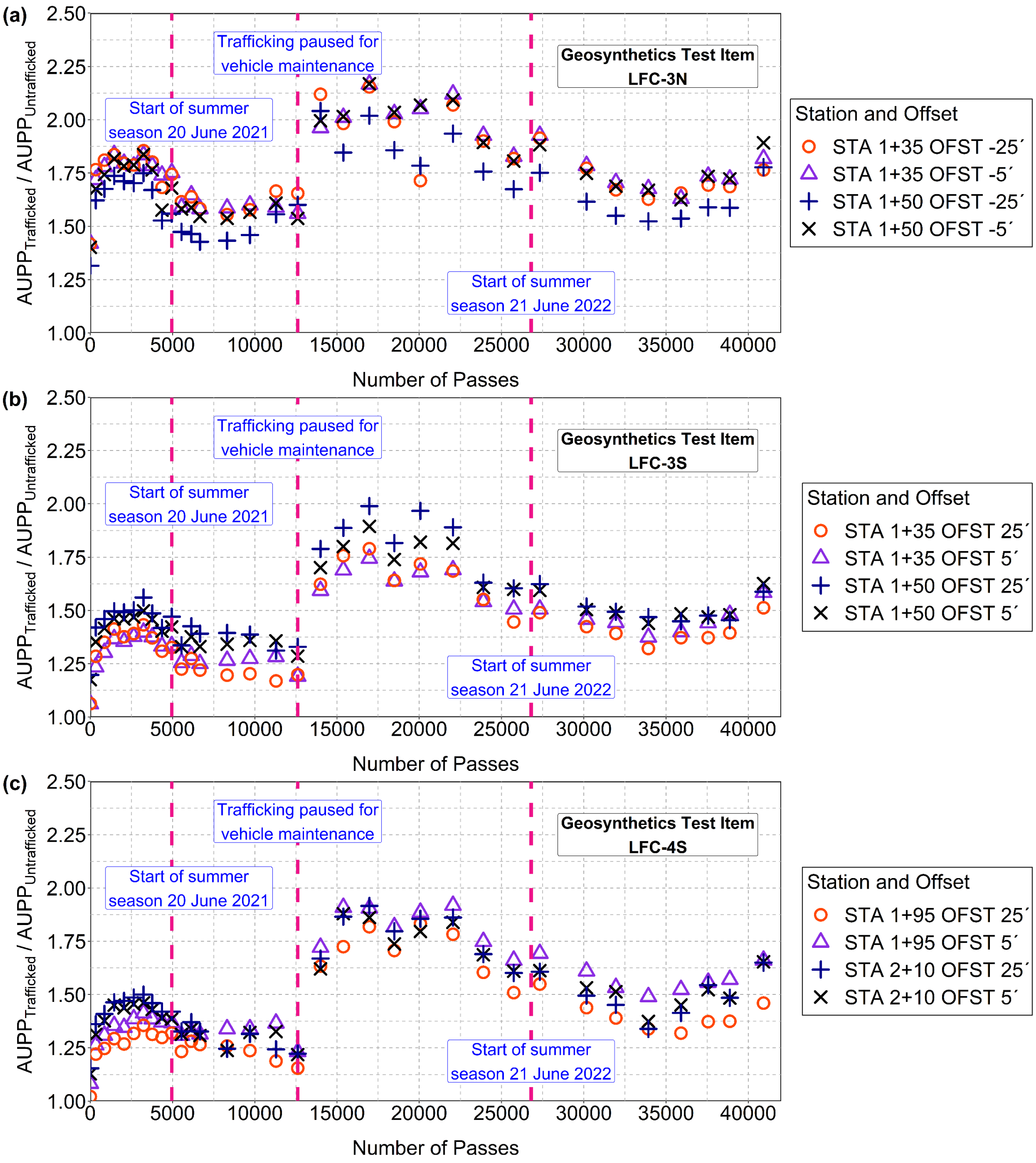

Figure 61. Variation of AUPP Ratios Between Trafficked and Non-Trafficked Areas of Geosynthetics Test Items

## 6. CONCLUSIONS

All three test items constituting the geosynthetics test (LFC-3N, LFC-3S, and LFC-4S) exhibited structural failure by the end of the test, including severe rutting and upheaval exceeding 1.0 in. In the case of LFC-3S (including geosynthetic separation fabric), measured upheaval outside the traffic lane was as much as 3.5 in. Contrary to the common expectation that geogrid reinforcement and/or geotextile separation would improve structural performance under heavy full-scale loads, the actual performance of the reinforced test items under traffic was found to be the same or worse compared to the control (unreinforced) test item. Construction issues, including nonuniform compaction of base and subbase layers, may have contributed to initial heavy rutting of the geogrid-reinforced test item LFC-3N, such that mobilization of the geogrid was delayed until late in the test. Confirmation of the contributions of various structural layers will be provided by post-traffic investigations during layer removal later. Due to the limited number of test items, and specific construction issues that may have negatively impacted performance, further testing of geogrid-reinforced flexible pavements at full scale is recommended. The following are key findings from the traffic tests on the geosynthetics test items.

1. The number of passes to failure (based on 1-in. upheaval) were: 34,751 for LFC-3N (geogrid plus separation fabric), 30,106 for LFC-3S (separation fabric only), and 36,675 for LFC-4S (control). Given the high variability of factors contributing to flexible pavement performance, these results may be considered approximately equal.

2. Test item LFC-3S (with geosynthetic separation fabric) failed with substantially higher upheaval than the other two test items. NDT results (i.e., D-PSPA and GeoGauge) indicated a localized soft subbase in LFC-3S, which is likely related to the large upheaval.

3. Regardless of the test method, the average modulus of the base course in geogrid-reinforced LFC-3N was lower than that of the base courses in LFC-3S and LFC-4S. NDT provides evidence of poor compaction control and inadequate foundation support in LFC-3N.

4. Test item LFC-3N (geogrid-reinforced) ended the test with less upheaval than LFC-4S (control), although it had higher rutting. However, by the end of the test the rate of rut increase in LFC-3S overtook LFC-3N. Lower total upheaval and a reduced rate of rutting point to eventual engagement of the tension membrane effect from geogrid. However, no benefit was apparent until rut depth exceeded 3 in. and upheaval approached 1 in., i.e., until the test item was already near failure.

5. PCs in the base and subbase layers were of limited utility because they were undersized. Repeated exposure to peak stresses beyond their rated capacity damaged the PCs and caused their early failure.

6. CS pairs in the granular pavement layers provided important data on both accumulated permanent deformation in the layers and on the vertical strain response to load. Due to excessive deformation, most CS pairs in the base and subbase failed early in the test. As expected, the peak strain response in granular layers is primarily a function of the current wander position (critical when the wheel passes directly over the sensor). However, it is also

strongly affected by the track associated with the previous pass, demonstrating the rearrangement of aggregate particles that takes place during wandered traffic.

7. Lower permanent deformation and strain in the subbase layer in test item LFC-3N compared to the other two test items, as indicated by CS pairs, suggest a benefit from geogrid reinforcement in improving stress distribution. The inclusion of geogrid aided in lateral confinement and resulted in lower permanent deformation in the subbase layer of LFC-3N than in the subbase layers of LFC-3S and LFC-4S.

8. In situ subgrade moisture content was higher in LFC-3S than in the other test items since the beginning of test item construction and remained high during testing. Higher moisture content in LFC-3S is associated with lower shear strength of the clay and may have contributed to local bearing capacity failure of the subgrade. This will be further investigated during post-traffic deconstruction.

## 7. REFERENCES

American Association of State Highway and Transportation Officials (AASHTO). (2008). *Mechanistic-empirical pavement design guide—A manual of practice* (AASHTO MEPDG-1). American Association of State Highway and Transportation Officials, Washington, DC.

AASHTO. (2019). *Standard method of test for determining dynamic modulus of hot mix asphalt (HMA)* (AASHTO T 342-11). AASHTO, Washington, DC.

AASHTO. (2021). *Determining the resilient modulus of soils and aggregate materials* (AASHTO T 307-99). AASHTO, Washington, DC.

Ahlvin, R. G., Turnbull, W. J., Sale, J. P., & Maxwell, A. A. (1971). *Multiple-wheel heavy gear load pavement tests, Volume 1* (Technical Report No. AFWL-TR-70-113). Air Force Weapons Laboratory, Kirkland AFB, New Mexico. https://apps.dtic.mil/sti/pdfs/AD0889705.pdf

Alimohammadi, H., Zheng, J., Schaefer, V. R., Siekmeier, J., & Velasquez, R. (2021). Evaluation of geogrid reinforcement of flexible pavement performance: A review of large-scale laboratory studies. *Transportation Geotechnics*, *27*. https://doi.org/10.1016/J.TRGEO.2020.100471

Al-Qadi, I. L., Dessouky, S. H., Kwon, J., & Tutumluer, E. (2012). Geogrid-reinforced low-volume flexible pavements: Pavement response and geogrid optimal location. *Journal of Transportation Engineering*, *138*(9), 1083–1090. American Society of Civil Engineers (ASCE). https://doi.org/10.1061/(ASCE)TE.1943-5436.0000409

ASTM. (2015). *Standard test method for measuring rut-depth of pavement surfaces using a straightedge* (ASTM E1703/E1703M-10(2015)). ASTM International, West Conshohocken, PA.

ASTM. (2017). *Standard test method for indirect tensile (IDT) strength of asphalt mixtures* (ASTM D6931-17). ASTM International, West Conshohocken, PA.

ASTM. (2020). *Standard test method for airport pavement condition index surveys* (ASTM D5340-20). ASTM International, West Conshohocken, PA.

ASTM. (2021). *Standard test methods for laboratory compaction characteristics of soil using modified effort (56,000 ft-lbf/ft$^3$ (2,700 kN-m/m$^3$))* (ASTM D1557-12). ASTM International, West Conshohocken, PA.

Batioja-Alvarez, D., Kazmee, H., & Garg, N. (2024). Laboratory and field performance evaluation of cracking of airfield warm mix asphalt with reclaimed asphalt pavement at the National Airport Pavement and Materials Research Center. *Transportation Research Record: Journal of the Transportation Research Board, 2678(11),* 530–546. https://doi.org/10.1177/03611981241242071 (Original work published 2024)

Bilodeau, J. P., & Doré, G. (2014). Stress distribution experienced under a portable light-weight deflectometer loading plate. *International Journal of Pavement Engineering*, *15*(6), 564–575. https://doi.org/10.1080/10298436.2013.772612

Byun, Y.-H., & Tutumluer, E. (2017). Bender elements successfully quantified stiffness enhancement provided by geogrid–aggregate interlock. *Transportation Research Record*, *2656*(1), 31–39. https://doi.org/10.3141/2656-04

Chang, G., Xu, Q., Rutledge, J., Horan, B., Michael, L., White, D., & Vennapusa, P. (2011). *Accelerated implementation of intelligent compaction technology for embankment subgrade soils, aggregate base, and asphalt pavement materials* (Report FHWA-IF-12-002). Federal Highway Administration, Washington, DC. https://rosap.ntl.bts.gov/view/dot/41036/dot_41036_DS1.pdf

Chow, L. C. (2014). *Permanent deformation behavior of unbound granular materials and rutting model development* [Master's thesis, University of Illinois at Urbana-Champaign]. Illinois Digital Environment for Access to Learning and Scholarship (IDEALS). Graduate Dissertations and Theses at Illinois. https://hdl.handle.net/2142/50674

Dawson, A. (1994). *The ε-mu System, User's Manual* (2nd ed.). Nottingham, UK: University of Nottingham.

Donovan, P. R. (2009). Analysis of unbound aggregate layer deformation behavior from full scale aircraft gear loading with wander [Doctoral Dissertation, University of Illinois at Urbana-Champaign]. Illinois Digital Environment for Access to Learning and Scholarship (IDEALS). Graduate Dissertations and Theses at Illinois. https://hdl.handle.net/2142/83400

Donovan, P. R., & Tutumluer, E. (2008, August 25–27). The anti-shakedown effect. In E. Ellis, H.-S. Yu, G. McDowell, A. R. Dawson, & N. Thom (Eds.), *Advances in Transportation Geotechnics—Proceedings of the 1st International Conference on Transportation Geotechnics held in Nottingham, UK* (1st ed., pp. 111–116). CRC Press.

Donovan, P. R., Tutumluer, E., & Huang, H. (2010). Unbound aggregate deformation behavior due to traffic wander. *Transportation Research Record: Journal of the Transportation Research Board*, *2154*(1), 164–175. https://doi.org/10.3141/2154-17

FAA Reauthorization Act of 2018. (2018). H. R. 4—115th Congress: FAA Reauthorization Act of 2018. https://uscode.house.gov/statutes/pl/115/254.pdf

FAA. (2018). *Standards for Specifying Construction of Airports* (Advisory Circular 150/5370-10H). U.S. Department of Transportation, Federal Aviation Administration. Washington, D.C. https://www.faa.gov/airports/resources/advisory_circulars/index.cfm/go/document.current/documentnumber/150_5370-10

Garg, N., Li, Q., & Brill, D. (2020). Accelerated pavement testing of perpetual pavement test sections under heavy aircraft loading at FAA's National Airport Pavement Test Facility. *Journal of Testing and Evaluation*, *48*(1), 107–119. https://doi.org/10.1520/JTE20180906

Jayalath, C., Gallage, C., Wimalasena, K., Lee, J., & Ramanujam, J. (2021). Performance of composite geogrid reinforced unpaved pavements under cyclic loading. *Construction and Building Materials*, *304*, 124570. https://doi.org/10.1016/J.CONBUILDMAT.2021.124570

Jersey, S., J. Tingle, G. Norwood, J. Kwon, and M. Wayne. 2012. Full-scale evaluation of geogrid-reinforced thin flexible pavements. *Transportation Research Record: Journal of the Transportation Research Board, (2310):* 61–71. https://doi.org/10.3141/2310-07.

Kang, M., Qambia, I. I. A., Tutumluer, E., Garg, N., & Villafane, W.  (2022). Airport pavement stiffness monitoring and assessment of mechanical stabilization using bender element field sensor. *Transportation Research Record: Journal of the Transportation Research Board, 2676*(8): 542–553. https://doi.org/10.1177/03611981221084685

Kang, M., Wang, H., Qamhia, I. I. A., Tutumluer, E., Garg, N., Villafane, W., & Murrell, S. (2023). Evaluation of airport pavement base layer stiffness characteristics via embedded field sensors. *Transportation Research Record: Journal of the Transportation Research Board*, *2677*(8) https://doi.org/10.1177/03611981231156938

Kazmee, H., Garg, N., Tomlinson, C., & Ricalde, L. (2019). Warm mix asphalt (WMA) for airport pavements—Relating laboratory test results to performance under accelerated pavement testing (APT). *Journal of the Association of Asphalt Paving Technologists*, *88*: 30.

Kazmee, H., N. Garg, and L. Ricalde. 2022. Estimating asphalt concrete strains in airport pavements using geometric property of the pavement surface deflection basin from heavy weight deflectometer tests. *Proceedings of the Eleventh International Conference on the Bearing Capacity of Roads, Railways and Airfields, Volume 3*, I. Hoff, R. Saba, and H. Mork, eds., 22–32. Trondheim, Norway: CRC Press.

Kazmee, H., Garg, N., Tomlinson, C. & Ricalde, L. 2019. Warm mix asphalt (WMA) for airport pavements – Relating laboratory test results to performance under accelerated pavement testing (APT). *Journal of the Association of Asphalt Paving Technologists*, *88*, 30p.

Kazmee, H., Murrell, S., Ricalde, L., Parsons, T., Duah, E., & Brill, D.R. (2026). *National Airport Pavement Test Facility Construction Cycle 9, Volume 1—Traffic Test Summary* (DOT/FAA/TC-26/1), U.S. Dept. of Transportation, Federal Aviation Administration.

Li, Q., Garg, N., & Haggag, M. (2015). Evaluation of rutting performance of airport pavement hot-mix asphalt using gradation-based method and laboratory testing. *94th Annual Meeting of Transportation Research Board*, *16*. Transportation Research Board, Washington, DC.

Liu, S., Huang, H., Qiu, T., & Gao, L. (2017). Comparison of laboratory testing using SmartRock and discrete element modeling of ballast particle movement. *Journal of Materials in Civil Engineering*, *29*.

Mooney, M. A., & Miller, P. K. (2009). Analysis of lightweight deflectometer test based on in situ stress and strain response. *Journal of Geotechnical and Geoenvironmental Engineering*, *135*(2), 199–208. https://doi.org/10.1061/(ASCE)1090-0241(2009)135:2(199)

Nazarian, S., Baker, M., & Crain, K. (1993). *Development and testing of a seismic pavement analyzer* (Research Report No. SHRP-H-375). Washington, DC: Strategic Highway Research Program, National Research Council.

Norwood, G. J., & Tingle, J. S., 2014. *Performance of geogrid-stabilized gravel flexible base with bituminous surface treatment* (Report No. ERDC/GSL-TR-14-15). U.S. Army Engineer Research and Development Center Geotechnical and Structures Laboratory, Vicksburg, MS.

Offenbacker, D., Brill, D. R., & Garg, N. (2026). Evaluation of the mechanical responses in clay subgrade under aircraft loading. *Transportation Research Record: Journal of the Transportation Research Board*. https://doi.org/10.1177/03611981251411258

Robinson, W. J. (2022). *Full-scale evaluation of multi-axial geogrids in road applications* (Research Report No. ERDC/GSL TR-22-4). U.S. Army Engineer Research and Development Center, Geotechnical and Structures Laboratory. Vicksburg, MS.

Robinson, W. J., Tingle, J., & Norwood, G. (2017). *Full-scale accelerated testing of multi-axial geogrid stabilized flexible pavements* (Research Report No. ERDC/GSL TR-17-9). U.S. Army Engineer Research and Development Center, Vicksburg, MS.

Robinson, W. J., Tingle, J. S., Norwood, G. J., & Howard, I. L. (2018). Assessment of equivalent thickness design principles for geosynthetic reinforced pavements by way of accelerated testing, *Transportation Research Record: Journal of the Transportation Research Board*, *2672*(40), 132–142. https://doi.org/10.1177/0361198118781682

Robinson, W. J., Tingle, J. S., Wayne, M. H., Kwon, J., & Norwood, G. (2020). Instrumentation response of full-scale multi-axial geogrid stabilized flexible pavements. In Chabot, A., Hornych, P., Harvey, J., Loria-Salazar, L. (Eds.), *Accelerated Pavement Testing to Transport Infrastructure Innovation. Lecture Notes in Civil Engineering (Vol. 96, pp. 564–573)*. Springer, Cham. https://doi.org/10.1007/978-3-030-55236-7_58

Selig, E. T., & Grangaard, O. H. (1970). A new technique for soil strain measurement. *Materials Research and Standards*, *10*(11), 19–21. ASTM International.

Thompson, M. R., & Bejarano, M. O. (1997). Subgrade criteria for airport flexible pavement design. *Proceedings of the Conference on Aircraft/Pavement Technology in the Midst of Change*, 18–32. American Society of Civil Engineers, New York, NY.

Tomlinson, C., Traverso, D., Cary, C., & Brynick, M. (2022). *Construction Cycle 9 (CC9) Construction Report* (DOT/FAA/TC-22/1). U.S. Dept. of Transportation, Federal Aviation Administration. https://www.airporttech.tc.faa.gov/Products/Airport-Pavement-Papers-Publications/Airport-Pavement-Detail/construction-cycle-9-cc9-construction-report

Tutumluer, E., Kang, M., & Qamhia, I. I. A. (2024). *Analysis of granular base/subbase in airport pavements using embedded sensors* (DOT/FAA/TC-24/31). U.S. Department of Transportation, Federal Aviation Administration. https://rosap.ntl.bts.gov/view/dot/77747

## APPENDIX A—LOCATIONS OF EMBEDDED SENSORS

Table A-1. Stations and Offsets of Embedded Sensors in Test Item LFC-3N

| Sensor ID | Longitudinal Offset (ft) | Transverse Offset (ft) | Embedment Depth (in.) |
|---|---|---|---|
| CS-LFC3N-1 | 142.5 | -12.75 | 14 |
| CS-LFC3N-2 | 142.5 | -12.75 | 17 |
| CS-LFC3N-3 | 142.5 | -12.75 | 43 |
| CS-LFC3N-4 | 142.5 | -12.75 | 46 |
| LSG-LFC3N-1 | 125 | -17.25 | 5 |
| LSG-LFC3N-2 | 127 | -17.25 | 5 |
| LSG-LFC3N-3 | 125 | -12.75 | 5 |
| LSG-LFC3N-4 | 127 | -12.75 | 5 |
| MS-LFC3N-1 | 141.5 | -15 | 48.96 |
| PC-LFC3N-1 | 142.5 | -15 | 5 |
| PC-LFC3N-2 | 142.5 | -15 | 15 |
| PC-LFC3N-3 | 142.5 | -15 | 21 |
| PC-LFC3N-4 | 142.5 | -15 | 44 |
| T-LFC3N-1 | 142.5 | -27 | 0 |
| T-LFC3N-2 | 142.5 | -27 | 1 |
| T-LFC3N-3 | 142.5 | -27 | 2 |
| T-LFC3N-4 | 142.5 | -27 | 3 |
| T-LFC3N-5 | 142.5 | -27 | 4 |
| T-LFC3N-6 | 142.5 | -27 | 5 |
| TSG-LFC3N-1 | 129 | -17.25 | 5 |
| TSG-LFC3N-2 | 131 | -17.25 | 5 |
| TSG-LFC3N-3 | 129 | -12.75 | 5 |
| TSG-LFC3N-4 | 131 | -12.75 | 5 |

Table A-2. Stations and Offsets of Embedded Sensors in Test Item LFC-3S

| Sensor ID | Longitudinal Offset (ft) | Transverse Offset (ft) | Embedment Depth (in.) |
|---|---|---|---|
| CS-LFC3S-1 | 142.5 | 12.75 | 14 |
| CS-LFC3S-2 | 142.5 | 12.75 | 17 |
| CS-LFC3S-3 | 142.5 | 12.75 | 43 |
| CS-LFC3S-4 | 142.5 | 12.75 | 46 |
| CS-LFC3S-5 | 150 | 15 | 5.54 |
| CS-LFC3S-6 | 150 | 15 | 8.54 |
| CS-LFC3S-7 | 150 | 15 | 11.54 |
| CS-LFC3S-8 | 150 | 15 | 14.54 |

| Sensor ID | Longitudinal Offset (ft) | Transverse Offset (ft) | Embedment Depth (in.) |
|---|---|---|---|
| LSG-LFC3S-1 | 125 | 12.75 | 5 |
| LSG-LFC3S-2 | 127 | 12.75 | 5 |
| LSG-LFC3S-3 | 125 | 17.25 | 5 |
| LSG-LFC3S-4 | 127 | 17.25 | 5 |
| MS-LFC3S-1 | 141.5 | 15 | 48 |
| PC-LFC3S-1 | 142.5 | 15 | 5 |
| PC-LFC3S-2 | 142.5 | 15 | 13 |
| PC-LFC3S-3 | 142.5 | 15 | 19 |
| PC-LFC3S-4 | 142.5 | 15 | 44 |
| TSG-LFC3S-1 | 129 | 12.75 | 5 |
| TSG-LFC3S-2 | 131 | 12.75 | 5 |
| TSG-LFC3S-3 | 129 | 17.25 | 5 |
| TSG-LFC3S-4 | 131 | 17.25 | 5 |

Table A-3. Stations and Offsets of Embedded Sensors in Test Item LFC-4S

| Sensor ID | Longitudinal Offset (ft) | Transverse Offset (ft) | Embedment Depth (in.) |
|---|---|---|---|
| CS-LFC4S-1 | 202.5 | 12.75 | 14 |
| CS-LFC4S-2 | 202.5 | 12.75 | 17 |
| CS-LFC4S-3 | 202.5 | 12.75 | 43 |
| CS-LFC4S-4 | 202.5 | 12.75 | 46 |
| CS-LFC4S-5 | 210 | 15 | 5.54 |
| CS-LFC4S-6 | 210 | 15 | 8.54 |
| CS-LFC4S-7 | 210 | 15 | 11.54 |
| CS-LFC4S-8 | 210 | 15 | 14.54 |
| LSG-LFC4S-1 | 185 | 12.75 | 5 |
| LSG-LFC4S-2 | 187 | 12.75 | 5 |
| LSG-LFC4S-3 | 185 | 17.25 | 5 |
| LSG-LFC4S-4 | 187 | 17.25 | 5 |
| MS-LFC4S-1 | 202.5 | 15 | 48 |
| PC-LFC4S-1 | 202.5 | 15 | 5 |
| PC-LFC4S-2 | 202.5 | 15 | 13 |
| PC-LFC4S-3 | 202.5 | 15 | 19 |
| PC-LFC4S-4 | 202.5 | 15 | 42 |
| TSG-LFC4S-1 | 189 | 12.75 | 5 |
| TSG-LFC4S-2 | 191 | 12.75 | 5 |
| TSG-LFC4S-3 | 189 | 17.25 | 5 |
| TSG-LFC4S-4 | 191 | 17.25 | 5 |

# APPENDIX B—MAXIMUM SURFACE UPHEAVALS IN GEOSYNTHETICS TEST ITEMS

Table B-1. Maximum Surface Upheavals—Geosynthetic Test Items

| Test Item | Date | Pass | Longitudinal Station, X (ft) | Transverse Offset, Y (ft) | Maximum Surface Upheaval, $Z_{max}$ (in.) |
|---|---|---|---|---|---|
| LFC-3N | 08/13/2021 | 6,666 | 164.5833 | -7.08333 | 0.28605 |
| LFC-3S | 08/13/2021 | 6,666 | 124.75 | 4.083333 | 0.357692 |
| LFC-3N | 10/20/2021 | 12,610 | 142.25 | -7.08333 | 0.58717 |
| LFC-3S | 10/20/2021 | 12,610 | 134.75 | 22.58333 | 0.627523 |
| LFC-4S | 10/20/2021 | 12,610 | 224.5833 | 22.41667 | 0.420719 |
| LFC-3N | 03/04/2022 | 13,992 | 164.4167 | -6.25 | 0.488803 |
| LFC-3S | 03/04/2022 | 13,992 | 131.9167 | 5.916667 | 0.560381 |
| LFC-4S | 03/04/2022 | 13,992 | 181.4167 | 6.416667 | 0.340798 |
| LFC-3N | 03/18/2022 | 15,378 | 163.4167 | -6.75 | 0.471526 |
| LFC-3S | 03/18/2022 | 15,378 | 134.9167 | 23.41667 | 0.522252 |
| LFC-4S | 03/18/2022 | 15,378 | 180.5833 | 5.75 | 0.328343 |
| LFC-3N | 04/01/2022 | 16,962 | 142.0833 | -6.25 | 0.51306 |
| LFC-3S | 04/01/2022 | 16,962 | 128.5833 | 2.083333 | 0.665927 |
| LFC-4S | 04/01/2022 | 16,962 | 181.75 | 6.083333 | 0.385471 |
| LFC-3N | 04/15/2022 | 18,480 | 164.75 | -5.91667 | 0.496056 |
| LFC-3S | 04/15/2022 | 18,480 | 134.5833 | 22.75 | 0.54664 |
| LFC-3N | 04/29/2022 | 20,064 | 142.0833 | -6.25 | 0.487455 |
| LFC-3S | 04/29/2022 | 20,064 | 134.75 | 22.75 | 0.559047 |
| LFC-4S | 04/29/2022 | 20,064 | 204.75 | 2.583333 | 2.994674 |
| LFC-3N | 05/13/2022 | 22,044 | 140.75 | -6.25 | 0.504772 |
| LFC-3S | 05/13/2022 | 22,044 | 134.4167 | 23.58333 | 0.575767 |
| LFC-3N | 05/26/2022 | 23,892 | 141.75 | -5.91667 | 0.482391 |
| LFC-3S | 05/26/2022 | 23,892 | 134.9167 | 23.75 | 0.595932 |
| LFC-3N | 06/10/2022 | 25,740 | 164.75 | -6.25 | 0.532258 |
| LFC-3S | 06/10/2022 | 25,740 | 134.75 | 22.75 | 0.629142 |
| LFC-4S | 06/10/2022 | 25,740 | 224.4167 | 23.08333 | 0.344274 |
| LFC-3N | 06/24/2022 | 27,324 | 164.25 | -7.08333 | 0.543956 |
| LFC-3S | 06/24/2022 | 27,324 | 134.9167 | 23.75 | 0.688295 |
| LFC-4S | 06/24/2022 | 27,324 | 181.9167 | 5.75 | 0.342675 |
| LFC-3N | 08/12/2022 | 33,924 | 164.0833 | -6.25 | 0.915364 |
| LFC-3S | 08/12/2022 | 33,924 | 136.9167 | 23.91667 | 1.427795 |
| LFC-4S | 08/12/2022 | 33,924 | 180.25 | 22.91667 | 0.594603 |
| LFC-3N | 08/26/2022 | 35,904 | 163.25 | -6.91667 | 1.117918 |
| LFC-3S | 08/26/2022 | 35,904 | 137.25 | 24.58333 | 1.848922 |
| LFC-4S | 08/26/2022 | 35,904 | 180.0833 | 23.58333 | 0.845307 |

| Test Item | Date | Pass | Longitudinal Station, X (ft) | Transverse Offset, Y (ft) | Maximum Surface Upheaval, $Z_{max}$ (in.) |
|---|---|---|---|---|---|
| LFC-3N | 09/09/2022 | 37,554 | 142.0833 | -6.08333 | 1.317183 |
| LFC-3S | 09/09/2022 | 37,554 | 137.5833 | 24.91667 | 2.369294 |
| LFC-4S | 09/09/2022 | 37,554 | 180.0833 | 23.58333 | 1.176216 |
| LFC-3N | 09/23/2022 | 38,874 | 162.25 | -6.08333 | 1.440603 |
| LFC-3S | 09/23/2022 | 38,874 | 138.0833 | 26.41667 | 2.726152 |
| LFC-4S | 09/23/2022 | 38,874 | 180.0833 | 23.58333 | 1.349925 |
| LFC-3N | 10/07/2022 | 40,920 | 143.4167 | -6.08333 | 1.562355 |
| LFC-3S | 10/07/2022 | 40,920 | 138.4167 | 27.41667 | 3.351324 |
| LFC-4S | 10/07/2022 | 40,920 | 180.0833 | 24.25 | 1.705598 |
| LFC-3N | 10/20/2022 | 43,428 | 142.4167 | -5.91667 | 1.578597 |
| LFC-3S | 10/20/2022 | 43,428 | 138.25 | 27.08333 | 3.394885 |
| LFC-4S | 10/20/2022 | 43,428 | 180.4167 | 26.25 | 1.7553 |
| LFC-3N | 11/04/2022 | 47,652 | 143.0833 | -6.08333 | 1.537381 |
| LFC-3S | 11/04/2022 | 47,652 | 137.5833 | 27.41667 | 3.343168 |
| LFC-4S | 11/04/2022 | 47,652 | 180.0833 | 25.41667 | 1.66696 |
| LFC-3N | 11/18/2022 | 51,084 | 142.4167 | -5.91667 | 1.529865 |
| LFC-3S | 11/18/2022 | 51,084 | 137.9167 | 27.91667 | 3.335158 |
| LFC-4S | 11/18/2022 | 51,084 | 180.25 | 25.58333 | 1.669837 |
| LFC-3N | 12/02/2022 | 54,054 | 142.4167 | -6.25 | 1.508222 |
| LFC-3S | 12/02/2022 | 54,054 | 138.25 | 27.08333 | 3.350256 |
| LFC-4S | 12/02/2022 | 54,054 | 180.0833 | 25.41667 | 1.637098 |
| LFC-3N | 12/23/2022 | 56,628 | 142.4167 | -5.91667 | 1.542815 |
| LFC-3S | 12/23/2022 | 56,628 | 137.75 | 27.25 | 3.382694 |
| LFC-4S | 12/23/2022 | 56,628 | 180.0833 | 25.41667 | 1.685439 |
| LFC-3N | 01/13/2023 | 58,476 | 143.9167 | -6.25 | 1.552026 |
| LFC-3S | 01/13/2023 | 58,476 | 137.75 | 27.58333 | 3.381548 |
| LFC-4S | 01/13/2023 | 58,476 | 180.4167 | 26.25 | 1.726225 |
| LFC-3N | 02/17/2023 | 60,786 | 144.4167 | -5.75 | 1.514445 |
| LFC-3S | 02/17/2023 | 60,786 | 138.25 | 27.08333 | 3.341712 |
| LFC-4S | 02/17/2023 | 60,786 | 180.4167 | 25.25 | 1.654355 |
| LFC-3N | 03/03/2023 | 63,558 | 144.75 | -6.08333 | 1.548941 |
| LFC-3S | 03/03/2023 | 63,558 | 138.25 | 27.08333 | 3.367954 |
| LFC-4S | 03/03/2023 | 63,558 | 180.0833 | 25.41667 | 1.684975 |
| LFC-3N | 03/17/2023 | 66,924 | 143.0833 | -6.08333 | 1.507857 |
| LFC-3S | 03/17/2023 | 66,924 | 138.4167 | 27.75 | 3.318928 |
| LFC-4S | 03/17/2023 | 66,924 | 180.0833 | 25.41667 | 1.64433 |

# APPENDIX C—VISUAL DISTRESS LOG

Table C-1. Log of Cracks Observed for Geosynthetics North Test Item (LFC-3N)

| Crack Number | Date of Recording | Start | | End | | Length of Crack (in.) |
|---|---|---|---|---|---|---|
| | | X | Y | X | Y | |
| | | (Offset from Centerline) (in.) | (Offset from Station) (in.) | (Offset from Centerline) (in.) | (Offset from Station) (in.) | |
| 1 | 31-Mar-22 | 220.5 | 121 from 1+35↓ | 220.5 | 87 from 1+35↓ | 34 |
| 2 | 31-Mar-22 | 222.5 | 66 from 1+35↓ | 229.5 | 59 from 1+35↑ | 125 |
| 3 | 31-Mar-22 | 192 | 103 from 1+35↓ | 191 | 70 from 1+35↓ | 33 |
| 4 | 31-Mar-22 | 135.5 | 29 from 1+35↑ | 135.5 | 0 from 1+35↑ | 29 |
| 5 | 31-Mar-22 | 108.5 | 4 from 1+35↓ | 107.5 | 148 from 1+35↑ | 144 |
| 6 | 31-Mar-22 | 235.5 | 78 from 1+35↑ | 228.5 | 118 from 1+35↑ | 40 |
| 7 | 31-Mar-22 | 220.5 | 89 from 1+50↓ | 220.5 | 70 from 1+50↓ | 19 |
| 8 | 31-Mar-22 | 220 | 46.5 from 1+50↓ | 221 | 15 from 1+50↓ | 31.5 |
| 9 | 31-Mar-22 | 139 | 100 from 1+50↓ | 139 | 14 from 1+50↑ | 114 |
| 10 | 31-Mar-22 | 112 | 32 from 1+50↓ | 111.5 | 23.5 from 1+50↑ | 8.5 |
| 11 | 31-Mar-22 | 112.5 | 138 from 1+50↑ | 111 | 130 from 1+50↑ | 8 |
| 1 | 8-Apr-22 | 218 | 40.5 from 1+35↓ | 222 | 83 from 1+35↓ | 42.7 |
| 19 | 8-Apr-22 | 210 | 167 from 1+35↓ | 213 | 160 from 1+35↓ | 7.6 |
| 3 | 8-Apr-22 | 194 | 67 from 1+35↓ | 194 | 101 from 1+35↓ | 34.0 |
| 20 | 8-Apr-22 | 215 | 0 from 1+35↓ | 212.5 | 9 from 1+35↓ | 9.3 |
| 2 | 8-Apr-22 | 224 | 68 from 1+35↓ | 233 | 66 from 1+35↑ | 134.3 |
| 6 | 8-Apr-22 | 238 | 76 from 1+35↑ | 235 | 116 from 1+35↑ | 40.1 |
| 7 | 8-Apr-22 | 221.5 | 90 from 1+35↑ | 220.5 | 123 from 1+35↑ | 33.0 |
| 8 | 8-Apr-22 | 220.5 | 132 from 1+35↑ | 220.5 | 164 from 1+35↑ | 32.0 |
| 21 | 8-Apr-22 | 196.5 | 62 from 1+35↑ | 192 | 87 from 1+35↑ | 25.4 |
| 5 | 8-Apr-22 | 109 | 147.5 from 1+35↑ | 110 | 0 from 1+20↑ | 327.5 |
| 11 | 8-Apr-22 | 111 | 39 from 1+65↓ | 111 | 71 from 1+65↓ | 32.0 |
| 25 | 8-Apr-22 | 109.5 | 31.5 from 1+50↑ | 110.5 | 20 from 1+50↑ | 11.5 |
| 22 | 8-Apr-22 | 135.5 | 101.5 from 1+50↓ | 136.5 | 15.5 from 1+50↑ | 117.0 |
| 27 | 19-Apr-22 | 138 | 51 from 1+35↑ | 138.5 | 69.5 from 1+35↑ | 18.5 |
| 9 | 19-Apr-22 | 141 | 77 from 1+35↑ | 139.5 | 66 from 1+35↑ | 11.1 |
| 28 | 19-Apr-22 | 192.5 | 62.5 from 1+35↑ | 191.5 | 52 from 1+35↑ | 10.5 |
| 29 | 19-Apr-22 | 230 | 43.5 from 1+35↑ | 234.5 | 36.5 from 1+35↑ | 8.3 |
| 30 | 19-Apr-22 | 233.5 | 39.5 from 1+35↑ | 233 | 0 from 1+35↑ | 39.5 |
| 31 | 19-Apr-22 | 230 | 0 from 1+35↓ | 224 | 16 from 1+35↓ | 17.1 |
| 32 | 19-Apr-22 | 232 | 12 from 1+35↓ | 232.5 | 113 from 1+35↓ | 101.0 |
| 33 | 19-Apr-22 | 191.5 | 20.5 from 1+35↓ | 191.5 | 28 from 1+35↓ | 7.5 |
| 34 | 19-Apr-22 | 182 | 45 from 1+35↓ | 183 | 70 from 1+35↓ | 25.0 |
| 35 | 19-Apr-22 | 214.5 | 47 from 1+35↓ | 215.5 | 104 from 1+35↓ | 57.0 |
| 36 | 19-Apr-22 | 204.5 | 34 from 1+35↓ | 201 | 46 from 1+35↓ | 12.5 |
| 37 | 19-Apr-22 | 137 | 29 from 1+35↑ | 135 | 32 from 1+35↓ | 61.0 |
| 38 | 19-Apr-22 | 135 | 32 from 1+35↓ | 139 | 36 from 1+35↓ | 5.7 |
| 39 | 19-Apr-22 | 139 | 36 from 1+35↓ | 138 | 52 from 1+35↓ | 16.0 |
| 40 | 19-Apr-22 | 147 | 21.5 from 1+35↑ | 147 | 92 from 1+35↑ | 70.5 |
| 41 | 19-Apr-22 | 217 | 11.5 from 1+50↑ | 222 | 47 from 1+50↓ | 58.7 |
| 42 | 19-Apr-22 | 194 | 7 from 1+50↑ | 193 | 29 from 1+50↑ | 22.0 |
| 43 | 19-Apr-22 | 140.5 | 44 from 1+50↑ | 140.5 | 64.5 from 1+50↑ | 20.5 |
| 44 | 19-Apr-22 | 108.5 | 41 from 1+50↑ | 108.5 | 108 from 1+50↑ | 67.0 |
| 45 | 19-Apr-22 | 108 | 9.5 from 1+65↓ | 108 | 32 from 1+65↓ | 22.5 |

| Crack Number | Date of Recording | Start | | End | | Length of Crack (in.) |
|---|---|---|---|---|---|---|
| | | X (Offset from Centerline) (in.) | Y (Offset from Station) (in.) | X (Offset from Centerline) (in.) | Y (Offset from Station) (in.) | |
| 46 | 19-Apr-22 | 11.5 | 72 from 1+65↓ | 112.5 | 33 from 1+65↓ | 108.3 |
| 47 | 19-Apr-22 | 112 | 7 from 1+65↓ | 112 | 0 from 1+65↓ | 7.0 |
| 48 | 19-Apr-22 | 128.5 | 4.5 from 1+65↓ | 129 | 13.5 from 1+65↓ | 9.0 |
| 49 | 19-Apr-22 | 139.5 | 0 from 1+65↓ | 141 | 7.5 from 1+65↓ | 7.6 |
| 50 | 19-Apr-22 | 13 | 19 from 1+65↓ | 139.5 | 49 from 1+65↓ | 130.0 |
| 51 | 19-Apr-22 | 224.5 | 3 from 1+65↓ | 225 | 8 from 1+65↓ | 5.0 |
| 61 | 28-Apr-22 | 126.5 | 9 from 1+20↑ | 126.5 | 2 from 1+20↑ | 7.0 |
| 62 | 28-Apr-22 | 127 | 10.5 from 1+20↑ | 126 | 47 from 1+20↑ | 36.5 |
| 63 | 28-Apr-22 | 139 | 18.5 from 1+20↑ | 138.5 | 27.5 from 1+20↑ | 9.0 |
| 64 | 28-Apr-22 | 138 | 13 from 1+20↑ | 137 | 18 from 1+20↑ | 5.1 |
| 65 | 28-Apr-22 | 138 | 6 from 1+20↑ | 13.25 | 0 from 1+20↑ | 124.9 |
| 66 | 28-Apr-22 | 225 | 48.5 from 1+20↑ | 233 | 47 from 1+20↑ | 8.0 |
| 67 | 28-Apr-22 | 231.5 | 47 from 1+20↑ | 233.5 | 40 from 1+20↑ | 7.3 |
| 68 | 28-Apr-22 | 233.5 | 40 from 1+20↑ | 221 | 33 from 1+20↑ | 14.3 |
| 69 | 28-Apr-22 | 221.5 | 38.5 from 1+20↑ | 221 | 28 from 1+20↑ | 10.5 |
| 70 | 28-Apr-22 | 221 | 28 from 1+20↑ | 224 | 25 from 1+20↑ | 4.2 |
| 71 | 28-Apr-22 | 224 | 25 from 1+20↑ | 216.5 | 15.5 from 1+20↑ | 12.1 |
| 72 | 28-Apr-22 | 216.5 | 15.5 from 1+20↑ | 217 | 5.5 from 1+20↑ | 10.0 |
| 73 | 28-Apr-22 | 219 | 5.5 from 1+20↑ | 219 | 0 from 1+20↑ | 5.5 |
| 74 | 28-Apr-22 | 216.5 | 15.5 from 1+20↑ | 208.5 | 12.5 from 1+20↑ | 8.5 |
| 75 | 28-Apr-22 | 208.5 | 12.5 from 1+20↑ | 206.5 | 23 from 1+20↑ | 10.7 |
| 76 | 28-Apr-22 | 208.5 | 12.5 from 1+20↑ | 205 | 5.5 from 1+20↑ | 7.8 |
| 77 | 28-Apr-22 | 205 | 5.5 from 1+20↑ | 193.5 | 3.75 from 1+20↑ | 11.6 |
| 78 | 28-Apr-22 | 193.5 | 25 from 1+35↑ | 192 | 0 from 1+35↑ | 25.0 |
| 79 | 28-Apr-22 | 193.5 | 25 from 1+35↑ | 201 | 24 from 1+35↑ | 7.6 |
| 80 | 28-Apr-22 | 201 | 24 from 1+35↑ | 202 | 5.5 from 1+35↑ | 18.5 |
| 81 | 28-Apr-22 | 202 | 5.5 from 1+35↑ | 193.25 | 8 from 1+35↑ | 9.1 |
| 82 | 28-Apr-22 | 202 | 5.5 from 1+35↑ | 202 | 5.5 from 1+35↓ | 11.0 |
| 83 | 28-Apr-22 | 253 | 12.5 from 1+35↑ | 250.5 | 111 from 1+35↓ | 7.4 |
| 84 | 28-Apr-22 | 253 | 113 from 1+35↓ | 251 | 143 from 1+35↓ | 30.1 |
| 85 | 28-Apr-22 | 257 | 148 from 1+35↓ | 252.5 | 166 from 1+35↓ | 18.6 |
| 86 | 29-Apr-22 | 147 | 65.5 from 1+20↑ | 149 | 99.25 from 1+20↑ | 33.8 |
| 87 | 29-Apr-22 | 149 | 19 from 1+35↓ | 148.5 | 44 from 1+35↓ | 25.0 |
| 88 | 29-Apr-22 | 146.5 | 45 from 1+35↓ | 149.5 | 60 from 1+35↓ | 15.3 |
| 89 | 29-Apr-22 | 147 | 16.5 from 1+35↑ | 147.5 | 21 from 1+35↑ | 4.5 |
| 90 | 29-Apr-22 | 148.5 | 11.5 from 1+35↑ | 149 | 4 from 1+35↑ | 7.5 |
| 104 | 5-May-22 | 210 | 25.5 from 1+20↑ | 213 | 27.5 from 1+20↑ | 3.6 |
| 105 | 5-May-22 | 214 | 31 from 1+20↑ | 213 | 27.5 from 1+20↑ | 9.6 |
| 106 | 5-May-22 | 220 | 31 from 1+20↑ | 214 | 21 from 1+20↑ | 11.7 |
| 107 | 5-May-22 | 220 | 31 from 1+20↑ | 224 | 48.5 from 1+20↑ | 18.0 |
| 108 | 5-May-22 | 224 | 48.5 from 1+20↑ | 219.5 | 61 from 1+20↑ | 13.3 |
| 109 | 5-May-22 | 219.5 | 61 from 1+20↑ | 225 | 61.5 from 1+20↑ | 5.5 |
| 110 | 5-May-22 | 225 | 61.5 from 1+20↑ | 222 | 79 from 1+20↑ | 17.8 |
| 111 | 5-May-22 | 222 | 79 from 1+20↑ | 219.5 | 79 from 1+20↑ | 2.5 |
| 112 | 5-May-22 | 193 | 6 from 1+20↑ | 194 | 9 from 1+20↑ | 3.2 |
| 113 | 5-May-22 | 193 | 11.5 from 1+20↑ | 194.5 | 17 from 1+20↑ | 5.7 |
| 114 | 5-May-22 | 194.5 | 17 from 1+20↑ | 193 | 22 from 1+20↑ | 5.2 |
| 115 | 5-May-22 | 193 | 22 from 1+20↑ | 192 | 22 from 1+20↑ | 1.0 |
| 116 | 5-May-22 | 192 | 22 from 1+20↑ | 191 | 29.5 from 1+20↑ | 7.6 |

| Crack Number | Date of Recording | Start | | End | | Length of Crack (in.) |
|---|---|---|---|---|---|---|
| | | X (Offset from Centerline) (in.) | Y (Offset from Station) (in.) | X (Offset from Centerline) (in.) | Y (Offset from Station) (in.) | |
| 117 | 5-May-22 | 190.5 | 30 from 1+20↑ | 194.5 | 47 from 1+20↑ | 17.5 |
| 118 | 5-May-22 | 183.5 | 50.5 from 1+20↑ | 186 | 72 from 1+20↑ | 21.6 |
| 119 | 5-May-22 | 229 | 18 from 1+20↑ | 229 | 13 from 1+20↑ | 5.0 |
| 120 | 5-May-22 | 252 | 14 from 1+20↑ | 250.5 | 0 from 1+20↑ | 14.1 |
| 121 | 5-May-22 | 219.5 | 58 from 1+20↑ | 202 | 53.5 from 1+20↑ | 18.1 |
| 122 | 5-May-22 | 200.5 | 42 from 1+20↑ | 201 | 56.5 from 1+20↑ | 14.5 |
| 123 | 5-May-22 | 225.5 | 113 from 1+20↑ | 225.5 | 110 from 1+20↑ | 3.0 |
| 124 | 5-May-22 | 225 | 94 from 1+20↑ | 220 | 95 from 1+20↑ | 5.1 |
| 125 | 5-May-22 | 219.5 | 100 from 1+20↑ | 220 | 95 from 1+20↑ | 5.0 |
| 126 | 5-May-22 | 219.5 | 100 from 1+20↑ | 215 | 100 from 1+20↑ | 4.5 |
| 127 | 5-May-22 | 219.5 | 100 from 1+20↑ | 222 | 102 from 1+20↑ | 3.2 |
| 128 | 5-May-22 | 221 | 103 from 1+20↑ | 223 | 110 from 1+20↑ | 7.3 |
| 129 | 5-May-22 | 224 | 85 from 1+20↑ | 210 | 89 from 1+20↑ | 14.6 |
| 130 | 5-May-22 | 204.5 | 96 from 1+20↑ | 200.5 | 106 from 1+20↑ | 10.8 |
| 131 | 5-May-22 | 200 | 106 from 1+20↑ | 192 | 109 from 1+20↑ | 8.5 |
| 132 | 5-May-22 | 202 | 100.5 from 1+20↑ | 207 | 103.5 from 1+20↑ | 5.8 |
| 133 | 5-May-22 | 200 | 106 from 1+20↑ | 203 | 112 from 1+20↑ | 6.7 |
| 134 | 5-May-22 | 212 | 2 from 1+35↑ | 213 | 20 from 1+35↑ | 18.0 |
| 135 | 5-May-22 | 213 | 16.5 from 1+35↑ | 221 | 16.5 from 1+35↑ | 8.0 |
| 136 | 5-May-22 | 213 | 16.5 from 1+35↑ | 212 | 18 from 1+35↑ | 1.8 |
| 137 | 5-May-22 | 220 | 19.5 from 1+35↑ | 221 | 17.5 from 1+35↑ | 2.2 |
| 138 | 5-May-22 | 225 | 39 from 1+35↑ | 224 | 50 from 1+35↑ | 11.0 |
| 139 | 5-May-22 | 227 | 42.5 from 1+35↑ | 215 | 46 from 1+35↑ | 12.5 |
| 140 | 5-May-22 | 218 | 64.5 from 1+35↑ | 217 | 58 from 1+35↑ | 6.6 |
| 141 | 5-May-22 | 218 | 64.5 from 1+35↑ | 225.5 | 65 from 1+35↑ | 7.5 |
| 142 | 5-May-22 | 227 | 63 from 1+35↑ | 225.5 | 65 from 1+35↑ | 2.5 |
| 143 | 5-May-22 | 227 | 63 from 1+35↑ | 232.5 | 63 from 1+35↑ | 5.5 |
| 144 | 5-May-22 | 206 | 70 from 1+35↑ | 218 | 64.5 from 1+35↑ | 13.2 |
| 145 | 5-May-22 | 233.5 | 65 from 1+35↑ | 237.5 | 67 from 1+35↑ | 4.5 |
| 146 | 5-May-22 | 237.5 | 67 from 1+35↑ | 238.5 | 65.5 from 1+35↑ | 1.8 |
| 147 | 5-May-22 | 237.5 | 67 from 1+35↑ | 236 | 76 from 1+35↑ | 9.1 |
| 148 | 5-May-22 | 203 | 62 from 1+35↑ | 203 | 83 from 1+35↑ | 21.0 |
| 149 | 5-May-22 | 203 | 62 from 1+35↑ | 200.5 | 60 from 1+35↑ | 3.2 |
| 150 | 5-May-22 | 200.5 | 60 from 1+35↑ | 193 | 60.5 from 1+35↑ | 7.5 |
| 151 | 5-May-22 | 195 | 61 from 1+35↑ | 191 | 85 from 1+35↑ | 24.3 |
| 152 | 5-May-22 | 203 | 83 from 1+35↑ | 189 | 85.5 from 1+35↑ | 14.2 |
| 153 | 5-May-22 | 200 | 90 from 1+35↑ | 199 | 98 from 1+35↑ | 8.1 |
| 154 | 5-May-22 | 199 | 98 from 1+35↑ | 200.5 | 104.5 from 1+35↑ | 6.7 |
| 155 | 5-May-22 | 199 | 98 from 1+35↑ | 190 | 99.5 from 1+35↑ | 9.1 |
| 156 | 5-May-22 | 189 | 97.5 from 1+35↑ | 192 | 121.5 from 1+35↑ | 24.2 |
| 157 | 5-May-22 | 183 | 66.5 from 1+35↑ | 184.5 | 80 from 1+35↑ | 13.6 |
| 158 | 5-May-22 | 141 | 29 from 1+35↑ | 138.5 | 32 from 1+35↑ | 3.9 |
| 159 | 5-May-22 | 139.5 | 38.5 from 1+35↑ | 138.5 | 49.5 from 1+35↑ | 11.0 |
| 9&27 | 5-May-22 | 137 | 48 from 1+35↑ | 140 | 17 from 1+50↑ | 149.0 |
| 160 | 5-May-22 | 136.5 | 5 from 1+35↑ | 138 | 215 from 1+35↑ | 210.0 |
| 161 | 5-May-22 | 140 | 65 from 1+50↓ | 148 | 64 from 1+50↓ | 8.1 |
| 162 | 5-May-22 | 148.5 | 2 from 1+50↓ | 149 | 88 from 1+50↓ | 86.0 |
| 163 | 5-May-22 | 250 | 117 from 1+50↓ | 248 | 40 from 1+50↓ | 77.0 |
| 164 | 5-May-22 | 195 | 2 from 1+50↓ | 195 | 5 from 1+50↓ | 3.0 |

| Crack Number | Date of Recording | Start | | End | | Length of Crack (in.) |
|---|---|---|---|---|---|---|
| | | X (Offset from Centerline) (in.) | Y (Offset from Station) (in.) | X (Offset from Centerline) (in.) | Y (Offset from Station) (in.) | |
| 165 | 5-May-22 | 195.5 | 3.5 from 1+50↑ | 194.5 | 7 from 1+50↑ | 3.6 |
| 166 | 5-May-22 | 143 | 18 from 1+50↑ | 140 | 15.5 from 1+50↑ | 3.9 |
| 167 | 5-May-22 | 141 | 43 from 1+50↑ | 140 | 49 from 1+50↑ | 6.1 |
| 168 | 5-May-22 | 127 | 16 from 1+65↓ | 132 | 39 from 1+65↓ | 23.5 |
| 169 | 5-May-22 | 140 | 48 from 1+65↓ | 136 | 61.5 from 1+65↓ | 14.1 |
| 170 | 5-May-22 | 131 | 62.5 from 1+65↓ | 130 | 87.5 from 1+65↓ | 25.0 |
| 171 | 5-May-22 | 130 | 87.5 from 1+65↓ | 138 | 89 from 1+65↓ | 8.1 |
| 172 | 5-May-22 | 137 | 90.5 from 1+65↓ | 140 | 67.5 from 1+65↓ | 23.2 |
| 173 | 5-May-22 | 224 | 2 from 1+65↓ | 226 | 9 from 1+65↓ | 7.3 |
| 174 | 5-May-22 | 191 | 15 from 1+65↓ | 194 | 28 from 1+65↓ | 13.3 |
| 175 | 5-May-22 | 194.5 | 28 from 1+65↓ | 192.5 | 29 from 1+65↓ | 2.2 |
| 176 | 5-May-22 | 192.5 | 29 from 1+65↓ | 191.5 | 31 from 1+65↓ | 2.2 |
| 177 | 5-May-22 | 192.5 | 29 from 1+65↓ | 189.5 | 27 from 1+65↓ | 3.6 |
| 199 | 27-May-22 | 229.5 | 13 from 1+20↑ | 225 | 25 from 1+20↑ | 12.8 |
| 200 | 27-May-22 | 210 | 5 from 1+20↑ | 219 | 5.5 from 1+20↑ | 9.0 |
| 201 | 27-May-22 | 208.5 | 39 from 1+20↑ | 211 | 52.5 from 1+20↑ | 13.7 |
| 202 | 27-May-22 | 211 | 89 from 1+20↑ | 222 | 61 from 1+20↑ | 30.1 |
| 203 | 27-May-22 | 211 | 89 from 1+20↑ | 209 | 77 from 1+20↑ | 12.2 |
| 204 | 27-May-22 | 211 | 89 from 1+20↑ | 206 | 56 from 1+20↑ | 33.4 |
| 205 | 27-May-22 | 198 | 90 from 1+20↑ | 205 | 99 from 1+20↑ | 11.4 |
| 206 | 27-May-22 | 212 | 8 from 1+35↓ | 205.5 | 31 from 1+35↓ | 23.9 |
| 207 | 27-May-22 | 212 | 8 from 1+35↓ | 202 | 14 from 1+35↓ | 11.7 |
| 208 | 27-May-22 | 202 | 14 from 1+35↓ | 202.5 | 27.5 from 1+35↓ | 13.5 |
| 209 | 27-May-22 | 202 | 14 from 1+35↓ | 192 | 21 from 1+35↓ | 12.2 |
| 210 | 27-May-22 | 192 | 21 from 1+35↓ | 192 | 28 from 1+35↓ | 7.0 |
| 211 | 27-May-22 | 192 | 21 from 1+35↓ | 181 | 17 from 1+35↓ | 11.7 |
| 212 | 27-May-22 | 148 | 2 from 1+35↓ | 147 | 44 from 1+35↓ | 42.0 |
| 213 | 27-May-22 | 192 | 24.5 from 1+35↑ | 189 | 31 from 1+35↑ | 7.2 |
| 214 | 27-May-22 | 251.5 | 21.5 from 1+35↑ | 253 | 12 from 1+35↑ | 9.6 |
| 215 | 27-May-22 | 210.5 | 39 from 1+35↑ | 217 | 31.5 from 1+35↑ | 9.9 |
| 216 | 27-May-22 | 222 | 47 from 1+50↓ | 222 | 69 from 1+50↓ | 22.0 |
| 217 | 27-May-22 | 210 | 16.5 from 1+50↑ | 223 | 13 from 1+50↑ | 13.5 |
| 218 | 27-May-22 | 147.5 | 112 from 1+50↑ | 148 | 139 from 1+50↑ | 27.0 |
| 219 | 27-May-22 | 114 | 139 from 1+50↑ | 110 | 150 from 1+50↑ | 11.7 |
| 261 | 10-Jun-22 | 237.5 | 50 from 1+20↑ | 232 | 47 from 1+20↑ | 6.3 |
| 262 | 10-Jun-22 | 221 | 32.5 from 1+20↑ | 220.5 | 34.5 from 1+20↑ | 2.1 |
| 263 | 10-Jun-22 | 220 | 36 from 1+20↑ | 220 | 40.5 from 1+20↑ | 4.5 |
| 264 | 10-Jun-22 | 233 | 81.5 from 1+20↑ | 226 | 80 from 1+20↑ | 7.2 |
| 265 | 10-Jun-22 | 237 | 90 from 1+20↑ | 234 | 90 from 1+20↑ | 3.0 |
| 266 | 10-Jun-22 | 233 | 103.5 from 1+20↑ | 222 | 104 from 1+20↑ | 11.0 |
| 267 | 10-Jun-22 | 210 | 89 from 1+20↑ | 205 | 87 from 1+20↑ | 5.4 |
| 268 | 10-Jun-22 | 204 | 71.5 from 1+20↑ | 202 | 62 from 1+20↑ | 9.7 |
| 269 | 10-Jun-22 | 192.5 | 3.5 from 1+20↑ | 194 | 4 from 1+20↑ | 1.6 |
| 270 | 10-Jun-22 | 146 | 21.5 from 1+20↑ | 139 | 22 from 1+20↑ | 7.0 |
| 271 | 10-Jun-22 | 137 | 30 from 1+20↑ | 135.5 | 38.5 from 1+20↑ | 8.6 |
| 272 | 10-Jun-22 | 145 | 67 from 1+20↑ | 139 | 65 from 1+20↑ | 6.3 |
| 273 | 10-Jun-22 | 139 | 59 from 1+20↑ | 139 | 65 from 1+20↑ | 6.0 |
| 274 | 10-Jun-22 | 139 | 59 from 1+20↑ | 138 | 56.5 from 1+20↑ | 2.7 |
| 275 | 10-Jun-22 | 139 | 59 from 1+20↑ | 144 | 59 from 1+20↑ | 5.0 |

| Crack Number | Date of Recording | Start | | End | | Length of Crack (in.) |
|---|---|---|---|---|---|---|
| | | X | Y | X | Y | |
| | | (Offset from Centerline) (in.) | (Offset from Station) (in.) | (Offset from Centerline) (in.) | (Offset from Station) (in.) | |
| 276 | 10-Jun-22 | 108 | 0 from 1+20↑ | 114.5 | 34 from 1+50↑ | 394.1 |
| 277 | 10-Jun-22 | 252 | 32 from 1+20↑ | 250 | 37 from 1+20↑ | 5.4 |
| 278 | 10-Jun-22 | 252 | 65 from 1+20↑ | 251 | 70 from 1+20↑ | 5.1 |
| 279 | 10-Jun-22 | 232.5 | 13 from 1+35↓ | 229 | 12 from 1+35↓ | 3.6 |
| 280 | 10-Jun-22 | 234 | 14.5 from 1+35↓ | 238 | 11 from 1+35↓ | 5.3 |
| 281 | 10-Jun-22 | 221 | 58.5 from 1+35↓ | 212.5 | 61.5 from 1+35↓ | 9.0 |
| 282 | 10-Jun-22 | 203.5 | 57.5 from 1+35↓ | 202 | 69.5 from 1+35↓ | 12.1 |
| 283 | 10-Jun-22 | 193 | 63 from 1+35↓ | 193 | 67 from 1+35↓ | 4.0 |
| 284 | 10-Jun-22 | 204.5 | 31 from 1+35↓ | 191.5 | 25.5 from 1+35↓ | 14.1 |
| 285 | 10-Jun-22 | 207 | 6.5 from 1+35↓ | 202 | 5.5 from 1+35↓ | 5.1 |
| 286 | 10-Jun-22 | 201.5 | 4.5 from 1+35↓ | 192.5 | 5 from 1+35↓ | 9.0 |
| 287 | 10-Jun-22 | 190 | 2 from 1+35↓ | 192.5 | 5 from 1+35↓ | 3.9 |
| 288 | 10-Jun-22 | 190 | 2 from 1+35↑ | 192 | 2 from 1+35↑ | 2.0 |
| 289 | 10-Jun-22 | 147 | 36.5 from 1+35↑ | 139.5 | 37 from 1+35↑ | 7.5 |
| 290 | 10-Jun-22 | 135 | 33 from 1+35↑ | 128 | 32 from 1+35↑ | 7.1 |
| 291 | 10-Jun-22 | 128 | 8 from 1+35↑ | 128 | 32 from 1+35↑ | 24.0 |
| 292 | 10-Jun-22 | 138 | 22 from 1+35↑ | 138 | 28 from 1+35↑ | 6.0 |
| 293 | 10-Jun-22 | 138.5 | 60.5 from 1+35↑ | 140 | 69 from 1+35↑ | 8.6 |
| 294 | 10-Jun-22 | 149 | 79 from 1+35↑ | 148 | 74 from 1+35↑ | 5.1 |
| 295 | 10-Jun-22 | 195 | 87 from 1+35↑ | 187.5 | 86.5 from 1+35↑ | 7.5 |
| 296 | 10-Jun-22 | 189.5 | 85 from 1+35↑ | 187.5 | 85.5 from 1+35↑ | 2.1 |
| 297 | 10-Jun-22 | 191 | 98.5 from 1+35↑ | 177 | 94 from 1+35↑ | 14.7 |
| 298 | 10-Jun-22 | 201 | 94.5 from 1+35↑ | 208 | 97 from 1+35↑ | 7.4 |
| 299 | 10-Jun-22 | 184 | 49 from 1+35↑ | 192 | 52 from 1+35↑ | 8.5 |
| 300 | 10-Jun-22 | 190 | 52 from 1+35↑ | 195 | 45.5 from 1+35↑ | 8.2 |
| 301 | 10-Jun-22 | 191 | 32 from 1+35↑ | 193 | 34 from 1+35↑ | 2.8 |
| 302 | 10-Jun-22 | 209.5 | 21 from 1+35↑ | 209.5 | 18.5 from 1+35↑ | 2.5 |
| 303 | 10-Jun-22 | 212 | 17.5 from 1+35↑ | 209.5 | 18.5 from 1+35↑ | 2.7 |
| 304 | 10-Jun-22 | 222 | 23 from 1+35↑ | 233 | 25 from 1+35↑ | 11.2 |
| 305 | 10-Jun-22 | 234 | 23.5 from 1+35↑ | 242 | 30 from 1+35↑ | 10.3 |
| 306 | 10-Jun-22 | 244 | 37 from 1+35↑ | 242 | 30 from 1+35↑ | 7.3 |
| 307 | 10-Jun-22 | 244 | 37 from 1+35↑ | 236 | 54 from 1+35↑ | 18.8 |
| 308 | 10-Jun-22 | 235 | 78 from 1+35↑ | 225 | 76.5 from 1+35↑ | 10.1 |
| 309 | 10-Jun-22 | 215 | 47 from 1+35↑ | 210.5 | 45.5 from 1+35↑ | 4.7 |
| 310 | 10-Jun-22 | 200.5 | 27.5 from 1+35↑ | 201 | 31 from 1+35↑ | 3.5 |
| 311 | 10-Jun-22 | 200 | 31 from 1+35↑ | 200.5 | 33 from 1+35↑ | 2.1 |
| 312 | 10-Jun-22 | 209 | 80.5 from 1+35↑ | 204.5 | 82 from 1+35↑ | 4.7 |
| 313 | 10-Jun-22 | 221 | 100 from 1+35↑ | 221 | 103 from 1+35↑ | 3.0 |
| 314 | 10-Jun-22 | 221 | 100 from 1+35↑ | 231.5 | 103 from 1+35↑ | 10.9 |
| 315 | 10-Jun-22 | 187 | 61 from 1+35↑ | 182 | 61.5 from 1+35↑ | 5.0 |
| 316 | 10-Jun-22 | 180 | 66.5 from 1+35↑ | 187 | 61.5 from 1+35↑ | 8.6 |
| 317 | 10-Jun-22 | 249 | 27.5 from 1+50↓ | 249 | 39.5 from 1+50↓ | 12.0 |
| 318 | 10-Jun-22 | 232 | 31.5 from 1+50↓ | 232 | 40 from 1+50↓ | 8.5 |
| 319 | 10-Jun-22 | 221 | 47 from 1+50↓ | 224 | 50 from 1+50↓ | 4.2 |
| 320 | 10-Jun-22 | 226 | 61 from 1+50↓ | 230 | 62 from 1+50↓ | 4.1 |
| 321 | 10-Jun-22 | 231 | 64 from 1+50↓ | 230 | 62 from 1+50↓ | 2.2 |
| 322 | 10-Jun-22 | 192 | 27.5 from 1+50↓ | 192 | 36.5 from 1+50↓ | 9.0 |
| 323 | 10-Jun-22 | 109.5 | 41 from 1+50↑ | 111 | 23 from 1+50↑ | 18.1 |
| 324 | 10-Jun-22 | 194 | 25 from 1+50↑ | 194 | 30 from 1+50↑ | 5.0 |

| Crack Number | Date of Recording | Start | | End | | Length of Crack (in.) |
|---|---|---|---|---|---|---|
| | | X (Offset from Centerline) (in.) | Y (Offset from Station) (in.) | X (Offset from Centerline) (in.) | Y (Offset from Station) (in.) | |
| 325 | 10-Jun-22 | 188.5 | 64 from 1+50↑ | 201 | 67 from 1+50↑ | 12.9 |
| 326 | 10-Jun-22 | 205 | 65 from 1+50↑ | 201 | 66.5 from 1+50↑ | 4.3 |
| 327 | 10-Jun-22 | 199.5 | 74 from 1+50↑ | 187 | 79 from 1+50↑ | 13.5 |
| 328 | 10-Jun-22 | 193.5 | 69 from 1+65↓ | 188.5 | 69.5 from 1+65↓ | 5.0 |
| 329 | 10-Jun-22 | 188 | 72 from 1+65↓ | 188.5 | 69 from 1+65↓ | 3.0 |
| 330 | 10-Jun-22 | 224 | 2 from 1+65↓ | 220.5 | 0 from 1+65↓ | 4.0 |
| 331 | 15-Jun-22 | 194 | 28 from 1+65↓ | 202.5 | 25.5 from 1+65↓ | 8.9 |
| 332 | 15-Jun-22 | 194 | 28.5 from 1+65↓ | 197 | 31 from 1+65↓ | 3.9 |
| 333 | 15-Jun-22 | 194 | 25.5 from 1+65↓ | 189.5 | 28 from 1+65↓ | 5.1 |
| 334 | 15-Jun-22 | 181.5 | 27.5 from 1+65↓ | 189.5 | 28 from 1+65↓ | 8.0 |
| 335 | 15-Jun-22 | 189.5 | 29 from 1+65↓ | 187 | 31 from 1+65↓ | 3.2 |
| 336 | 15-Jun-22 | 142 | 9 from 1+65↓ | 139.5 | 0 from 1+65↓ | 9.3 |
| 337 | 15-Jun-22 | 140.5 | 16.5 from 1+65↓ | 137 | 19 from 1+65↓ | 4.3 |
| 338 | 15-Jun-22 | 112 | 7 from 1+65↓ | 107 | 10.5 from 1+65↓ | 6.1 |
| 339 | 15-Jun-22 | 106.5 | 71.5 from 1+65↓ | 112 | 69 from 1+65↓ | 6.0 |
| 389 | 1-Jul-22 | 127 | 2.5 from 1+65↓ | 128 | 4.5 from 1+65↓ | 2.2 |
| 390 | 1-Jul-22 | 128 | 14 from 1+65↓ | 126.5 | 16 from 1+65↓ | 2.5 |
| 391 | 1-Jul-22 | 181.5 | 1.5 from 1+65↓ | 183.5 | 3 from 1+65↓ | 2.5 |
| 392 | 1-Jul-22 | 185 | 0 from 1+65↓ | 197 | 2 from 1+65↓ | 12.2 |
| 393 | 1-Jul-22 | 225.5 | 11 from 1+65↓ | 222.5 | 15.5 from 1+65↓ | 5.4 |
| 394 | 1-Jul-22 | 199 | 68 from 1+65↓ | 193 | 68.5 from 1+65↓ | 6.0 |
| 395 | 1-Jul-22 | 139.5 | 43.5 from 1+50↑ | 140.5 | 39.5 from 1+50↑ | 4.1 |
| 396 | 1-Jul-22 | 145 | 42.5 from 1+50↑ | 146.5 | 38 from 1+50↑ | 4.7 |
| 397 | 1-Jul-22 | 138.5 | 20 from 1+50↑ | 138 | 16.5 from 1+50↑ | 3.5 |
| 398 | 1-Jul-22 | 193 | 8.5 from 1+50↑ | 196 | 9.5 from 1+50↑ | 3.2 |
| 399 | 1-Jul-22 | 196 | 9 from 1+50↑ | 202.5 | 7.5 from 1+50↑ | 6.7 |
| 400 | 1-Jul-22 | 204 | 69.5 from 1+50↓ | 206 | 63.5 from 1+50↓ | 6.3 |
| 401 | 1-Jul-22 | 220.5 | 66 from 1+50↓ | 206.5 | 66 from 1+50↓ | 14.0 |
| 402 | 1-Jul-22 | 219 | 81 from 1+50↓ | 214 | 80 from 1+50↓ | 5.1 |
| 403 | 1-Jul-22 | 235.5 | 74 from 1+50↓ | 232 | 76.5 from 1+50↓ | 4.3 |
| 404 | 1-Jul-22 | 174.5 | 87 from 1+50↓ | 169.5 | 86.5 from 1+50↓ | 5.0 |
| 405 | 1-Jul-22 | 166.5 | 94 from 1+50↓ | 165.5 | 96 from 1+50↓ | 2.2 |
| 406 | 1-Jul-22 | 211 | 55.5 from 1+35↑ | 215 | 58 from 1+35↑ | 4.7 |
| 407 | 1-Jul-22 | 207.5 | 39 from 1+35↑ | 209 | 39 from 1+35↑ | 1.5 |
| 408 | 1-Jul-22 | 217 | 31.5 from 1+35↑ | 220 | 31 from 1+35↑ | 3.0 |
| 409 | 1-Jul-22 | 222.5 | 11.5 from 1+35↑ | 228 | 13.5 from 1+35↑ | 5.9 |
| 410 | 1-Jul-22 | 251 | 21 from 1+35↑ | 251.5 | 22 from 1+35↑ | 1.1 |
| 411 | 1-Jul-22 | 248.5 | 35 from 1+35↑ | 248.5 | 37 from 1+35↑ | 2.0 |
| 412 | 1-Jul-22 | 229 | 0 from 1+35↑ | 234.5 | 8 from 1+35↑ | 9.7 |
| 413 | 1-Jul-22 | 190 | 51 from 1+35↓ | 181 | 52 from 1+35↓ | 9.1 |
| 414 | 1-Jul-22 | 213 | 44 from 1+35↓ | 213 | 47.5 from 1+35↓ | 3.5 |
| 415 | 1-Jul-22 | 199.5 | 44.5 from 1+35↓ | 199.5 | 46.5 from 1+35↓ | 2.0 |
| 416 | 1-Jul-22 | 209 | 7.5 from 1+20↑ | 218 | 6 from 1+20↑ | 9.1 |
| 417 | 1-Jul-22 | 210 | 12.5 from 1+20↑ | 217.5 | 15.5 from 1+20↑ | 8.1 |
| 418 | 1-Jul-22 | 210 | 13 from 1+20↑ | 206 | 6.5 from 1+20↑ | 7.6 |
| 419 | 1-Jul-22 | 222 | 32 from 1+20↑ | 223 | 33 from 1+20↑ | 1.4 |
| 420 | 1-Jul-22 | 228.5 | 36 from 1+20↑ | 223 | 33 from 1+20↑ | 6.3 |
| 421 | 1-Jul-22 | 227 | 62 from 1+20↑ | 232 | 61.5 from 1+20↑ | 5.0 |
| 422 | 1-Jul-22 | 236 | 64 from 1+20↑ | 234 | 63 from 1+20↑ | 2.2 |

| Crack Number | Date of Recording | Start | | End | | Length of Crack (in.) |
|---|---|---|---|---|---|---|
| | | X | Y | X | Y | |
| | | (Offset from Centerline) (in.) | (Offset from Station) (in.) | (Offset from Centerline) (in.) | (Offset from Station) (in.) | |
| 423 | 1-Jul-22 | 236 | 64 from 1+20↑ | 236 | 68 from 1+20↑ | 4.0 |
| 424 | 1-Jul-22 | 239 | 51 from 1+20↑ | 238 | 49 from 1+20↑ | 2.2 |
| 425 | 1-Jul-22 | 239 | 95 from 1+20↑ | 239 | 98.5 from 1+20↑ | 3.5 |
| 426 | 1-Jul-22 | 223 | 102.5 from 1+20↑ | 222 | 102 from 1+20↑ | 1.1 |
| 427 | 1-Jul-22 | 222.5 | 100.5 from 1+20↑ | 222 | 102 from 1+20↑ | 1.6 |
| 428 | 1-Jul-22 | 219 | 75.5 from 1+20↑ | 214 | 75 from 1+20↑ | 5.0 |
| 429 | 1-Jul-22 | 217.5 | 64 from 1+20↑ | 215 | 67 from 1+20↑ | 3.9 |
| 430 | 1-Jul-22 | 214 | 105 from 1+20↑ | 210 | 102.5 from 1+20↑ | 4.7 |
| 431 | 1-Jul-22 | 208 | 87 from 1+20↑ | 205 | 86.5 from 1+20↑ | 3.0 |
| 432 | 1-Jul-22 | 210 | 78.5 from 1+20↑ | 206.5 | 77.5 from 1+20↑ | 3.6 |
| 433 | 1-Jul-22 | 199.5 | 80 from 1+20↑ | 206.5 | 77.5 from 1+20↑ | 7.4 |
| 434 | 1-Jul-22 | 198.5 | 73.5 from 1+20↑ | 206.5 | 77.5 from 1+20↑ | 8.9 |
| 435 | 1-Jul-22 | 196 | 76 from 1+20↑ | 196 | 74 from 1+20↑ | 2.0 |
| 436 | 1-Jul-22 | 200 | 127.5 from 1+20↑ | 205 | 129 from 1+20↑ | 5.2 |
| 437 | 1-Jul-22 | 252 | 65.5 from 1+20↑ | 254.5 | 65 from 1+20↑ | 2.5 |
| 438 | 1-Jul-22 | 183 | 49 from 1+20↑ | 184 | 51 from 1+20↑ | 2.2 |
| 439 | 1-Jul-22 | 151 | 53 from 1+20↑ | 147.5 | 58.5 from 1+20↑ | 6.5 |
| 440 | 1-Jul-22 | 149 | 66 from 1+20↑ | 148.5 | 64 from 1+20↑ | 2.1 |
| 441 | 1-Jul-22 | 141.5 | 59 from 1+20↑ | 140 | 56 from 1+20↑ | 3.4 |
| 442 | 1-Jul-22 | 148 | 24 from 1+20↑ | 147.5 | 22 from 1+20↑ | 2.1 |
| 443 | 1-Jul-22 | 150 | 8.5 from 1+20↑ | 148.5 | 0 from 1+20↑ | 8.6 |
| 444 | 1-Jul-22 | 146 | 18 from 1+35↑ | 146 | 15 from 1+35↑ | 3.0 |
| 445 | 1-Jul-22 | 147.5 | 12 from 1+35↑ | 144.5 | 15 from 1+35↑ | 4.2 |
| 446 | 1-Jul-22 | 138 | 39 from 1+35↑ | 137.5 | 36 from 1+35↑ | 3.0 |
| 447 | 1-Jul-22 | 138 | 31.5 from 1+35↑ | 136.5 | 32.5 from 1+35↑ | 1.8 |
| 448 | 1-Jul-22 | 207 | 44.5 from 1+35↑ | 208.5 | 45 from 1+35↑ | 1.6 |

Table C-2. Log of Cracks Observed for Geosynthetics South Test Item (LFC-3S)

| | | **Start** | | **End** | | |
|---|---|---|---|---|---|---|
| **Crack Number** | **Date of Recording** | **X (Offset from Centerline) (in.)** | **Y (Offset from Station) (in.)** | **X (Offset from Centerline) (in.)** | **Y (Offset from Station) (in.)** | **Length of Crack (in.)** |
| 12 | 31-Mar-22 | 250 | 0 from 1+20↑ | 251 | 156 from 1+35↑ | 336.0 |
| 13 | 31-Mar-22 | 107.5 | 160.5 from 1+35↓ | 108.5 | 11.5 from 1+35↓ | 149.0 |
| 14 | 31-Mar-22 | 226 | 10.5 from 1+35↑ | 231 | 70 from 1+35↑ | 59.5 |
| 15 | 31-Mar-22 | 218 | 123 from 1+35↑ | 218 | 141 from 1+35↑ | 18.0 |
| 16 | 31-Mar-22 | 107 | 85.5 from 1+65↓ | 108 | 105 from 1+65↓ | 19.5 |
| 17 | 31-Mar-22 | 106 | 72 from 1+65↓ | 109 | 85.5 from 1+65↓ | 13.5 |
| 18 | 31-Mar-22 | 108 | 5 from 1+65↓ | 109 | 74.5 from 1+65↓ | 69.5 |
| 19 | 31-Mar-22 | 241 | 36 from 1+65↓ | 241 | 44.5 from 1+65↓ | 8.5 |
| 12 | 8-Apr-22 | 252 | 0 from 1+20↑ | 251.5 | 0 from 1+65↓ | 540.0 |
| 23 | 8-Apr-22 | 130 | 0 from 1+20↑ | 130 | 24.5 from 1+20↑ | 24.5 |
| 13 | 8-Apr-22 | 109.5 | 0 from 1+20↑ | 108 | 146 from 1+35↑ | 326.0 |
| 24 | 8-Apr-22 | 218 | 92 from 1+35↓ | 218 | 139 from 1+35↓ | 47.0 |
| 14 | 8-Apr-22 | 222 | 18 from 1+35↓ | 228.5 | 73.5 from 1+35↑ | 91.7 |
| 15 | 8-Apr-22 | 217.5 | 38 from 1+50↓ | 218.5 | 59 from 1+50↓ | 21.0 |
| 18&17 | 8-Apr-22 | 107.5 | 0 from 1+65↓ | 108.5 | 118 from 1+65↓ | 118.0 |
| 52 | 19-Apr-22 | 216 | 17.5 from 1+20↑ | 215 | 31 from 1+20↑ | 13.5 |
| 53 | 19-Apr-22 | 215 | 35 from 1+20↑ | 215.5 | 84 from 1+20↑ | 49.0 |
| 54 | 19-Apr-22 | 160 | 74 from 1+20↑ | 160 | 83.5 from 1+20↑ | 9.5 |
| 55 | 19-Apr-22 | 151 | 86.5 from 1+20↑ | 150.5 | 100.5 from 1+20↑ | 14.0 |
| 14 | 19-Apr-22 | 227.5 | 26 from 1+35↓ | 226 | 77 from 1+35↓ | 51.0 |
| 13 | 19-Apr-22 | 112 | 155 from 1+35↑ | 108 | 0 from 1+20↑ | 335.0 |
| 56 | 19-Apr-22 | 127.5 | 13 from 1+50↑ | 132 | 9.5 from 1+50↓ | 22.9 |
| 57 | 19-Apr-22 | 215.5 | 54 from 1+50↑ | 218 | 21 from 1+50↑ | 33.1 |
| 58 | 19-Apr-22 | 129.5 | 79 from 1+50↑ | 135 | 124.5 from 1+50↑ | 45.8 |
| 59 | 19-Apr-22 | 217 | 0 from 1+65↓ | 217 | 14 from 1+65↓ | 14.0 |
| 60 | 19-Apr-22 | 150 | 10.5 from 1+65↓ | 149 | 0 from 1+65↓ | 10.5 |
| 91 | 29-Apr-22 | 195 | 48 from 1+20↑ | 196 | 91 from 1+20↑ | 43.0 |
| 92 | 29-Apr-22 | 17.5 | 67 from 1+20↑ | 168 | 93 from 1+20↑ | 152.7 |
| 93 | 29-Apr-22 | 172 | 79 from 1+20↑ | 161 | 79.5 from 1+20↑ | 11.0 |
| 94 | 29-Apr-22 | 189.5 | 69.5 from 1+20↑ | 188.5 | 101 from 1+20↑ | 31.5 |
| 95 | 29-Apr-22 | 186.5 | 115 from 1+20↑ | 187 | 105.5 from 1+20↑ | 9.5 |
| 96 | 29-Apr-22 | 218 | 6 from 1+35↑ | 219 | 39 from 1+35↑ | 33.0 |
| 97 | 29-Apr-22 | 214.5 | 42.5 from 1+35↑ | 215.5 | 57 from 1+35↑ | 14.5 |
| 98 | 29-Apr-22 | 133 | 98 from 1+35↑ | 134 | 108.5 from 1+35↑ | 10.5 |
| 99 | 29-Apr-22 | 129.5 | 17.5 from 1+50↓ | 128.5 | 28 from 1+50↓ | 10.5 |
| 100 | 29-Apr-22 | 166.5 | 18 from 1+50↓ | 168 | 1.5 from 1+50↓ | 16.6 |
| 101 | 29-Apr-22 | 132.5 | 38 from 1+50↑ | 130 | 54.5 from 1+50↑ | 16.7 |
| 102 | 29-Apr-22 | 133 | 68 from 1+50↑ | 130.5 | 76 from 1+50↑ | 8.4 |
| 103 | 29-Apr-22 | 155 | 22.5 from 1+50↑ | 153.5 | 45 from 1+50↑ | 22.5 |
| 23 | 5-May-22 | 130 | 25.5 from 1+20↑ | 131 | 33 from 1+20↑ | 7.6 |
| 178 | 5-May-22 | 217 | 14 from 1+20↑ | 218 | 18 from 1+20↑ | 4.1 |
| 189 | 5-May-22 | 217 | 17.5 from 1+20↑ | 217.5 | 6 from 1+20↑ | 11.5 |
| 53 | 5-May-22 | 215 | 35 from 1+20↑ | 216 | 87 from 1+20↑ | 52.0 |
| 180 | 5-May-22 | 216 | 87 from 1+20↑ | 227.5 | 93.5 from 1+20↑ | 13.2 |
| 181 | 5-May-22 | 200 | 77.5 from 1+20↑ | 200 | 91 from 1+20↑ | 13.5 |
| 54 | 5-May-22 | 159 | 72.5 from 1+20↑ | 162 | 97 from 1+20↑ | 24.7 |

| Crack Number | Date of Recording | Start | | End | | Length of Crack (in.) |
|---|---|---|---|---|---|---|
| | | X | Y | X | Y | |
| | | (Offset from Centerline) (in.) | (Offset from Station) (in.) | (Offset from Centerline) (in.) | (Offset from Station) (in.) | |
| 182 | 5-May-22 | 152 | 74 from 1+20↑ | 150 | 100.5 from 1+20↑ | 26.6 |
| 183 | 5-May-22 | 134 | 61.5 from 1+35↓ | 165 | 60 from 1+35↓ | 31.0 |
| 184 | 5-May-22 | 139.5 | 56 from 1+35↓ | 144 | 65 from 1+35↓ | 10.1 |
| 185 | 5-May-22 | 125 | 6 from 1+35↓ | 145 | 0 from 1+35↓ | 20.9 |
| 186 | 5-May-22 | 145 | 0 from 1+35↓ | 176 | 7 from 1+35↓ | 31.8 |
| 187 | 5-May-22 | 227 | 27 from 1+35↓ | 228 | 86 from 1+35↑ | 59.0 |
| 188 | 5-May-22 | 188 | 10 from 1+35↓ | 187 | 18 from 1+35↓ | 8.1 |
| 189 | 5-May-22 | 184 | 5 from 1+35↓ | 196 | 5 from 1+35↓ | 12.0 |
| 190 | 5-May-22 | 196 | 5 from 1+35↓ | 197 | 1 from 1+35↑ | 4.1 |
| 191 | 5-May-22 | 131 | 65.5 from 1+35↑ | 133.5 | 59 from 1+35↑ | 7.0 |
| 192 | 5-May-22 | 175 | 20 from 1+50↑ | 167 | 52 from 1+50↑ | 33.0 |
| 193 | 5-May-22 | 220 | 21.5 from 1+50↑ | 217 | 55 from 1+50↑ | 33.6 |
| 194 | 5-May-22 | 135 | 37 from 1+50↑ | 133 | 31 from 1+50↑ | 6.3 |
| 195 | 5-May-22 | 136 | 65.5 from 1+50↑ | 134 | 76 from 1+50↑ | 10.7 |
| 60 | 5-May-22 | 148 | 0 from 1+65↓ | 150 | 10.5 from 1+65↓ | 10.7 |
| 196 | 5-May-22 | 171 | 8.5 from 1+65↓ | 177 | 13.5 from 1+65↓ | 7.8 |
| 197 | 5-May-22 | 188 | 13 from 1+65↓ | 189 | 0 from 1+65↓ | 13.0 |
| 198 | 5-May-22 | 189 | 14 from 1+65↓ | 189 | 19 from 1+65↓ | 5.0 |
| 220 | 27-May-22 | 178 | 1 from 1+20↑ | 176 | 7 from 1+20↑ | 6.3 |
| 221 | 27-May-22 | 176 | 7 from 1+20↑ | 179 | 10.5 from 1+20↑ | 4.6 |
| 222 | 27-May-22 | 176 | 7 from 1+20↑ | 170 | 2.5 from 1+20↑ | 7.5 |
| 223 | 27-May-22 | 179 | 10.5 from 1+20↑ | 177 | 17 from 1+20↑ | 6.8 |
| 224 | 27-May-22 | 179 | 10.5 from 1+20↑ | 195 | 9.5 from 1+20↑ | 16.0 |
| 225 | 27-May-22 | 187 | 15 from 1+20↑ | 182 | 32.5 from 1+20↑ | 18.2 |
| 226 | 27-May-22 | 185 | 34.5 from 1+20↑ | 185 | 42 from 1+20↑ | 7.5 |
| 227 | 27-May-22 | 178 | 55 from 1+20↑ | 176.5 | 60 from 1+20↑ | 5.2 |
| 228 | 27-May-22 | 159 | 94.5 from 1+20↑ | 157 | 119 from 1+20↑ | 24.6 |
| 229 | 27-May-22 | 175 | 115.5 from 1+20↑ | 158 | 114.5 from 1+20↑ | 17.0 |
| 230 | 1-Jun-22 | 184.5 | 90.5 from 1+20↑ | 165 | 95 from 1+20↑ | 20.0 |
| 231 | 1-Jun-22 | 165 | 97 from 1+20↑ | 165 | 95 from 1+20↑ | 2.0 |
| 232 | 1-Jun-22 | 159 | 93 from 1+20↑ | 165 | 95 from 1+20↑ | 6.3 |
| 233 | 1-Jun-22 | 156.5 | 78.5 from 1+20↑ | 169.5 | 78 from 1+20↑ | 13.0 |
| 234 | 1-Jun-22 | 174 | 67 from 1+20↑ | 164.5 | 88.5 from 1+20↑ | 23.5 |
| 235 | 1-Jun-22 | 176 | 111 from 1+20↑ | 176.5 | 120.5 from 1+20↑ | 9.5 |
| 236 | 1-Jun-22 | 207.5 | 87 from 1+20↑ | 215 | 87 from 1+20↑ | 7.5 |
| 237 | 1-Jun-22 | 214.5 | 37 from 1+20↑ | 212.5 | 36.5 from 1+20↑ | 2.1 |
| 238 | 1-Jun-22 | 119 | 5 from 1+35↓ | 125 | 5.5 from 1+35↓ | 6.0 |
| 239 | 1-Jun-22 | 197 | 35 from 1+35↓ | 206 | 6 from 1+35↓ | 30.4 |
| 240 | 1-Jun-22 | 227 | 0 from 1+35↑ | 226 | 12 from 1+35↑ | 12.0 |
| 241 | 1-Jun-22 | 226 | 4.5 from 1+35↑ | 204 | 0 from 1+35↑ | 22.5 |
| 242 | 1-Jun-22 | 109 | 17 from 1+50↓ | 110.5 | 27 from 1+50↓ | 10.1 |
| 243 | 1-Jun-22 | 132.5 | 9.5 from 1+50↓ | 127 | 18.5 from 1+50↓ | 10.5 |
| 99 | 1-Jun-22 | 132 | 49 from 1+50↓ | 127 | 18.5 from 1+50↓ | 30.9 |
| 244 | 1-Jun-22 | 132.5 | 9.5 from 1+50↓ | 130.5 | 0 from 1+50↓ | 9.7 |
| 56 | 1-Jun-22 | 132.5 | 9.5 from 1+50↓ | 135 | 10.5 from 1+50↓ | 2.7 |
| 245 | 1-Jun-22 | 213 | 29.5 from 1+50↓ | 216 | 39 from 1+50↓ | 10.0 |
| 12 | 1-Jun-22 | 249 | 0 from 1+50↑ | 248 | 53 from 1+50↑ | 53.0 |
| 246 | 1-Jun-22 | 231 | 43.5 from 1+50↑ | 236 | 51 from 1+50↑ | 9.0 |
| 247 | 1-Jun-22 | 169.5 | 27 from 1+50↑ | 167.5 | 24 from 1+50↑ | 3.6 |

| Crack Number | Date of Recording | Start | | End | | Length of Crack (in.) |
|---|---|---|---|---|---|---|
| | | X (Offset from Centerline) (in.) | Y (Offset from Station) (in.) | X (Offset from Centerline) (in.) | Y (Offset from Station) (in.) | |
| 248 | 1-Jun-22 | 148.5 | 23.5 from 1+50↑ | 167.5 | 24 from 1+50↑ | 19.0 |
| 249 | 1-Jun-22 | 150 | 23 from 1+50↑ | 147 | 30 from 1+50↑ | 7.6 |
| 250 | 1-Jun-22 | 146 | 37 from 1+50↑ | 148.5 | 44.5 from 1+50↑ | 7.9 |
| 251 | 1-Jun-22 | 165 | 51 from 1+65↓ | 161 | 53 from 1+65↓ | 4.5 |
| 252 | 1-Jun-22 | 161 | 59 from 1+65↓ | 189 | 60 from 1+65↓ | 28.0 |
| 253 | 1-Jun-22 | 131.5 | 25 from 1+65↓ | 134.5 | 32 from 1+65↓ | 7.6 |
| 254 | 1-Jun-22 | 135 | 52 from 1+65↓ | 135 | 55 from 1+65↓ | 3.0 |
| 255 | 1-Jun-22 | 157 | 42 from 1+65↓ | 166 | 45 from 1+65↓ | 9.5 |
| 256 | 1-Jun-22 | 167.5 | 47 from 1+65↓ | 186.5 | 51 from 1+65↓ | 19.4 |
| 257 | 1-Jun-22 | 160 | 5 from 1+65↓ | 160 | 8 from 1+65↓ | 3.0 |
| 258 | 1-Jun-22 | 161 | 10.5 from 1+65↓ | 162 | 8.5 from 1+65↓ | 2.2 |
| 259 | 1-Jun-22 | 170.5 | 9 from 1+65↓ | 162 | 8.5 from 1+65↓ | 8.5 |
| 196 | 1-Jun-22 | 176 | 16 from 1+65↓ | 177.5 | 13.5 from 1+65↓ | 2.9 |
| 260 | 1-Jun-22 | 188 | 12 from 1+65↓ | 177.5 | 13.5 from 1+65↓ | 10.6 |
| 340 | 15-Jun-22 | 215 | 17.5 from 1+20↑ | 214 | 32 from 1+20↑ | 14.5 |
| 341 | 15-Jun-22 | 198.5 | 75.5 from 1+20↑ | 197.5 | 91.5 from 1+20↑ | 16.0 |
| 342 | 15-Jun-22 | 185.5 | 76 from 1+20↑ | 172.5 | 78 from 1+20↑ | 13.2 |
| 343 | 15-Jun-22 | 186.5 | 108.5 from 1+20↑ | 187.5 | 113 from 1+20↑ | 4.6 |
| 344 | 15-Jun-22 | 173 | 104.5 from 1+20↑ | 161.5 | 105 from 1+20↑ | 11.5 |
| 345 | 15-Jun-22 | 108 | 0 from 1+20↑ | 108.5 | 0 from 1+35↓ | 180.0 |
| 346 | 15-Jun-22 | 178 | 23 from 1+20↑ | 180.5 | 23.5 from 1+20↑ | 2.5 |
| 347 | 15-Jun-22 | 194.5 | 9.5 from 1+20↑ | 197 | 9 from 1+20↑ | 2.5 |
| 348 | 15-Jun-22 | 227 | 87 from 1+35↓ | 226.5 | 84 from 1+35↓ | 3.0 |
| 349 | 15-Jun-22 | 228 | 26 from 1+35↓ | 228.5 | 27.5 from 1+35↓ | 1.6 |
| 350 | 15-Jun-22 | 190.5 | 62 from 1+35↓ | 176.5 | 62.5 from 1+35↓ | 14.0 |
| 351 | 15-Jun-22 | 164.5 | 23.5 from 1+35↓ | 157.5 | 21 from 1+35↓ | 7.4 |
| 352 | 15-Jun-22 | 131.5 | 37 from 1+35↑ | 131.5 | 41 from 1+35↑ | 4.0 |
| 345 | 15-Jun-22 | 108.5 | 0 from 1+35↑ | 109.5 | 0 from 1+50↓ | 180.0 |
| 353 | 15-Jun-22 | 225 | 5 from 1+35↑ | 196.5 | 0 from 1+35↑ | 28.9 |
| 354 | 15-Jun-22 | 195.5 | 3.5 from 1+35↑ | 195.5 | 0 from 1+35↑ | 3.5 |
| 356 | 15-Jun-22 | 135.5 | 48 from 1+50↓ | 133 | 44.5 from 1+50↓ | 4.3 |
| 357 | 15-Jun-22 | 183 | 26 from 1+50↓ | 186 | 20.5 from 1+50↓ | 6.3 |
| 358 | 15-Jun-22 | 185.5 | 20 from 1+50↓ | 193 | 22.5 from 1+50↓ | 7.9 |
| 359 | 15-Jun-22 | 155.5 | 5 from 1+50↓ | 165 | 7.5 from 1+50↓ | 9.8 |
| 360 | 15-Jun-22 | 168 | 5.5 from 1+50↓ | 165 | 7.5 from 1+50↓ | 3.6 |
| 361 | 15-Jun-22 | 168.5 | 20 from 1+50↓ | 165 | 7.5 from 1+50↓ | 13.0 |
| 362 | 15-Jun-22 | 168.5 | 20 from 1+50↓ | 166.5 | 22.5 from 1+50↓ | 3.2 |
| 363 | 15-Jun-22 | 135 | 66 from 1+50↓ | 132.5 | 52 from 1+50↓ | 14.2 |
| 364 | 15-Jun-22 | 222 | 59 from 1+50↓ | 219.5 | 64 from 1+50↓ | 5.6 |
| 365 | 15-Jun-22 | 222 | 59 from 1+50↓ | 218.5 | 68.5 from 1+50↓ | 10.1 |
| 366 | 15-Jun-22 | 213 | 13 from 1+50↓ | 212.5 | 8 from 1+50↓ | 5.0 |
| 367 | 15-Jun-22 | 217 | 4 from 1+50↓ | 212.5 | 8 from 1+50↓ | 6.0 |
| 368 | 15-Jun-22 | 217.5 | 21.5 from 1+50↑ | 222 | 20 from 1+50↑ | 4.7 |
| 369 | 15-Jun-22 | 234.5 | 51 from 1+50↑ | 236 | 60 from 1+50↑ | 9.1 |
| 370 | 15-Jun-22 | 195.5 | 60 from 1+50↑ | 190 | 62 from 1+50↑ | 5.9 |
| 371 | 15-Jun-22 | 183 | 30 from 1+50↑ | 172 | 27 from 1+50↑ | 11.4 |
| 372 | 15-Jun-22 | 166.5 | 45 from 1+50↑ | 175 | 45.5 from 1+50↑ | 8.5 |
| 373 | 15-Jun-22 | 176.5 | 50 from 1+50↑ | 175 | 45.5 from 1+50↑ | 4.7 |
| 374 | 15-Jun-22 | 187 | 84 from 1+50↑ | 169 | 83 from 1+50↑ | 18.0 |

|  |  | Start |  | End |  |  |
|---|---|---|---|---|---|---|
|  |  | X | Y | X | Y |  |
| Crack Number | Date of Recording | (Offset from Centerline) (in.) | (Offset from Station) (in.) | (Offset from Centerline) (in.) | (Offset from Station) (in.) | Length of Crack (in.) |
| 375 | 15-Jun-22 | 169 | 72 from 1+50↑ | 168 | 73 from 1+50↑ | 1.4 |
| 376 | 15-Jun-22 | 154 | 71 from 1+50↑ | 168 | 73 from 1+50↑ | 14.1 |
| 377 | 15-Jun-22 | 162 | 73.5 from 1+50↑ | 162 | 79 from 1+50↑ | 5.5 |
| 378 | 15-Jun-22 | 161.5 | 58.5 from 1+50↑ | 164.5 | 59 from 1+50↑ | 3.0 |
| 379 | 15-Jun-22 | 177 | 98.5 from 1+50↑ | 173.5 | 105.5 from 1+50↑ | 7.8 |
| 380 | 15-Jun-22 | 171.5 | 102 from 1+50↑ | 161 | 99.5 from 1+50↑ | 10.8 |
| 381 | 15-Jun-22 | 134 | 63 from 1+65↓ | 134 | 73 from 1+65↓ | 10.0 |
| 382 | 15-Jun-22 | 108.5 | 0 from 1+50↑ | 107.5 | 0 from 1+65↓ | 180.0 |
| 383 | 15-Jun-22 | 132 | 25.5 from 1+65↓ | 136 | 33.5 from 1+65↓ | 8.9 |
| 384 | 15-Jun-22 | 165.5 | 48.5 from 1+65↓ | 168.5 | 48.5 from 1+65↓ | 3.0 |
| 385 | 15-Jun-22 | 215.5 | 55 from 1+65↓ | 214.5 | 72.5 from 1+65↓ | 17.5 |
| 386 | 15-Jun-22 | 189 | 27 from 1+65↓ | 178 | 28 from 1+65↓ | 11.0 |
| 387 | 15-Jun-22 | 177.5 | 29.5 from 1+65↓ | 178 | 27 from 1+65↓ | 2.5 |
| 388 | 15-Jun-22 | 190 | 13.5 from 1+65↓ | 188.5 | 13 from 1+65↓ | 1.6 |
| 449 | 1-Jul-22 | 154 | 18.5 from 1+20↑ | 157 | 14 from 1+20↑ | 5.4 |
| 450 | 1-Jul-22 | 166.5 | 13.5 from 1+20↑ | 157 | 14 from 1+20↑ | 9.5 |
| 451 | 1-Jul-22 | 166.5 | 12.5 from 1+20↑ | 173 | 12.5 from 1+20↑ | 6.5 |
| 452 | 1-Jul-22 | 217.5 | 4 from 1+20↑ | 220 | 11 from 1+20↑ | 7.4 |
| 453 | 1-Jul-22 | 219 | 62 from 1+20↑ | 208 | 62 from 1+20↑ | 11.0 |
| 454 | 1-Jul-22 | 199.5 | 71.5 from 1+20↑ | 199.5 | 75.5 from 1+20↑ | 4.0 |
| 455 | 1-Jul-22 | 196.5 | 48 from 1+20↑ | 196 | 47.5 from 1+20↑ | 0.7 |
| 456 | 1-Jul-22 | 196.5 | 47 from 1+20↑ | 195.5 | 47.5 from 1+20↑ | 1.1 |
| 457 | 1-Jul-22 | 199.5 | 9.5 from 1+20↑ | 198 | 9.5 from 1+20↑ | 1.5 |
| 458 | 1-Jul-22 | 186.5 | 34.5 from 1+20↑ | 180 | 34 from 1+20↑ | 6.5 |
| 459 | 1-Jul-22 | 179 | 41 from 1+20↑ | 177.5 | 39.5 from 1+20↑ | 2.1 |
| 460 | 1-Jul-22 | 178 | 38.5 from 1+20↑ | 177.5 | 39.5 from 1+20↑ | 1.1 |
| 461 | 1-Jul-22 | 168.5 | 40 from 1+20↑ | 177.5 | 39.5 from 1+20↑ | 9.0 |
| 462 | 1-Jul-22 | 168.5 | 40 from 1+20↑ | 158.5 | 38.5 from 1+20↑ | 10.1 |
| 463 | 1-Jul-22 | 171.5 | 60.5 from 1+20↑ | 171.5 | 61.5 from 1+20↑ | 1.0 |
| 464 | 1-Jul-22 | 169.5 | 61 from 1+20↑ | 171.5 | 61.5 from 1+20↑ | 2.1 |
| 465 | 1-Jul-22 | 158 | 65 from 1+20↑ | 156.5 | 69.5 from 1+20↑ | 4.7 |
| 466 | 1-Jul-22 | 155 | 69.5 from 1+20↑ | 156.5 | 69.5 from 1+20↑ | 1.5 |
| 467 | 1-Jul-22 | 157.5 | 73 from 1+20↑ | 156.5 | 69.5 from 1+20↑ | 3.6 |
| 468 | 1-Jul-22 | 131 | 96 from 1+20↑ | 131 | 103 from 1+20↑ | 7.0 |
| 469 | 1-Jul-22 | 159 | 62 from 1+35↓ | 153 | 62 from 1+35↓ | 6.0 |
| 470 | 1-Jul-22 | 133 | 10 from 1+35↓ | 133 | 17 from 1+35↓ | 7.0 |
| 471 | 1-Jul-22 | 132 | 16 from 1+35↓ | 132 | 18.5 from 1+35↓ | 2.5 |
| 185 | 1-Jul-22 | 143 | 2 from 1+35↓ | 145 | 0 from 1+35↓ | 2.8 |
| 186 | 1-Jul-22 | 148 | 2 from 1+35↓ | 145 | 0 from 1+35↓ | 3.6 |
| 472 | 1-Jul-22 | 176 | 6 from 1+35↓ | 183.5 | 4.5 from 1+35↓ | 7.6 |
| 473 | 1-Jul-22 | 214 | 80 from 1+35↓ | 218.5 | 69.5 from 1+35↓ | 11.4 |
| 474 | 1-Jul-22 | 108 | 47 from 1+20↑ | 108 | 59 from 1+20↑ | 12.0 |
| 475 | 1-Jul-22 | 176.5 | 41 from 1+35↓ | 180 | 42 from 1+35↓ | 3.6 |
| 476 | 1-Jul-22 | 176.5 | 41 from 1+35↓ | 177 | 37 from 1+35↓ | 4.0 |
| 477 | 1-Jul-22 | 176.5 | 41 from 1+35↓ | 167 | 42.5 from 1+35↓ | 9.6 |
| 478 | 1-Jul-22 | 166 | 40.5 from 1+35↓ | 167 | 42.5 from 1+35↓ | 2.2 |
| 479 | 1-Jul-22 | 163 | 46 from 1+35↓ | 167 | 42.5 from 1+35↓ | 5.3 |
| 480 | 6-Jul-22 | 217 | 32.5 from 1+35↑ | 217 | 38.5 from 1+35↑ | 6.0 |
| 481 | 6-Jul-22 | 220.5 | 101 from 1+35↑ | 219 | 109 from 1+35↑ | 8.1 |

| | | Start | | End | | |
|---|---|---|---|---|---|---|
| | | X | Y | X | Y | |
| Crack Number | Date of Recording | (Offset from Centerline) (in.) | (Offset from Station) (in.) | (Offset from Centerline) (in.) | (Offset from Station) (in.) | Length of Crack (in.) |
| 482 | 6-Jul-22 | 216.5 | 82.5 from 1+35↑ | 215 | 88.5 from 1+35↑ | 6.2 |
| 483 | 6-Jul-22 | 188 | 86 from 1+35↑ | 185 | 87.5 from 1+35↑ | 3.4 |
| 484 | 6-Jul-22 | 174.5 | 86.5 from 1+35↑ | 185 | 87.5 from 1+35↑ | 10.5 |
| 485 | 6-Jul-22 | 174.5 | 86.5 from 1+35↑ | 172.5 | 88 from 1+35↑ | 2.5 |
| 486 | 6-Jul-22 | 174.5 | 90 from 1+35↑ | 172.5 | 88 from 1+35↑ | 2.8 |
| 487 | 6-Jul-22 | 168.5 | 88.5 from 1+35↑ | 172.5 | 88 from 1+35↑ | 4.0 |
| 488 | 6-Jul-22 | 132 | 56 from 1+35↑ | 132 | 59 from 1+35↑ | 3.0 |
| 489 | 6-Jul-22 | 131.5 | 60.5 from 1+35↑ | 130 | 66 from 1+35↑ | 5.7 |
| 490 | 6-Jul-22 | 168 | 19 from 1+50↓ | 174.5 | 19 from 1+50↓ | 6.5 |
| 491 | 6-Jul-22 | 174.5 | 18 from 1+50↓ | 174.5 | 19 from 1+50↓ | 1.0 |
| 492 | 6-Jul-22 | 175.5 | 20 from 1+50↓ | 174.5 | 19 from 1+50↓ | 1.4 |
| 493 | 6-Jul-22 | 175.5 | 20 from 1+50↓ | 179 | 19 from 1+50↓ | 3.6 |
| 494 | 6-Jul-22 | 197.5 | 22.5 from 1+50↓ | 196.5 | 21.5 from 1+50↓ | 1.4 |
| 495 | 6-Jul-22 | 184 | 37.5 from 1+50↓ | 183.5 | 45 from 1+50↓ | 7.5 |
| 496 | 6-Jul-22 | 184 | 37.5 from 1+50↓ | 185.5 | 36 from 1+50↓ | 2.1 |
| 497 | 6-Jul-22 | 184 | 37.5 from 1+50↓ | 182.5 | 36.5 from 1+50↓ | 1.8 |
| 498 | 6-Jul-22 | 176 | 40 from 1+50↓ | 182.5 | 36.5 from 1+50↓ | 7.4 |
| 499 | 6-Jul-22 | 176 | 40 from 1+50↓ | 175 | 42.5 from 1+50↓ | 2.7 |
| 500 | 6-Jul-22 | 176 | 40 from 1+50↓ | 172 | 38 from 1+50↓ | 4.5 |
| 501 | 6-Jul-22 | 136 | 63 from 1+50↑ | 136 | 65 from 1+50↑ | 2.0 |
| 502 | 6-Jul-22 | 131.5 | 78.5 from 1+50↑ | 132.5 | 75 from 1+50↑ | 3.6 |
| 503 | 6-Jul-22 | 178.5 | 17.5 from 1+50↑ | 171 | 20 from 1+50↑ | 7.9 |
| 504 | 6-Jul-22 | 185 | 8 from 1+50↑ | 173 | 8 from 1+50↑ | 12.0 |
| 505 | 6-Jul-22 | 172 | 7.5 from 1+50↑ | 173 | 8 from 1+50↑ | 1.1 |
| 506 | 6-Jul-22 | 171.5 | 9 from 1+50↑ | 173 | 8 from 1+50↑ | 1.8 |
| 507 | 6-Jul-22 | 164.5 | 77.5 from 1+50↑ | 164.5 | 79 from 1+50↑ | 1.5 |
| 508 | 6-Jul-22 | 153.5 | 72 from 1+50↑ | 156 | 71 from 1+50↑ | 2.7 |
| 509 | 6-Jul-22 | 215.5 | 54.5 from 1+65↓ | 216 | 52.5 from 1+65↓ | 2.1 |
| 510 | 6-Jul-22 | 188.5 | 49 from 1+65↓ | 185.5 | 50.5 from 1+65↓ | 3.4 |
| 511 | 6-Jul-22 | 189 | 2 from 1+65↓ | 176 | 0 from 1+65↓ | 13.2 |

Table C-3. Log of Cracks Observed for Control Test Item (LFC-4S)

| Crack Number | Date of Recording | Start | | End | | Length of Crack (in.) |
|---|---|---|---|---|---|---|
| | | X (Offset from Centerline) (in.) | Y (Offset from Station) (in.) | X (Offset from Centerline) (in.) | Y (Offset from Station) (in.) | |
| 3 | 22-Apr-22 | 141 | 0 from 1+80↑ | 141 | 7 from 1+80↑ | 7.0 |
| 4 | 22-Apr-22 | 216 | 0 from 1+80↑ | 17.5 | 104 from 1+80↑ | 224.1 |
| 5 | 22-Apr-22 | 226.5 | 0 from 1+80↑ | 234.5 | 61 from 1+80↑ | 61.5 |
| 6 | 22-Apr-22 | 248 | 0 from 1+80↑ | 250.5 | 129.5 from 1+80↑ | 129.5 |
| 7 | 22-Apr-22 | 110 | 71.5 from 1+95↓ | 112 | 69from 1+95↓ | 3.2 |
| 8 | 22-Apr-22 | 112 | 68 from 1+95↓ | 109 | 30 from 1+95↓ | 38.1 |
| 9 | 22-Apr-22 | 108 | 24 from 1+95↓ | 108 | 29.5 from 1+95↓ | 5.5 |
| 10 | 22-Apr-22 | 188.5 | 30 from 1+95↓ | 188.5 | 47 from 1+95↓ | 17.0 |
| 11 | 22-Apr-22 | 187.5 | 30 from 1+95↓ | 188.5 | 15 from 1+95↓ | 15.0 |
| 12 | 22-Apr-22 | 188 | 14 from 1+95↓ | 188.5 | 5 from 1+95↓ | 9.0 |
| 13 | 22-Apr-22 | 217 | 75 from 1+95↓ | 218 | 46 from 1+95↓ | 29.0 |
| 14 | 22-Apr-22 | 219 | 45 from 1+95↓ | 216 | 32.5 from 1+95↓ | 12.9 |
| 15 | 22-Apr-22 | 217 | 32 from 1+95↓ | 218 | 28 from 1+95↓ | 4.1 |
| 16 | 22-Apr-22 | 218.5 | 21.75 from 1+95↓ | 217 | 3.5 from 1+95↑ | 25.3 |
| 17 | 22-Apr-22 | 217.5 | 58.5 from 1+95↑ | 217.5 | 49 from 1+95↑ | 9.5 |
| 18 | 22-Apr-22 | 224.5 | 80 from 1+95↓ | 226 | 34.75 from 1+95↓ | 45.3 |
| 19 | 22-Apr-22 | 227 | 78.5 from 1+95↓ | 227.5 | 65 from 1+95↓ | 13.5 |
| 20 | 22-Apr-22 | 228.5 | 27.5 from 1+95↓ | 227.5 | 160.5 from 1+95↓ | 133.0 |
| 21 | 22-Apr-22 | 249.5 | 49 from 1+95↓ | 252 | 49 from 1+95↑ | 98.0 |
| 22 | 22-Apr-22 | 228.5 | 23.5 from 1+95↑ | 229.5 | 34.75 from 1+95↑ | 11.3 |
| 23 | 22-Apr-22 | 245.5 | 71 from 2+10↑ | 246 | 65 from 2+10↓ | 136.0 |
| 24 | 22-Apr-22 | 245.5 | 64.5 from 2+10↑ | 251 | 160.5 from 2+10↑ | 96.2 |
| 25 | 22-Apr-22 | 251 | 18.5 from 2+25↓ | 250.25 | 7.5 from 2+25↓ | 11.0 |
| 26 | 22-Apr-22 | 250 | 0 from 2+25↓ | 250 | 6 from 2+25↓ | 6.0 |
| 27 | 22-Apr-22 | 132 | 45 from 2+25↓ | 134 | 32 from 2+25↓ | 13.2 |
| 28 | 22-Apr-22 | 133 | 27 from 2+25↓ | 132.5 | 24 from 2+25↓ | 3.0 |
| 29 | 22-Apr-22 | 132.5 | 23 from 2+25↓ | 133.5 | 20.5 from 2+25↓ | 2.7 |
| 30 | 22-Apr-22 | 133 | 19.5 from 2+25↓ | 133 | 16 from 2+25↓ | 3.5 |
| 31 | 22-Apr-22 | 110 | 13 from 2+25↓ | 109 | 0 from 2+25↓ | 13.0 |
| 36 | 27-Apr-22 | 139 | 31.5 from 1+80↑ | 130 | 56.5 from 1+80↑ | 26.6 |
| 9 | 27-Apr-22 | 109.5 | 24.5 from 1+95↓ | 110 | 4 from 1+95↓ | 20.5 |
| 37 | 27-Apr-22 | 136.5 | 23 from 1+95↓ | 154 | 23.5 from 1+95↓ | 17.5 |
| 38 | 27-Apr-22 | 154 | 23 from 1+95↓ | 153 | 40 from 1+95↓ | 17.0 |
| 39 | 27-Apr-22 | 154 | 23 from 1+95↓ | 164 | 20.5 from 1+95↓ | 10.3 |
| 40 | 27-Apr-22 | 164 | 20.5 from 1+95↓ | 163.5 | 22 from 1+95↓ | 1.6 |
| 41 | 27-Apr-22 | 163.5 | 22 from 1+95↓ | 174 | 20.5 from 1+95↓ | 10.6 |
| 46 | 5-May-22 | 227 | 70 from 1+80↑ | 230 | 77.5 from 1+80↑ | 8.1 |
| 47 | 5-May-22 | 153 | 6.5 from 1+80↑ | 150.5 | 31.5 from 1+80↑ | 25.1 |
| 48 | 5-May-22 | 188.5 | 51.5 from 1+80↑ | 187 | 56 from 1+80↑ | 4.7 |
| 49 | 5-May-22 | 187.5 | 60.5 from 1+80↑ | 187 | 88 from 1+80↑ | 27.5 |
| 50 | 5-May-22 | 109 | 5 from 1+95↓ | 108 | 78 from 1+95↓ | 73.0 |
| 51 | 5-May-22 | 134 | 50 from 2+25↓ | 132 | 15 from 2+25↓ | 35.1 |
| 79 | 15-Jun-22 | 110.5 | 37 from 1+80↑ | 110.5 | 44 from 1+80↑ | 7.0 |
| 80 | 15-Jun-22 | 135.5 | 42.5 from 1+80↑ | 136.5 | 38.5 from 1+80↑ | 4.1 |
| 81 | 15-Jun-22 | 135.5 | 8 from 1+80↑ | 140 | 6 from 1+80↑ | 4.9 |
| 82 | 15-Jun-22 | 136 | 62 from 1+80↑ | 137 | 65.5 from 1+80↑ | 3.6 |

| Crack Number | Date of Recording | Start | | End | | Length of Crack (in.) |
|---|---|---|---|---|---|---|
| | | X (Offset from Centerline) (in.) | Y (Offset from Station) (in.) | X (Offset from Centerline) (in.) | Y (Offset from Station) (in.) | |
| 83 | 15-Jun-22 | 140.5 | 67.5 from 1+80↑ | 137 | 65.5 from 1+80↑ | 4.0 |
| 84 | 15-Jun-22 | 221.5 | 100.5 from 1+80↑ | 214.5 | 100.5 from 1+80↑ | 7.0 |
| 85 | 15-Jun-22 | 192 | 47.5 from 1+95↓ | 189.5 | 47 from 1+95↓ | 2.5 |
| 86 | 15-Jun-22 | 189 | 46 from 1+95↓ | 173 | 45.5 from 1+95↓ | 16.0 |
| 87 | 15-Jun-22 | 163.5 | 40.5 from 1+95↓ | 173 | 45.5 from 1+95↓ | 10.7 |
| 88 | 15-Jun-22 | 162.5 | 38.5 from 1+95↓ | 164.5 | 30.5 from 1+95↓ | 8.2 |
| 89 | 15-Jun-22 | 216.5 | 65.5 from 1+95↑ | 218 | 0 from 1+95↑ | 65.5 |
| 90 | 15-Jun-22 | 108.5 | 78 from 1+95↑ | 106 | 105.5 from 1+95↑ | 27.6 |
| 91 | 15-Jun-22 | 249.5 | 109.5 from 1+95↑ | 249.5 | 106 from 1+95↑ | 3.5 |
| 92 | 15-Jun-22 | 109 | 13 from 2+25↓ | 110 | 16 from 2+25↓ | 3.2 |
| 93 | 15-Jun-22 | 122 | 16 from 2+25↓ | 126 | 15.5 from 2+25↓ | 4.0 |
| 94 | 15-Jun-22 | 133 | 50 from 2+25↓ | 136 | 50.5 from 2+25↓ | 3.0 |
| 95 | 15-Jun-22 | 173 | 12 from 2+25↓ | 176 | 14 from 2+25↓ | 3.6 |
| 96 | 15-Jun-22 | 183.5 | 12 from 2+25↓ | 176 | 14 from 2+25↓ | 7.8 |
| 100 | 1-Jul-22 | 171.5 | 14 from 1+80↑ | 169.5 | 8.5 from 1+80↑ | 5.9 |
| 101 | 1-Jul-22 | 160 | 7.5 from 1+80↑ | 169.5 | 8.5 from 1+80↑ | 9.6 |
| 102 | 1-Jul-22 | 157 | 9.5 from 1+80↑ | 160 | 7.5 from 1+80↑ | 3.6 |
| 103 | 1-Jul-22 | 162.5 | 0 from 1+80↑ | 186 | 2.5 from 1+80↑ | 23.6 |
| 104 | 1-Jul-22 | 168.5 | 17 from 1+80↑ | 171 | 19.5 from 1+80↑ | 3.5 |
| 105 | 1-Jul-22 | 173.5 | 67 from 1+80↑ | 186.5 | 67.5 from 1+80↑ | 13.0 |
| 106 | 1-Jul-22 | 162 | 65 from 1+80↑ | 165 | 63 from 1+80↑ | 3.6 |
| 107 | 1-Jul-22 | 165 | 63 from 1+80↑ | 171.5 | 65 from 1+80↑ | 6.8 |
| 108 | 1-Jul-22 | 110 | 36.5 from 1+80↑ | 109 | 35 from 1+80↑ | 1.8 |
| 109 | 1-Jul-22 | 159.5 | 83 from 1+80↑ | 161 | 87 from 1+80↑ | 4.3 |
| 110 | 1-Jul-22 | 153 | 67 from 1+95↓ | 157 | 68.5 from 1+95↓ | 4.3 |
| 111 | 1-Jul-22 | 196 | 73 from 1+95↓ | 200.5 | 73 from 1+95↓ | 4.5 |
| 112 | 1-Jul-22 | 109 | 56.5 from 1+95↓ | 109 | 46 from 1+95↓ | 10.5 |
| 113 | 1-Jul-22 | 122 | 17.5 from 1+95↓ | 123 | 18 from 1+95↓ | 1.1 |
| 114 | 1-Jul-22 | 164.5 | 27.5 from 1+95↓ | 165 | 31.5 from 1+95↓ | 4.0 |
| 115 | 1-Jul-22 | 163.5 | 38.5 from 1+95↓ | 164.5 | 39.5 from 1+95↓ | 1.4 |
| 116 | 1-Jul-22 | 200.5 | 21 from 1+95↓ | 203 | 21 from 1+95↓ | 2.5 |
| 117 | 1-Jul-22 | 170.5 | 0 from 1+95↓ | 193 | 2 from 1+95↓ | 22.6 |
| 118 | 1-Jul-22 | 170.5 | 0 from 1+95↑ | 166 | 4.5 from 1+95↑ | 6.4 |
| 119 | 1-Jul-22 | 155 | 19 from 1+95↑ | 173.5 | 19.5 from 1+95↑ | 18.5 |
| 120 | 1-Jul-22 | 170.5 | 22.5 from 1+95↑ | 171.5 | 21.5 from 1+95↑ | 1.4 |
| 121 | 1-Jul-22 | 169.5 | 37 from 1+95↑ | 172.5 | 35 from 1+95↑ | 3.6 |
| 122 | 1-Jul-22 | 171.5 | 34 from 1+95↑ | 172.5 | 35 from 1+95↑ | 1.4 |
| 123 | 1-Jul-22 | 172.5 | 35 from 1+95↑ | 179 | 34.5 from 1+95↑ | 6.5 |
| 124 | 1-Jul-22 | 228.5 | 33 from 1+95↑ | 229 | 34.5 from 1+95↑ | 1.6 |
| 125 | 1-Jul-22 | 229.5 | 34.5 from 1+95↑ | 229.5 | 37.5 from 1+95↑ | 3.0 |
| 126 | 1-Jul-22 | 106 | 73.5 from 2+10↓ | 106.5 | 72 from 2+10↓ | 1.6 |
| 127 | 1-Jul-22 | 109 | 16 from 2+25↓ | 109 | 17 from 2+10↓ | 181.0 |
| 128 | 1-Jul-22 | 122 | 15 from 2+25↓ | 123.5 | 16 from 2+25↓ | 1.8 |
| 129 | 1-Jul-22 | 182.5 | 11.5 from 2+25↓ | 185.5 | 11 from 2+25↓ | 3.0 |

# APPENDIX D—VISUAL DISTRESS MAPS

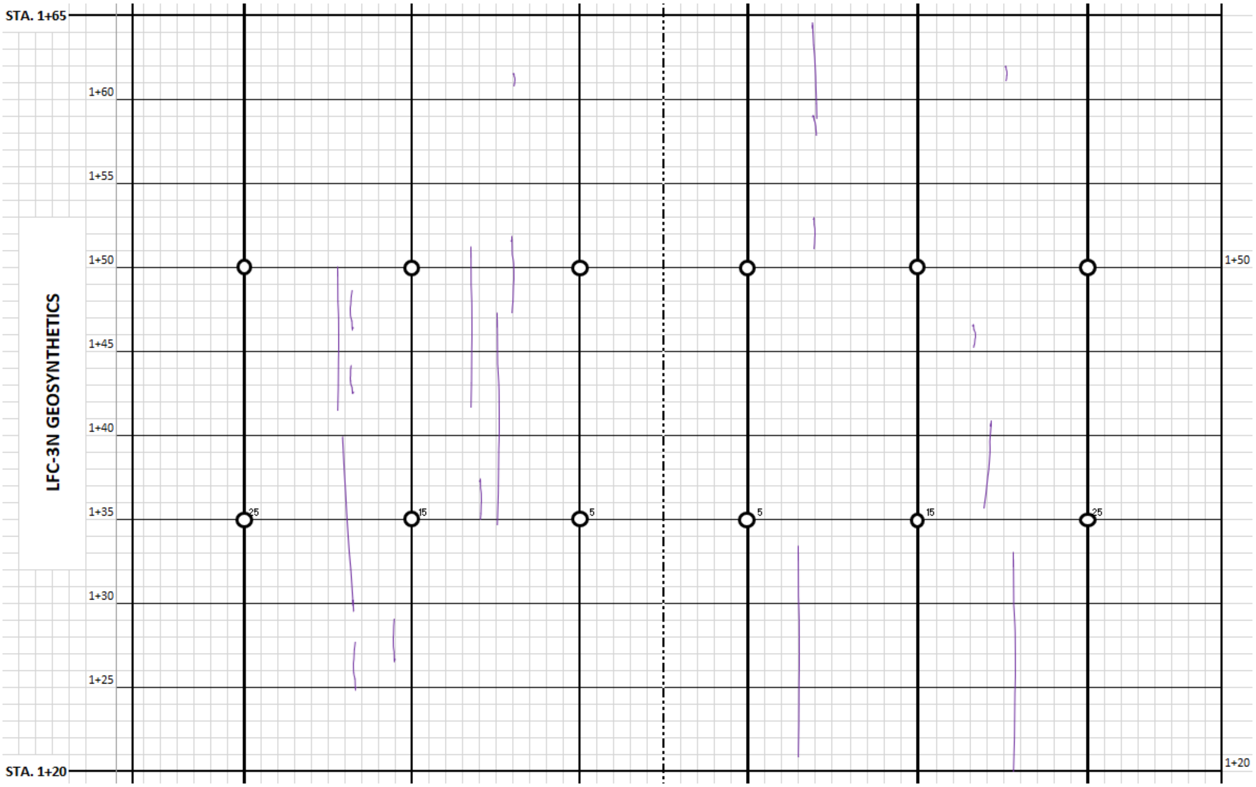

(a)

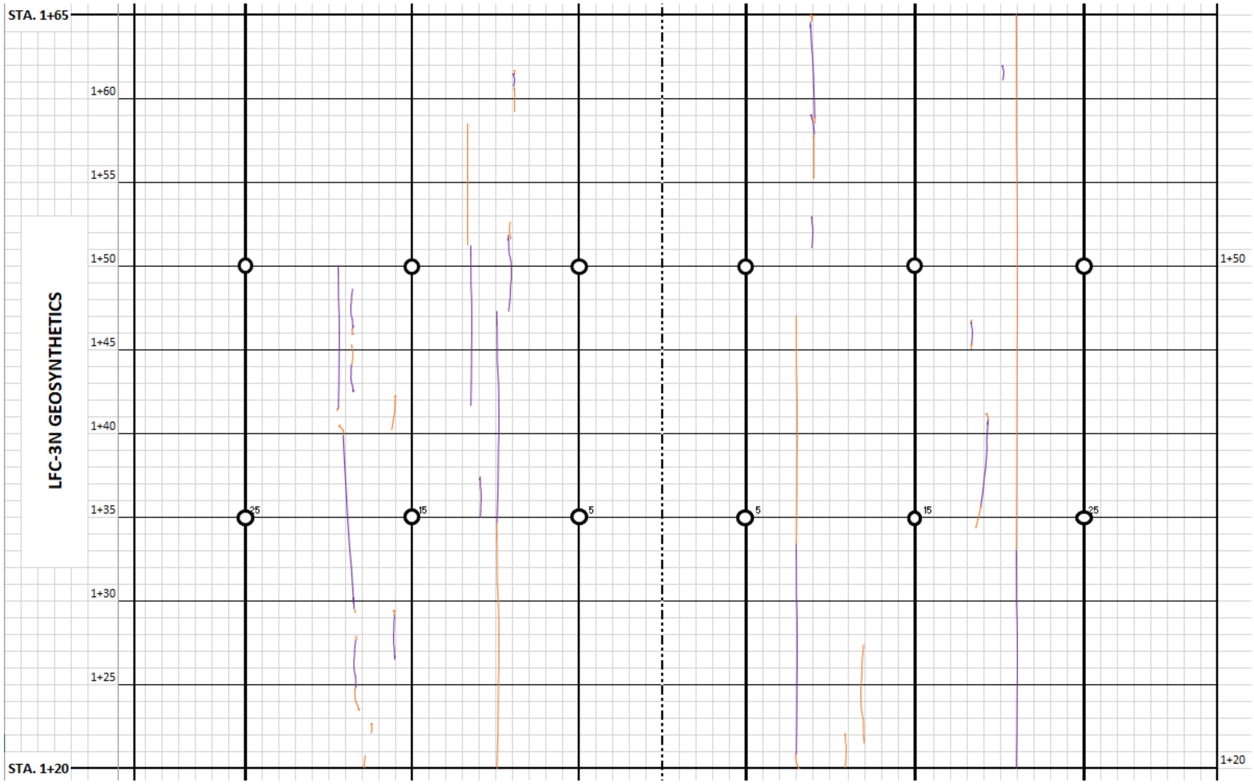
STA. 1+65
1+60
1+55
LFC-3N GEOSYNTHETICS
1+50
1+45
1+40
1+35
25
15
5
5
15
25
1+30
1+25
STA. 1+20
1+50
1+20

(b)

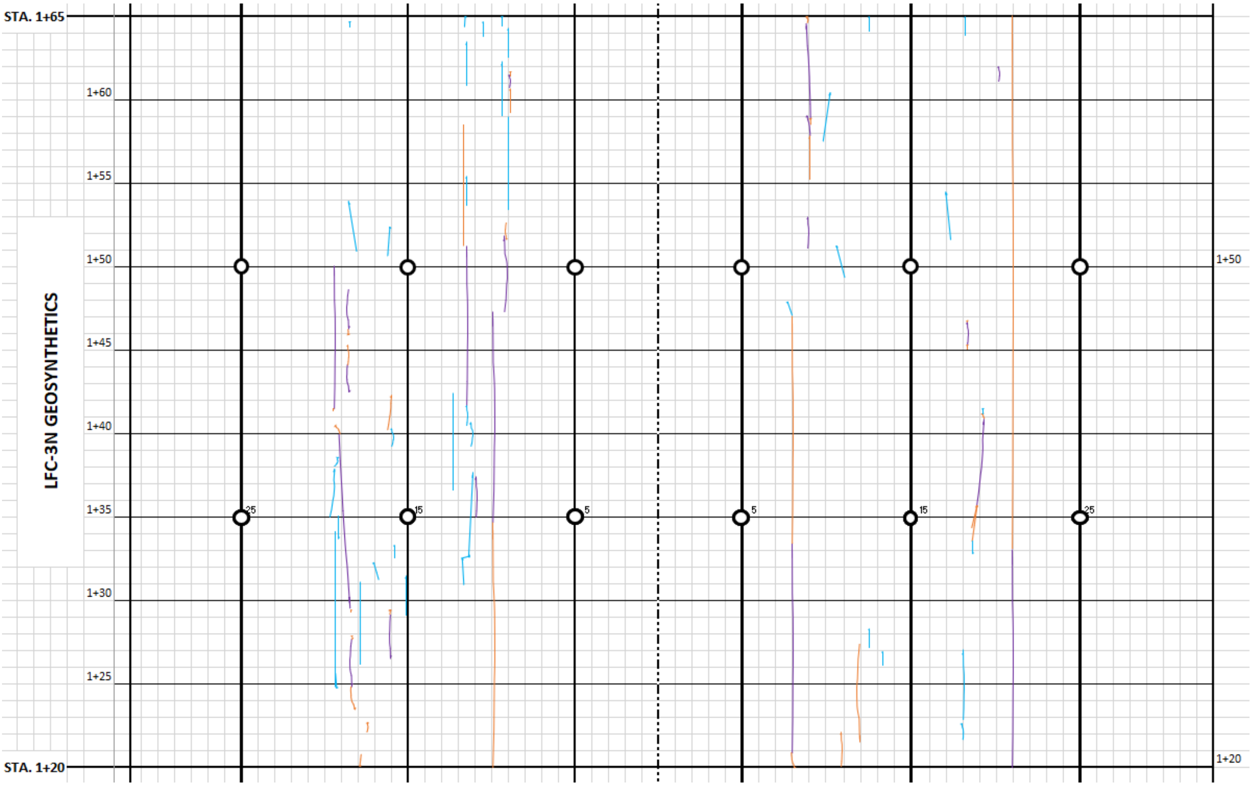
STA. 1+65
1+60
1+55
LFC-3N GEOSYNTHETICS
1+50
1+45
1+40
1+35
25
15
5
5
15
25
1+30
1+25
STA. 1+20
1+50
1+20

(c)

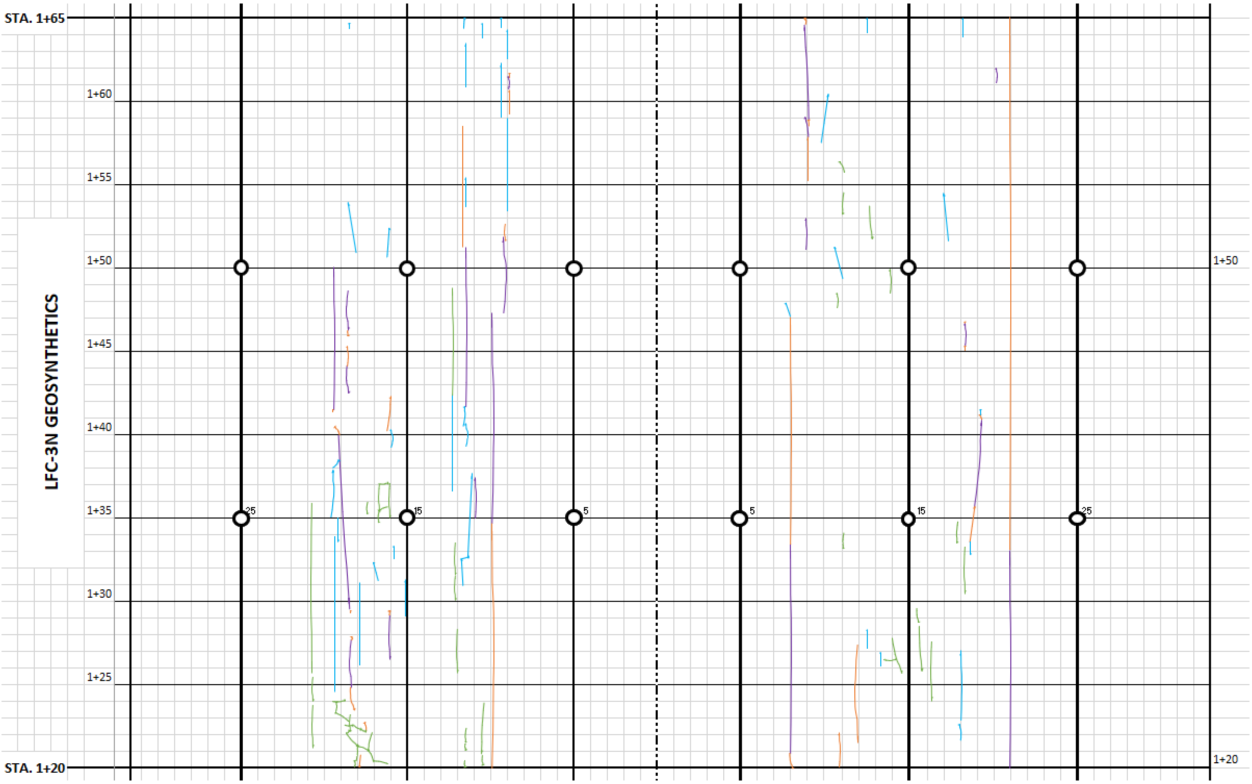
STA. 1+65
1+60
1+55
1+50
1+45
1+40
1+35
1+30
1+25
STA. 1+20
LFC-3N GEOSYNTHETICS
25
15
5
5
15
25
1+50
1+20

(d)

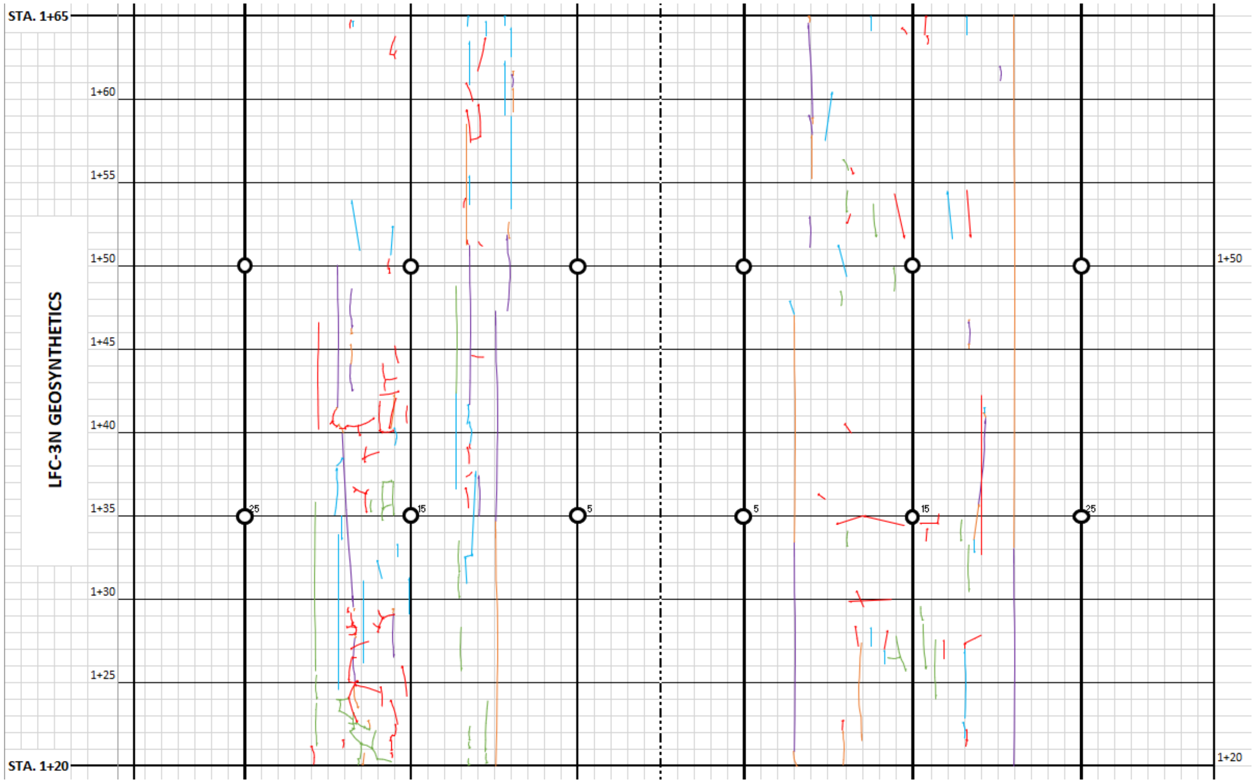
STA. 1+65
1+60
1+55
1+50
1+45
1+40
1+35
1+30
1+25
STA. 1+20
LFC-3N GEOSYNTHETICS
25
15
5
5
15
25
1+50
1+20

(e)

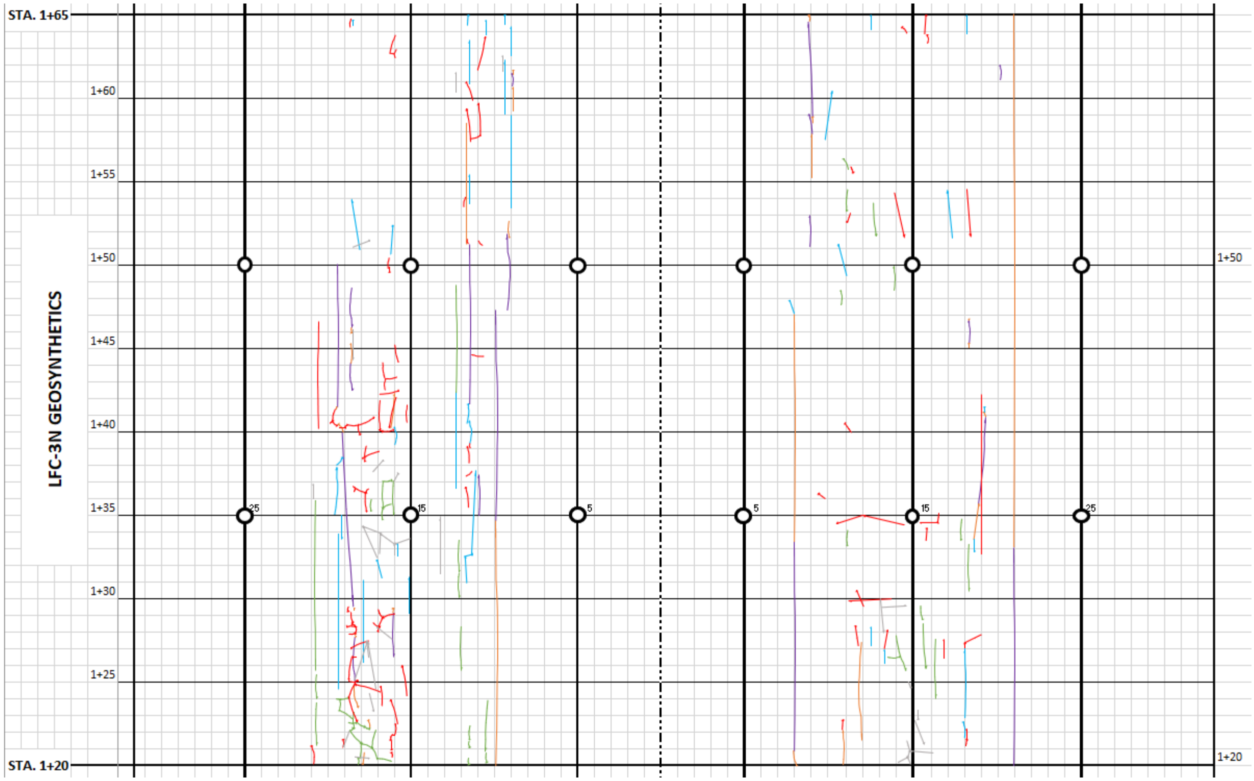
STA. 1+65
1+60
1+55
1+50
1+45
1+40
1+35
1+30
1+25
STA. 1+20
LFC-3N GEOSYNTHETICS
25
15
5
5
15
25
1+50
1+20

(f)

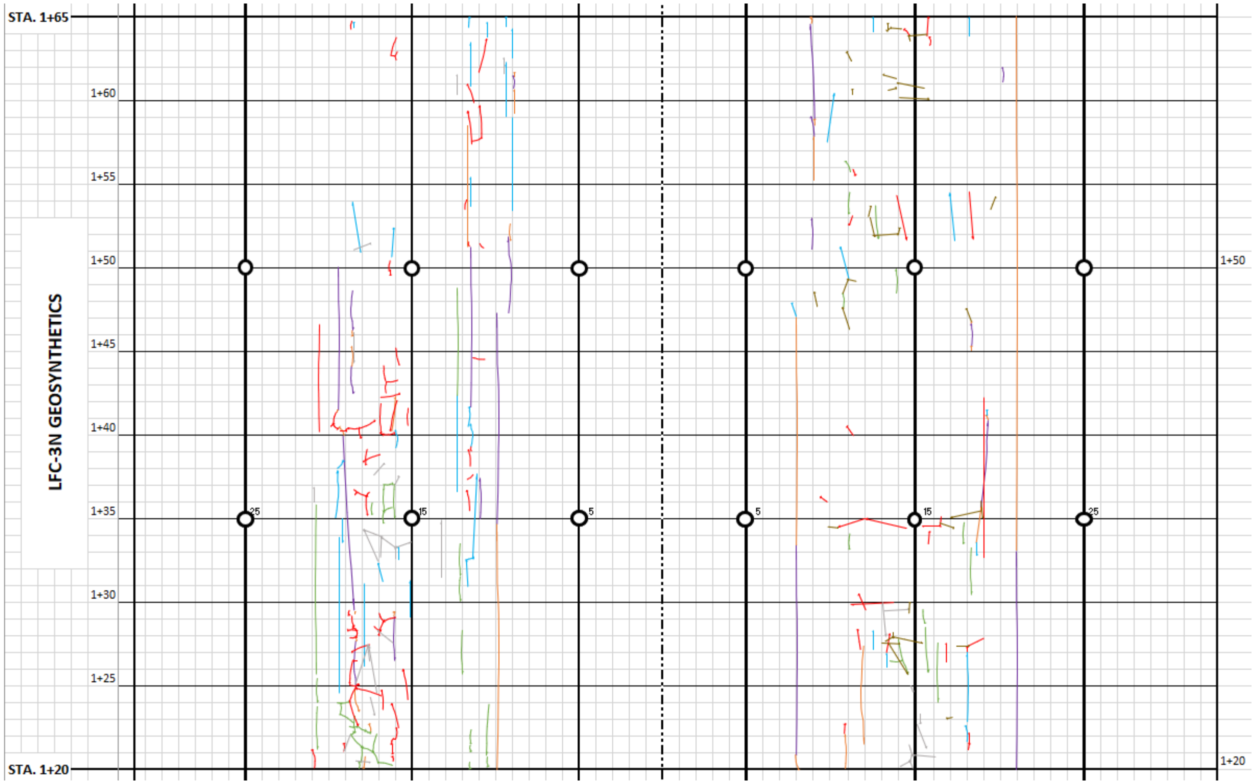
LFC-3N GEOSYNTHETICS
STA. 1+65
1+60
1+55
1+50
1+45
1+40
1+35
1+30
1+25
STA. 1+20
1+50
1+20
25
15
5
5
15
25

(g)

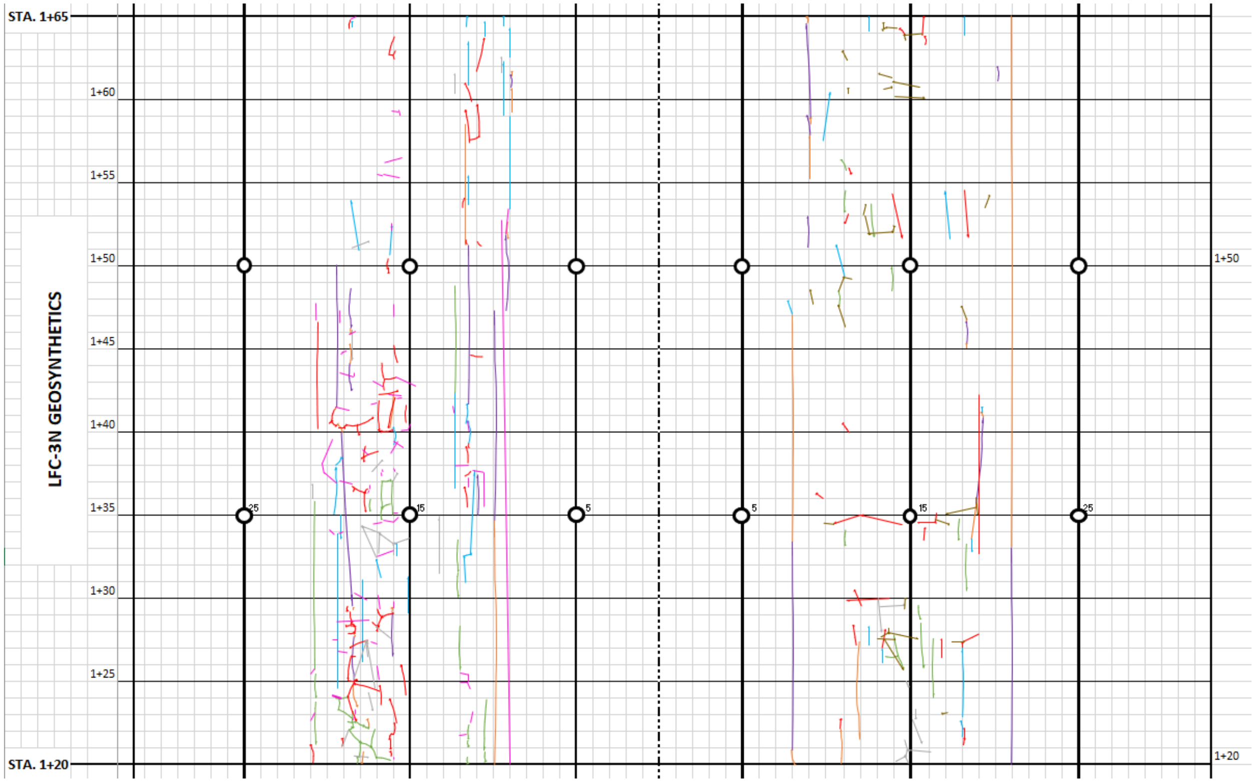
STA. 1+65
1+60
1+55
1+50
1+45
1+40
1+35
1+30
1+25
STA. 1+20
LFC-3N GEOSYNTHETICS
25
15
5
5
15
25
1+50
1+20

(h)

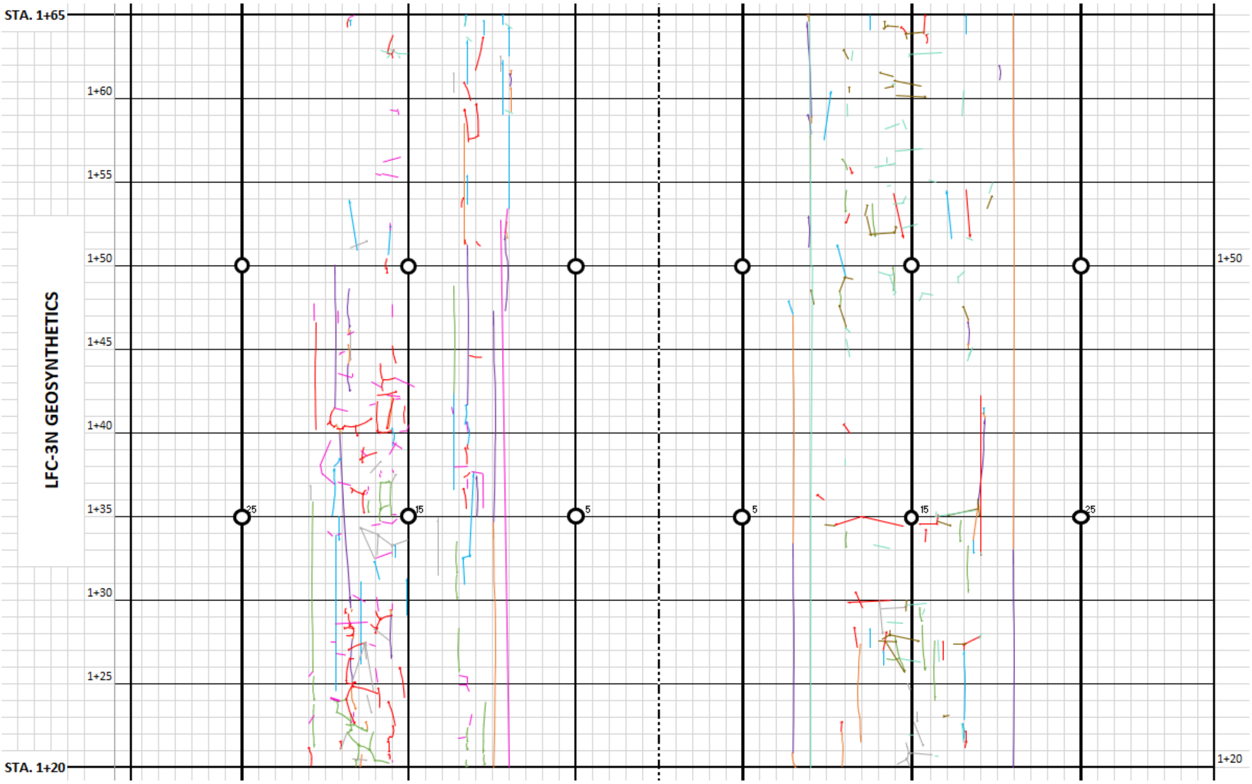
STA. 1+65
1+60
1+55
1+50
1+45
1+40
1+35
1+30
1+25
STA. 1+20
LFC-3N GEOSYNTHETICS
25
15
5
5
15
25
1+50
1+20

(i)

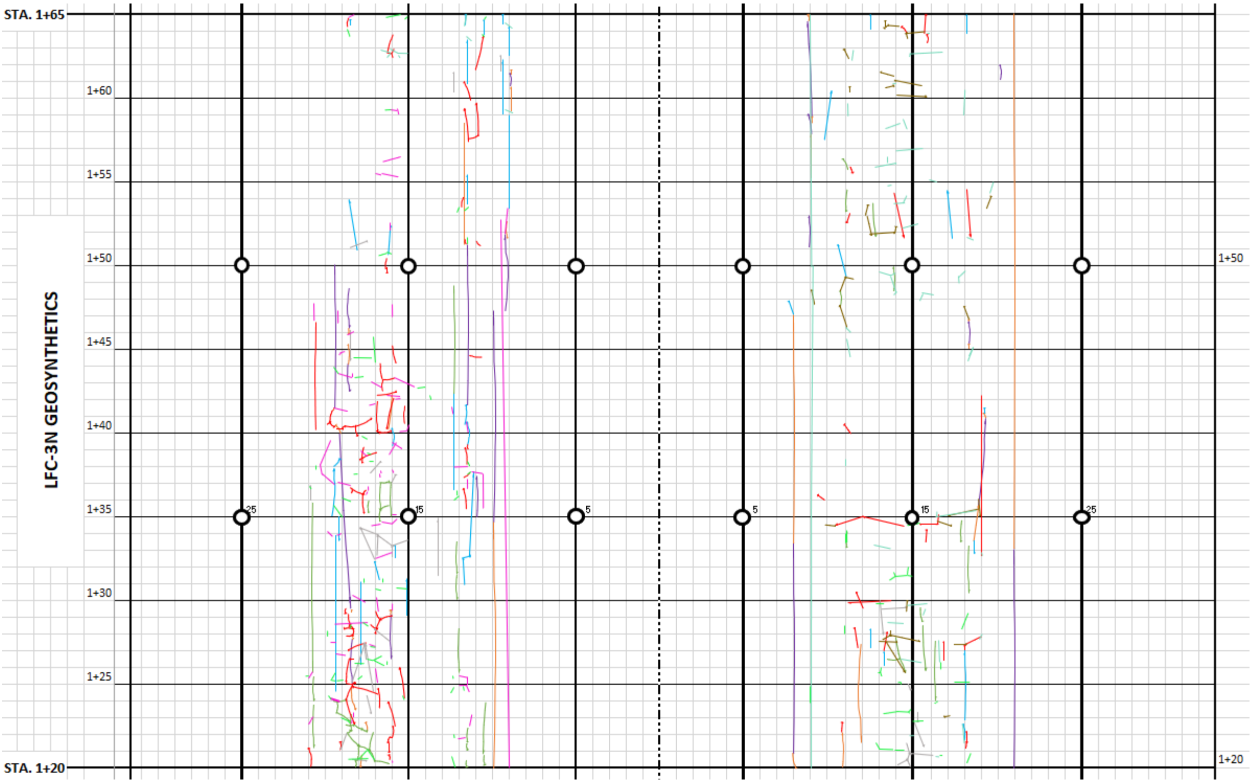
STA. 1+65
1+60
1+55
1+50
1+45
1+40
1+35
1+30
1+25
STA. 1+20
LFC-3N GEOSYNTHETICS
25
15
5
5
15
25
1+50
1+20

(j)

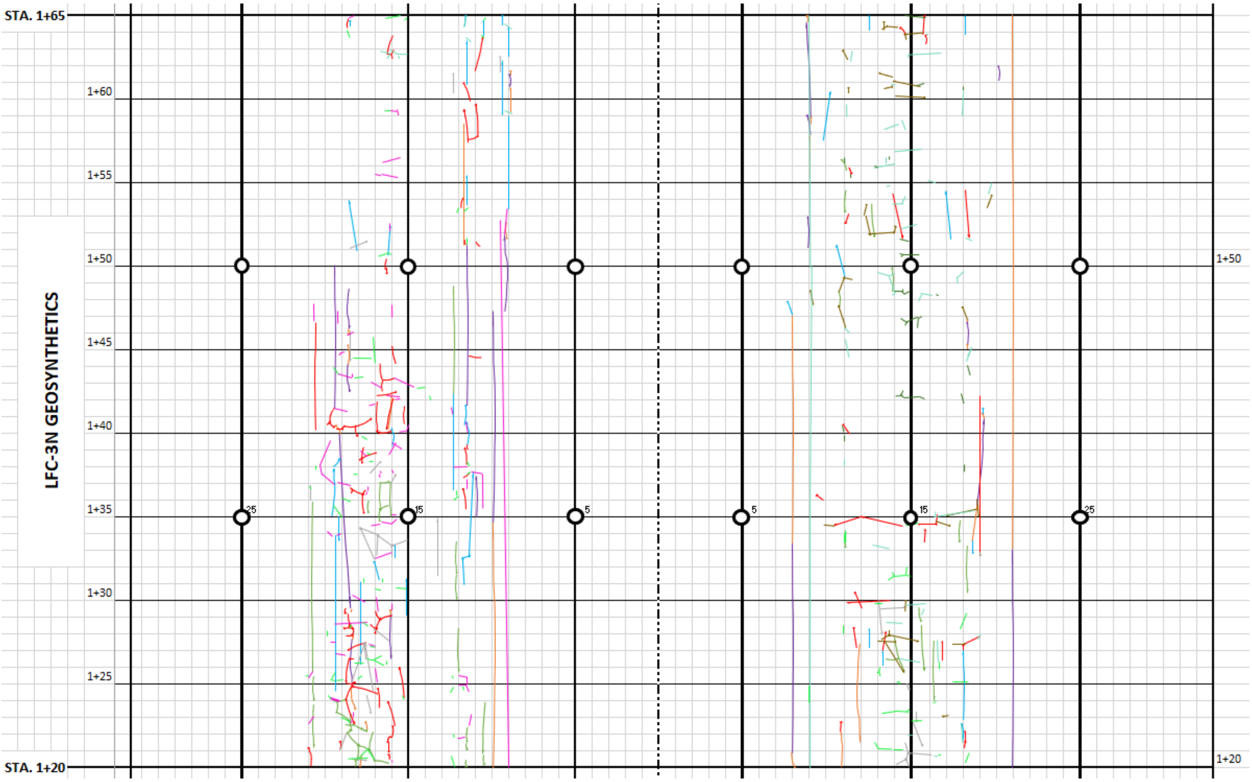

(k)

Figure D-1. Crack Progression LFC-3N & LFC-3S: (a) March 31, 2022, (b) April 8, 2022, (c) April 19, 2022, (d) April 29, 2022, (e) May 5, 2022, (f) May 27, 2022, (g) June 1, 2022, (h) June 10, 2022, (i) June 15, 2022, (j) July 1, 2022, and (k) July 6, 2022

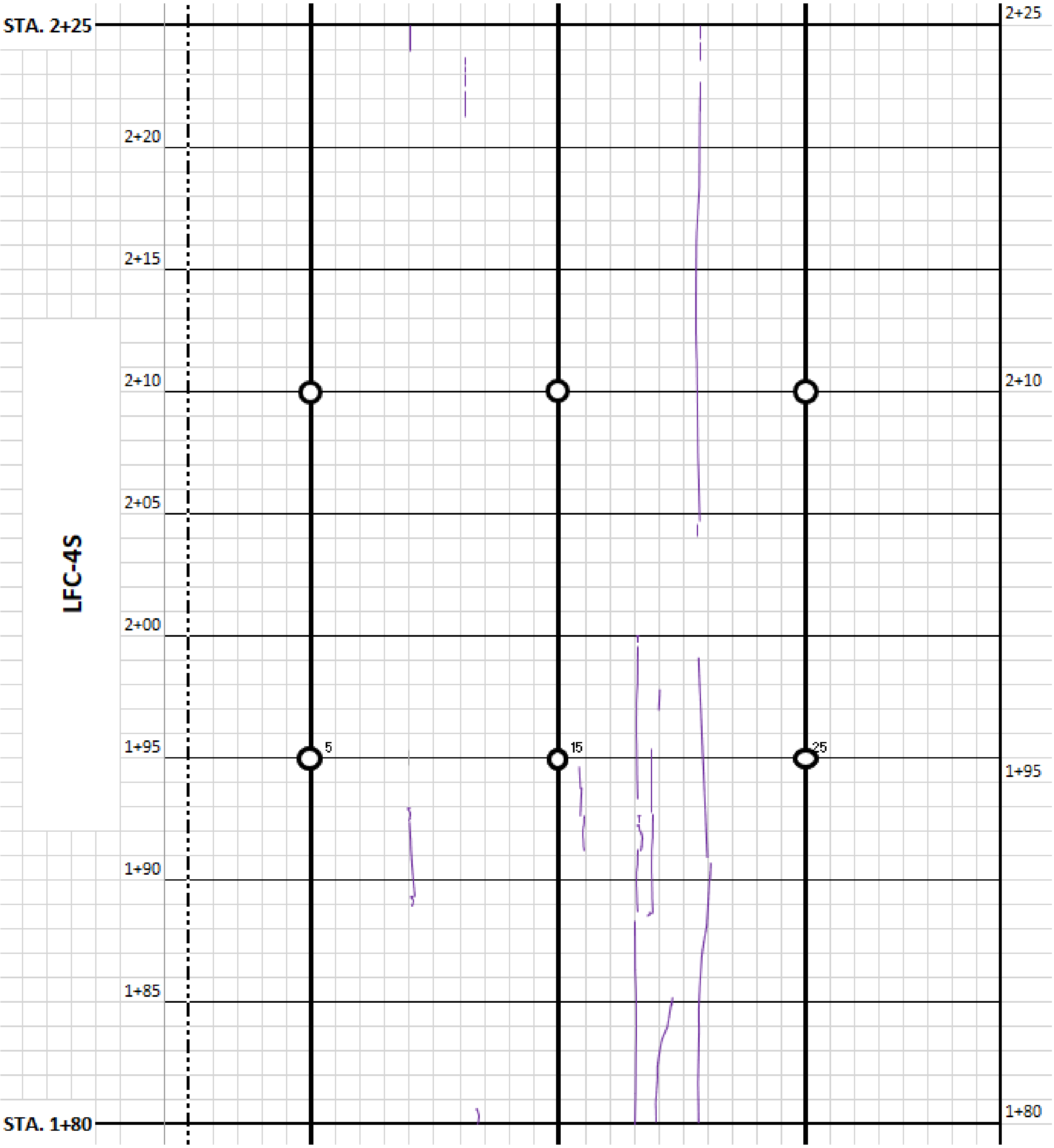
STA. 2+25
2+25
2+20
2+15
2+10
2+10
2+05
LFC-4S
2+00
1+95
5
15
25
1+95
1+90
1+85
STA. 1+80
1+80

(a)

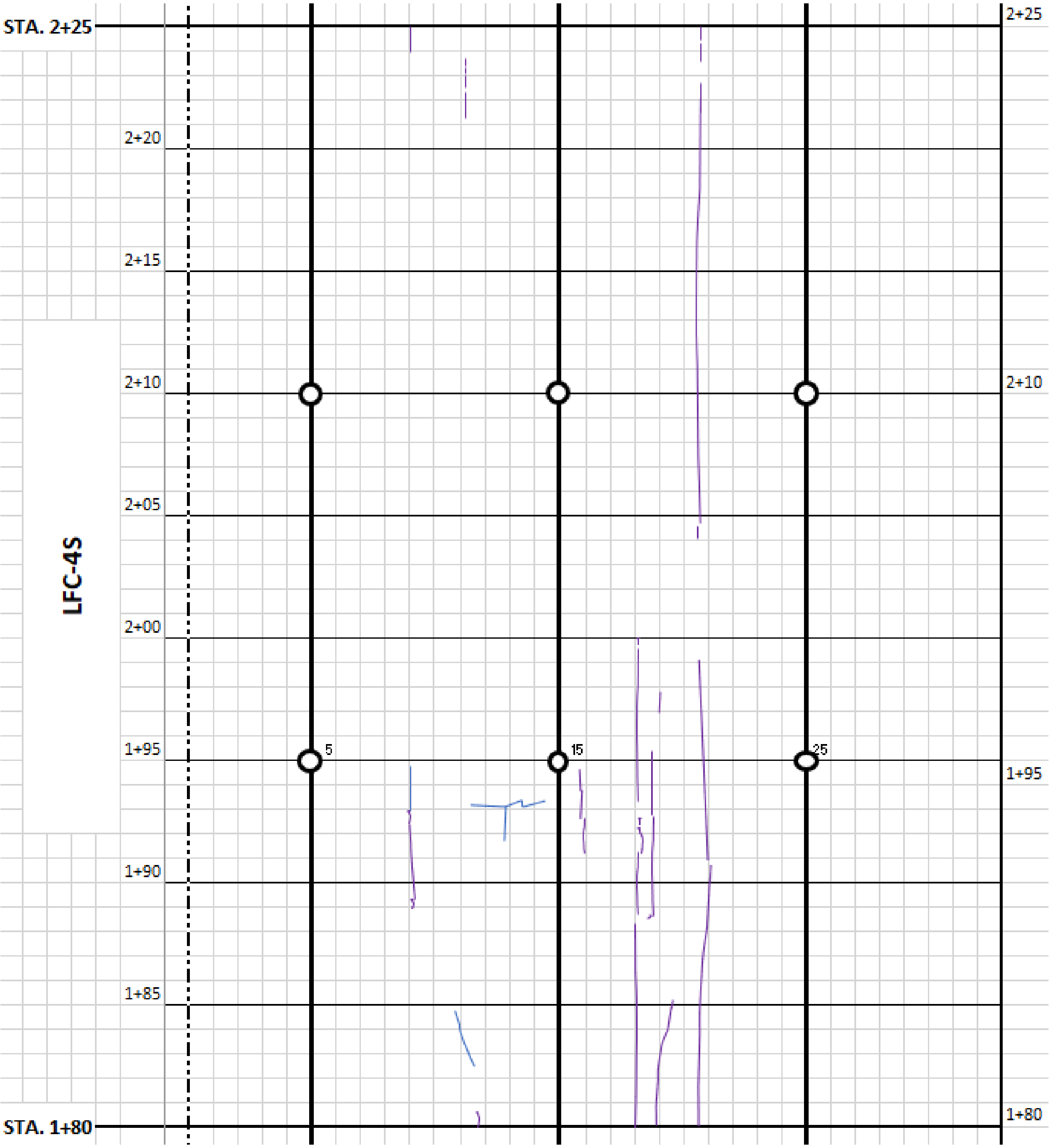

STA. 2+25
2+25
2+20
2+15
2+10
2+10
LFC-4S
2+05
2+00
1+95
5
15
25
1+95
1+90
1+85
STA. 1+80
1+80

(b)

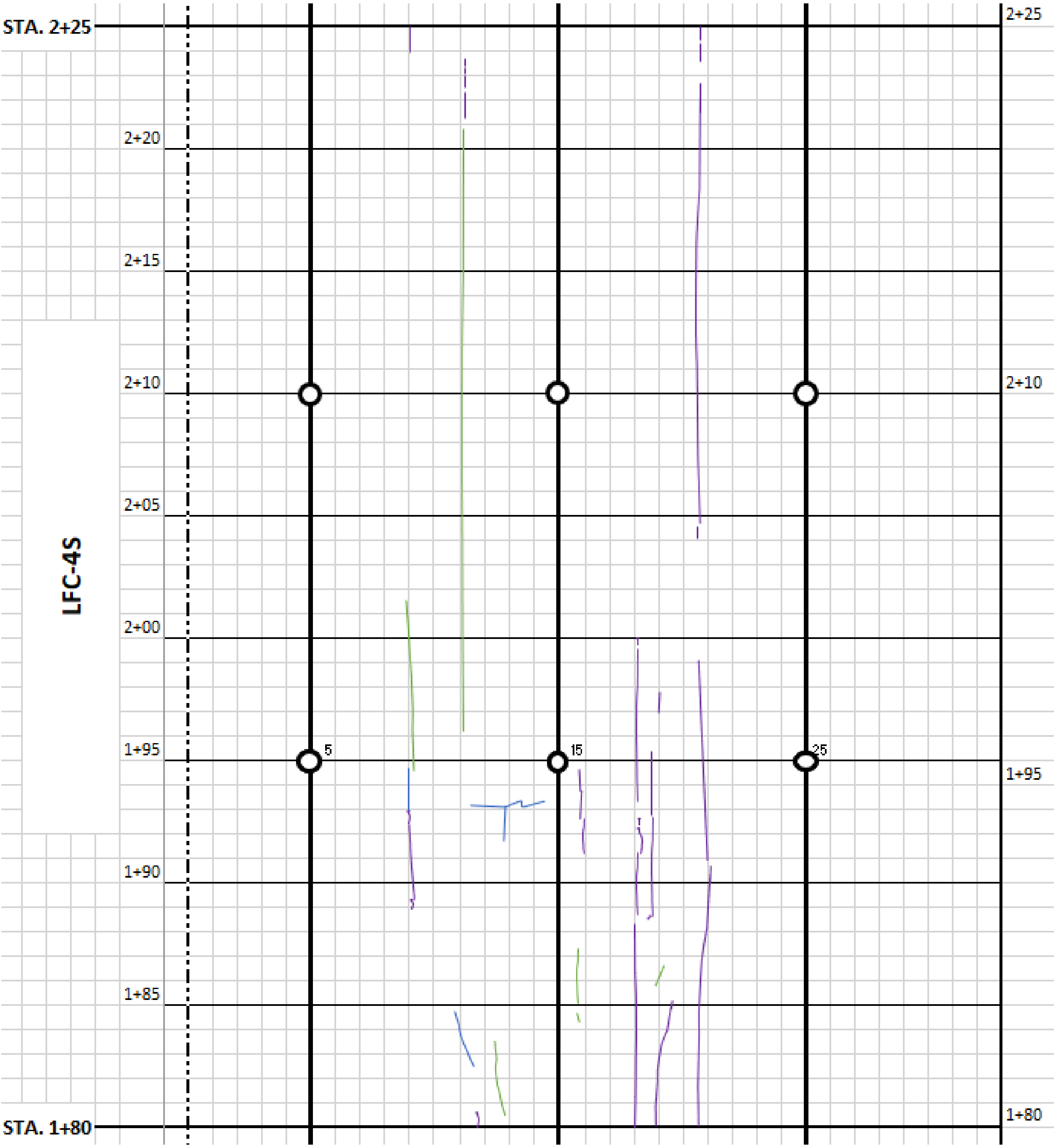
STA. 2+25
2+25
2+20
2+15
2+10
2+10
2+05
LFC-4S
2+00
1+95
5
15
25
1+95
1+90
1+85
STA. 1+80
1+80

(c)

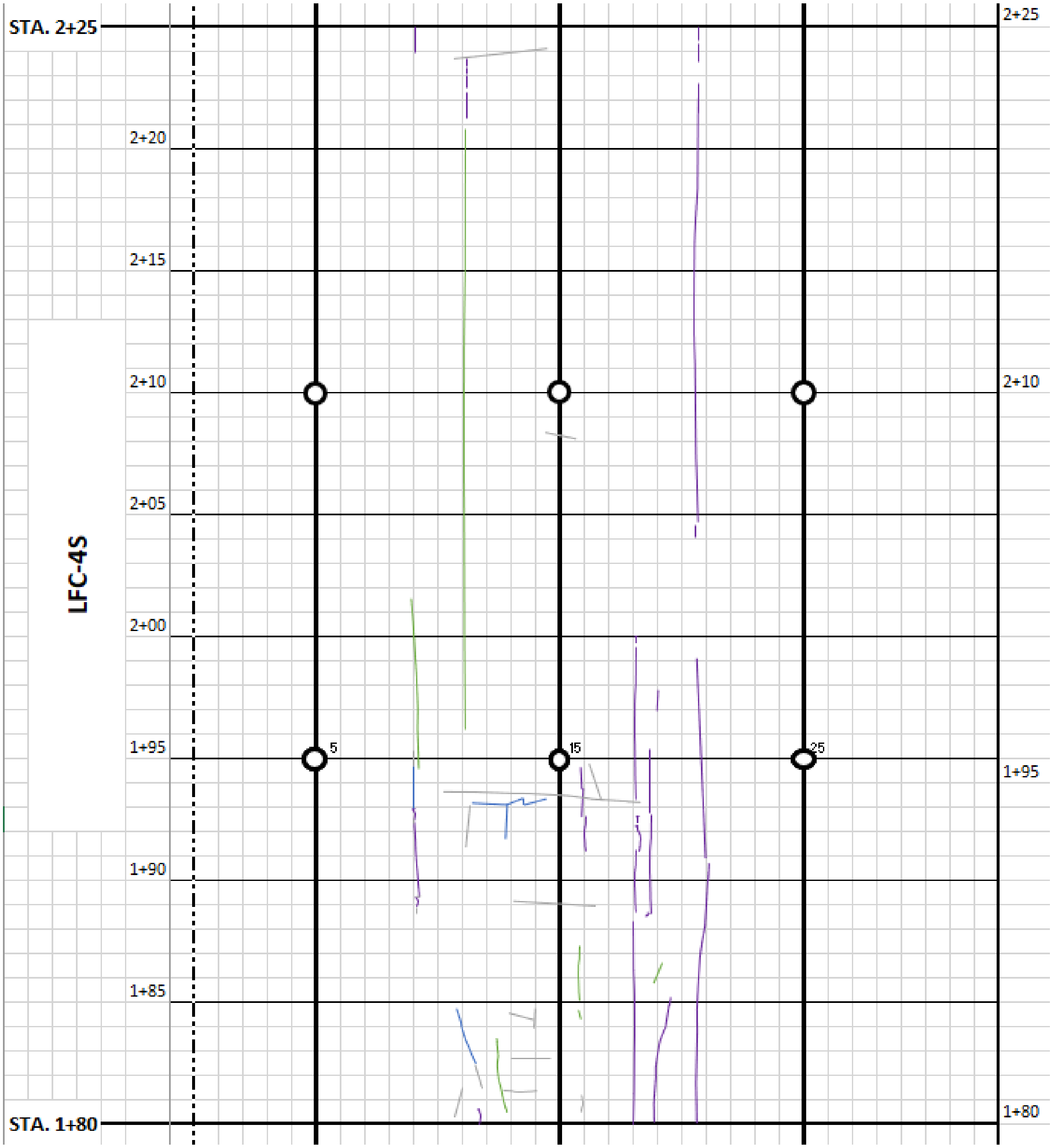
STA. 2+25
2+25
2+20
2+15
2+10
2+10
2+05
LFC-4S
2+00
1+95
5
15
25
1+95
1+90
1+85
STA. 1+80
1+80

(d)

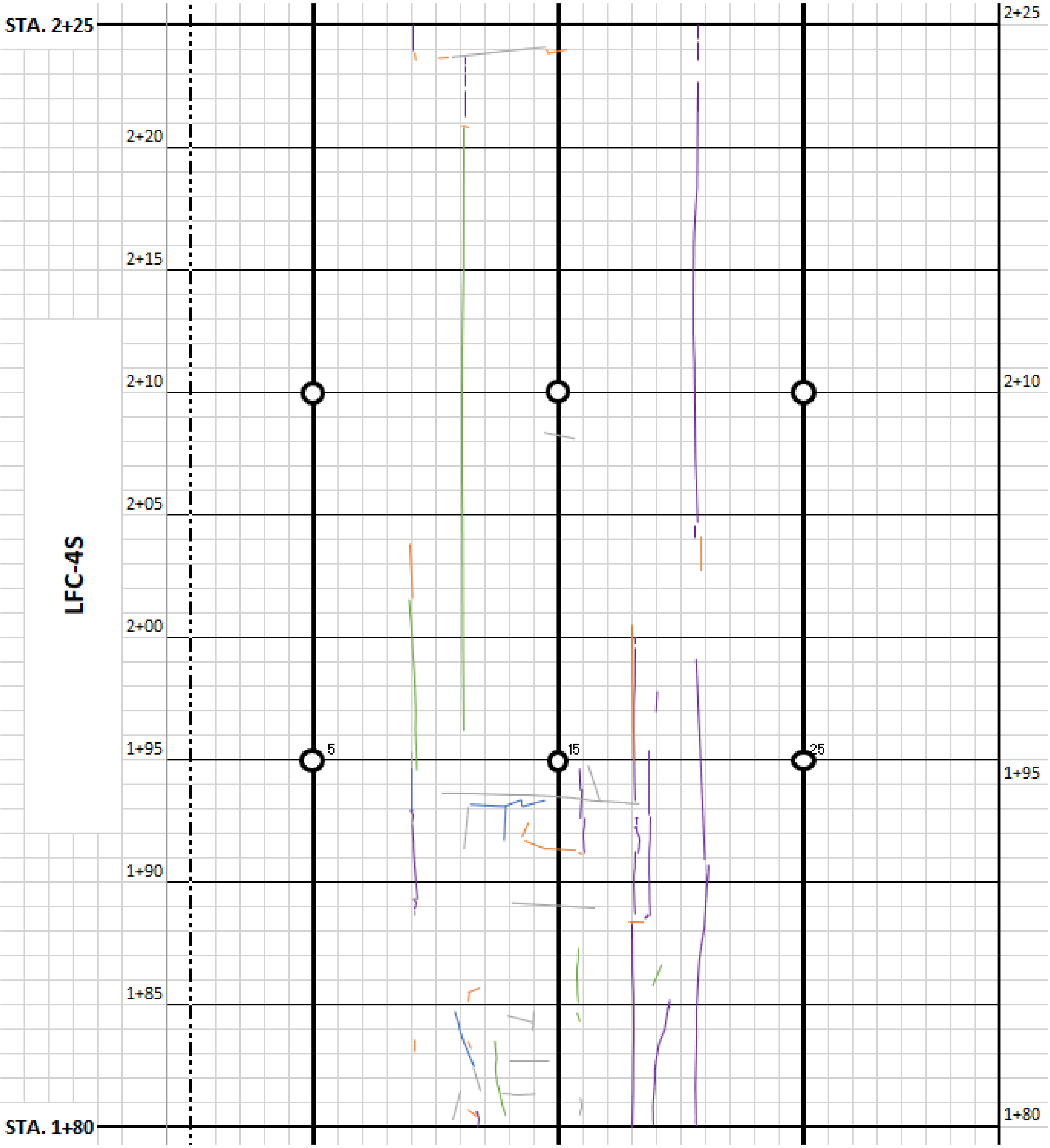
STA. 2+25
2+25
2+20
2+15
LFC-4S
2+10
2+10
2+05
2+00
1+95
5
15
25
1+95
1+90
1+85
STA. 1+80
1+80

(e)

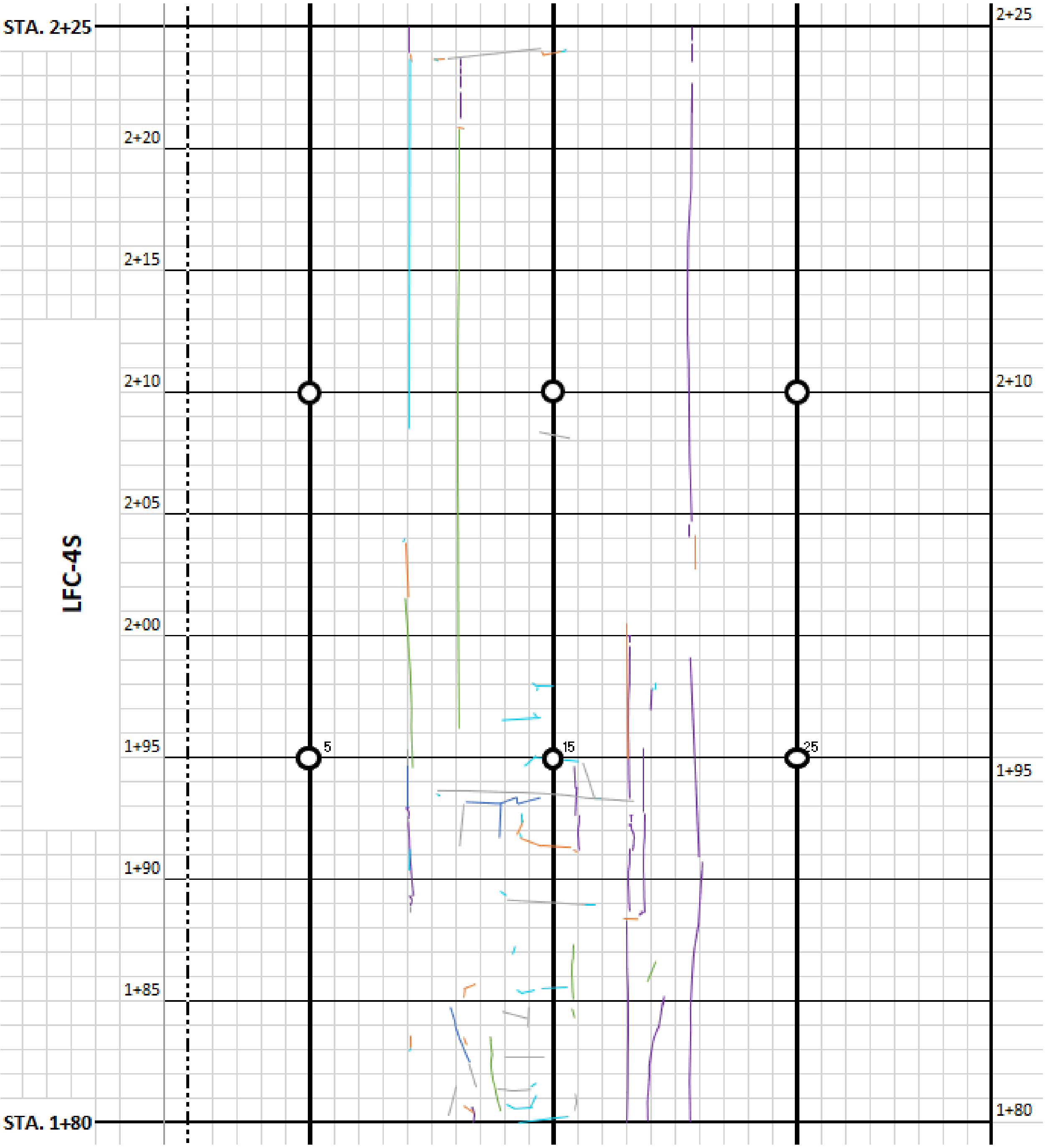

(f)

Figure D-2. Crack Progression LFC-4S: (a) April 22, 2022, (b) April 27, 2022, (c) May 5, 2022, (d) May 27, 2022, (e) June 15, 2022, and (f) July 1, 2022